ROTOR ENDTURN TEMPERATURE PREDICTOR IN LARGE AIR-COOLED TURBO-GENERATORS

A Dissertation
Presented to
The Academic Faculty

By

Ke Xiao

In Partial Fulfillment
of the Requirements for the Degree
Doctor of Philosophy in the
School of Mechanical Engineering

Georgia Institute of Technology

December 2018

ROTOR ENDTURN TEMPERATURE PREDICTOR IN LARGE AIR-COOLED TURBO-GENERATORS

Approved by:

Dr. J.Rhett Mayor, Advisor
School of Mechanical Engineering
Georgia Institute of Technology

Dr. Mostafa Ghiaasiaan
School of Mechanical Engineering
Georgia Institute of Technology

Dr. Thomas G.Habetler
School of Electrical Engineering
Georgia Institute of Technology

Dr. Sheldon M. Jeter
School of Mechanical Engineering
Georgia Institute of Technology

Dr. Yogendra Joshi
School of Mechanical Engineering
Georgia Institute of Technology

Date Approved: October 30, 2018

ACKNOWLEDGEMENTS

The pursuit of this work would not have been possible without the help and contribution of numerous people. I would like to thank my committee members, Dr. Jeter, Dr. Habetler, Dr. Ghiaasiaan, and Dr. Joshi for their time and effort. I am grateful to Dr. Donnell and Ms. Karen Tucker for who did not count their time to help with technical writing.

I would like to thank my lab mate for the lively discussion and debates that have helped my become a better collaborator and engineer. I am especially grateful to Dr. Gallandat for his help with developing the thermal-fluidic network presented in this work. The financial support of this research by Siemens Inc. is gratefully acknowledged.

I am especially grateful to Dr. Mayor for giving me the opportunity to pursue graduate study. Dr. Mayor has constantly challenged me and pushed me to reach higher standards to become a better engineer.

Last but not least, I would like to thank my parents and my friends for their steady support throughout the years. I would have been lost without their companionship.

TABLE OF CONTENTS

LIST OF TABLES

LIST OF FIGURES

SUMMARY

The increasing demand for more electricity have brought about the need for improved rotor ventilation performances of the large industrial turbo-generators. Overheating in the rotor endturn region under the expected operating conditions is one of the major ventilation concern for the air-cooled machines, but a fast and accurate temperature monitoring method is not yet available. The rotor endturn coil temperature evaluations are currently heavily relied on the time-consuming computational fluid dynamics simulations, which posses difficulties in the rotor ventilation design. This presented work develops a fast-solving analytical predictor, which can estimate the rotor end-arc coil temperatures at the expected operating conditions. The predictor is developed using the lumped-circuit method, which has been implemented by many researchers to successfully apply for many electric machines. To do so, the fluid properties in the nested cavities adjacent to the heated coils are first numerically captured with detailed CFD simulations. The cavity flow phenomenon is inspected and a virtual pipe method is proposed to describe and quantify the observed internal bulk flow characteristics. The virtual pipe hydraulic diameters are quasi-analytically determined, by mathematically matching the CFD extracted velocity profile with the expected theoretical profile for the internal turbulent pipe flow. Generic correlations of the defined local virtual pipe segments are developed in terms of the identified design parameters, as a tool to estimate the D_h values for any design scenarios within the applicable ranges of the design parameters. A set of CFD parametric studies are conducted to provide a reasonable sampling set to use for the correlation development. Finally, a thermal-fluidic network is developed by implementing the virtual pipe description of the cavity internal bulk flow, which accounts for convective and conductive heat transfers at the coils to calculate the coil temperatures under different heat loads. The predictor is verified with both the reported factory sensor readings and CHT simulation, and is concluded to be able to achieve the desired ± 5 degrees of Celsius error.

CHAPTER 1

INTRODUCTION AND BACKGROUND

1.1 Introduction

The overarching goal of this research is to develop a generic and fast-solving analytical method to accurately predict the rotor end winding temperature of large-scale, air-cooled turbo-generators in the 350 MVA class, which allows for rapid design sizing and online operation monitoring of the generator systems. Today, generator designs must be cost effective while achieving high reliability and improved efficiency, in order to remain competitive in the global market. The rotor coil temperature, especially in the rotor end winding regions, is known to limit the output of a generator and is one of the major causes of catastrophic rotor failure. Fast and accurate rotor coil temperature predictions would increase performance and prevent losses of millions in revenue from repair and downtime; therefore the ability to make such prediction is crucial.

1.2 Introduction to Large Scale Generators

A generator is a rotating mechanical energy converter which converts mechanical power from the shaft of a turbine into electrical power. The generators used in power plants can be defined in many ways; one classification is based on their cooling systems, which can be by air, hydrogen or liquid cooling. The least efficient cooling system uses water, which include manufacturing complexities including auxiliary water cooling and de-ionizing skids, plus associated piping, control and protection features [1]. Hydrogen is more effective in dissipating heat than air, and its cooling ability increases as the pressure increases. The most commonly used cooling system uses air. This system is low cost, and

can be installed, operated and maintained more easily [2].

The air-cooled turbine generator, or turbo-generator has been a good solution for converting steam turbine power into electrical power ever since the invention of the high-speed generator in 1901. Outputs of these turbo-generators range from relatively small numbers of MegaWatts (MW) to significantly high values, up to 19000 MW. Turbo-generators are designed with two or four poles, operating at rotational speeds of 3600 or 1800 rpm. Generators are made of two basic components, namely the stator and the rotor. The rotor is the high-speed rotating member of the two; it undergoes severe dynamic mechanical loading as well as electromagnetic thermal loading. The stator is stationary but sees significant electromagnetic, thermal and high-voltage loading, as well as dynamic forces in terms of vibration and torsional loads.

This presented research studies a two-pole synchronous turbo-generator, at rated power up to 375 MVA, operating at 60 Hz and power rating of 0.85 to 0.95, as shown in Figure 1.1. The overall machine is about 12 meters long, and 4 by 4 meters in the cross sectional area. This machine is symmetrical in the mid-plane and about the quadrature axis (q). The stator consists of stator windings, an iron core and a frame, as labeled. The core is used to produce a strong magnetic field for the generation of voltage, and is built up from thin laminations with each lamination insulated on both sides to reduce eddy-current loss and its associated temperature rise. The stator frame can be divided into an inner and an outer part. The inner frame is designed to support the stator core and the windings while providing guidance for the air flow into the machine. The outer frame is simply an enclosure. Finally, the stator winding is made up of insulated copper conductor bars that are distributed around the inner diameter of the stator core.

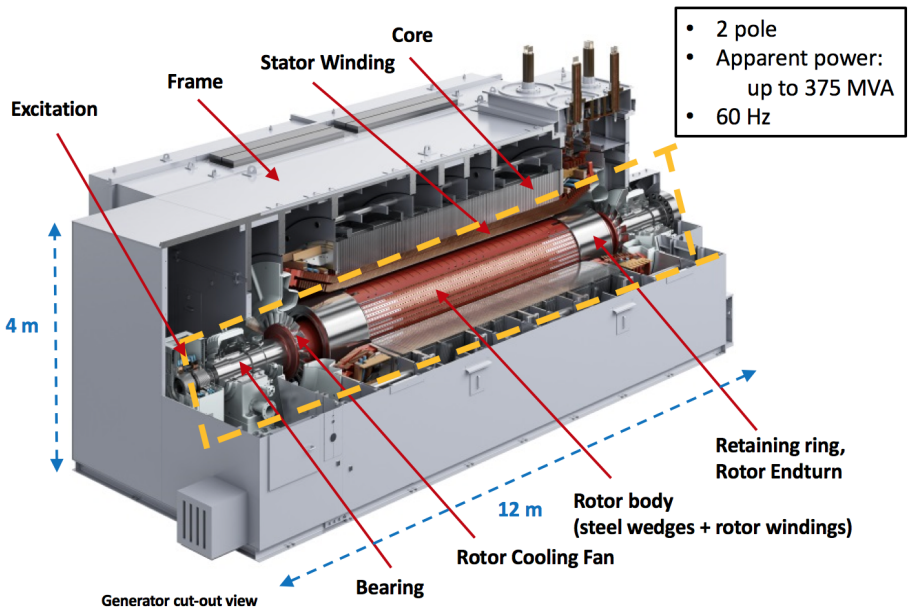

Figure 1.1: Cutout view of the generator model studied [3].

Overhung in the middle is the rotor which produces the rotating electromagnetic field necessary for the excitation of the stator windings. This rotor consists of two axial fans, a rotor forging, two retaining rings and rotor windings. The rotor forging is generally a one-piece solid forging, which is made of highly permeable magnetic steel to carry the flux produced by the rotor windings. The rotor windings are installed in the slots in the forging body, placed symmetrically around the rotor between the two poles. Each winding itself is made up of stacked turns of copper to form a series of connected windings. The retaining rings are used to hold the end-winding rotor windings against the strong centrifugal force during operation, and thus are the most stressed components in the generator. Generator designs are limited by many factors, one of which is the I^2R heating of generator components. For example, for a 750 MW generator, the I2R loss per unit mass of conductor material is of the order of 150 W/kg in the stator but 500 W/kg in the rotor [4]. Therefore, the rotor is the limiting factor that defines the generator output. As a result, an effective rotor cooling design is critical.

A number of tests are performed to measure the characteristics and losses of the generator. The tests of interest in study are [4]:

1. The ***mechanical test (MR)*** that drives the machine at the rated speed with a small or no field current supply to the rotor windings, in order to evaluate the mechanical loss and windage loss of the system.

2. The ***short-circuit test (SC)*** drives the machine at the rated speed with the stator windings on short-circuited while the field current are varied to give the stator currents up to the full-load value. The short-circuit tests are performed to measure the mechanical, stator and load losses summated.

3. The ***open-circuit test (OC)*** drives the machine at the rated speed with the stator windings on open circuit while varying the field current, to measure the friction and windage losses, and the core loss and mechanical loss separated.

As complicated as the tests are, the aspect that relates to this study is the amount of Ohmic loss (I^2R) in the rotor windings that heats up the rotor coils.

1.2.1 Common Generator Ventilation Scheme

Ventilation designs are directly related to the generator performance, including its efficiency, reliability, power output and service life. Losses in a generator are from currents in conductors and fluxes in ferromagnetic circuits, which all appear as heat. The internal flows of heat, from the start region to the surfaces where heat is being transferred to the coolant, are important in determining the thermal conditions and hot spot temperatures to which the associated insulation is subjected. Heat is dissipated, by the combination of three-dimensional conduction, radiation and convection heat transfer effects, to the ambient air and the surroundings, through cooling domains with various geometric features and length scales. The radiant energy interchanges between two surfaces is affect by: (1) the view factor, (2) their surface emissivity, and (3) absolute temperatures. Convection heat transfer from a surface to the coolant fluid causes fluid to expand, to create a thermal head and a consequent circulation [4]. The temperature rise in machine components is related

to: (1) the rate of heat production, (2) the thermal capacity, and (3) the rate of cooling [4]. In the design of a generator, electrical design determines the dimensions of components but needs to be redone if the computed loss distribution of each section can not meet the satisfactory temperature distribution [2]. Many air cooling schemes have been developed over the years for various types and sizes of turbo-generators.

The overall generator cooling systems can be first categorized based on the configurations; these are open ventilated systems or totally enclosed systems with water-air cooling. In large machines, absorbed heat in air is always transferred to water in heat exchangers that are located within the machine enclosure at the end of the ventilation cycle. The cooling systems can also be radial or axial ventilation systems, which are implemented mainly depending on the size, type and power rating of the machine. In the axial system, the air is mainly driven by the fans situated at the extremities of the rotor. The air flows through the inter-polar spaces and the air gap before entering the stator ventilation channels. In the case of the radial cooling configurations, the rotor is also used as a radial fan which contributes to the air pressure build up. The air eventually flows radially through the ducts in the rotor into the stator channels [5].

For the overhung cylindrical rotor in the middle, there are two cooling schemes, single ended or double ended, as shown in Figure 1.2. The single ended ventilation system only has one area for the air intake and one area for the air outtake. The double end ventilation circuit has two air inlets at the drive end and the non-drive end, with one air outlet at the stator lamination core. In both cases, the airflow occurs though a number of parallel branches. The double ended system presents a symmetric airflow circuit, which provides a better airflow distribution in the machine. Porepp [6] compared the resulting thermal distribution in both systems by using a thermal calculation software, and showed that the single ended system has the advantage of being easily incorporated into heat designs because the total flow rate can be changed simply by changing the fan. But the double ended system has a better cooling performance that provides a more homogeneous heat distribution along

the rotor length at a higher ventilation efficiency.

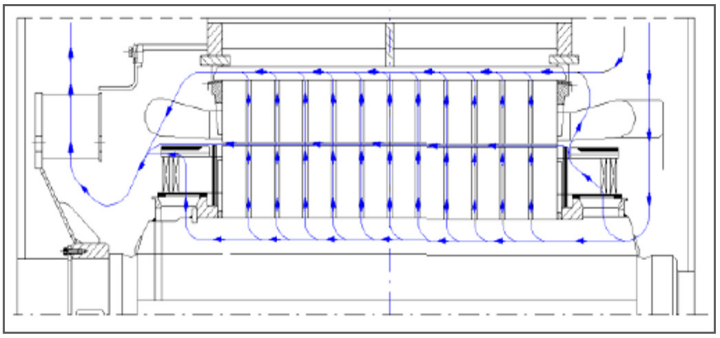

(A) Single ended

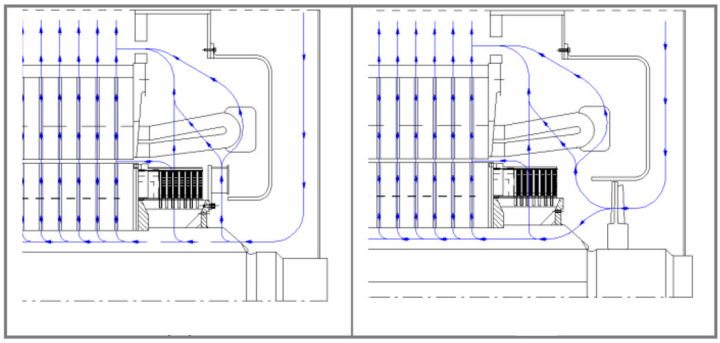

(B) Double ended

Figure 1.2: Flow paths of (A) single ended and (B) double ended with (left) and without (right) axial fans ventilation system of cylindrical rotor machines [6].

The studied turbo-generator is a double ended axial cooling machine. Due to symmetry in the generator construction, the ventilation circuits are also symmetric and therefore only a quarter of the machine needs to be studied, as shown in Figure 1.3. This is a nine zone machine, with four inlet zones and five outlet zones. After the fans, the air is divided into three paths, as labeled. Path 1 flows directly into the rotor into the regions beneath the rotor end winding. Part of this air is discharged through the ventilation holds at the end of retaining ring. The rest enters the rotor ventilation slots (subslots), and is radially discharged near the end of the rotor in the airgap over the entire length of the rotor until it reaches the symmetry mid-plane. Path 2 flows over the stator end windings into the endbox, then into the feed pipes, feeding the stator inlet zones. Path 3 enters the air gap over the rotor retaining ring, feeding the stator outlet zones, then exits through the outlet stator vents

into the outer enclosure, and feeds back to the blower inlet where the ventilation circuits re-start.

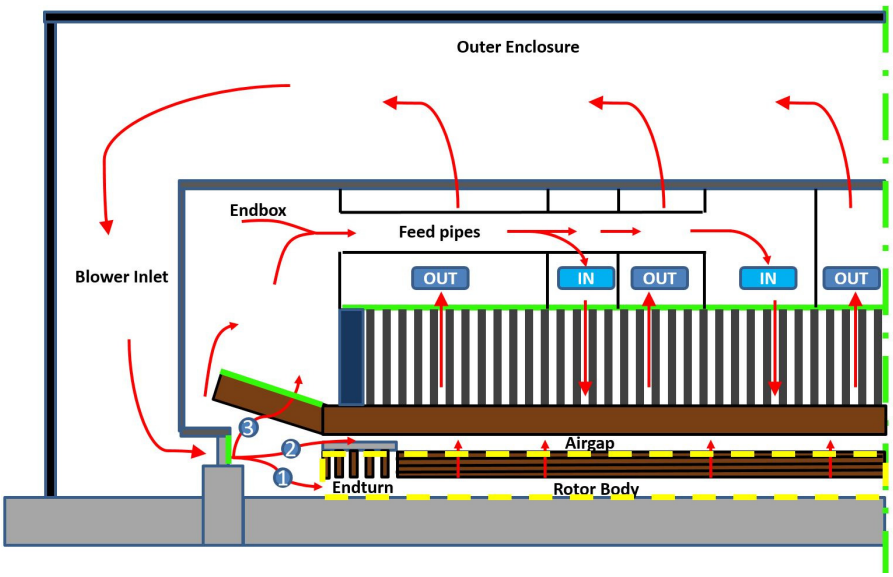

Figure 1.3: Simplified ventilation diagram of the double ended generator model studied.

At present, the initial analytical design sizing of large-scale electrical generators is based on empirical correlations, rule of thumb criteria and heuristics. These design methods can no longer meet the expected level of accuracy for high power rating machines to ensure cooling efficiency. This issue is especially compelling in the rotor cooling regions, since they inherently pose more complex flow physics which require advanced analysis, due in part to the three-dimensional fluid dynamics and heat transfer associated with the rotational and internal flow distributions. Therefore, a comprehensive thermal-fluidic study of the rotor ventilation system is necessary. But for large and complex electric machines, analytical solutions are often times not available, since the three-dimensional Navier-Stokes equations cannot be solved. As a result, generally there are three approaches to conducting thermal analysis for electric machines [7]: through experimentation, through using the analytical lumped circuit method, and through the use of numerical methods such as finite element analysis (FEA) or computational fluid dynamics (CFD).

1.3 Importance of Rotor Winding Temperature Prediction

Winding temperatures in the generator rotor at given operating conditions need to be accurately predicted for two reasons: (1) From the service perspective, accurate temperature predictions improve generator performance and service life, minimize maintenance downtime and cost, and most importantly avoid the high cost in time and money for rotor winding to be rewound and even rebuilt due to damage from overheating; (2) From the design perspective, improvements in thermal predictions can also reduce the number of prototype iterations needed, therefore minimizing cost.

1.3.1 Service Perspective

Generators are the most expensive pieces of equipment in a power plant; therefore improving the operating efficiency and reducing the maintenance costs of generators is critical in today's competitive environment. Utilities are now starting to incorporate real-time online monitoring and diagnostic systems for the generators to prevent generator failure. Early warning of generator overheating can mean the difference between a brief shutdown versus a major overhaul that could take months of costly downtime.

The most common cause of rotor failure is the shorted turns that are the result of insulation failure between individual windings in the rotors. The insulation failure can be caused by heat related damage, mechanical wear or operating incidents, and are more likely to occur as the generator rotor ages [8, 9]. Even though realistically, most commissioning generators are operated with shorted turns, but the number of shorted turns should not exceed 5% of the total number of turns, as concluded by AGT services, Inc. [8]. Shorts can occur anywhere in a generator, but they most commonly occur in the end windings under the retaining rings [9]. Even though at the early stage, shorts do not present detrimental

risks to the machine, the consequences of operating a field with shorts can be substantial. Problems with shorted turns include [8, 9]:

1. Uneven Ohmic losses I^2R in windings between the poles, since the shorted turns operate at lower temperatures than the active turns, which leads to uneven heating of the rotor forging, and leads to rotor bowing and thereby excessive vibrations.

2. The generator's inability to reach the reach the nameplate rating, since the output of a generator is a direct function of the amp-turns values of the rotating field. If the field current is increased as a remedy to maintain the amp-turn value, it adds additional cost to the power producer (for example, if two out of a seven-coil field are shorted, a 14% increase in field current is required), and increases the hot spot temperatures at the same time. These will in turn accelerate the damage to the insulation systems, thereby accelerating the temperature related deformation of the windings.

3. Retaining ring arcing damage, similar to the one in Figure 1.4. Here, the top turn of one coil comes into contact with the top turn of an adjacent coil, and this leads to arcing, which burns though the retaining insulation and causes defects in the retaining ring itself. Structural damage in the retaining ring is a very serious condition which can lead to direct rotor failure and rise to increased safety issues to the plant personnel.

4. A thermally sensitive generator field may be developed.

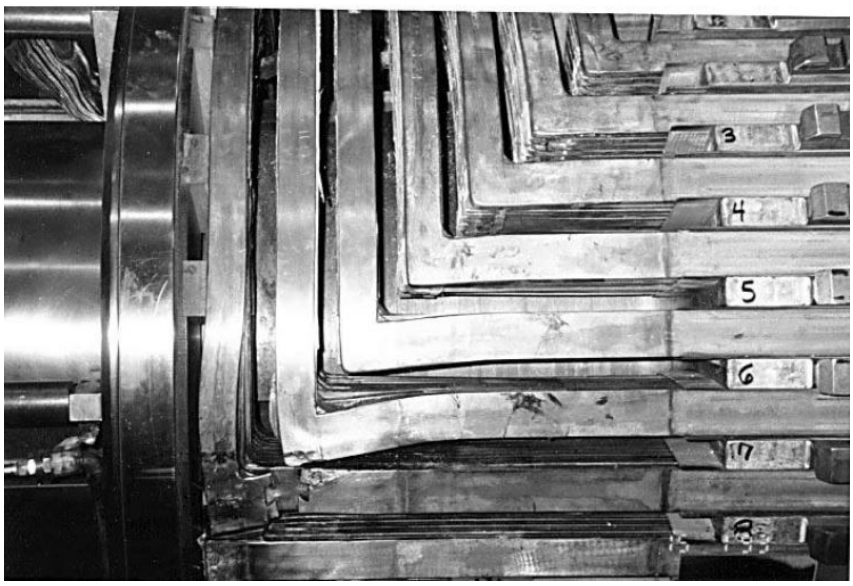

Figure 1.4: Elongated coil contacts coil caused by shorted turns [8].

These short related issues affect the rotor performance at different levels, which at the worst case scenario, may require a full field rewind to replace all winding insulation.

Equally important as the generator performance capabilities, power reliability is a critical issue for many customers, representing a quantifiable business, safety and health risk to their operations. In addition, the direct repair cost of a failure can range from a few hundred-thousand dollars to many tens of millions of dollars. The cost of a major generator failure to a utility or IPP (Independent Power Producer) owner is not only the cost of repair or replacement of the damaged machine, but also the substantial cost of purchasing replacement power when the unit is out of service [10]. Loss-of-generation costs can exceed $200 million on a major failure of a large generator [11]. During the blackout of 2003, portions of the Midwest, Northeast, and Ontario, Canada were without power for up to four days in some locations. Total losses related to the power outage were estimated to top $10 billion, with more than $50 million people affected. During the failure of a generator at PacifiCorp's Hunter Unit 1 in Utah in November 2000, not only did IPP had to cover the expense of a complete generator rebuild, it also was very costly to replace the lost power. According to the utility, from the time the unit went off line to its return

to service in May 2001, the additional cost for purchasing replacement power was $270.1 million. Therefore, rotor end winding temperatures need to be accurately and freqently assessed, to assure their temperatures are within the allowable operating temperature of the insulation layers.

1.3.2 Design Perspective

A comprehensive synthesis program might take several years to develop, and could be both restrictive and obsolescent when completed [4]. Therefore, even a small improvement can be substantially helpful in generator design. Electrical design is conducted first to determine generator construction; the entire design will need to be redone if it does not meet the ventilation requirement. Therefore, fast and accurate coil temperature prediction can also provide the opportunity to optimize the thermal design of machines at an early stage without the need for extensive and costly experimentation. Accurate thermal predictions also allow the calculation of maximum continuous rating which the cooling scheme allows without overheating, considering that the torque, or the maximum RMS current density in the windings is thermally limited in a machine of good electromagnetic design. Uncertainties in coil temperature predictions lead to the use of excessive safety margins [12] and thereby the service factor.

Reducing material has been a common method employed in order to meet the requirement for cost reduction, but one consequence is the increase in rotor temperature. For example, decreases in the cross-sectional area of the windings can increase the resistance, and thus increase the I^2R losses and increase the winding temperature. With the existence of a fast-solving coil temperature predictor, changes in winding designs can be easily tested to save design time.

While the presented work focuses on developing an analytical method for winding temperature prediction in the end winding region of one specific rotor design, the rotor has a construction widely used in many generators at similar power ratings. In fact, the developed

method can be easily implemented on 50Hz and hydrogen cooled machines with similar ventilation designs, since the physics behind the analysis is universal.

CHAPTER 2

LITERATURE SURVEY

2.1 Introduction

Generators have been studied extensively ever since they were first invented by Tesla and Westinghouse. The scientific literature has documented the many related studies, focusing on reducing material losses (rotor and stator core losses) and improving power ratings and generating efficiency [7, 13]. Published articles about generators include topics ranging from electromagnetic performance enhancements, through improved insulation and conductor properties, to structural and ventilation design investigations. Among those topics, ventilation studies, especially rotor ventilation systems, have received less attention than they deserve.

Rotor ventilation is a broad topic that includes the study of coupled physical interactions of the fluid dynamics of the rotor cooling gas and the associated thermal transport of the winding heat to the cooling gas streams. While some studies have addressed various aspects of these cooling schemes, a detailed inspection of the literature identified less than one hundred studies that specifically consider the thermal analysis of the rotors of large-scale, air-cooled turbo-generators. Published literature on fluid and thermal studies of similar electrical machines is discussed in this chapter. The number of papers found based on keyword searches is summarized in Table 2.1.

Table 2.1: Summary of literature survey results on thermal analysis of related topics

Keywords	**Num. of Articles**
Thermal analysis AND generator	1621
Thermal analysis AND Large generator	304
Thermal analysis AND Large generator AND Rotor	44
Ventilation AND Generator	225
Ventilation AND Large-Generator	79
Ventilation AND Large-Generator AND Rotor	26
Computational fluid dynamics AND Generator	189
Computational fluid dynamics AND Large-Generator	31
Computational fluid dynamics AND Large Generator AND Rotor	7

In addition to the actual content of the publications, it is also of interest to study the evolution in research over the years, specifically in the fields of rotor ventilation. The number of publications by year through the lens *rotor ventilation* is summarized and shown in Figure 2.1. It is found that the studies of rotor ventilation of generators can be traced back to the early 1920s, and they increase every few years. Studies of this topic peaked in 2012. Even so, publications in this category still do not provide a good understanding of ventilation systems in large generator rotors.

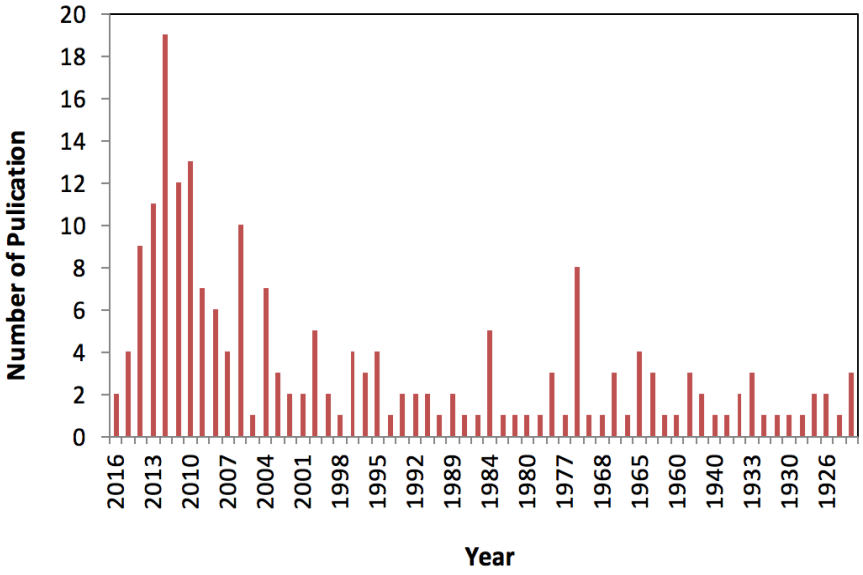

Figure 2.1: Summary of the number of relevant publication by year.

Publications on the use of CFD software to investigate the performance of large generators, papers included the study of smart blade design [14], through the investigation of insulation properties on rotor temperature distribution [15], to fluid conditions and the cooling performance of airgap with no axial flow [16], to wind generators [17], and to rotor body length [18–20]. An even broader range of topics is found on ventilation studies. They include ventilation design issues and improvements over the years, focusing on material, electro-magnetic or mechanical considerations [20–27]. Some studies mentioned the methods of conducting ventilation studies on electric machines, which include hydro-generators, wind generators or air-cooled generators at various power ratings and with different geometries and operating systems[18, 28–32]; other studies are focused on the ventilation performance of sub-domains in the stator or the rotor body only [18, 27, 32–38]. The largest number of papers found are related to thermal analysis. Other papers found include electro-magnetic/mechanical related studies such as structural analysis, field loading and material selections investigations [15, 39–41][42–59]. Many studies focused exclusively on wind generators and hydro-generator[43, 53, 54, 57, 60–64], and the rest are focused on designs of field monitoring systems [39, 47–50, 52, 54, 59, 65–67].

Only a few studies were found to be related, though weakly, to the proposed study [16, 29, 30, 37, 46, 61, 68–70]. These papers can be categorized into two perspectives: (1) ventilation methodologies for electric machines, including both numerical and analytical methods; (2) large scale air-cooled generator ventilation domains' thermo-fluidic performances. Both are summarized and discussed in the next sections.

2.2 Ventilation Study Methodologies of Electric Machines

This section reviews the methodologies that can be applied for generator ventilation studies. The feasibilities, advantages, and disadvantages of each method will be discussed and compared to determine a ventialtion study approach for the presented generator model.

2.2.1 Difficulties in Winding Temperature Measurements

The most straight forward way to study ventilation is through direct temperature measurements. The temperatures of parts of a electric machine can be measured by: (1) using a thermometer for one point at the surface of the part; (2) tracking resistance for the windings only, which estimates the mean temperature rise by use of the resistance temperature coefficient; and (3) using an embedded temperature detector that gives the temperature at one internal point [4]. But in practice, the implementation of these detectors is very difficult for large scale, high speed, high voltage generators. First, the problem of insulation prevents the detectors from being placed too close to the conductors [4]. Second, embedding resistance temperature detectors into the strands is difficult, since they must be wired along the line of a strand and to the end a bar, therefore sensors are conventionally embedded between the top and bottom bars to detect winding temperature [71]. Last, sensor failure can happen during assembly since the sensors are at risk to break during bending, stacking, consolidating, insulation taping and curing of copper turns. The sensors need to be calibrated after assembly to ensure reliability and accuracy. The sensors may also fail

to survive during operation, as a result of the additional forces experienced from the rotational motion. As a result, detector location avaliabilities are low, and sensors cannot detect the hot spot temperatures. In sum, the level of complexity required is not proportional to the quality of output for direct temperature measurements with thermal detectors; therefore this method is not considered in this study.

2.2.2 Analytical Lumped Circuit Method

The analytical method was developed and implemented long before the invention of numerical analysis software, and continues to serve as an effective approach to temperature prediction for electric machines. This method has been widely used and verified for modeling complex cooling systems. It offers a quick way to determine the temperature distribution and offers an economical way for users to observe the changes in output that result from changed inputs. Traditional ventilation analysis uses the analytical lumped circuit method, which is to develop fluid and thermal networks along the body of the target machine. Networks are developed by lumping components with similar temperatures together as a single node.

When using this method of analysis, definitions of resistances are important for setting up the networks. Thermal resistances include the effects of conduction, convection and radiactive heat transfer. Radiactive heat transport in electric machines is found to be small compared to the other two forms of thermal resistance, as Boglietti et al. [7] have mentioned that the radiactive heat transfer coefficients range from 5.7 $w/(m^2 \cdot C))$ to 8.5, from part to part, in a typical motor assembly. These values are almost negligible compared to the conduction and convection coefficients, which are expected to be on the order of hundreds. Therefore, radiactive heat transfer is not considered in this study. Flow resistances include changes of flow conditions or fluid friction at wall surfaces [7]. In electric machines, the latter is negligible compared to the first. Flow resistances for all types of changes along the flow passage can be calculated by characterizing these losses with the

coefficient k, which is the dimensionless coefficient of local fluid resistance (obstruction, expansion, etc.), and which can be calculated with empirical formulations available in the technical literature.

With these calculations completed, networks can then be developed following the construction of electric circuits. A thermal network (TNM) is built on the following equivalences: temperature to voltage, power to current, and thermal resistance to electrical resistance. A flow network is built based on the following equivalences: pressure to voltage, volume flow rate to current, and flow resistance to electrical resistance. A thermal network is developed by dividing uniform nodes along the rotor body and rotor conductors, then applying thermal resistances and losses to calculated temperatures in each node [68]. This method calculates an average temperature for each element and employs network theories to analyze the thermal characteristics of the system.

Today, commercial software is also available to build and solve detailed fluid and thermal networks. Figure 2.2 is a circuit developed for a 22.5-kVA synchronous machine using a commercial software named $MotorCad$, which calculates both airflow and heat transfer in the machine. Conduction, convection and radiation are all considered in this presented network. The predictions of rise in the network's temperature and changes in its air flow are proved to be within 10% of the measured values [72].

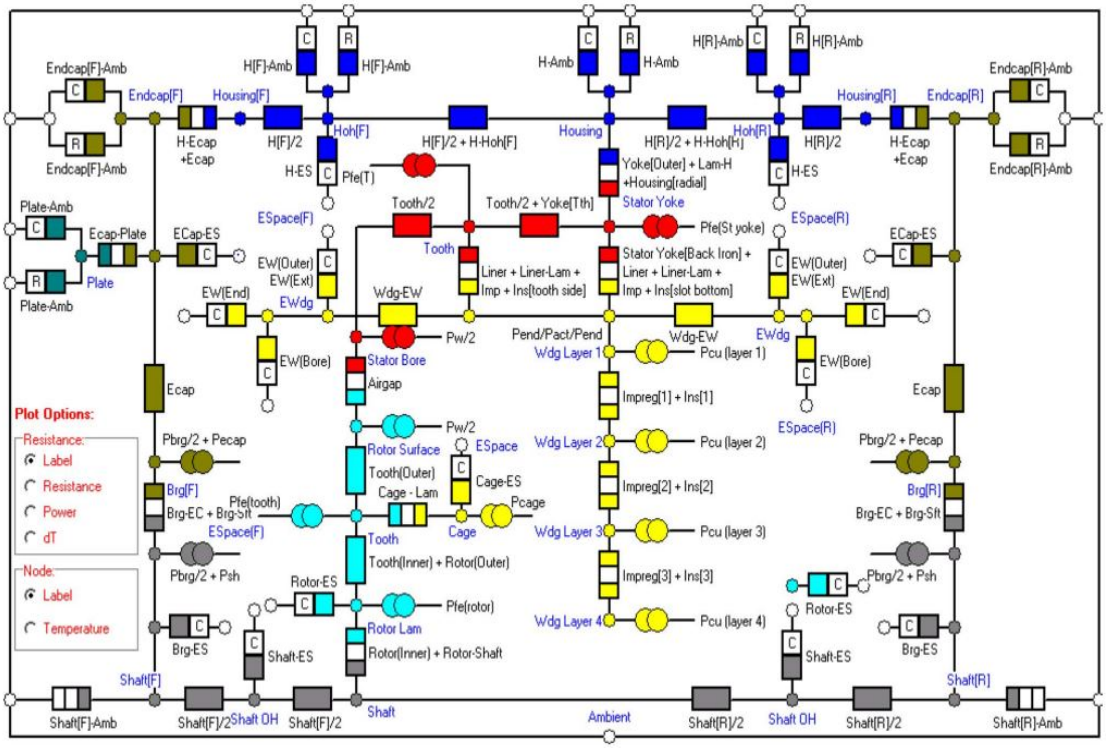

Figure 2.2: Example of a heat transfer network for an electric machine developed with the commercial software *MotorCad* [7]

In short, lumped-circuit thermal models have been validated on numerous machines, which gives a high level of confidence in such models [7]. But major downsides of this method are

1. It can be very big for complex machines and is less accurate when applied for complex geometries. For example, the above MotorCAD model network is already big and complex, but is only for a kWA class machine; it will be many times larger for a MVA class machine.

2. The discretization level for complex machines becomes more difficult to define as the temperature distribution become a less uniform and more unpredictable.

3. The definitions of the thermal network also largely affect the accuracy of the network, especially when it is not easy to find an appropriate description of

the characteristic lengths of cooling domains in these complex machines to calculate thermal resistances.

Therefore, even though the networks can be quickly computed once set up, the developer is required to have extensive experience and knowledge of the machines to make appropriate assumptions and simplifications. A developer must make a major time investment beforehand in order to model the fluid and heat transfer paths. Therefore, when applying the circuit method on large scale electric machines, it is more realistic to implement on segmented smaller sub-domains, where quantitatively descriptive bulk flow is available, and temperature paths are considerably more uniform.

If the lumped circuit method were to be developed for the rotor end winding region, many obstacles would be presented. Based on the literature survey, very little information is available to help quantitatively describe this domain; therefore the parameters needed, such as the characteristic length and the loss coefficients etc., are hard to define. The rotor end winding flow domain is also noticed to have geometries that, constantly vary in features and length scales, which adds additional difficulties for this method. Last, the temperature distribution is unknown which leaves the discretization level yet to be properly determined. Until more information become available, circuits will end up being either over simplified, which reduces accuracy, or overly detailed that reduces the time efficiency advantage.

2.2.3 Numerical Methods

Numerical methods have become more and more popular in the past few years, especially for the study of electric machines. They have become more user friendly with improved capability of solving big and complex models, as a result of the development of computer technologies. Commonly used numerical methods available for thermo-fluidic studies are computational fluid dynamics (CFD) and finite element analysis (FEA). Both methods have an advantage over the lumped circuit method because they are visually accessible during results extraction and comparison. Individually, FEA allows the study of

heat transfer in solid regions only, and when convection heat transfer is involved, it requires the same analytical or empirical algorithms used in the thermal network approach [7]. FEA also offers solutions for very complex geometries where the lumped parameter method is no longer applicable. FEA still requires simplifications and assumptions to be made when a model is set up, regarding the randomness of the conductor placement, the impregnation goodness and any gaps between the slot liner and the stator lamination [7].

Modern CFD codes normally use the finite-volume technique to solve the Navier-Stokes equations, complimented by a selection of validated and proven physical models, to solve laminar or turbulent flows and their associated heat transfer to a high degree of accuracy. CFD applied to the design of an electrical machine primarily aims to determine flow properties such as the coolant flow rate, velocity, and pressure distribution in the cooling passages or around the machine; in addition to the associated heat transfer properties, such as the levels of surface heat transfer, for subsequent analysis of temperature in the active material and remaining solid structures[5]. In general, CFD studies for large electric machines require expensive software and hardware implementations along with major time investments for the researchers. But many times, even with the addition of computer clusters, CFD anaysis can still take a great deal of computational time to complete a simulation. But CFD has the ability to predict flow and heat conditions in complex regions where the other methods cannot ensure acceptable accuracy. In addition, simulation allows visualization of flow distribution and dynamics, temperature and heat, which gives great insight for ventilation designs. In addition, to further improve model accuracy, conjugated heat transfer (CHT) simulations can be performed where solid and fluid domains are both modeled and solved simultaneously. But the hardware requirements for such simulations are even higher, with longer run-times and more user effort required; many times CHT simulations cannot be realistically performed.

Many studies have discussed CFD modeling techniques for large-scale generators. Pickering et al. [18] compared the CFD results of a salient pole electrical machine to its

testing data. Thirty heat transfer coefficients for the rotor were extracted and the same response trends were seen for measured and computed values. Predictions of velocity profiles at the outlets of radial ducts also showed good agreement. This study has proven that CFD has the ability to predict air flow and heat transfer on the rotors of salient pole machines. Boglietti et al. [7] introduced four common assumptions when conducting CFD analysis for an electrical machine[8]: periodicity of geometry, steadiness of flow and heat transfer with rotation, surface roughness, and the possibility of geometry simplicity.

Neale et al. [73] studied the feasibility of using CFD to determine surface convective heat transfer coefficients on both laminar and turbulent flows. This study focused on the simple cases of laminar flow between parallel plates with constant wall heat flux and constant wall temperature, and turbulent flow over surfaces. Heat transfer coefficients were calculated using the analytical method and compared to CFD results. In short, a good agreement was found, and results indicated that CFD can be used to find convective heat transfer coefficients in similar geometry. It is also encouraging to notice that, in the forced convection turbulence cases, models with low Reynolds number resulted in velocity profiles that match well with both the "universal" law-of-the-wall relationships and the "universal" Spalding curve, which were both developed based on experimental data. But it is also noticed that wall functions under-predict heat transfer coefficients for the thermally developing flows. In a separate study, Connor et al. [74] modeled an entire synchronous generator using Ansys Fluent 13.0 for a CFD study. Connor's generator is a mid-sized, four-pole synchronous machine in the sub 250 kVA class. A 3D hybrid mesh, multiple reference frame (MRF), standard k-epsilon model with enhanced wall function settings was used, under the assumptions that the flow is steady, incompressible, isothermal and turbulent. When the results were compared with experimental data, it was concluded that using CFD, the mass flow rate under-predicted by 4%, while the torque was under-predicteded by 7%, which are both acceptable values. Both studies above validated the feasibility of getting accurate flow results with the use of CFD.

Jarczynski et al. [75] discussed the use of advanced analytical techniques coupled with test validation, to enable designers to drive higher levels of performance and efficiency, specifically for the internal cooling circuits of large power generators. Multidisciplinary optimization was recognized in this work as the means to achieve robustness in the overall design and continue to improve. The models offer systematic means for predicting not only average rotor temperatures, but also distributed temperatures throughout the body to aid the designer in mitigating any local elevated temperatures [75]. The following methodologies were adopted by Jarczynski's team to predict rotor cooling flows and the resulting operating temperatures

1. Simulate the rotational 3D gas flow and heat transfer field in rotors using CFD.

2. CFD results can then be directly used for machine design. Extracted flow and heat transfer coefficients can be stored to apply for similar machines.

3. The use of series-parallel branch circuits coupled with fully parametrized 3D thermal finite element models can be used for both designs for new models as well as modifications for existing designs. Fluid elements are coupled with electrical/thermal elements, along with appropriate boundary conditions, for predicting detailed copper operating temperature distribution in the rotor.

Based on these presented papers, it is first concluded that CFD can be used to study this generator at high level of confidence, and outputs such as the fluid temperature and velocity, the surface temperature and heat transfer coefficient can be extracted for analysis. But it is expected to be very time consuming to develop such a model, and data extraction may be difficult as well. Additional information will be needed in order to make appropriate simplifications and thereafter to define boundary conditions.

In short, both the analytical lumped circuit method and the numerical CFD model can be used to study ventilation performance of large turbo-generator in the MW class. In terms of the method setup, CFD is easier than the analytical model, since less information

is needed. But in practice, the analytical method is more appealing and practical for the design engineer and the plant operators, to serve as a fast-solving and user-friendly tool. Taking all factors into consideration, a coupled quasi-analytical approach is proposed, following the general guidance provided by Jarczynski et al.: (1) visually study the ventilation performance of this machine through a detailed, high fidelity CFD study; (2) quantify the necessary thermal-fluidic resistances and segment the target fluid domain to determine the discretization, level by analyzing the CFD results; and (3) the lumped circuit method can be developed by implementing those descriptive resistances at the chosen node locations.

2.3 CFD Theories

Based on preliminary inspection and past research, turbulent flow is expected to dominate in this CFD model. Turbulent flows are characterized by fluctuating velocity fields. These fluctuations mix transported quantities such as momentum, energy, and species concentration and cause the transported quantities to fluctuate as well [76]. These fluctuations can be high frequency and small scale, which makes it difficult to solve the exact solution. Instead, the exact governing equations can be time-averaged, ensemble-averaged, or otherwise manipulated to remove the resolution of small scales, resulting in a modified set of equations that are computationally less expensive to solve [76]. Fluent introduced various Reynolds-averaged Navier-Stokes (RANS) turbulence models to achieve this CFD calculation.

This section will briefly discuss theories behind the Fluent models selected in the previous section to better understand how thermo-fluidic transports are calculated in this CFD model. Materials covered included velocity calculation in the moving reference frame, transport equations and a comparison of turbulence models in Fluent. Only key equations will be mentioned; detailed information can be found in the ANSYS theory guide [77].

2.3.1 Turbulence Models

Solving the *Navier-Stokes equations* for turbulent flows is impossible, since the equations are elliptic, non-linear, and the coupled pressure-velocity, temperature-velocity etc. effects [78]. Therefore, numerical methods are developed as alternatives. Turbulent flows are challenging to compute, and the appropriate solvers are difficult to determine because of their [76]: (1) unsteady aperiodic motion, (2) random spatial variations of flow properties in three dimensions, (3) strong dependence from the initial condition, and (4) wide ranges of scales, such as the degree of freedom or eddies.

FLUENT solvers use Reynolds-averaged Navier-Stokes equations, which define the Reynolds stress in terms of known averaged quantities by implementing the following two methods [76]. The *Boussinesq hypothesis* is valid when density variations are small, and assumes isotripic air property that treats the eddy viscosity as a scalar. The complicated and expansive *Reynolds stress transport models*, use equations directly derived from the Navier Stokes equation with no assumptions of isotropy.

Time-averaged quantities are appropriate for engineering purposes and the resolution is enough for applications. FLUNET offers several of different turbulent models, but the most appropriate ones to solve the generator are the two-equation k-epsilon group, or the four-equation transition SST model, based on observations and conclusions drawn from past simulations [79] [80].

- The **standard K-epsilon model** has the advantages of being robust, economical, and reasonably accurate; but it delivers mediocre results for complex flows with severe pressure gradients, strong separation, and strong streamline curvature, swirl and rotation.

- The **renormalization group (RNG) K-epsilon model** derives constants in standard k-epsilon model using renormalization group theory and is good for moderately complex behaviors such as jet impingement, separating flows,

swirling flows, and secondary flows; but it is subject to limitations due to the isotropic eddy viscosity assumption.

- The **realizable K-epsilon model** satisfies certain mathematical constraints on the Reynolds stresses and is consistent with the physics of the turbulent flows; it offers about the same benefits as the RNG model, in addition to being able to resolve the round-jet anomaly and likely to provide superior performance for flows involving rotation, and boundary layers under strong adverse pressure gradients, separation, or recirculation. It is also subject to limitations due to the isotropic eddy viscosity assumption.

- The **transition SST model** is the combination of the K-epsilon and the K-omega models, but does not use the wall-functions which tend to be more accurate in solving the near-wall regions; but it can be computationally intensive and does not converge easily.

Therefore, choosing the right turbulence model involves the trade-off between the level of accuracy required, and the available computational resources (CPUs, time etc.). Comparing the strengths and weaknesses of the above turbulence models, the wall-function coupled Realizable K-epsilon model and the Transition SST model are the best options. The Realizable K-epsilon model is more suitable for large geometry, and the Transition SST model is able to output more accurate results when resources are available.

2.3.2 Moving Reference Frame

The *moving reference frame* setup needs to be applied in the rotor fluid domain to account for its relative motion during operation. This creates additional fluid velocity representations u_r and v_r, as calculated in Equation 2.1.

$$\vec{v_r} = \vec{v} - \vec{u_r} \tag{2.1}$$

where absolute velocity $\vec{v}$ is changed to the relative velocity $\vec{v_r}$ by subtracting the rotational velocity u_r, which is the product of the rotational speed and the local radial location, using Equation 2.2.

$$\vec{u_r} = \vec{\omega} \times \vec{r} \tag{2.2}$$

Therefore, the traditional transport equations can be transformed in terms of the relative velocities, following forms shown in APPENDIX A.1, to calculate the corresponding flow properties with respect to its motion.

2.3.3 Wall Boundary Condition

When a heat flux input is defined at the wall surface, the corresponding wall surface temperature adjacent to a fluid cell as shown in Equation 2.3 [81]

$$T_w = \frac{q - q_{rad}}{h_f} + T_f \tag{2.3}$$

where T_w is wall surface temperature; h_f and T_f are fluid side local heat transfer coefficient and local fluid temperature, respectively; q_{rad} is radiative heat flux, which in this study is not considered.

2.3.4 Near Wall Treatment

In a fluid model, the near wall treatment defines a number of flow characteristics. Solid walls are the main sources of vorticity and turbulence that affect wall quantities such as the velocity gradients and pressure; and the near wall predictions determine flow phenomena such as flow separation and reattachment[76]. The accuracy of the near wall calculations also affects the heat transport between fluid and the adjacent imposed solid boundary. In general, there are two ways to capture the near wall regions: (1) solving the viscous sub-layer by adding inflation layers, and (2) using the FLUENT provided wall-function models. Either way, the near wall calculations are evaluated by the y-plus value y^+

The definition of the turbulent boundary layer is as shown in Figure 2.3 below. The inner layer is the region of interest, which is divided based on the y^+ value that is calculated based on the wall shear stress, fluid velocity and the distance to the wall, as shown in APPENDIX A.2. The layers closest and furthest to the wall are, the *viscous sublayer* at $y^+ \approx 5$, the *buffer layer* at $y^+ \approx 60$, and the *fully turbulent region*, the more commonly referred to as the *log-law region*.

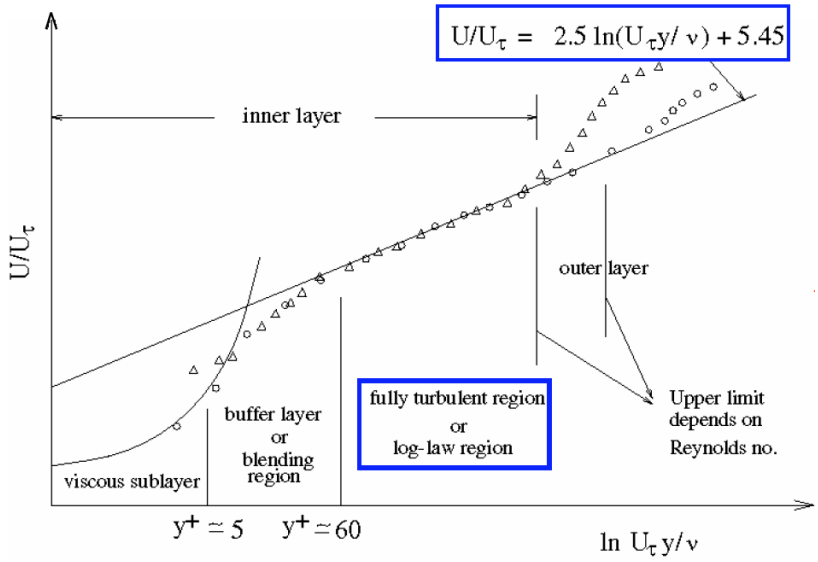

Figure 2.3: Structure of the turbulent boundary layer [79]

The wall-function approaches are offered for the two-equation K-epsilon models, which do not solve the laminar sublayer. For high Reynolds number applications, it is normally not affordable to set up the model to solve at that resolution 2.3, and therefore the K-epsilon models are especially appealing. The first grid point is assumed to be in the logarithmic layer $y^+ > 11$ and velocity is assumed to be described as in Equation 2.4.

$$u^+ = \frac{1}{k} ln(Ey^+) \tag{2.4}$$

The wall-function calculates parameters in the wall boundary region as:

1. A slip condition is imposed at the wall

2. k boundary condition is usually imposed as a zero-gradient

3. ϵ is obtained by equlibrum condition

4. If the first grid point is too close, then the velocity is defined by

$$u^+ = y^+ \tag{2.5}$$

In addition, ANSYS employs the log-law at $y_* < 11$. It is therefore recommended that if wall functions are favorable for the epsilon (ϵ) equation, use scalable wall function [82]. It is recommended that for standard for non-equilibrium wall fuctions, each wall-adjacent cell centroid should be located within the log-law layer, or $y_p^+ \approx 30 - 300$ [79]. For enhanced wall treatment (EWT), each wall-adjacent cell centroid should be located within the viscous sublayer, or $y_p^+ \approx 1$ and it will automatically accommodate cells placed in the log-law layer 2.3. Enhanced wall functions is a y^+ insensitive method and will act like a wall function if the first grid point is in the log-layer [80]. Inflation layers can be created with structured mesh approach, by defining the first point location, the total thickness, the first/last aspect ratio, or smooth transition [83].

2.4 Ventilation and Cooling in the Rotor

A number of research studies have looked at the field of rotor ventilation for large generators. The following studies were exaimined because they specifically focused on the target machine; techniques such as CFD setup, assumptions, and simplifications mentioned will be considered, and thermal-fluidic results will be referenced later to validate CFD results in this study.

The generator studied here uses a once-through path system, which was discussed in detail by Taniyama et al. [84]. The once-through path system has a flow schematic similar to the one shown in Figure 2.8. In this cooling system, the coolant gas from the

fan is separated into three paths, namely the rotor, the airgap and the stator coil end. The coolant gas to the rotor passes the coil end and the internal ducts and is exhausted to the airgap. Above it in the airgap, coolant gas from the fan and from the rotor converge; then this coolant gas is distributed from the airgap to the ducts of the stator. Finally, the gas is cooled by the cooler after it passes the stator duct, after which it returns to the fan area again.

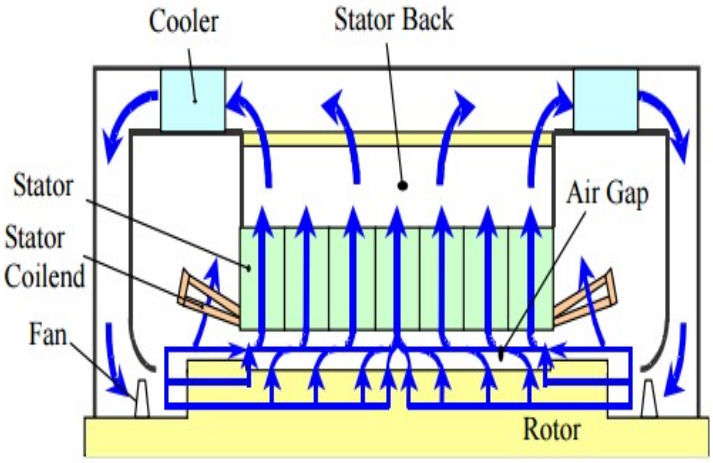

Figure 2.4: Flow schematic of the once through system [84]

For this cooling scheme, the authors used the circuit network method to analyze the ventilation pattern in the machine. The network is based on a one-dimensional piping network system that satisfies the continuous condition and the pressure condition in each branch, and the analysis considers the divergence loss on branch points and the convergence loss on joint points by one dimensional transient fluid analysis. This study provides some interesting insights for modeling similar complex flow paths. The volume-junction method was implemented and has a structure as shown in Figure 2.5. The anaytical parameters that need to be applied to each position are pressure, density, temperature and total enthalpy for *Junction*; and mass flux, velocity and volume force for *Volume*.

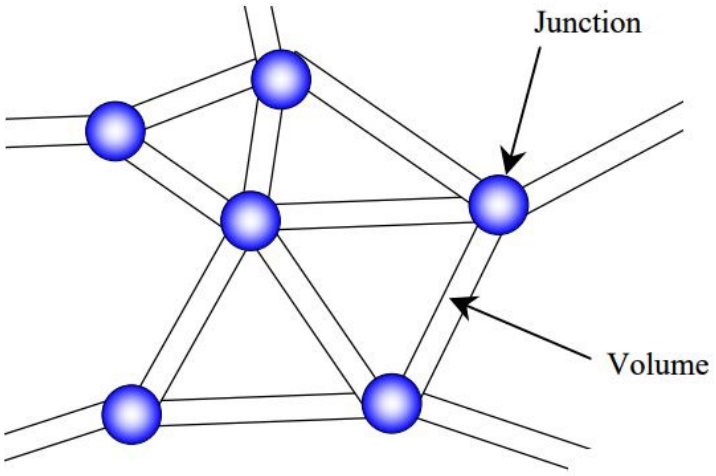

Figure 2.5: Definition of the Volume-Junction network [84]

Wang and Han investigated the change of rotation speed and inlet pressure on the distribution of air mass flow rate over an entire generator. It was realized that with increased rotating speeds, from 0 to 3000 rpm, the inlet air mass flow rate increased only 19.8 %, and the end duct air mass flow rate and relative air mass flow rate gradually increased; but the axial inlet relative air mass flow rate decreased, and the sub-slot relative air mass flow rate first increased and then decreased. When inlet pressure increased from 500 Pa to 5000 Pa, the total inlet air mass flow rate increased by 79.3 %, and the subslot and axial inlet air mass flow rates increased as well, while the end duct mass flow rate gradually decreased [85].

The rotor outer domains, including the airgap and stator cooling paths have been studied extensively. Han et al. [86] studied the airgap performance with the use of CFD. The generator model that they studied had a multi-zone stator, having a lamination geometry as shown in in Figure 2.6 (1). It was concluded that the flow velocity of the airgap between the stator and the rotor in the hot-zone/outlet-zone was larger than that in the cool-zone/inlet-zone, as shown in the contour plots figure 2.6 (2) and Figure 2.6 (3). Fluid entered the airgap as a swirling jet from the rotor outlets, and rotated with the rotor, flowing with a helical trajectory.

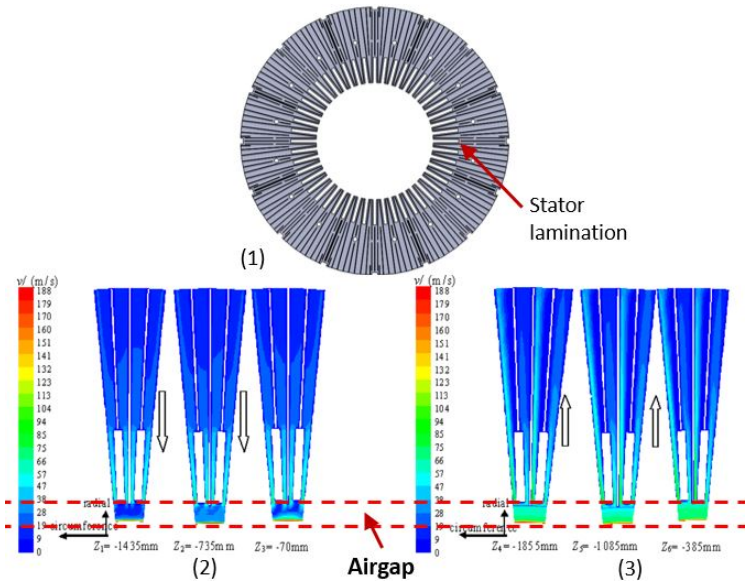

Figure 2.6: Flow field in a rotating cavity: (1)Stator lamination model studied; (2)Stator intake zones; (3)Stator outtake zones [85]

Next, Howey et al. compared the convective heat transfer within the airgaps of cylindrical rotating electrical machines. It was realized that in general, larger and faster machines have higher convective heat transfer coefficients in the airgap. In smaller machines, the temperature gradients in the flow were lower, and the flow was most likely to be laminar. In addition, introducing an externally pumped superposed airflow would increase the heat transfer in the the gap, as would an increase in the surface roughness of the internal flow passages [12].

Based on the above study, the stator domains do have relatively simple geometry features and flow conditions, as expected. But stators are so big in size that engineers should look into possibilities for simplification during modeling. Stator outer boundaries are controlled to guide pressure distribution in the machine, and more importantly to affect the local pressure in the airgap. The airgap on the other hand, is much more complicated. The airgap exists to facilitate the movement between parts, and it acts as a thermal insulator such that the temperature rise in the rotor and stator are not interdependent [4]. It connects all three flow circuits, adjacent to numerous inlet and outlet surfaces that are at different flow rates and velocity magnitudes. The airgap is also adjacent to both stationary and

rotating bodies in the machine. All of the above contribute to making the airgap a highly complex, uniform and unpredictable flow region. Therefore, when developing the generator CFD model, it is better to avoid imposing simplifications or assumptions in this region.

Generator rotor cooling domains have been mentioned in a number of studies as well. Both the analytical circuit and the numerical CFD approaches have been used in the past; however, circuit method has been successfully implemented and validated on many small and mid-size electric machines with various operating conditions [7]. Mohammadi et al. [68] performed a thermal analysis of the rotor for a large air-cooled generator using the thermal network approach with MATLAB Simulink. The model focused on the regions along the rotor body length, namely the tapered subslots, the equally-spaced radial vents and the airgap. It was concluded that temperature rises were caused mainly by losses due to friction, windage and electrical current in conductors. The results also indicated that in modeling similar machines, special consideration should be paid to the insulation temperature limits.

Antonyuk et al. [87] summarized the self-ventilation of the rotor from underslot ducts for a direct gas cooling system with identical radial ducts uniformly distributed along the rotor length. The rotor studied for this thesis project has a ventilation design in this region similar to that used by Antonyuk. Results show that the inlet area of the underslot duct has a crucial effect on the capacity of the ventilation system, and that limits the active length of the rotor. Total rotor gas flow also determines the average temperature of the winding. The self-ventilation of the rotor from the underslot duct was concluded to be not limited by the rated capacity, for both air or hydrogen coolant [87].

Lu et al. [88] studied the air mass flow rate distribution in rotor radial ducts with sub-slot ventilation, as shown in Figure 2.7. The purpose of the study was to investigate the mechanism of uniform distribution of air mass flow rate, in order to reduce the axial temperature differences due to uneven axial ventilation. The team investigated ventilation efficiency based on a few design parameters, including the effect of rotational velocity,

center section variation of the sub-slot, the radial duct quantity and the inlet angle variation of radial ducts. It was concluded that by increasing the number of radial ducts, the uneven characteristics of sub-slot ventilation along the axial direction can be enhanced. And the differences in air mass flow rate were the least when the inlet angle of the radial ducts reached 40 degrees.

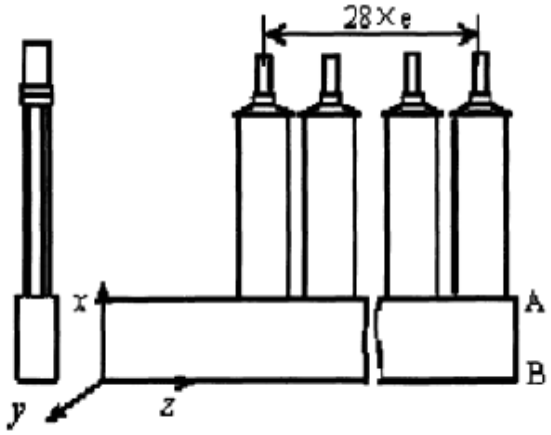

Figure 2.7: Schematic diagram for the rotor cooling ducts configuration along the rotor body [88]

Mohammadi et al. [68] conducted a thermal analysis of the rotor of a typical 202 MVA class, 50 Hz large air-cooled turbo generator. The generator was a conventionally designed, air-cooled, 2-pole machine with a cylindrical rotor. The rotor was modelled using MATLAB Simulink accompanied by an iterative code. The network was developed by applying uniform nodes in the rotor body along the rotor conductors. Associated flow and thermal resistances and losses were applied to calculate temperature distribution. The rotor cooling domain geometries and the corresponding developed network are as shown in Figure 2.8. It was concluded that the amount of flow and the angle of inclination of the radial sub-slots, both had dominant roles in the cooling effect of the air [68].

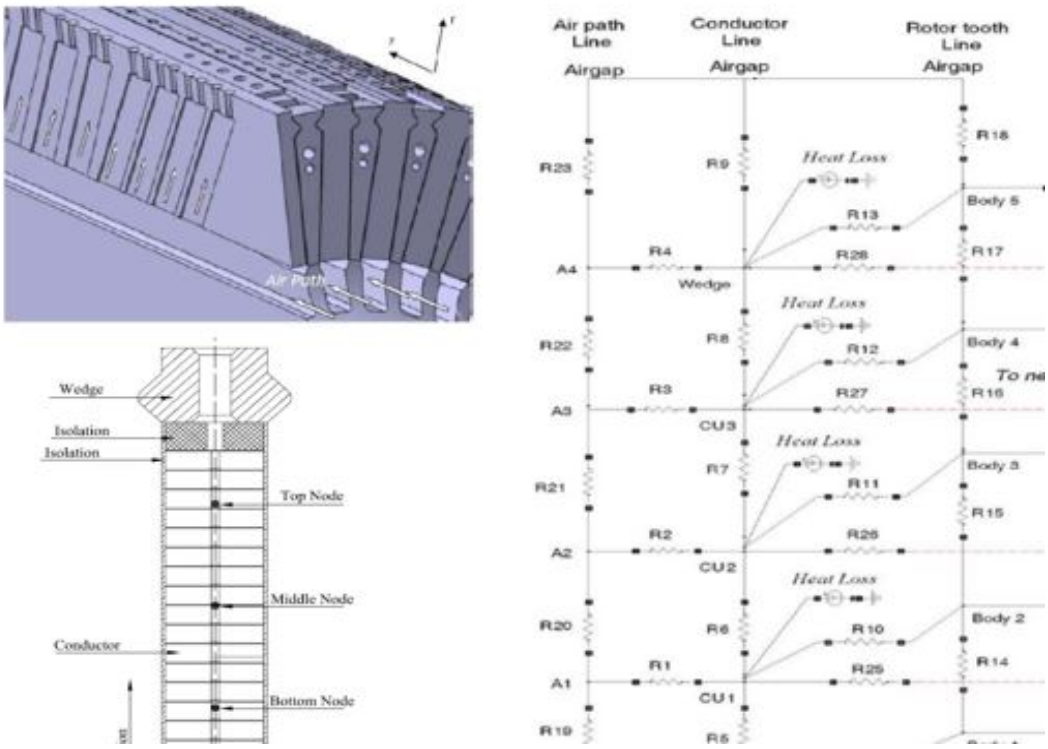

Figure 2.8: The heat transfer paths for the rotor subslot cooling ducts (left) rotor coil geometry; (right) analytical thermal-fluidic network [68]

The rotor end-region is one of most complicated parts in the generator. There is a high heat transfer rate from the end windings to the cooling air, while the cooling internal flow is already highly unpredictable, due in part to its turbulent properties and internal flow distributions. Previously, turbomachines with similar geometries were investigated, and some of the papers shed a light on the flow conditions in this region. Hayase, et al. [89] performed a numerical study on the laminar flow heat transfer between a pair of coaxial cylinders with the outer one fixed and the inner one rotating, and with either one of the cylinders having circumferentially periodic cavities embedded. Figure 2.9 (1) presents the flow domain and Figure 2.9 (2) and (3) are two representative vector field results. It was shown that spanwise-dependent Taylor vortex flow existed in the annulus interacted with the recirculating flow in the cavity along its aperture plane, together enhancing the heat transfer inside the cavity. In addition, a larger cavity opening resulted in Taylor vortices interacting more strongly with the annulus. The right side of the cavity, where it was

sheared by the flow penetrating from the annular space, had a higher Nusselt number than the rest of the cavity walls. In addition, the existence of embedded cavities intensified the heat transfer in the annular space. Similar flow results are expected in the rotor end winding fluid region in this study. But the endturn cavities are different from the one studied by Hayase in the following aspects: (1) turbulent flow is expected in the endturn cavities as the result of the rotor's fast rotating speed; (2) forced inlet flow exist at the front of the rotor, or differences in the upstream versus downstream cavity flow results are expected; (3) cavities in this study is open to annular flow as they are bounded by three walls only, compared to the five-wall enclosed endturn cavities; (4) a series of cavities present in the endturn, which vary in size and layout; (5) endturn cavities are separated by insulation blocks, which stick into the annular space that disturb the bypass flow but improve the flow momentum into the cavities. As the result of the different flow condition, endturn cavity flows have unique flow characteristics that are not captured by Hayase's study and needs to be understood in order to capture the associated heat transfer.

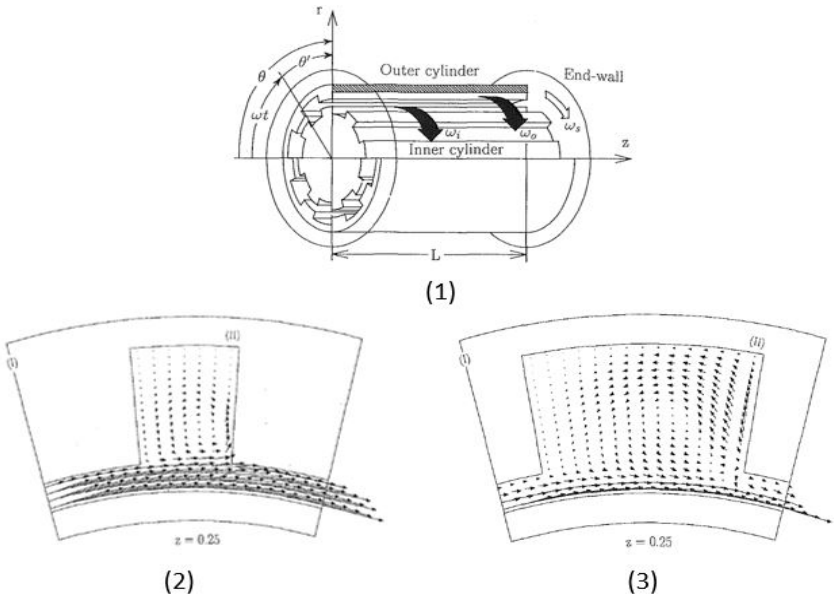

Figure 2.9: Rotating cavity: (1) Flow field geometry; (2) flow field for a cavity with 10 degree opening; (3) flow field for a cavity with 20 degree opening [89]

These studies showed that the rotor endturn presents complex flow physics and there

is not any empirical correlation available to quantitatively describe the flow properties in the target endturn cavities. Therefore, the rotor ventilation path needs to be numerically studied. The rotor geometries should be modeled as built in the three dimensional CFD model to achieve the highest level of accuracy possible; only negligible constructional features such as bolts are ignored. The internal flows in the radial vents along the rotor length are relatively simpler and do not limit the generator's capacity, but a comparatively uniform temperature distribution is expected for a working machine. The radial vent, along with the underslot performance, are only modeled for model verification and as a step to understand the rotor ventilation performance and to improve the accuracy of upstream endturn regions. The regional CFD results will be cross compared with results from the circuit methods performed by Mohammadi and Lu, paying special attention to the magnitude and level of uniformity of temperature, and to the mass flow distributions among the individual subslots. Even though the internal flow in the end winding region is expected to be similar to that of the Hayse study. But flow might be even more chaotic due to the force flow in the annular. But the same higher heat transfer at the right edge, or the inlet was expected.

2.5 Research Gaps and Objectives

The study of rotor ventilation-related topics has been discussed in several prior studies. However, most of the efforts involve numerical methods using CFD/FEA techniques, with a few adopting simplified lumped-circuit approaches for regional domain investigations. For both methods, extensive time and effort are required to model, setup and conduct the study for machines at this scale. Also, based on the literature survey conducted, there has been no published work focusing on a quantitive description of the thermal-fluidic transport in the unique rotor end winding cooling regions of air-cooled large turbo-generators. The current research was the first to consider geometry similar to the pumped, rotating sector-shaped fluid domains. The presented work intends to fill in this gap for a descriptive representation

of the thermo-fluidic phenomenon in this commonly used, but highly complex segment domain that presents formidable difficulties with traditional analytical aerodynamics correlations. The goal of the proposed research is to develop a generic, fast-solving analytical algorithm to efficiently and accurately predict thermal transport in large-scale, air-cooled turbo generators, in the rotor end-winding region.

In support of this goal, the following research objectives were pursued:

1. Construct simplified three-dimensional models to investigate and quantify thermo-fluid transport through the generator ventilation passages.

2. Investigate and analytically model heat transfer in one endturn circumferential cavity, which is a rotating sector with heated parallel walls.

3. Construct a generic, fast-solving thermal network for the nested structured ventilation cavities in rotor endturn to predict average coil temperature under given rotor geometry and operating conditions.

2.6 Research Approach

This work focuses on four main research areas. The study first investigates and quantifies the rotor flow field through a high-fidelity, large-scale CFD generator model, constructed using ANSYS Fluent. A quasi-analytical study of the fluid and thermal transports in a typical rotor circumferential endturn cell was developed, using fluid transport descriptors obtained directly from CFD. A novel 'virtual pipe' method captures the bulk flow phenomenon within the unit cell. This work presents a generic description of the height of the so-called virtual pipes, developed using correlations based on a parametric study investigating the effect of key endturn design parameters. Finally, the virtual pipe method is implemented into a thermal-fluidic network as an algorithm that can quickly estimate regional coil temperature with given inlet condition and rotor geometry, for the expected operating conditions at the desired level of accuracy.

2.6.1 Computational Fluid Dynamics Study of Rotor Flow Field

A large scale, high fidelity CFD generator model was developed in this section to quantify the flow regions, especially those in the rotor cooling passages presented in Figure 1. The three-dimensional CFD model included the entire generator flow domain, with the length starting axially behind the cooling fan up to the center of the machine in the generator enclosure. It includes cooling volumes up to the outer diameter of the stator lamination plates. But the focus was the rotor endturn region, the equally-spaced radial vents and tapered subslots in the rotor body. The stator cooling regions and the thin annular airgap were included to capture the rotor far-field boundaries at higher accuracy. They were simplified in geometry to save mesh size and computation time. The CFD approach included: (1) geometry simplification, (2) boundary condition assignment, (3) mesh refinement, and (4) model verification.

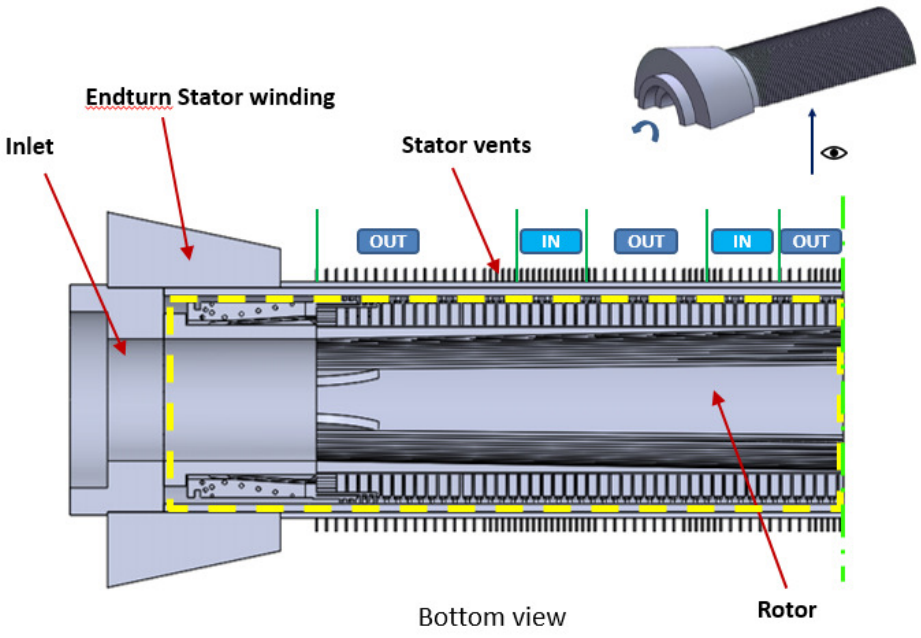

Figure 2.10: CFD geometry for the genenrator simulation.

2.6.2 Quasi-analytical study of rotor endturn

An analytical description of the endturn cavity bulk flow is needed first in order to achieve the ultimate research goal of developing a fast-solving analytical code for temperature prediction. So far, no flow field at similar conditions has been found in the literature; thus no empirical correlations can be used. The most appropriate analogy found was that of Taylor-Couette flow, with the addition of forced flow at the domain inlet, and periodically embedded sector-shaped cavities on the outer cylinder. All of these resulted in a complex three-dimensional flow, with unpredictable swirl inside cavities and Taylor-vortices at the cavity-annulus interface. Therefore, a complete solution to the three-dimensional Navier-Stokes equations, as presented in Appendix A was required to fully understand this flow domain for an analytical description. But such a solution was as of yet not available.

Based on the preliminary CFD study, all cavities appear to have the same bulk flow phenomenon, which is expected to contribute significantly to heat transport inside. If this bulk flow phenomenon can be understood and approximated with a known fundamental flow, an analytical solution can be developed. This part of the study has two goals: a) To prove that all cavities in the endturn system have the same flow phenomenon; b) To develop a fast and effective data process method to processing the massive CFD data. Extracted bulk flow velocity profiles are investigated and 'matched' with those of known fundamental flows, for the possibility of developing a simplified yet accurate description. Thereafter, thermo-fluidic transports in this unknown, unique cavity bulk flow can be reasonably approximated and quantified with developed empirical correlations. Because there are only three physical walls bounding the flow, this proposed novel approximation method is named the 'virtual pipe method'.

With the 'virtual pipe method', transports in this rotating flow domain are treated as the superposition of a peripheral bulk flow and tangential flow from rotational motion, as illustrated in Figure 4. In this way, regional heat transfer coefficients can be quickly calcu-

lated using empirical correlations found in heat transfer textbooks, and the corresponding regional coil temperatures follow routinely.

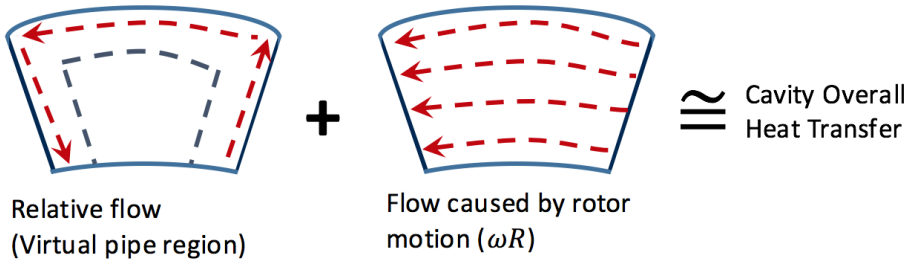

Figure 2.11: Propagation of the thermal-fludic heat transfer within the endturn cavity.

2.6.3 Virtual Pipe Hydraulic Diameter Description

In order to use any empirical correlations for thermo-fluidic heat transfer analysis, a description of the flow characteristic length D_h was needed. Previous cavity studies have shown that the bulk flow regions have velocity profiles similar to the one shown in Figure 2.11, which has a shape similar to that of the internal pipe flows. To determine D_h, the length of the *virtual pipe height* labeled in Figure 2.11 needed to be quantified. Therefore, this part of the study developed a generic way to calculate the local characteristic length in the bulk flow regions, based on given flow field conditions of flow inlet and rotor geometric parameters. To improve the applicability of the proposed method, two types of design parameters were identified for the flow fields of the endturn cavities: operating conditions and endturn geometries. Parametric experimental cases were therefore designed and studied quasi-analytically, by first conducting a series of CFD simulations on a partial endturn domain. CFD results were extracted and analytically processed to find a way to approximate the size of the bulk flow regions such that they were able to capture the flow momentum. In short, this study has two objectives: a) to verify that the flow characteristics used in the virtual pipe development are valid and applicable for a variety of designs; and b) to calculate the pipe heights for each region. The pipe heights are calculated and mathematically fitted using regression models to analytically represent the pipe height in terms

of the identified design parameters. A generic algorithm was developed when calculating virtual pipe D_h, in a way such that pipe heights are calculated solely based on the shapes of the extracted CFD relative velocity profiles.

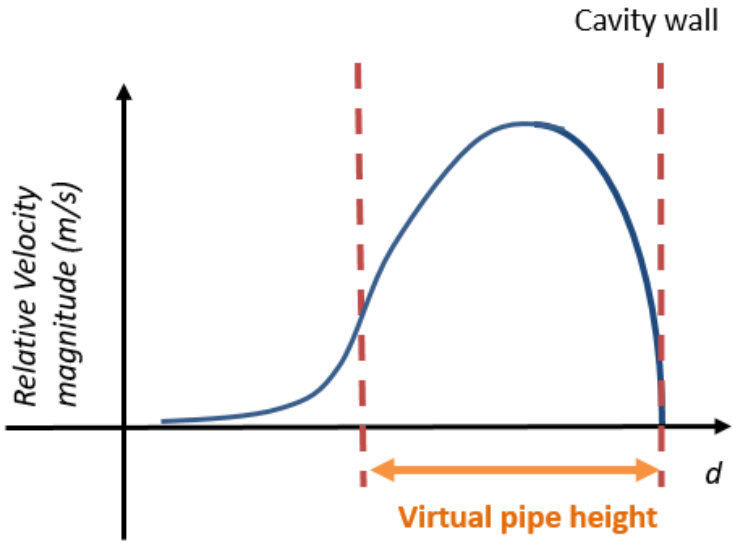

Figure 2.12: Representative velocity profile of the identified virtual pipe region.

2.6.4 Analytical Endturn Temperature Prediction

The ultimate goal of this research was to develop a fast-solving and accurate analytical algorithm to estimate regional coil temperatures in the rotor end winding regions. With the virtual pipe approach, an analytical network could be developed by implementing the lumped circuit method. Air velocities and temperatures in endturn cavities could be estimated using well developed empirical correlations for fundamental flows. The analytical algorithm has two levels: the unit cell/cavity basis, and the nested endturn system basis. The network has two parts fluid and thermal paths. First, inside the individual cavity, local bulk flow velocities and temperatures were calculated iteratively by balancing the pressure gains and the associated losses along the bulk flow path within the cavity. Next, the thermal network was developed. Local heat transfer coefficients and the wall temperatures were calculated at the fluid properties calculated from the fluid network.

The final analytical predictor aims to predict the rotor endturn coil temperatures within $\pm$ 5 degrees Celsius error. The analytical predictions will be compared with available testing data and simulation results from edturn CHT models to verify the accuracy of the predictor.

2.7 Thesis Organization

Chapter 1 provides a general introduction to the topic. Chapter 2 presents an overview of the relevant literature with concluded research objectives and research approaches. Chapter 3 develops one detailed rotor CFD model and two small domain rotor CFD models that are solved using the commercial CFD software, and discussed the flow results. Chapter 4 numerically studies the endturn cavity flow phenomenon and proposes a novel method, or the virtual pipe method, to describe and quantify the thermo-fluidic transport in the individual endturn circumferential cavity. Chapter 5 proposes an analytical method to calculate the local cavity bulk flow hydraulic diameters. Chapter 6 develop parametric description for the local hydraulic diameter. Chapter 7 develops an the analytical temperature predictor for all coils in the nested rotor endturn region. Finally, Chapter 8 provides general conclusions on the presented research and recommendations for possible future work.

CHAPTER 3

CFD MODELING TECHNIQUE

3.1 Introduction

This chapter develops numerical CFD models that can be used to study the system and regional rotor ventilation performances of the targeted generator, using the commercial software named ANSYS FLUENT. In order to develop a temperature predictor for the rotor end-arc coils, the flow physics in their associated cooling domains need to be understood and quantitatively described. Since an analytical solution is not available, the numerical software could be implemented to solve the heat transfer problems in this highly complex three-dimensional regions. Therefore, three numerical models were developed: (1) a large scale, high fidelity generator CFD model for detailed flow calculations inside the generator rotor; (2) a partial endturn circumferential cavity flow model for economical parametric investigations of possible design scenarios of the endturn cooling structure; and (3) a parametric endturn CHT model to use for rotor end-arc coil temperature predictions at improved accuracy. The generator model achieves high level of accuracy inside the rotor domains, and provides preliminary understanding of the flow conditions inside the nested rotor endturn pattern. The two endturn models allow parametric design studies at higher efficiency, by simplifying the numerical models' complexity and therefore the simulation run-time.

The numerical CFD study for this large scale turbo-generator is intuitively difficult, due in part to its size and complexity of the flow domain that varies in three orders of length scales. As a result, uncertainties in the flow conditions present meshing difficulties and challenges in the modeling setup. This chapter discuses the modeling techniques applied for each numerical model, which includes (1) definitions of geometry, (2) boundary

condition assignments, (3) mesh generation, and (4) model verification. Simplifications and assumptions taken are justified as well. The flow results of the large generator model are inspected and discussed, whereas the endturn models are only proposed with settings listed.

3.2 Generator CFD Model Summary

This section develops a generator CFD model using the commercial CFD software, ANSYS FLUENT, to numerically study the rotor ventilation performances at the generator's expected operating conditions. In practice, a successful CFD study has to satisfy the following design requirements [76]: (1) characterize the *flow physics* such as turbulence and high gradients values, (2) evaluate the *computational requirement* to accommodate the grid resolution requirement to capture the flow physics at certain accuracy, and (3) evaluate the complexity of the solver models in order to meet the *project requirement*. The underlying difficulties in conducting a numerical study for the target rotor, due in part of (1) the level of complexity in geometric features necessary to capture the flow physics, (2) the big mesh size and therefore the high computational requirement and simulation run-time, and (3) the lack of flow information for the complicated flow physics presented in the ventilation flow domains to determine the appropriate solver settings and boundary conditions. Four commonly adopted modeling steps are followed, to find settings that satisfy the three design requirements.

1. **Definition of modeling objective:** identify the research goal and possible assumptions and simplifications.

2. **Definition of geometry:** identify geometric features needed.

3. **Meshing:** determine the meshing method and the meshing resolution.

4. **Model setup:** define turbulence solver and its associated settings and the model

boundary conditions.

3.2.1 Definition of Modeling Objective

The modeling objective of the this study is to obtain detailed, accurate and comprehensive knowledge of the flow physics everywhere in the generator rotor, to a point that the flow results are accurate enough to quantitatively describe the ventilation performances of the rotor. First, the geometries build the foundation of a CFD study, and therefore for the purpose of improved modeling accuracy, assumptions or simplifications are avoided in the rotor, except for cases with 100% certainty of their negligible importance. Second, the CFD software uses the finite element method and the meshing resolution determines the result accuracy. The rotor geometry complicates mesh generation, which requires curvature and proximity corrections to capture the three orders of variations in the length scales. The mesh also characterizes the flow physics such as the near-wall conditions for the expected turbulence flows. In addition, the mesh density should not be excessive in order to avoid a resulting meshing size that cannot be calculated or takes to long with the available computational resources. Most importantly, the model needs to be set up correctly so that the solver is able to capture the characteristics of each unique rotating, turbulence rotor flow region. The bordering boundaries of the rotor need to be accurately defined, or otherwise moved further out so that the boundary conditions correctly inform the distributions of the internal flow and do not add uncertainties to the fidelity of the rotor CFD results.

The following design settings are considered:

- The two commonly used and widely approved turbulence models for large electric machines, namely the four-equations SST model or the two-equations wall function treatment coupled K-epsilon model, are the most appropriate choices of the turbulence solvers in this case [74][79] [80]. But the actual selection has to be considered based on the evaluation of the overall CFD modeling since the additional two parameters in SST requires much more computational time.

- Simplifications are not available at the rotor outer boundaries and therefore the stator regions need to be included to improve rotor flow field accuracy. More specifically, the rotor entrance is neighboring the cooling fan exit, while the active length is underneath the airgap, where highly complex, nonuniform and unpredictable flows are expected at both locations; therefore, to assure the accuracy of the rotor flow domains, the rotor outer boundaries are moved to the outside of the stator lamination where the boundary conditions are fixed at the factory controlled values.

- The addition of the stator region and the airgap in the geometry make the size of the CFD model even bigger; and the direct consequence is the increase in simulation run-time. Since the stator regions are only added to make the rotor flow field less sensitive to the boundary values, geometry simplification can be taken at slightly relaxed standards to allow for the most minimized stator volumes.

3.2.2 Generator Flow Domain Identification

The first step in a CFD study is to define and create the flow geometry. The coverage, size and complexity of the geometries are defined based on the research goal, and together determine the mesh size and simulation run-time as well as the accuracy of the flow field results. This generator CFD model was to achieve the highest level of accuracy possible, such that the results could be extracted to study the rotor ventilation performances. To achieve this goal, a three-dimensional model was pursued, where all three flow paths in Figure 1.3 are included, even though only the rotor ventilation path is of interest here, The stator and airgap air paths are still included in order to improve the accuracy of the rotor far-field boundary conditions and are discussed in more detail below. This section presents the generator geometries and the associated flow geometries in all three paths, including any simplifications that were made.

As stated in CHAPTER 1, a generator has two types of components: the stationary outer stator and the inner rotor. The entire length of the generator can be first divided into two main zones, namely the *endturn* and the *active length*, as labeled in Figure 3.2 (A). All of the active components are overlaid according to this zone separation. The generator is symmetric half way on either side of the *symmetry plane*; and is also symmetric about the d and q axes labeled in Figure 3.1 (B). Therefore, symmetry simplifications can be applied when modeling the generator.

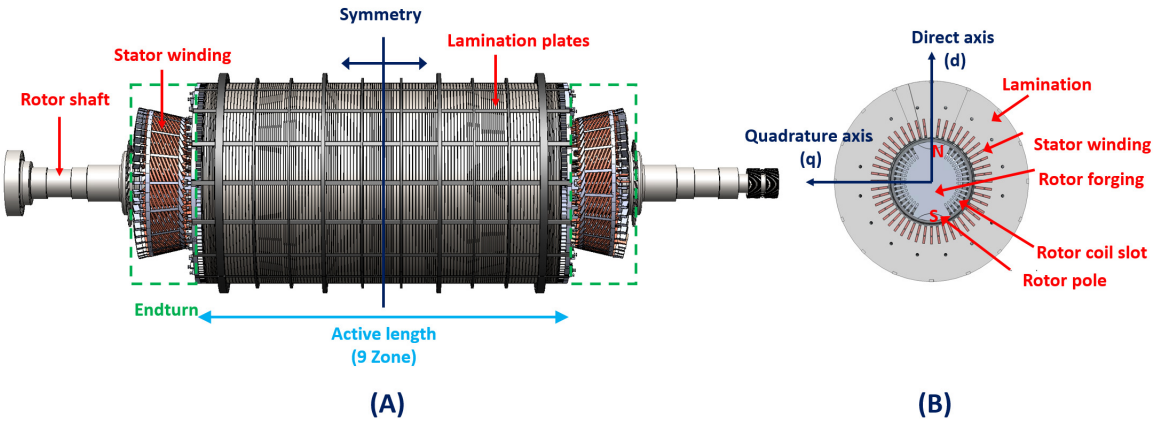

Figure 3.1: Generator model overview. (Left)Side view, and (Right)Cross-sectional view.

The three generator ventilation paths go through three active components, namely the stator winding, the rotor and the core/lamination, as shown in Figure 3.2. The flow regions through each component and in-between the components needed to be modeled to cover the entire generator ventilation domains. The stator is much bigger in size than the rotor, and modeling the stator regions would add significant volume to the overall CFD model. Since detailed flow results in the stator are not targeted, the stator regions can be simplified to ease the modeling difficulty.

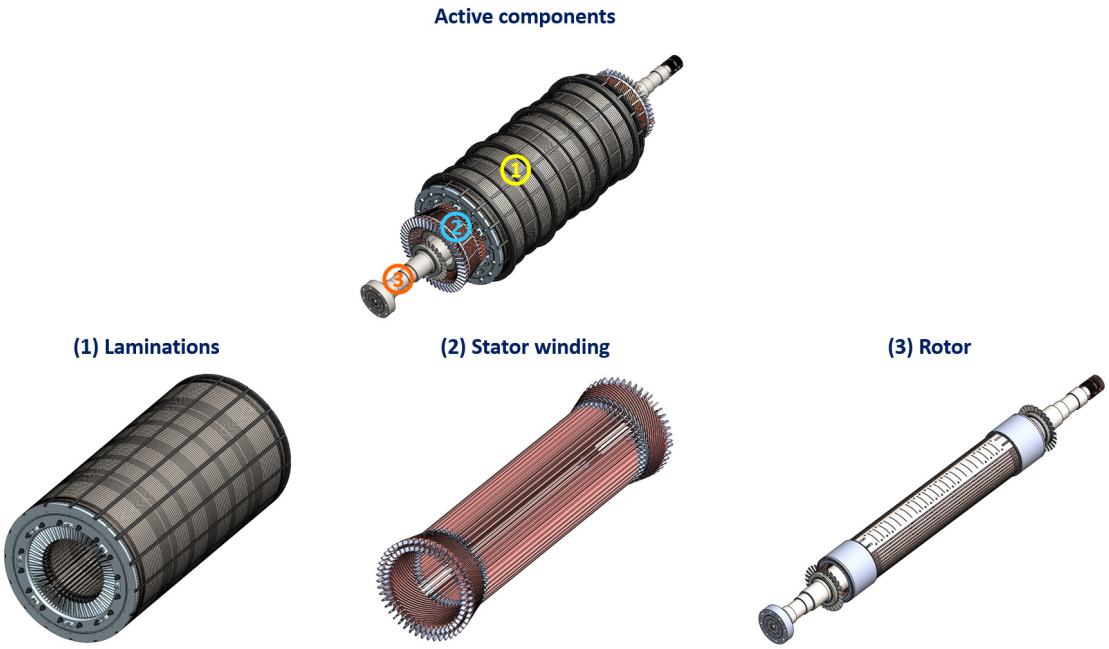

Figure 3.2: Generator active components overview. (Top)Assembled view, and (Bottom)Individual component view.

Two out of the three air paths behind the rotor axial cooling fans exist through the stationary stator. The stator endturn winding forms a conical-shaped, lattice construction, which allows air to pass through numerous rectangular-shaped void spaces bounded by any two adjacent twisted windings. The stator body length is supported by the stator core, which is made of thin lamination plates that divide the entire length into 9 zones with 130 cooling pathways. Ring-shaped gaps are formed between the lamination plates, which allow air to enter and leave through the airgap through these 9-zone stator vents. The geometric features of the stator vents are repeated, such that only a one-time modeling effort is needed. But each individual vent ranges over three length scales in dimension, and the total number of vents is substantial, adding up to a significant volume size. Thus, the stator vents present potential extra challenges in meshing and thereafter in the FLUENT solver. Therefore, these regions are simplified in this study by implementing the porous medium concept. The porous medium environment does not require modeling the solid geometric features inside the targeted flow domains. Instead, it applies diffusion properties

(loss resistances), which are calculated in accordance with the void fraction (porosity), dimension, and pressure drop in the flow and the cross-flow directions.

The stator vent regions are noticed to have the following flow characteristics: (1) the radial direction flows dominate inside, (as the result of the surface features on the lamination plates, the thinness does not allow the flow to expand in the other directions); (2) the pressure boundaries at the outer diameter are always controlled as generator operating inputs with known values. Note that the stator inner diameter is adjacent to the airgap; therefore, the flow condition is not uniform. It is given that the machine is designed to maintain an approximately constant gauge pressure value at this radial location. Therefore, given the pressure difference over the flow direction, the porosity and the dimensions of the domain, the corresponding loss resistances could be calculated.

Figure 3.3 below presents the geometry of the stator lamination on the left, and its simplified cooling domain on the right. Notice that evenly distributed extrusion features exist on the surface of the lamination plates, which guide the flow to travel radially through a distance of 261-inches through the lamination plates. This flow domain is simplified to a ring-shaped geometry shown on the right of Figure 3.3; its length in r direction is scaled down to 4 inches while keeping the vent's inner diameter and thickness constant. The 4-inches is the distance l needed in order to capture the entrance effect of the airgap flow when it first enters the stator vents, which is estimated based on the $l/D = 10$ relationship for turbulent pipe flow [90].

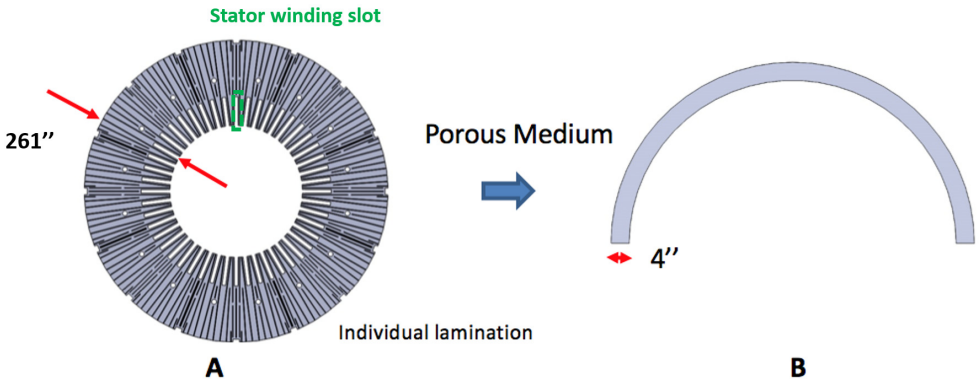

Figure 3.3: Stator vents simplification. (A)Stator lamination geometry, (B)Simplified stator vent flow geometry.

By inspection, the endturn stator windings region is a porous medium domain. Similar to the stator vents, the pressure difference between the inner and outer diameters can be estimated based on known factory controlled properties of this region. Per inspection of the stator winding geometry shown on the top of Figure 3.4, the winding assembly pattern forces the air to escape only through the holes that are normal to the winding surfaces. Therefore, the flow through this region dominates in the direction normal to inclination of the winding inner and outer surfaces. The flow resistances can be calculated, and the porosity can be determined based on this solid model as well. The stator endturn solid region is therefore modeled as a conical-shaped flow region, as shown on the bottom of Figure 3.4. This allows the highly complicated geometry to simplify to a region with significantly fewer geometric features, therefore requiring less modeling effort.

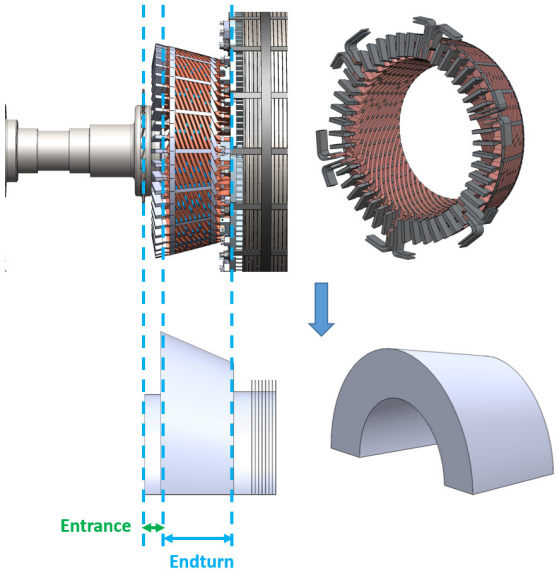

Figure 3.4: Stator endturn region demonstration. (Top)Stator coil construction, (Bottom)Simplified fluid region geometry.

The last generator air path passes through the rotating rotor, and is referred to here as the *near-field region*, which is the targeted volume. The rotor cooling regions were modeled without geometry simplifications to capture the assembly details; but small or miscellaneous constructional features, such as sharp corners, fillets and spaces for constructional parts (nail, screws etc) that are obviously irrelevant to the flow physics were ignored. The rotor geometry is shown in Figure 3.5. More complicated flow regions present in the rotor, which together with its fast rotating motion, result in more sophisticated and unpredictable flow physics, compared to those of the stator regions.

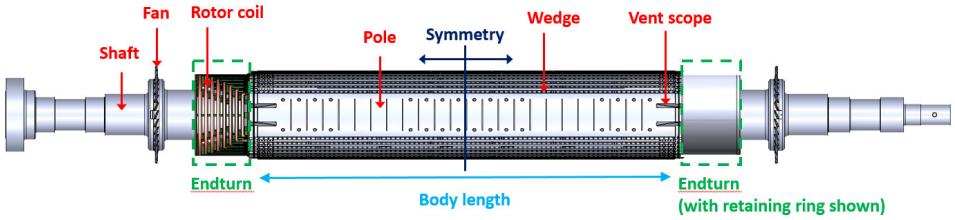

Figure 3.5: Rotor geometry overview

The rotor endturn solid parts form a nested, linearly decreased construction pattern, as shown in Figure 3.6, respectively. Note that even though the solid components are

symmetric about both the q and d axes, the endturn flow conditions are expected only symmetric about d due to the forced inlet flow and the alignment of the insulation blocking. Therefore, this study focuses on flow results in the bottom layout.

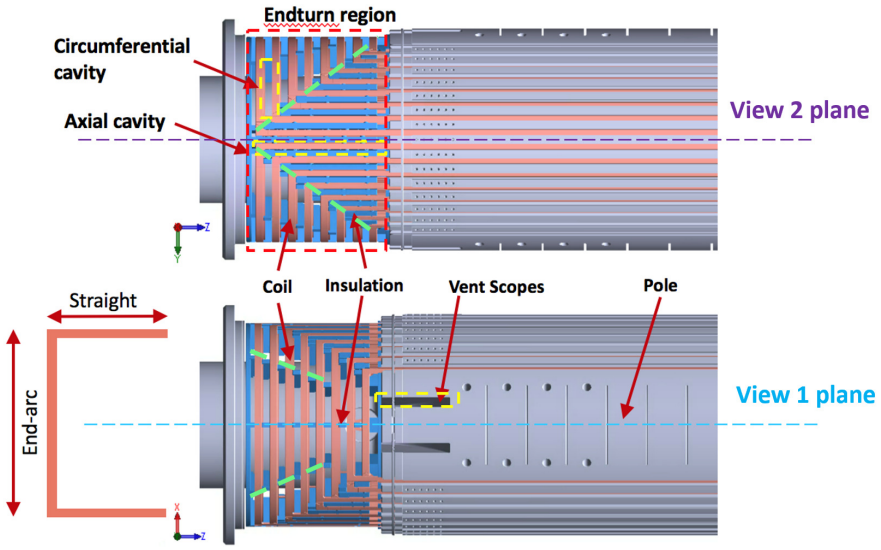

Figure 3.6: Rotor construction with labeled parts. (Top)Rotor construction besides pole, (Bottom)Rotor construction surrounding pole

Figure 3.7 slices between the endturn axial insulation, which presents two rotor features that are labeled on the bottom of Figure 3.7. On the left shows the long thin gap between the rotor coil and the insulation. This thin gap is referred to as the axial cavity in this study, which is located on top of the endturn annulus to allow a portion of the annulus flow to enter and cool the straight length of the endturn rotor coil. The second feature is the rotor vents behind the axial cavity. The rotor vents are located at the end of the retaining ring and before the appearance of the first radial vent on the rotor forging, which allow the axial cavity flows to pass through and cool the rotor forging before exiting into the airgap.

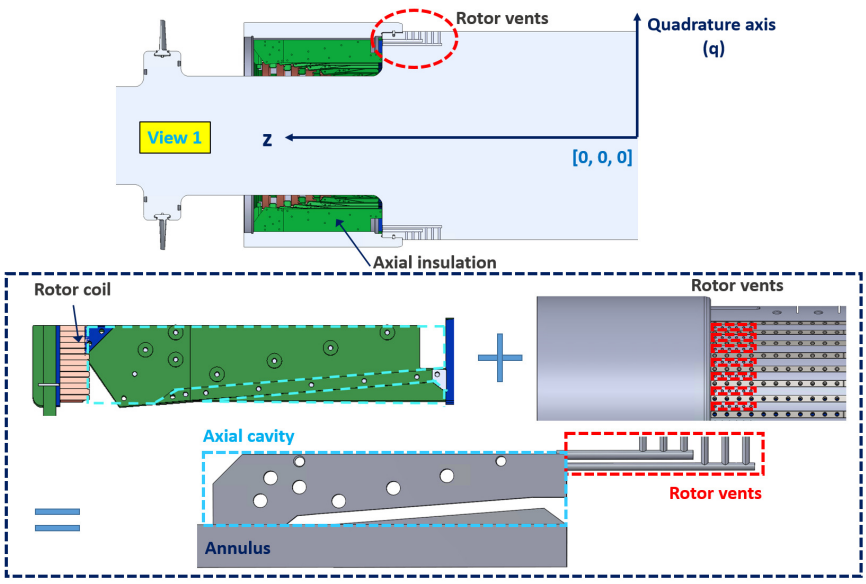

Figure 3.7: (Top)Rotor cutout view plane 1, (bottom)Endturn axial cavity and rotor vents construction.

Sector-shaped void spaces exist on the front and back of the coils, as shown on the top left of Figure 3.8. These cooling domains are named the circumferential cavity that are modeled as shown on the bottom of this figure. Note that the stacked coil is treated as one homogeneous copper block here, ignoring the small, adiabatic surface areas of the insulation layers in-between the coils, as shown on the top right in Figure 3.8. The twelve insulation layers are only $0.7mm$ thick each and occupy a total of 1% of the entire coil height, therefore having negligible impacts on heat transfer.

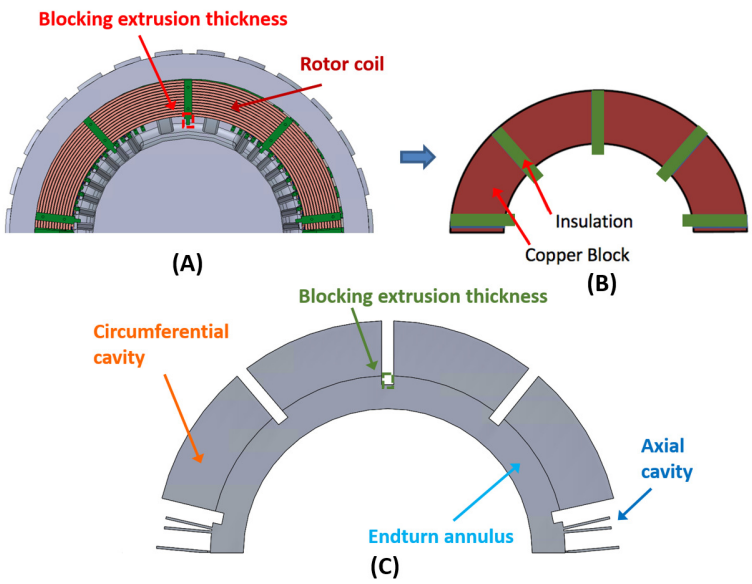

Figure 3.8: Rotor endturn coil simplification. (A)Rotor endturn coil construction, (B)Simplified coil structure, (C)Rotor circumferential cavity flow field geometry.

Repeated *radial vents* are presented inside the rotor coils, on top of the *tapered* subslot along the active length of the rotor. Note that the rotor coils located inside the endturn region are cooled from the outside, while the rest of the coils along the rotor active length are cooled internally by the radial vents. These radial vents have a shape as shown in the bottom of Figure 3.9. Each radial vent has three distinct geometries corresponding to the solid geometries shown on the top of Figure 3.9; the top cylindrical part is bounded by steel wedges, the small region below it is bounded by insulation, and the bottom rectangular-shaped region is bounded by rotor coils. The tapered subslot is decreasing in its cross-sectional area as the locations move downstream into the rotor. The radial vents need to be meshed extensively at fine resolution to capture their $5mm$ thickness. 70 radial vents present in half of the rotor, along a subslot of $5.4m$ long; sixteen radial vents plus subslot combinations exist in the generator CFD model, two for each turn of rotor coil (eight turns total) that add up to a significant number of mesh elements.

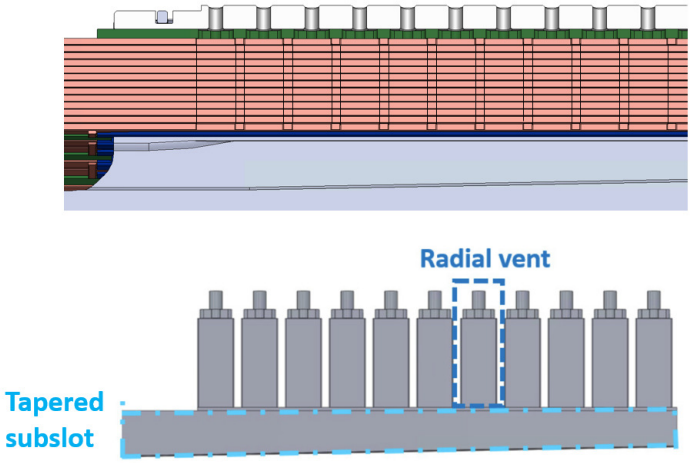

Figure 3.9: Rotor endturn coil simplification. (A)Rotor endturn coil front view, (B)Simplified coil structure

The void spaces in the generator enclosure, all of which have been discussed and individually modeled, are assembled together to create the generator CFD model. An overview of the model is presented below, as shown in Figure 3.10 for the stator regions and in Figure 3.11 for the rotor regions. Again, due to symmetry in the generator construction, only a quarter of the machine is modeled. The unique cooling geometries included are as follows.

- **Path 1:** rotor circumferential cavities, axial cavities, endturn annulus, tapered subslots, radial vents, rotor vents, and vent scopes.
- **Path 2:** stator simplified stator vents.
- **Path 3:** airgap airgap volume is separated into two, where half of the thickness belongs to the rotating rotor and the other half belongs to the stationary stator.
- **Inlet region:** This is the region where the forced inlet flow from the rotor fan separates into the three identified paths. This region starts right behind the rotor axial cooling fan, extending to the front of the retaining ring

The stator regions include the conical-shaped stator endturn winding region, and the ring-shaped stator vents, as shown in Figure 3.10. They are both simplified in geometry in

order to save modeling time and component volume. The simplifications taken in model setup are discussed in the next section.

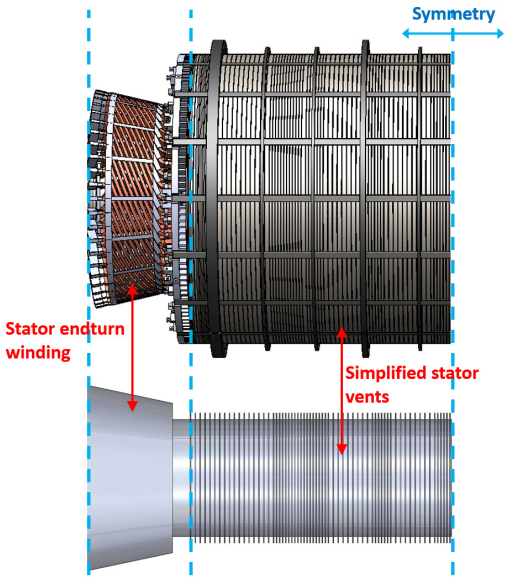

Figure 3.10: CFD model stator components overview

The rotor regions result in more complicated flow geometries, compared to those of the stator. Inside the endturn region, nested structured circumferential and axial cavities are bounded by the rotor coils and the insulation blocks. Along the active length of the rotor, tapered subslots feed air into the radial vents that are located within the rotor coils to cool them internally.

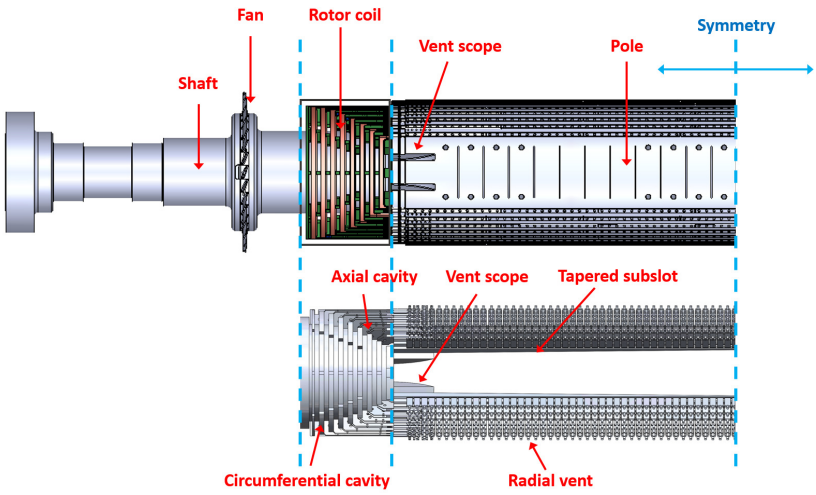

Figure 3.11: CFD model rotor components overview

A three-dimensional generator fluid domain model has been developed for the generator. Even after all the possible geometry simplifications, this model is still complicated and difficult to study. It is big in size, with constantly changing tricky geometric features that the associated length scales vary over three orders of magnitudes. All of the above present difficulties when creating the mesh in the next step, and later when setting up FLUENT solver settings in the last step.

3.2.3 Meshing

The mesh quality directly affects the convergence speed and the accuracy of the CFD results. Mesh generation is a model dependent process, which needs to address the underlying geometric features and solve the flow physics simultaneously. A good mesh is evaluated based on the density and the distribution of the elements. But a big mesh is not necessarily a good mesh.

The overall generator geometry presented is inherently difficult to mesh, since it is big in size, and involves many geometric features that can be as small as a few millimeters in one dimension and as wide as one meter in the other. This makes the traditional, manually structured meshing method no longer practical; instead, this study utilized the

advanced, automatic meshing method offered in ANSYS FLUENT. It generates unstructured tri- and quad-surface meshing that is driven by the curvature, proximity, smoothness and quality, in combination with a pinch capability that automatically removes insignificant features [82]. The automatic meshing also takes the analysis type into consideration when generating the mesh, which for this study is a CFD FLUENT study.

The near-wall treatment significantly affects the fidelity of the simulation for turbulence flows, where the flow momentum and other transports occur most vigorously [79]. It also determines the appropriate turbulence solver since the solvers have their own near-wall resolution requirements. For example, the four-equation SST model requires the implementation of inflation layers in order to refine the wall y-plus values to the order of 1, whereas the wall function based K-epsilon model commonly accepts wall y-plus values of 50 to 300. The uses of the wall-functions substantially saves the computation time for most high Reynolds number flows, while the addition of inflation layers improves the accuracy of near-the-wall calculations. The wall-function option has widspread use because it is an economical, robust and reasonably accurate alternative for the inflation layers [79], and has been used for many industrial flow simulations.

Mesh convergence study was performed on two rotor sub-domains, or the endturn cavities that are the focus of this study, and the radial subslots that are the highest density geometric feature in the CFD model. Five default element body sizes ([10, 8, 5, 3, 1] mm) were tested and convergence study was conducted with the implementation of the *advance wall function*, which offers additional improvements on program detected curvature and proximity features. At the body size of 8 mm, the average wall y-plus first decreased to within the desired 50 to 300 range; and at body size of 5 mm, the average wall temperatures and the local velocity magnitudes reaches convergence. Therefore, the initial mesh element sizes are selected to be 5 mm for the rotor body and 8 mm for the stator endturn region. The *conformal mesh* setting is forced so that all the inner surfaces are connected. The *match control* setting is used at the cut-out surfaces, or the 180-degree sides of the annulus, in or-

der to apply the *periodic* boundary condition in the FLUENT solver. Additional automatic mesh refinement is applied using the *advance functions* option, which applies 'curvature and proximity' improvements based on the detected geometric features. The initial mesh is shown in Figure 3.12, where denser mesh is located in the small dimension regions such as the radial vents. The stator parts are meshed with Hex elements, which minimize the local mesh sizes and work well for regions where the flows align with the mesh distribution.

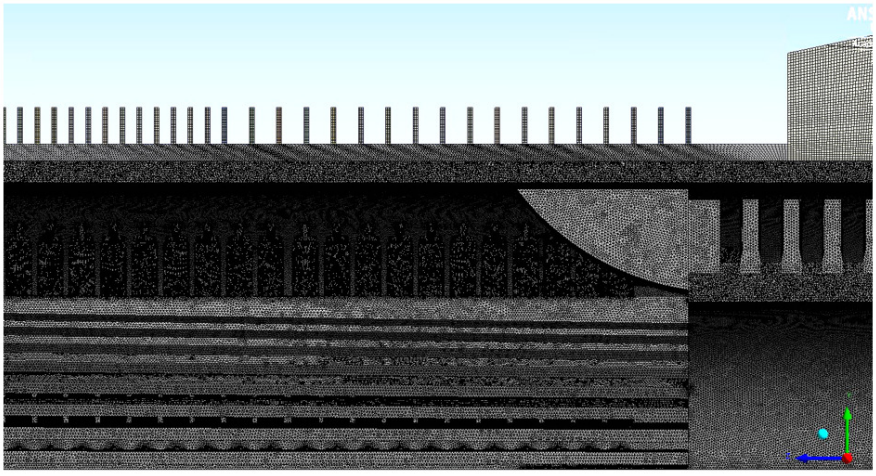

Figure 3.12: Overview of the original mesh generated by the automatic mesher

The initial mesh results in 63,644,547 elements and 20,649,421 nodes. Hexagonal elements dominate in the stator regions and tetrahedral elements dominate in the rotor, with wedges and pyramid elements existing in the transition regions. Two matrices are examined when assessing the quality of a mesh, which are the orthogonal quality and the skewness. The average skewness is 0.235 and the average orthogonal quality is 0.85; both values are inside the 'very good' range on the meshing matrices. The mesh matrix distributions are shown in Figures 3.13 and 3.14 below.

- Skewness
  - Avg: 0.235
  - Min: 0.000016
  - Max: 0.99

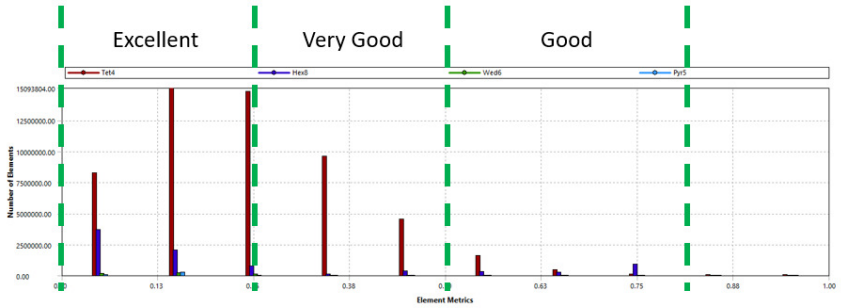

Skewness mesh metrics spectrum

Excellent	Very Good	Good	Acceptable	Bad	Unacceptable
0-0.25	0.25-0.50	0.50-0.80	0.80-0.94	0.95-0.97	0.98-1.00

Figure 3.13: Mesh matrix: skewness summary

- Orthogonal quality
  - Avg: 0.85
  - Min: 0.03
  - Max: 0.99

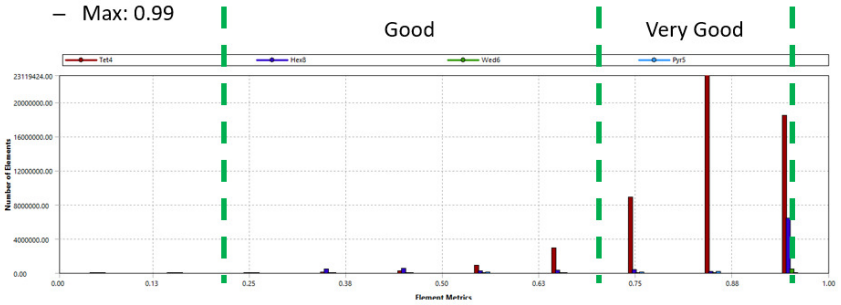

Orthogonal quality mesh metrics spectrum

Unacceptable	Bad	Acceptable	Good	Very Good	Excellent
0-0.001	0.001-0.14	0.15-0.20	0.20-0.69	0.70-0.95	0.95-1.00

Figure 3.14: Mesh matrix: orthogonal quality

Mesh adaptations are used to correct the near-wall elements based on the calculated local velocity magnitudes in order to meet the y-plus value requirement. Figure 3.15 presents the mesh comparison before and after adaptation for the radial vents and endturn cavities. On the left of Figure 3.15 are the uniform, initial meshes generated by the automatic mesher in ANSYS; on the right are the refined mesh after the first 2000 iterations

when the flow was initialized. This allows refinement on the high velocity regions, where denser mesh is needed, as illustrated by the circled regions in Figure 3.15.

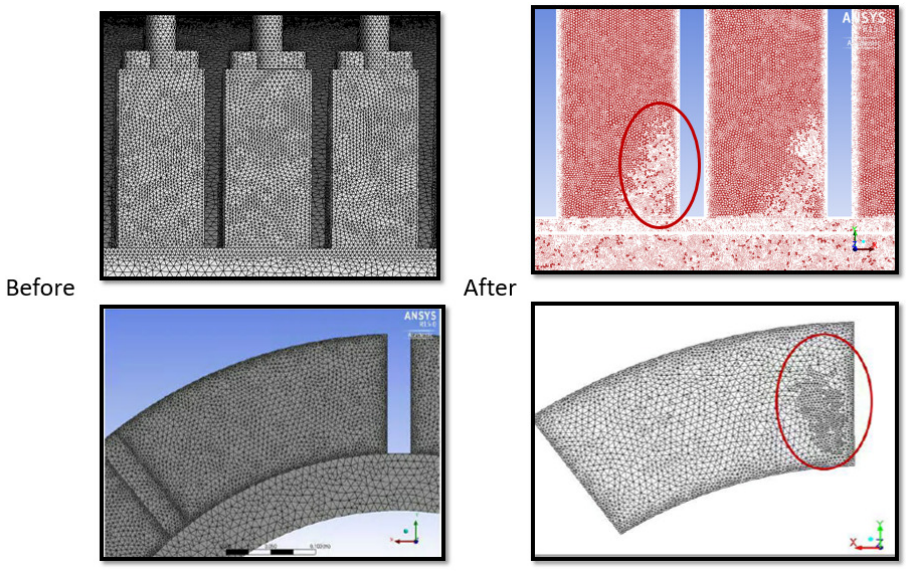

Figure 3.15: Mesh adaptation demonstration. (Left)Before adaptation, (right)After wall y-plus based adaptation.

3.2.4 CFD Model Setup

The most critical step in a CFD study is the model setup. If and only if the model is set up properly, can the simulation effectively and accurately capture all the flow characteristics. This section covers the settings the FLUENT program requires in order to perform the CFD study, including the definition of cell zone properties, the selection of a turbulence solver, and the definition of the boundary conditions.

3.2.4.1 Cell Zone Conditions

The *cell zone condition* in FLUENT defines the states of the flow geometries included. First, the steady state solution is pursed, with the energy equations turned on to calculate the accompanying changes in temperatures. Second, all volumes included in this generator CFD model are *fluid* and are defined to have the *Boussinesq* air property. The Boussinesq approximation assumes a simple relationship between the Reynolds stresses and velocity

gradients through the isotropic eddy viscosity. Third, due to the nature of the generator parts, two reference frames exist, where the stator regions and the top half of the airgap are stationary, and the rotor and the bottom half of the airgap are rotating at 3600 RPM, both looking with respect to the global coordinate system. Note that the airgap is split into two at the middle of its thickness, as a transition region between the stationary and rotating flow domains.

Second, the airgap and all of the fluid regions in the rotor have 100% of their volumes open for flow, but the stator regions above the airgap are given porous medium properties to account for the fact that in reality, only a percentage of the total volume modeled allows the flow to pass through due to simplification. As mentioned earlier, the porous medium environment allows the simplification of complex flow domain geometries by assigning additional directional resistances to compensate for the missing solid portion in the overall volume. The pressure drop is the driven forces in the porous medium and is the result of the viscous losses and the inertial losses; the former is directly proportional to the velocity magnitude but the latter is proportional to the velocity magnitude squared. Therefore, for the expected high velocity magnitude regions in the stator, the inertial resistances are assumed to be dominating. Several methods are available to calculate these porous medium parameters, which are mostly determined based on the data available, and the applicable assumptions and simplifications. In the stator regions, the flow directions and the pressure differences Δp are available. Therefore, the inertial resistances are calculated using Equation 3.1 based on the method provided by FLUENT, which derives the values based on the *superficial velocity* crossing a pressure loss over a measured length,

$$\Delta p = K_L(\frac{1}{2}\rho {v_s}^2) \tag{3.1}$$

here, all values are the real regional fluid properties calculated based on the actual geometric features. More specifically, Δp is the measured, averaged pressure difference cross the

lamination's inner and outer radius; ρ is the fluid density; Q is the volumetric flow rate; K_L is the loss factor in the same direction as the pressure loss; and v_s is the fluid velocity that is calculated based on actual opening of the fluid volume using Equation 3.2

$$v_s = \frac{Q}{A_s} \tag{3.2}$$

the loss factor K_L needs to be adjusted first by its porosity because FLUENT treats the porous entire cells as 100% open to flow

$$K'_L = K_L \frac{{v_{medium}}^2}{{v_{100\%opening}}^2} \tag{3.3}$$

last, the inertial loss factor C applied in FLUENT is per unit length of the porous medium basis, calculated as shown in Equation 3.4

$$C = \frac{K'_L}{l_{medium}} \tag{3.4}$$

here, l_{medium} is the length in the calculated direction and equals $4in$ for the simplified stator vents, and C needs to be calculated for each direction for anisotropic media. Equations 3.2 to 3.4 apply to both the stator vents and the endturn lattice-structured stator winding region. Note that l_{medium} equals the thickness of the lattice structure for the endturn stator winding region.

There are a total number of 130 vents over the active length of the rotor body separated into nine-zones and two types of domain according to the directions of the flows, 92 outlet vents and 38 inlet vents. Regional air flow rate is measured and reported for each domain type, and it is averaged over the number of vents counted inside, for an estimated flow rate for the individual vent. More specifically, 50411CFM of air are reported for the five outlet zones, which is equivalent to 548CFM of air per outlet vent; each outlet vent is also controlled to have a gauge pressure of 5 inches of water [in H2O] at the outer di-

ameter, with a pressure drop of 5 [in H2O] at the airgap; Similarly, the 38 inlet vents are calculated to carry 487CFM of air per vent, with a factory controlled inlet gauge pressure of 16 [in H2O] at the outer diameter over a 4.8 [in H2O] pressure drop when it arrives at the airgap. Note that the airgap is specifically designed to maintain roughly 12 inches of water throughout the active length of the rotor. The flow diagram is shown on the left of Figure 3.16 below.

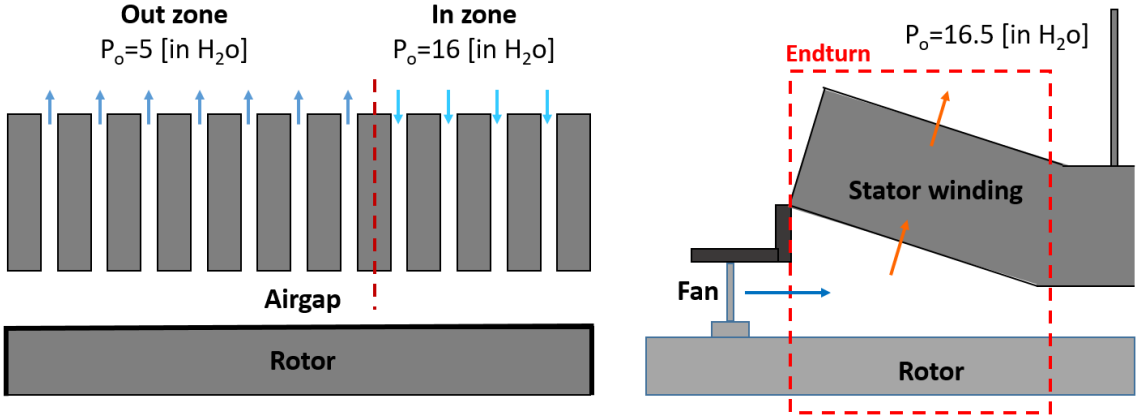

Figure 3.16: Flow schematics for: (Left) Stator vents, (Right) Endturn stator winding

The stator endturn winding region is reported to have an overall flow rate of 30,000 CFM, and an outlet gauge pressure of 16.5 [in H2O] and a total pressure drop of 0.2 [in H2O] over the thickness of this structure, as shown on the right of Figure 3.16 right. Thus far, the inertial resistances in the dominant directions of the simplified stator regions can be calculated. It is obvious that the stator flow regions are not isotropic; therefore, the inertial resistances in the other two directions need to be determined. Based on the previous inspections of the components' alignments and the structural patterns in the stator, it is reasonable to assume that the flow has nearly no potential to travel in the other two directions inside the bounded volume. Therefore, when assigning C values in FLUENT, the other two directions are assigned to have resistance values that are 100 times higher than those of the governing directions. The calculated inertial resistances in the dominant flow direction in each defined region are summarized in Table 3.1 below.

Table 3.1: Summary of the porous medium parameters for the simplified stator flow regions

Zone	Radial inertial resistance	Porosity
Stator endturn region	20.2	0.5
Stator vent outlet zone	35.6	0.5
Stator vent inlet zone	34.48	0.5

The solid components are not modeled in this study; however, the fluid adjacent surfaces need to be defined with the corresponding material properties in order to capture the heat transport in the energy equations. The actual locations and shapes of these surfaces are displayed in the next boundary condition section, in the discussion of the heat transfer related loading conditions. The material definitions are summarized in Table 3.2 below

Table 3.2: Summary of CFD model material properties

Material	Region/surfaces
Air	All modeled fluid domains
Copper	Rotor coil adjacent surfaces
Steel	Laminations, shaft, wedges, rotor core
Insulation	Endturn: axial and radial insulation Active length: insulation between wedges and rotor coil

3.2.4.2 Solver Selection

The wall function coupled K-epsilon model is chosen because the mesh cannot afford to create the inflation layers at the desired resolution to satisfy the y-plus value requirement for the SST model. After comparing the available K-epsilon models in FLUENT, the realizable K-epsilon model with enhanced wall function combination is chosen to solve the generator. The realizable model has the advantages of providing superior performances

for the flows involving rotation and boundary layers under strong adverse pressure gradients, separations, or recirculation, which are expected to occur in the generator[79] [80]; and the enhanced wall-function is suitable for flows with complex near-wall phenomena [79]. Together, they can capture the complex internal flow phenomena in the rotor more accurately.

3.2.4.3 Boundary conditions

Boundary conditions in this study apply to the surfaces of the modeled geometries, and are generally categorized into two types, namely the *operating conditions* and the *loading conditions*. First, the operating conditions apply to the inlets and outlets, or the borders of the model, to guide the flow distribution. They are defined based on the provided factory data or known design requirements, and some are modified according to the simplifications taken to meet the design objectives. The operating boundaries consist of the following:

- **Axial cooling fan inlet:** Pressure inlet, at the front of the CFD model is located at the inside of the cooling fan with known gauge pressure and the directional velocity vector.
- **Stator vent inlet:** Pressure inlet with known gauge pressure and the directional velocity vector.
- **Stator vent outlet:** Pressure outlet with known gauge pressure and back flow temperature.
- **Center of rotor:** Symmetry
- **Endturn annulus cutoff planes:** Periodic boundary (trailing side is the shadow surface)

The loading conditions define the amount of heat transfers from the internally heated solid components that need to be cooled, and the amount is a critical value that FLUENT

uses to calculate the wall temperatures to evaluate the ventilation performances. Since the solid components are not modeled, the heat sources are converted to equivalent surface heat fluxes that dissipate through the fluid adjacent surfaces. In the rotor, a constant field current applies to each strap in the rotor coil that results in an Ohmic loss Q that is calculated as Equation 3.5

$$Q = I^2 R \tag{3.5}$$

where I field current at the expected operating condition; R is the electrical resistance of the copper strap. The values of the electrical resistance are related to the geometry of the coil and its material property, which is calculated using Equation 3.6

$$R = \frac{L_{strap}}{A_{strap}} \rho \tag{3.6}$$

and ρ is the copper resistivity and is equal to $1.68E^{-8}\ \Omega \cdot m$; and A_{strap} and L_{strap} are the cross-sectional area and the length of the strap, respectively, as shown in Figure 3.17.

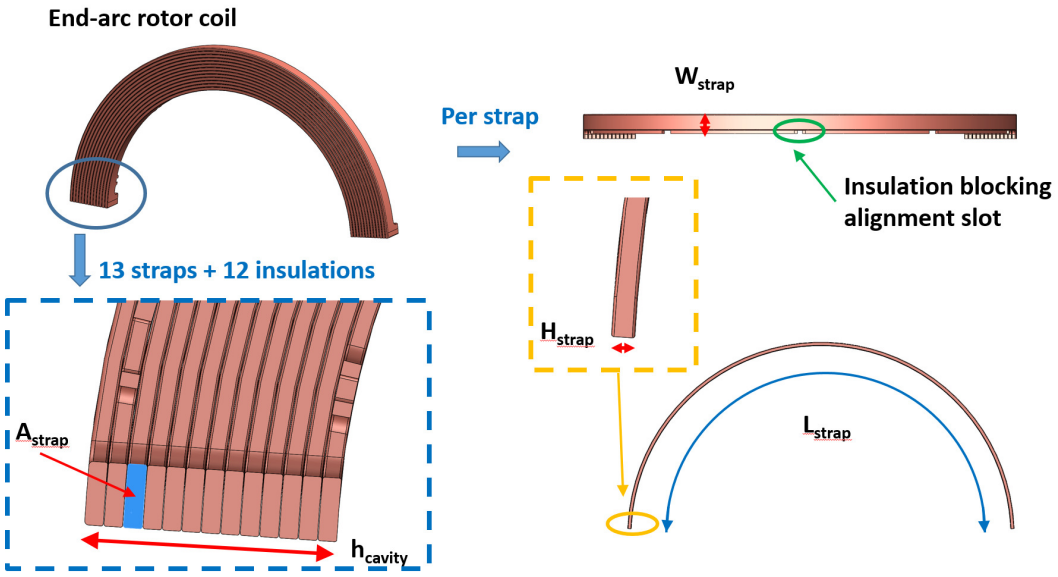

Figure 3.17: Rotor strap dimension demonstration.

The total amount of heat is distributed over the exposed surfaces, and therefore the

corresponding surface heat flux is calculated as in Equation 3.7

$$q'' = \frac{Q}{A_s} = \frac{(I)^2 \frac{L_c}{A_c} \rho}{A_{eff}} \tag{3.7}$$

where A_s is the coil surface area and needs to be individually determined for each cooling geometry. A_s is further adjusted to A_{eff} by minusing the surface areas of the cavity insulation, in order to account for the areas that do not contribute to heat transfer.

The rotor coils are directly adjacent to the endturn circumferential cavities, the axial cavities, and the bottom of the radial vents. Thus, before the calculations of the effective surface areas A_{eff}, one turn of the rotor coil lengths is divided into three region, namely the *end-arc, endturn straight length*, and *active length* as shown in Figure 3.18, which are divided based on the identified, unique cooling geometries. The separation of coils is performed based on the assumption that in the ideal cooling design, these regions are cooled effectively by their own cooling domains, and therefore these three labeled regions are thermally isolated where no heat transfer occurs in-between.

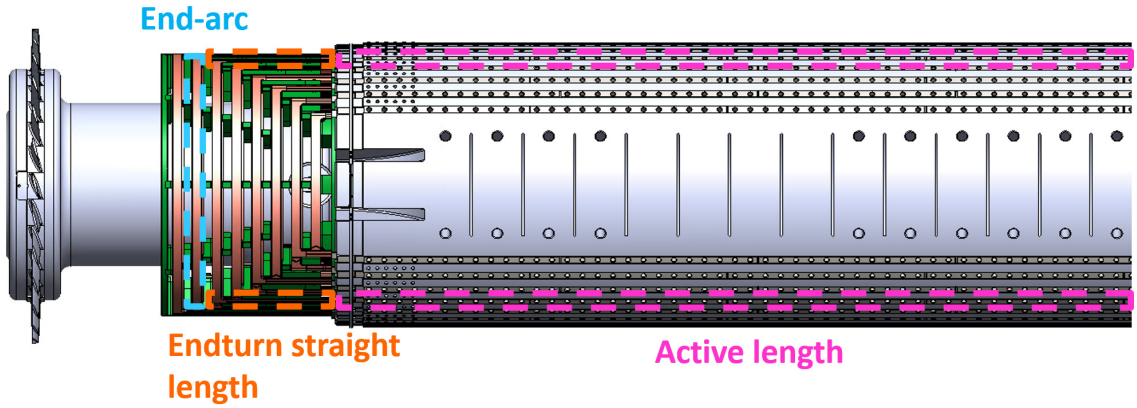

Figure 3.18: Endturn coil separation demonstration for the end-arc, endturn straight length and active length definition

To find the effective heat transfer dimensions, unit volumes in each defined cooling region need to be defined. The construction pattern in the endturn region results in each circumferential and axial cavity being bounded by one longer coil at one side and one

shorter coil at the opposite side; or the endturn coil dissipating heat to two different size cavities. First, one unit cell of the circumferential cavity is heated by half of the front coil and half of the back coil, as shown inside the yellow box in Figure 3.19 below. Therefore, each circumferential cavity is heated by the same surface heat flux on its front and back surfaces.

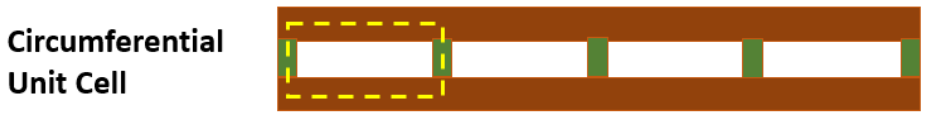

Figure 3.19: Circumferential cavity heat transfer unit cell definition

Thus, the amount of Ohmic loss that dissipates to immediate adjacent circumferential cavity surfaces Q_{circum} is generated from half of the coil thickness, or

$$Q = \frac{1}{2} I^2 R \tag{3.8}$$

and R needs to be calculated based on the dimensions of the defined unit cell copper for the circumferential cavity. The existences of the blockings, the effective surface area for heat transfer is the total coil surface area in Figure 3.20 B, less the sum of the blocking surface area, as shown in Figure 3.20 A. This effective surface area is calculated as

$$A_{eff} = n\pi \frac{\theta_c}{360} R_{avg} = \pi \frac{\theta_c}{360} ({R_o}^2 - {R_c}^2) = r^* A_{coil} \tag{3.9}$$

where θ_c is the cavity opening (degrees); n is the number of cavity per row; R_o and R_c are the outer and inner diameters of the rotor coil; and r^* is the ratio between cooling area and total surface area, calculated as

$$r_i^* = \frac{A_{total}}{A_{heat}} = \frac{A_{coil}}{A_{cavity}} = \frac{A_{coil}}{A_{coil} - \Sigma A_{insulation}} \tag{3.10}$$

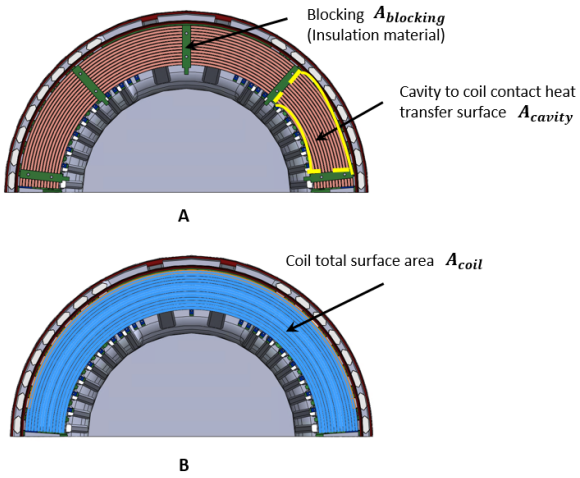

Figure 3.20: Coil total surface versus heat transfer surface (A)Endturn coil, blocking and fluid cavity construction; (B)Coil total surface area

The axial cavity cools the straight part of the rotor coil, and is composed of inner and outer cavities that are separated by axial insulation, and has a geometry as shown in Figure 3.19 before. These two sides are adjacent to two different coils; or each endturn straight length coil is cooled by the inner and outer cavities of two axial cavities, as shown in Figure 3.21. Only the two outer surfaces of the axial cavities directly touch the heated coils and have a heated boundary condition; their inner surfaces are adiabatic. The inner and outer cavities are each heated by half of the coil, and the inner cavity has a lower heat flux since the surface area of the cavity is bigger than that of the coil.

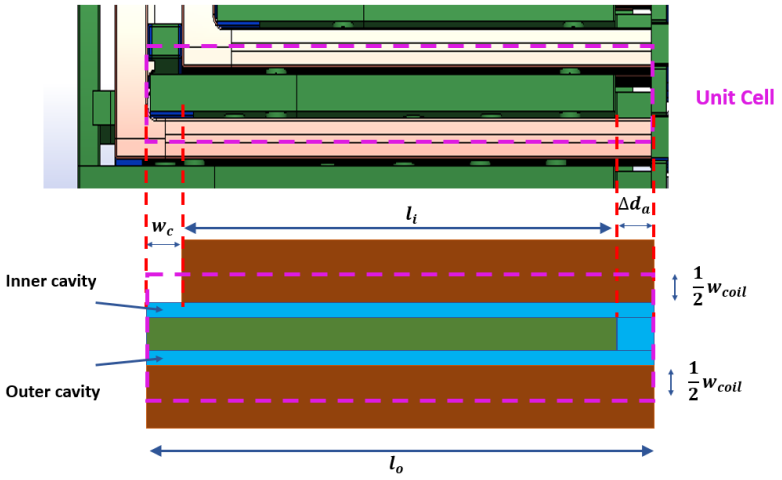

Figure 3.21: Axial cavity heat transfer unit cell definition.

The radial vents are the void spaces inside the rotor coils, which are evenly spaced along the rotor active length. This active length of copper is therefore divided into equal volume parts, and each unit cell of copper is cooled by the radial vent inside, as shown in Figure 3.22.

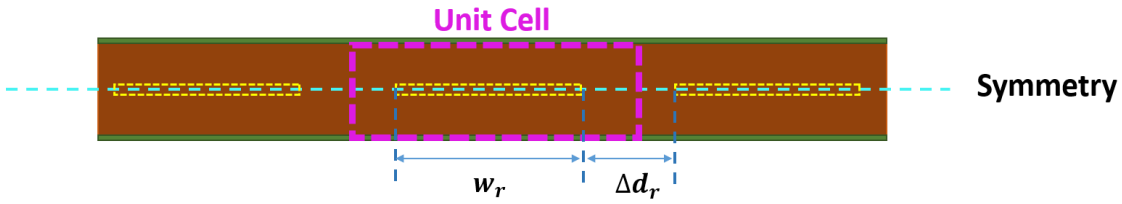

Figure 3.22: Radial cavity heat transfer unit cell definition.

Therefore, the unit cell of copper for the radial cavity has a top cross-sectional area that equals the product of the width of the coil and a length that is the sum of the length of the radial vent l_r and the radial vent separation distance Δl_r.

$$V_{cu}\,|_{rad} = w_c \cdot h_{strap} \cdot (l_r + \Delta l_r) \tag{3.11}$$

the amount of Ohmic loss in the unit volume copper needs to account for the void space in the middle, or

$$Q_{rad}\,|_{ad} = Q \cdot \frac{V_{cu}\,|_{rad} - V_{rad}}{V_{cu}\,|_{rad}} \tag{3.12}$$

here V_{rad} is the volume of the center void space and Q is the amount of heat for a solid copper strap, using Equation 3.5. This heat is dissipated only through the surface area of the radial vent A_{rad}, and is calculated as

$$q''_{rad} = \frac{Q_{rad}\,|_{ad}}{A_{rad}} \tag{3.13}$$

Two expected generator operating conditions are conducted using the developed CFD model, and their field currents are summarized in Table 3.3 below. Both cases are known to have inlet air maintained at 48 degrees Celsius, 16.6 inch-water and a 30-degree inlet

velocity angle. These two extreme operating conditions are chosen as the presentitive cases to study the current generator ventilation performance.

Table 3.3: CFD case summary

Case	Field current (Amp)
Mechanical	146
Short Circuit	1074

To sum up, the following boundaries in this CFD model are given specific boundary condition definitions and the corresponding settings are summarized in Table 3.4. The remaining surfaces that are not mentioned are given the default adiabatic wall boundary type, since they are adjacent to insulation with no heat transfer. The geometries of the boundaries are summarized in APPENDIX B SECTION B.2.

Table 3.4: Generator CFD model boundary condition summary

Boundary Type	Location	Definition	Input
Operating Condition	Fan inlet	Pressure inlet	Gauge pressure + Velocity vector + cold gas temperature
	Stator vent outlet	Pressure outlet	Gauge pressure + Back flow air temperature
	Stator vent inlet	Pressure inlet	Gauge pressure
Loading Condition	Endturn cavities	Heated walls	Surface heat flux
	Radial vents	Heated walls	Surface heat flux
Other	Center of rotor	Symmetry	NA
	Annulus cutoff	Periodic	NA

3.3 Simulation Results and Validation

Simulations are carried out successfully using the model developed in the previous section. As expected, the big mesh size and the solver complexity results in long run times; it takes about 3 weeks to complete one full run of simulation and is extensively time consuming. This section examines the simulation results to (1) verify the accuracy of the numerical generator model, and (2) understand the cooling performances in the rotor endturn regions. To reach these research goals, local CFD results are extracted and quantitatively compared with factory provided data, and phenomenological compared with the related papers presented in CHAPTER 2.

The flow conditions along the active length of the rotor, or inside the tapered subslots and the equally spaced radial vents are studied in the past already [88]. Though only a portion of the subslots are shown in this figure, it is noticed that the velocity magnitudes in the downstream radial vents are only slightly decreased, as the result of the decrease in the cross-sectional area of the tapered subslot, and therefore the cooling performances are expected to be approximately equal, which corresponds to the phenomenon discovered by Lu et al. [88].

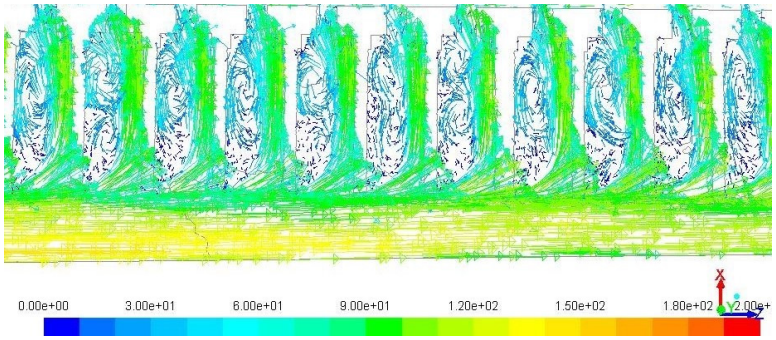

Figure 3.23: Rotor radial vents velocity plot (Relative velocity vectors colored by relative velocity magnitude

Next, the endturn axial cavities are inspected. Two representative vector field plots are shown in Figure 3.24, and the planes are taken at the middle of the axial cavities. They

are the shortest and the longest pieces in the axial cavity structure, where the flow results are the most interesting. Note that the axial cavities align with the z axis, pointing to the active length of the rotor. The flow patterns are as expected, where strong bulk flows present because of the confined thin space available; the flows travel radially upwards as the result of the rotational motion; and the flow directions follow closely with the alignments of the void, circular-shaped 'buttons', which force the flow to travel axially downstream at the same time.

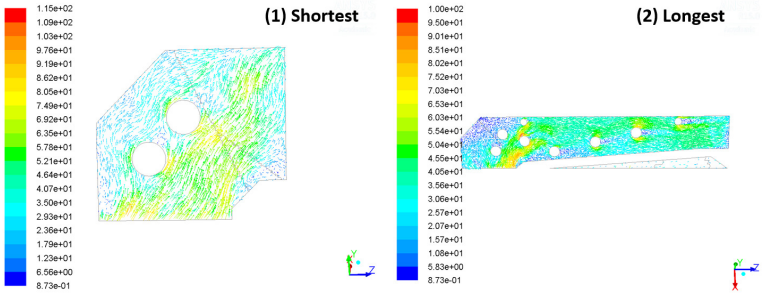

Figure 3.24: Endturn axial cavity velocity vector field plots (relative velocity vectors colored by relative velocity magnitude) for: (1) the shortest axial cavity, (2) the longest axial cavity

The endturn circumferential cavities are inspected, Figure 3.25 presents the streamlines inside the circumferential cavities. It appears that a swirl presents inside the circumferential cavities.

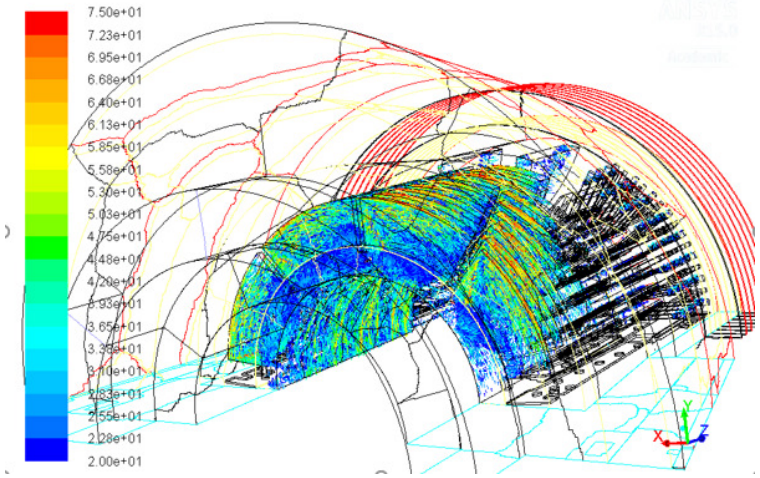

Figure 3.25: Streamline plot of the rotor endturn region.

For a clearer inspection of the flow conditions, vector fields on a plane through the cavities are extrated and presented in Figure 3.26. This figure presents the four save row cavities for comparison, where a swirl along the cavity perimeter is observed in each cavity, similar to that is observed by Hayase et al. [89], shown in Figure 2.9. Therefore, the flow results are as expected. But, it is also noticed that as the result of the additional forced inlet flow and the placement of the blocking, the cavity swirls inside the sector-shaped domain here do not spread over the entire cavity volume; rather they leave nearly stagnant regions in the middle, compared to those shown by Hayse [89].

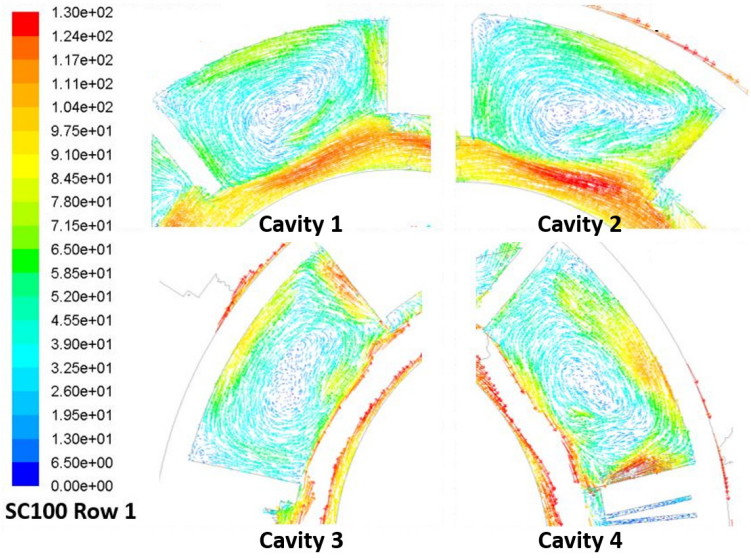

Figure 3.26: Endturn circumferential cavity velocity plot

The CFD calculated wall temperatures were used as references to evaluate the goodness of this CFD model, and a set of representative wall contour plots are shown in Figure 3.27 below. The factory sensors are located in the coil behind the blocking between two same-row cavities, and are not modeled in this fluid domain. Therefore, the labeled locations in Figure 3.27 were the approximated locations used for temperature comparison. The temperature differences between the CFD results and the reported sensors are summarized in Table 3.5 below. CFD temperatures were realized to under-estimate the wall temperature, but as expected. Temperature variations over the cavity surface were noticed to be

significant, since the fluid domain itself was unable to accurately capture the conduction heat transfer in the solid. Therefore, the part of the heat transport within straps (at same radial location) were not accounted for, and therefore resulted in under-estimated temperatures in the peripheral virtual pipe region; temperatures in the center of the cavity were over-estimated as well. But, the calculation errors were within the allowable range and the wall temperatures were not the target of this study.

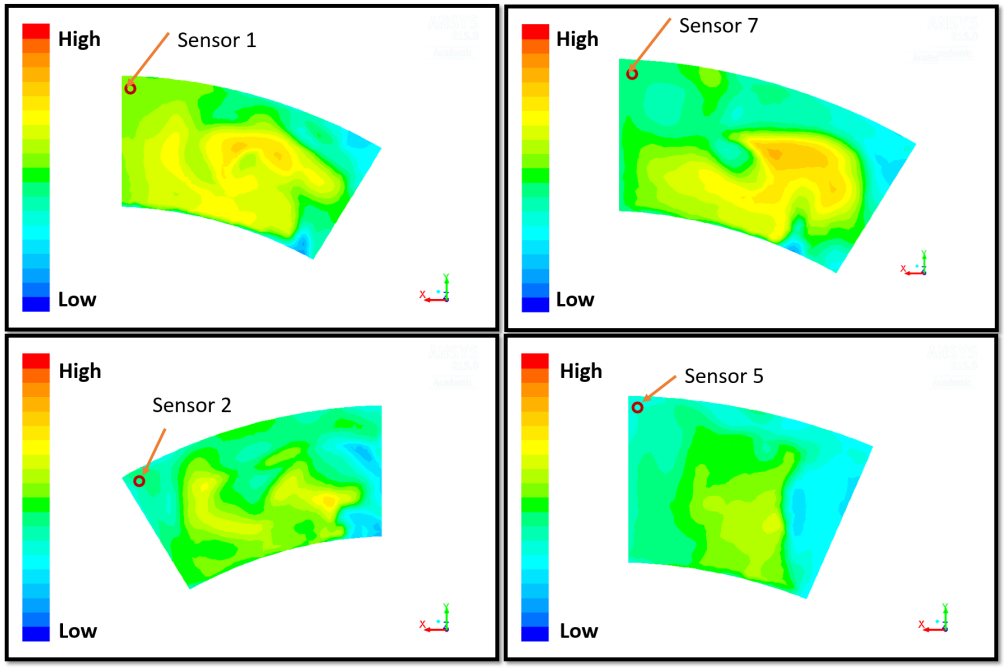

Figure 3.27: CFD wall temperature contour plots near the labeled comparable locations for the SC100 condition.

Table 3.5: Temperature difference between CFD results and reported sensor readings.

Sensor Location	Coil	Temperature Difference (C)
Center	Coil B	-4.1
	Coil D	-7.1
	Coil G	-6.3
Side	Coil B	-3.5

In sum, this generator model displays flow results as expected, which agreed with

both the literature presented results and the factory provided sensor values. Therefore, the results of this CFD study can be extracted for future study and this model can be implemented for other operating cases, if needed. The rotor endturn regions were inspected and a common flow pattern was noticed to present in the circumferential cavities, and were studied in detail in the next chapter.

3.4 Small Domain Rotor Endturn CFD Models

Now that the detailed generator CFD simulations have been completed and verified and the endturn region flows are understood, the next step is to investigate the end-arc cooling performances from the design perspective. This requires that the endturn regions to be studied parametrically for a comprehensive understanding of the cavity flows, such that a generic description can be developed for an analytical prediction of the end-arc coil temperatures. The generator model, however, involves too many changes in geometry and has a run-time that is too long for a parametric study. Therefore, this section develops two additional segmented endturn numerical models, which can be parametrically varied in geometry for the design study purposes. The first one includes only a partial circumferential cavity system to study the change of cavity flow conditions as the result of changes in the ventilation design parameters; and the other one includes the entire nested enturn cavities with the addition of their surrounding coils, to perform an endturn conjugated heat transfer (CHT) study for a comprehensive investigation of end-arc coil temperature. Assumptions and simplifications need to be taken for the segmented models, but they are possible mostly by adopting results directly taken from the trusted generator CFD simulations. The same four-step are followed to develop these two models and are briefly covered in this section, since the majority of the settings are the same. Only the changes in each step are discussed and explained in this section.

3.4.1 Three-row Endturn CFD Model

The generator CFD model provides insights on the flow conditions in the target endturn regions, but at a overly expensive cost in time and effort. In addition, only three cases are presented, which are not enough to conclude generalized observations. Therefore, a parametric three-row endturn cavity model was proposed as a time-efficient numerical tool, and is shown in Figure 3.28. Similar to the previous models, only 180 degrees is included because of the symmetry in rotor construction. The model starts at the front of the retaining ring; and it ends at a distance of $1/2w_{cu}$ behind the back walls of the 3rd row cavities so that the cavity internal flows are less sensitive to the applied outlet flow conditions. The second row cavities are given the parametric design values, and are the only ones extracted once simulations are completed. The extra rows of cavities upstream and downstream are included to position the center row cavities away from the far-field boundaries (the inlet and outlet surfaces), for an improved, steady and developed flow calculations. This model is parametrically defined in the dimensions such that the geometry can reflect any change in dimension and construction pattern if needed.

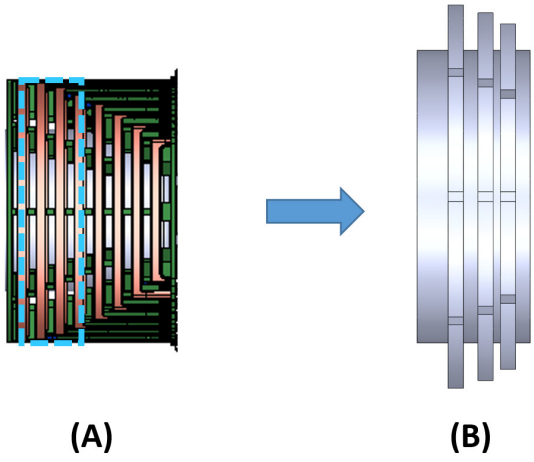

Figure 3.28: Partial endturn CFD model. (A) Endturn solid geometry, (B) Flow region geometry

Overall, the CFD model setups follow the same four steps, but three changes needed

in the settings are realized.

1. Benefitted from the decrease in the CFD geometry size, a significant decrease in simulation run-time is expected, which allows the use of the more expensive, higher-order transition SST turbulence model. Mentioned in SECTION 2.3, this model is superior to the two-equation k-epsilon model, at an improved accuracy, especially for rotating turbulence flows.

2. The outlet boundary is moved to a location inside the endturn region between two rows of cavities, in which the local gauge pressure is unknown. But an estimated value can be obtained from the generator CFD study. Here, it is assumed that the endturn redesigns discussed in the later parametric study are developed based on the requirement that the overall generator ventilation performances must remain almost consistent, especially in terms of the pressure distribution along the three main flow paths in the machine. This means that ideally, in order to reach the same discharge pressures at the radial vent outlets into the airgap, the upstream subslot pressure needs to remain constant, which requires that the further upstream endturn annulus pressures remain constant. Under this assumption, the pressure outlet boundary here is expected to be at the same value, or equal to the facet average pressure value extracted at the same location from the generator CFD study. This outlet boundary value is strictly forced regardless of the change in the design parameters.

3. The inlet of the rotor is moved to the front of the retaining ring, and is given a uniform velocity distribution with a constant axial and tangential velocity component inputs, for the convenience of the design of parametric cases. This boundary definition is also possible due to the observation that the forced inlet flow from the rotor fans are still relatively uniform when arriving at this location.

The unique settings for this three-row endturn CFD model are summarized in Table 3.6.

Table 3.6: Three-row endturn cavity CFD model Setup Summary

Setup	**Type**	**Input Value**	**Parameter (P)/ Constrain (C)**
Turbulence model	SST	NA	NA
Rotor inlet	Velocity Inlet	axial velocity	P
		tangential velocity	
		gauge pressure	
		temperature (48 °C)	
Outlet	Pressure outlet	-10000 pascal [2]	C

[1] Other model settings are the same as the ones listed in SECTION 3.2.4.

[2] Averaged pressure value taken from result of full generator CFD model in CHAPTER 3.

The automatic mesher in ANSYS WORKBENCH is once again implemented to generate the initial mesh. The meshing setups are the same as the generator model, except that additional inflation layers are added on the cavity walls to satisfy the near-wall requirements for the transition SST turbulence model. More strict boundary layer *y-plus* values are required in SST method, which requires the wall y-plus values to be within 0 to 10. The inflation layers are added using the 'total thickness' method, and are setup at the maximum thickness equal to the default mesh element size, at a growth rate of 1.2 for a total of 10 layers. This inflation method is chosen because the internal cavity bulk flow is neither uniform nor predictable; and without a quantifiable characteristics length for reference, none of the traditional y-plus definitions (i.e. first point method) are applicable to use on the cavity walls. Forcing the sum of near wall layers to equal the first node creates a smooth

transition into the inner elements, and should not over-constrain the y-plus value either. The initial inflation layers are later improved again in FLUENT after the flow is initialized, using the y-plus 'adaptation' option to reach the desirable near-wall first nodes' y-plus values. A cut-out view of the generated initial mesh is as shown in Figure 3.29, to show the initial inflation layers.

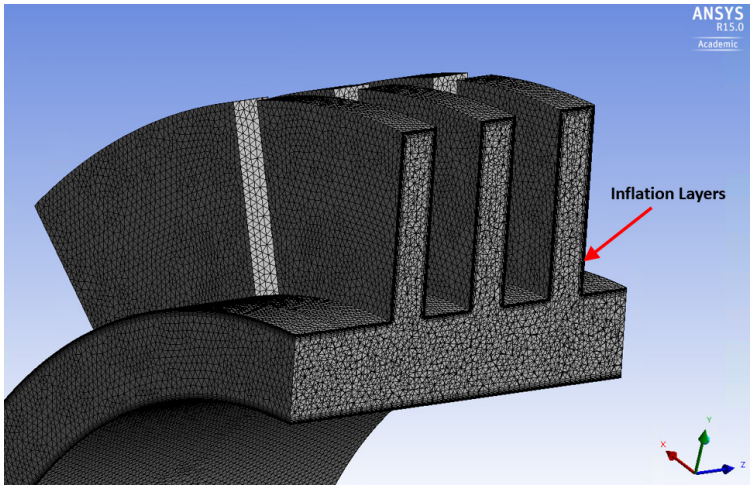

Figure 3.29: Meshing for simplified DOE model

3.4.2 Endturn Conjugated Heat Transfer Model

The previous models calculate the heat transfer equations by applying equivalent heat fluxes on the heated surfaces, which compromises the accuracy of the CFD wall temperature predictions since this neglects the significant circumferential conduction in each strap. To capture the conduction within the copper, a endturn CHT study is proposed, to obtain more accurate end-arc coil temperature calculations. The CFD geometry is shown in Figure 3.30, where all seven turns of rotor coils (shaded in dark) and their neighboring cavities (shaded in grey) are included. This model starts at the begining of the retaining ring and ends at $1/2w_c$ behind the last row of the cavity, before the annulus flow separates and enters the tapered subslots. By using the same coil length separation definition mentioned in the boundary condition section, the end-arc coils ended right after the 90 degree bent into the straight length; and the cutoff surfaces are given adiabatic wall boundaries, by taking the

thermally isolated regions assumption. Also, note that the first row of cavities in front of the longest coil has adiabatic surfaces facing the front, since they are adjacent to insulation placed at the beginning of the retaining ring. Taking the same, consistent generator pressure distribution assumption used in the parametric cavity case, the outlet of this region is given a pressure outlet definition at the facet average value evaluated from the generator simulation study again.

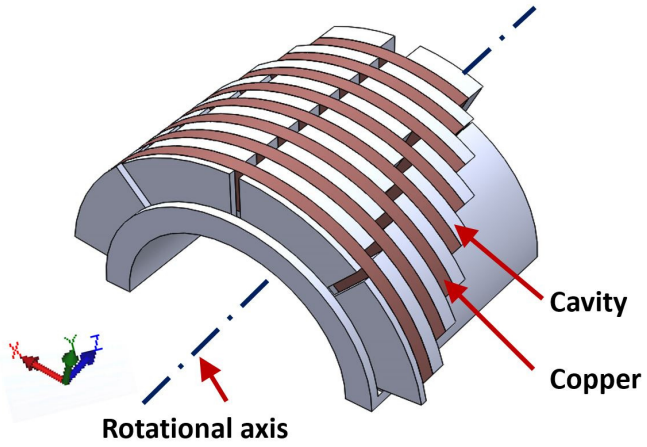

Figure 3.30: Endturn conjugated heat transfer model

Table 3.7: Conjugated heat transfer model setting summary [1]

Cell Zone/Boundary	Type	Value
Solid Zone	Copper	Radial orthotropic thermal conductivity
		Stationary
		Constant internal heat generation rate $\dot{Q}$

[1] The fluid settings are the same as the ones listed in Table 3.6

Here, the solid volumes are given a *radial orthotropic thermal conductivity* as an alternative for modeling the stacked 13 strap and 12 insulation layers construction. This method is possible for the fact that the insulation layers have significantly lower thermal conductivity such that they do not allow heat transfer between the adjacent coils in the radial direction. Therefore, instead of modeling these extremely thin volumes (0.7 mm

thick each), this CHT model defines its copper thermal conductivity in the radial direction as the sum of a series network of solid materials, using Equation 3.14 below.

$$k_{ra} = \frac{\sum_{i=1}^{n-1}(\delta_{copper} + \delta_i nsul) + \delta_{copper}}{\sum_{i=1}^{n-1}(\frac{\delta_{copper}}{K_{copper}} + \frac{\delta_{insul}}{K_{insul}}) + \frac{\delta_{insul}}{K_{insul}}} \tag{3.14}$$

here δ_{copper} and δ_{insul} are the thickness of each copper strap and insulation layer, respectively; K_{insul} is the thermal conductivity of the insulation, and is equal to 4.7 w/(m · K). This results in a radial conductivity of 6.7 w/(m · K), compared to 385 w/(m · K) for the normal isotropic copper.

Boundary conditions of this model are much simpler than the previous models, where only an inlet and an outlet condition need to be specified; they are given the *velocity inlet* and *pressure outlet* definitions, respectively. Meshing process follows a similar designs as that of the three-row endturn model, where inflation layers are added at the wall adjacent surfaces of the fluid volume. The volumes are mainly meshed using the *patch conforming method* with tetrahedral elements. A cut-out view of the CHT model mesh is shown in Figure 3.31 below.

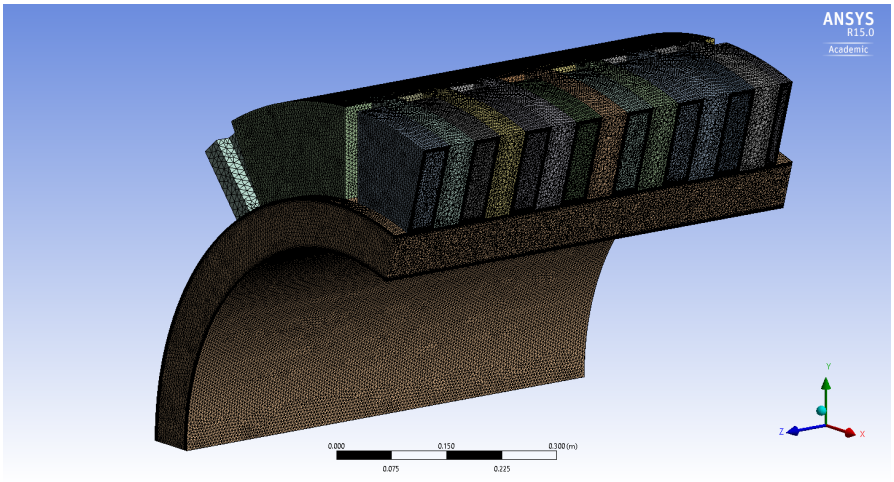

Figure 3.31: Mesh result for the conjugated heat transfer model.

This model is implemented later in CHAPTER 7 when verifying the accuracy of the final analytical temperature predictor. The CHT model is cross compared with the provided

temperature sensor readings to evaluate its accuracy.

3.5 Conclusion

Numerical studies were designed and conducted using ANSYS FLUENT for the target generator, to study the performance of the current generayot rotor ventilation design. The overall rotor ventilation regions are first studied using a detailed generator CFD model, of which the results are inspected and compared and verified with similar studies found in the literature, and provided temperature readings from factory testings. Even though many challenges existed when developing and conducting this CFD study, they were discreetly dealt with and the simulation results had demonstrated the model efficacy and accuracy. Preliminary inspections of the rotor endturn region indicate that highly complex three-dimensional internal flows present in the circumferential cavities, which have unique flow phenomena that cannot find a match to those available in the textbook. Therefore, a description of these cavity flows needs to be developed, in order to analytically determine the associated heat transfer and therefore the rotor coil temperature. Even though the cavity flow conditions are unknown, peripheral swirls are observed in all endturn circumferential cavities. This implies that the nested cavities might have the same flow phenomenon such that only one quantifiable description needs to be developed for the entire nest endturn system.

The generator model was able to provide detailed and accurate calculations of the flow conditions in the rotor, but at a high modeling and computation time. This limits the ability to use this CFD model to conduct parametric study in the endturn region for improved understandings of the flow phenomena in the circumferential cavities. Therefore, a three-row endturn cavity model was developed by defining boundary conditions with flow results obtained from the generator model, to offers opportunities to extend the endturn study to a comprehensive ventilation design study. In addition, a endturn CHT model

was developed for improved calculations in the solid region by allowing three dimensional conduction within the circumferential cavities' neighboring solid coils.

CHAPTER 4

PHENOMENOLOGICAL STUDY OF ENDTURN CIRCUMFERENTIAL CAVITIES

4.1 Introduction

This chapter studies the endturn cavity bulk flow phenomenon, as the second step in the endturn coil predictor development. The previous CFD study has established that these endturn cavities appear to have the same unique but repeated, counter-clockwise swirl, under all expected operating conditions. This internal bulk flow is the major contributor to the heat transport with the adjacent heated rotor coils; therefore, it requires detailed study. This chapter shows that the observed cavity swirls are phenomenologically the same in the nested endturn structure, and can be quantitatively described by a reasonable approximation of the extracted CFD data.

This study has two parts. First, a rank reduction in the CFD data domain was conducted in order to effectively extract, process, and visualize the massive three-dimensional data pool. The proposed extraction method allows each cavity to be represented with the same performance matrix $[\theta_c, r_c, V]$, with velocity profiles capable of representing regional bulk flow characteristics. Second, all endturn cavities were studied using this extraction method. Velocity profiles of the cavities at extreme conditions were compared to confirm the flow similarities.

4.2 Approach

4.2.1 Definition of Endturn Cavity

The segmented flow geometry, or here called the 'cavity', needs to be defined first before studying the CFD flow results in detail. For ease of future referencing, cavity volume was categorized and labeled into sub-domains, based on the streamline approximated internal flow results. Figure 4.1 is the rotor end winding streamline plot obtained from the full machine CFD study, which indicated that every endturn cavity flow volume had the same outer peripheral bulk flow with a center stagnant region, under all expected operating conditions. The characteristics of the outer peripheral bulk flow can influence the amount of heat transport with the adjacent heated rotor coils, and this is targeted in the present study.

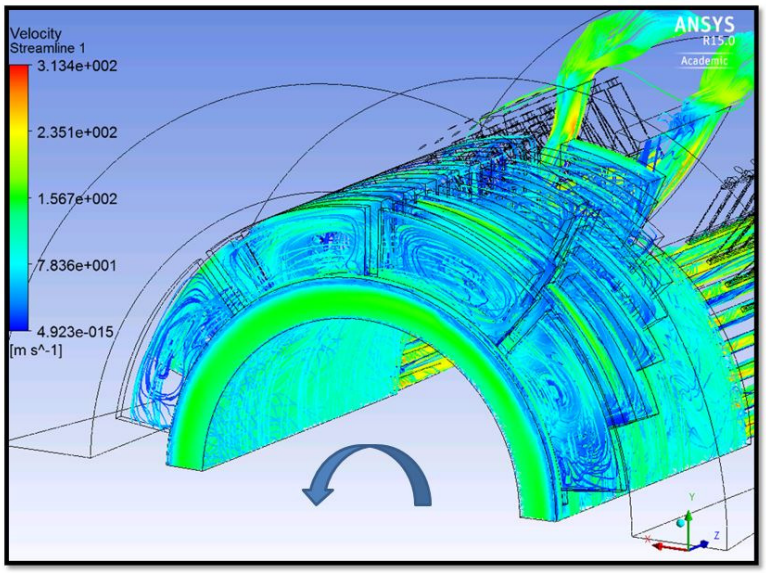

Figure 4.1: Rotor endturen streamline plot.

Figure 4.2 is a streamline plot of one representative cavity, which was extracted for detailed analysis. This cavity volume was examined from all directions, and the combined views indicate that the internal bulk flow follow closely with the cavity geometric features

and reach all five peripheral bounded walls. But the flow fails to cover the entire cavity volume, leaving the center of the cavity 'empty' with almost no flow. With the existence of this stagnant center, the cavity flow domain can be visually divided into separate regions.

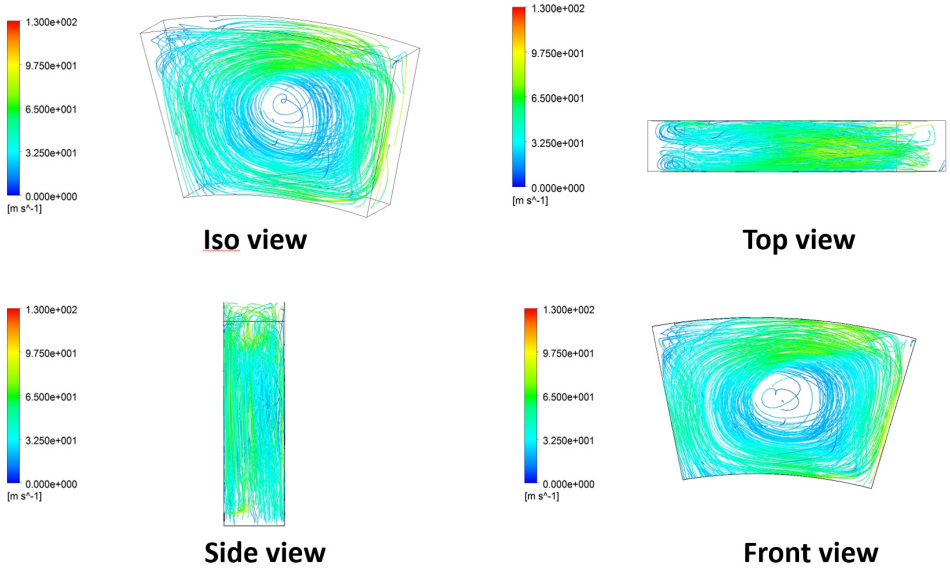

Figure 4.2: Streamline views of one endturn cavity.

The cavity can be first categorized into a bulk flow region and a center stagnation region, differentiated by the existence of streamlines. Next, the bulk flow regions can be further divided into smaller regions by their relative locations in the overall cavity internal flow path length. The bulk flow enters at the bottom right corner and exits at the bottom left corner, named *entrance* and *exit*, respectively. Between these two locations, the bulk flow changes directions three times, as a result of changes in bounding edges. Therefore three additional regions are named: *inlet*, *top*, and *outlet*. Sharp corners exist at the sides of the cavity's top curved edge, which connects two neighboring perpendicular cavity edges, and forces the bulk flow to change direction. These regions are therefore named the *bend transition* region, since complex flow physics are expected to occur. These definitions leave the inner, white empty space, named the *stagnant region*, which separates the three bulk flow volumes, and is expected to have little heat transport. The above local volume nomenclatures are labeled and shown in Figure 4.3 below. The sizes of these regions are

expected to vary on a case by case basis; thus the volumes labeled in this figure are for demonstration only, and are not to scale.

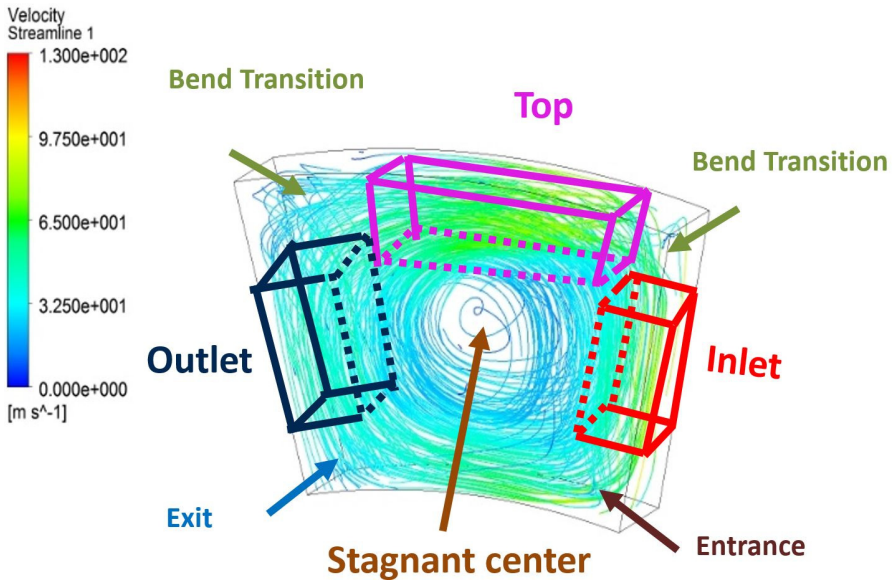

Figure 4.3: Cavity volume separation and definition.

Next, the global and local coordinate systems are defined. They are important when defining and comparing directions and magnitudes of the local bulk flows, and when referencing the extracted data locations with respect to the machine dimensions in general versus their bounding cavity dimensions. This flow domain is defined in cylindrical coordinates in this study because of its dominant cylindrical geometric properties. Therefore, the velocity components used are tangential, radial, and axial velocities. The positive $+\theta$ direction is pointing to the right and the positive $+z$ is pointing into the rotor. Therefore, the positive tangential velocity $+V_{tangential}$ is in a clockwise direction, the positive radial velocity $+V_{radial}$ is upwards to the outer diameter, and the positive axial velocity $+V_{axial}$ goes into the rotor, as labeled in Figure 4.4. On the other hand, local coordinates are defined on a cavity basis, over the cavity's own geometry dimensions $[\theta_c, w_c, \delta_r]$. Therefore, in the present study, inside each cavity, the extracted data's global coordinates are transformed into cavity local coordinates from right to left, from top to bottom and from front to back, by the cavity's dimensions.

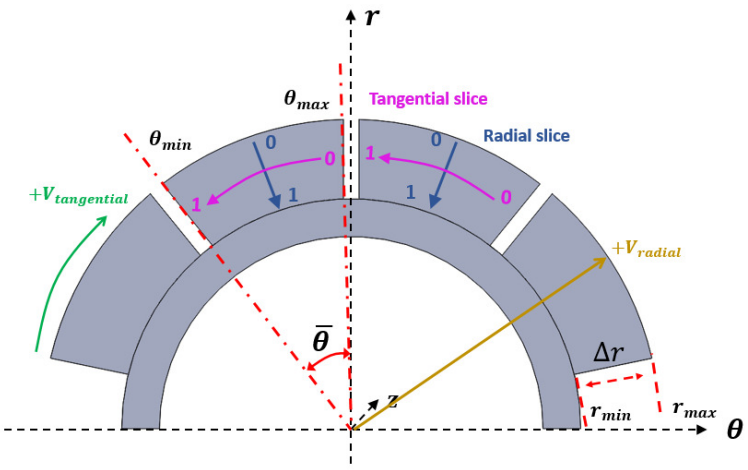

Figure 4.4: CFD global coordinates versus local cavity coordinates definition.

The velocity values and spatial coordinates of the extracted cavity data are normalized next for a generalized description. This normalization becomes very useful later in this chapter when comparing cavities with significantly different geometric and flow conditions. This being said, the ranges of each global spatial location $[\theta, r, z]$ are normalized to vary from 0 to 1, bounded by the edges of the cavity it is located in, following the defined local coordinate directions in the above figure. The local coordinates $\hat{r}$ are calculated using Equation 4.1, 4.3, and 4.2 for the tangential, axial and radial directions, respectively.

$$\hat{r} = \frac{r_o - r}{\Delta r} \tag{4.1}$$

here r_o is the rotor outer diameter and is a fixed value for all endturn cavities.

$$\hat{\theta} = \frac{\theta - \theta_{max}}{\bar{\theta}} \tag{4.2}$$

here θ_{max} is the global angular location of the cavity's left edge.

$$\hat{z} = \frac{z - z_{in}}{w_c} \tag{4.3}$$

here z_{in} is the global axial location of the cavity's front surface.

Velocity components are also normalized. When focusing on a single cavity, velocity components are normalized with respect to the constant average rotor rotating velocity $\overline{u}_{avg}$, and are calculated as

$$\hat{v} = \frac{v}{\overline{u}_{avg}} \tag{4.4}$$

here the averaged rotating velocity $\overline{u}_{avg}$ is calculated as

$$\overline{u}_{avg} = \omega \cdot r_{avg} = \omega \cdot \frac{r_o + r_{shaft}}{2} \tag{4.5}$$

Here, v can be the values of any velocity component.

But when cross comparing different cavities, velocity components are normalized based on the local maximum magnitudes; this limits the maximum velocity to be always 1 for the resulting profiles, such that profiles are comparable. This will be explained in more detail later in this chapter. This local velocity normalization follows Equation 4.6

$$\hat{v}_{mag} = \frac{v_{mag}}{v_{max}|_i} \tag{4.6}$$

here, $v_{max}|_i$ is the local maximum value of the studied component v.

Thus far, the endturn cavity's spatial locations and bulk flow components are fully defined. For the rest of the study, the descriptions of the resulting bulk flow characteristics all follow the sign and naming conventions listed here.

4.2.2 CFD Data Rank Reduction

Now that the endturn cavity nomenclature has been defined, this section starts the endturn bulk flow phenomenon study by developing a data extraction method in order to quantitatively and effectively inspect the flow properties. While there are many ways to extract the data, the vector field results are the most useful. Streamlines are useful to visualize the flow trajectory but only provide values of the velocity magnitudes. Also, for

a steady state flow, the vector fields and streamlines are known to be essentially the same, but vector field extraction offers much more information, such as values of all available velocity components. Vector field results are also easier to manipulate to study regional flow performances. Therefore, the data from cavity vector fields are extracted.

The endturn fluid domain is meshed at a fine resolution and as a result, an overwhelming number of nodal points is avaliable. In the absolute reference frame, nodal points are located at $[\theta, r, z]$ with velocities of $[V_{ax}, V_{tang}, V_{rad}]$. These points can also be expressed in terms of the sum of velocity vectors, or the velocity magnitudes V_{mag} at velocity angles θ_v. In the rotating reference frame, another two components are available, which are the relative tangential velocity $V_{tang}\mid_{rel}$ and the relative velocity magnitude $V_{mag}\mid_{rel}$. Based on the preliminary bulk flow inspections, it is obvious that some components are overpowering the others and not all values are necessary to describe the observed bulk flow. It is also not necessary to understand the behaviors of all of the above velocity components, since analytical results are not targeted in this study. Therefore, data reduction is performed when studying the cavity bulk flow, aiming to develop a generic and effective data extraction method. The rank reduction is proposed at two levels. First, a spatial reduction is considered, to change the three-dimensional domain to a pseudo one-dimensional domain. Second, a velocity component reduction is considered, to seek the simplest bulk flow representation.

4.2.2.1 Three-dimensional to Two-dimensional Data Reduction

First, the extracted data was tested to limit it to a two-dimensional plane. The ideal data extraction plane is the one covering most of the labeled bulk flow regions in Figure 4.3. The flow is intuitively more diverse in the $r\theta$ plane, since the cavity opening in $r\theta$ is much bigger than the width in the z direction. Even though the *bend transition* regions are not studied, it is necessary to include them in the data sample. In these regions, complex regional flow phenomena may occur and can affect the top bulk flow condition. With

these considerations in mind, two types of extraction planes are proposed. First, the obvious extraction plane are the ones following the definitions of cylindrical coordinates: (1) horizontal planes in the $r\theta$ direction, (2) axial planes in the rz direction, and (3) tangential planes in the θr direction, similar to the ones shown in Figure 4.5. With all three types of plane, regardless of which one is chosen, multiple ones are needed in order to cover the spread in dimensions in the cavity. But horizontal planes are preferred because each one is able to capture the entire spread in $r\theta$, and fewer planes are needed since the width is the smallest dimension in the cavity.

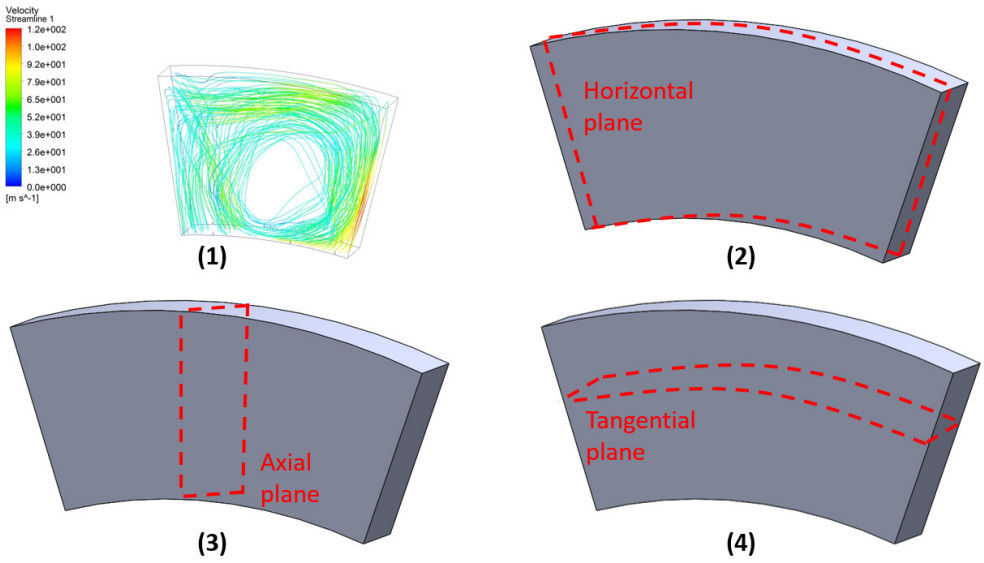

Figure 4.5: Attempted data extraction planes.

Second, a diagonal plane is another option for cavity data extraction. The diagonal plane has the advantage that even though it is a 2D plane, it occupies 3D space, with data points that vary in all three coordinates in space. From the preliminary CFD study, the cavity bulk flows are noticed to hit the back surfaces first, since annulus bypass flows need to overcome 'inertia' when being pumped radially into the cavity. Therefore, for each cavity, the diagonal plane crossing the back right edge and the front left edge is the best choice, since this plane follows the momentum flux.

Thus far, horizontal planes (number 1 in Figure 4.5) and diagonal planes are chosen

as the possible data extraction planes. In order to determine the more effective extraction plane type, velocity profiles across these planes are compared next. Figure 4.6 top labeled the three equally spaced horizontal planes taken, which cross the cavity width w_c and are labeled as *H1* to *H3*, with *H1* being closer to the rotor inlet. Figure 4.6 bottom labeled the four diagonal planes extracted, one for each cavity; these are labeled *D1* to *D4*, respectively. Comparisons are performed on all four cavities in the same row, all of which have exactly the same shape.

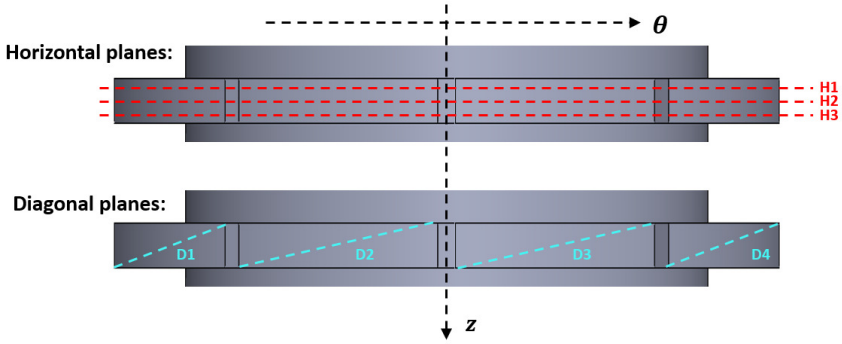

Figure 4.6: Data collection planes.

4.2.2.2 Two-dimensional to One-dimensional Data Reduction

To quantify the flow characteristics, the velocity components need to be plotted. For ease of demonstration, data on these 2D planes are further grouped into very thin segments, along the radial and tangential directions, since they either follow or cross the bulk flow bodies, as shown in Figure 4.7. These thin segments are each limited to the data located at a specific radial or angular location in order to study local flow characteristics. Since mesh points are not perfectly aligned with the global coordinates, each segment is limited to have a thickness equal to that of the global mesh element, which is *0.0025 m* or *0.315 degrees* for tangential and radial segments, respectively. In this way, a reasonable sampling pool can be obtained for analysis.

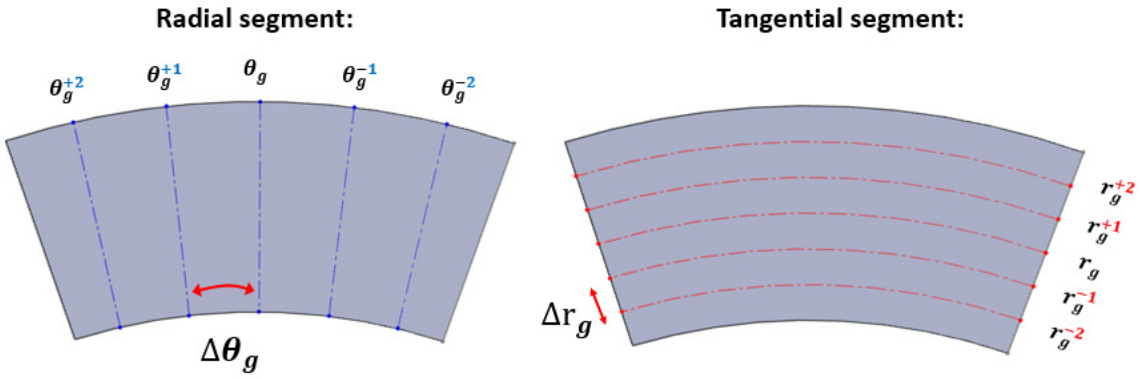

Figure 4.7: Local data collection areas

Sampling segments labeled in the above figure were separated at a constant radial or tangential distance Δr_g or $\Delta\theta_g$. They were calculated as

$$\Delta\theta_g = \frac{\theta_c}{6}\,; \quad \Delta r_g = \frac{\Delta r_c}{6} \tag{4.7}$$

The center tangential segment θ_g and radial segment r_g in Figure 4.6 were taken as the representative samples for a plane type comparison. Figure 4.8 below showes velocity profiles for the tangential segment, for one single cavity only. At first glance, all four profiles look very similar. Sharp peaks are located around the inlet or $'0'$ angular location, with the velocity magnitudes gradually decreasing as the normalized local angular locations increase. Velocity variations in the $\hat{\theta}$ direction are almost negligible in the middle of the cavity. The velocity magnitudes then slowly increase as locations move farther toward the outlet ($\hat{\theta} = 1$ side), where much flattened and wider parabolas are formed, at lower velocity magnitudes compared to their inlet profiles. These two outer peak regions are inside the bulk flow inlet and outlet regions and are the locations of interest in this study. These parabolas are narrow and sharp on the horizontal planes in the inlet regions, whereas they are smoother and wider on the diagonal planes. The 'Smoother' transitions indicate that well-followed streamline points are captured in the samples; the 'wider' shapes indicate that diagonal planes are able to capture the entire spreads of the local bulk flows. On

inspection, each inlet region on all horizontal planes occupies only about 10% in $\hat{\theta}$, but it occupies about 20% on the diagonal plane. Note that with the previous streamline plots and vector field plots for this particular cavity, horizontal planes underestimate the size of the inlet bulk flow. This observation indicates that the cavity bulk flow momentum follows closer with the suspected diagonal direction, or the bulk flow travels transversely towards the front surface in the cavity. On the opposite side, outlet profiles are similar in shape among these planes, and all velocity magnitudes start to slowly decay around 0.7. Therefore, in the inlet and outlet regions, the diagonal plane captures the velocity profiles more effectively.

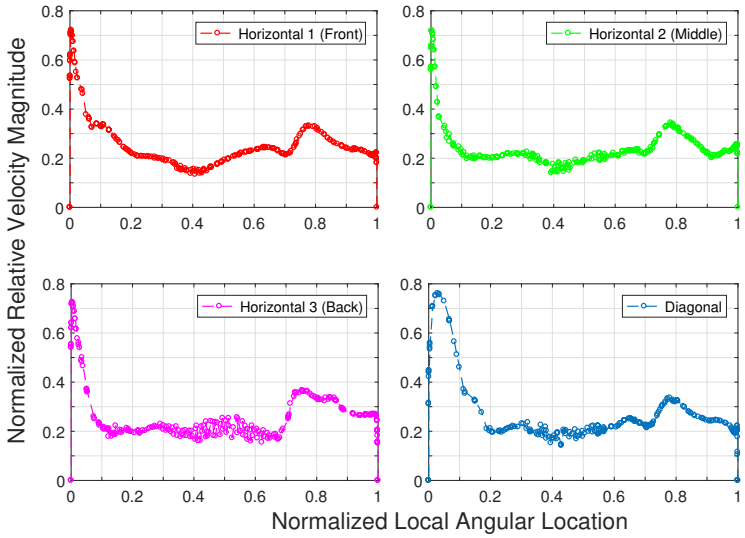

Figure 4.8: Single cavity Relative velocity magnitude profiles for the selected planes along tangential segments.

Next, Figure 4.9 shows a comparison across all four, same-row cavities. Note that velocity profiles from the horizontal planes and the diagonal planes are similar in magnitude and transition performances everywhere except for the inlet regions. Diagonal planes are able to capture the similar 'smoother' and 'wider' parabolas in the inlet regions and follow closer with the bulk flow momentum.

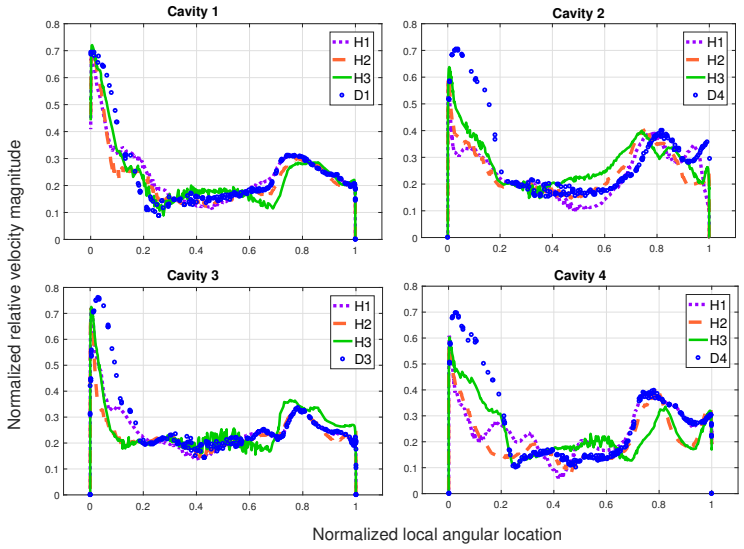

Figure 4.9: Relative velocity magnitude profiles for the selected extraction planes along tangential segments.

Figure 4.10 compares a representative set of velocity profiles along center radial segments. In these plots, axes are reversed so that velocity profiles are plotted following the same counter-clockwise swirl direction in the top bulk flow regions. All planes showed the expected parabola-shaped profiles at top, followed by smooth and continuous transitions going downwards. The maximum velocity magnitudes are still captured by the diagonal planes. There, along the radial direction crossing the cavity top bulk flow, flow momentum is still better aligned with the designed diagonal plane. Back swirls are noticed to occur at the bottom of the cavity since the velocity magnitudes gradually increase. Although the cavity bottom back swirls will not be investigated in this study, it is reassuring to notice that they all follow the same shape.

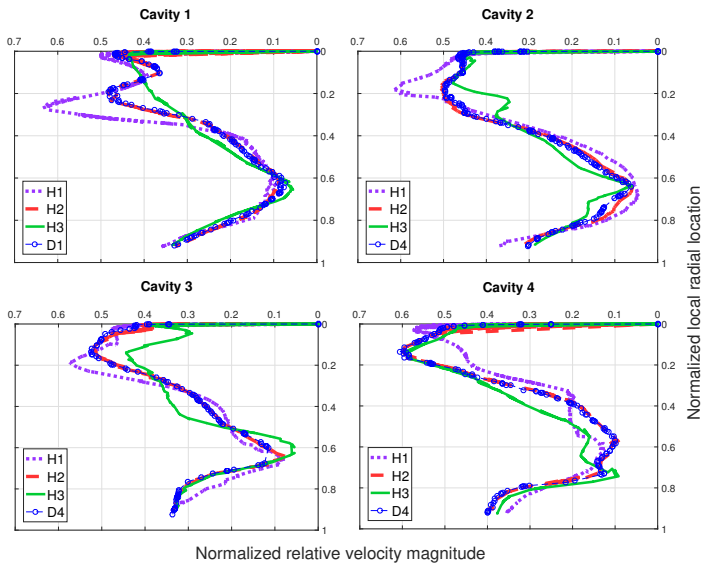

Figure 4.10: Relative velocity magnitude profiles for the selected extraction planes along radial segments.

In sum, the diagonal plane will be chosen since it is more effective in capturing the shapes, maximum velocity magnitudes and sizes of local bulk flow velocity profiles. But, relative velocity magnitudes did not reach the expected minimum magnitude (close to zero) in any of the above figures. An almost 'stagnant center' is expected in all cavities, as is indicated in both the cavity streamline plots and the velocity vector plots. It is therefore hypothesized that the three observed local cavity bulk flow regions are not 'centered' in the cavity geometric center. Finding this swirl 'center' location is important for the study of local bulk flow characteristics. The swirl center location confirms that there exists a center region with completely different flow characteristics from the peripheral bulk flow region. By going through the 'velocity center', the resulting velocity profiles are away from the neighboring transition regions, and can be used to distinguish the target three cavity bulk flow regions more precisely. To illustrate, cavity 3 in Figure 4.9 has a nearly constant yet non-negligible relative velocity magnitude in the center (roughly around 30% to 60% in normalized angular location). This velocity magnitude makes it difficult to define how much farther into the cavity the local bulk flow will 'disappear'; the velocity decays more slowly as distance from the two walls increases. Without the complete decay portion of the

profile at hand, it is difficult to accurately define the separation locations between the *bulk flow* and the *stagnant center*.

As a result, the absolute minimum velocity magnitude on the diagonal plane was used for data extraction. Since the the minimum velocity locations will be different from cavity to cavity, they are located manually instead of from each sampling diagonal plane, and are stored as $[\theta_v, r_v]$. Radial and tangential sampling segments r_v and θ_v are extracted through the velocity center locations. Taking the same sample cavities, the new velocity profiles are compared with those along the geometric center, as shown in Figures 4.11 and 4.12. For this cavity, minimum velocity is located at 13% lower in *r* and 7% lower in θ. In the tangential segments, velocity profiles for both types are closely aligned in the wall-side parabola regions. In the center areas of the cavities, the profiles through the velocity centers show rather constant decay patterns between the two outer peaks. At the local minimum velocity, the two outer parabolas of the inlet and outlet regions become much more distinguishable in comparison with the previous one, and are said to be completely separated from the top bulk flow region.

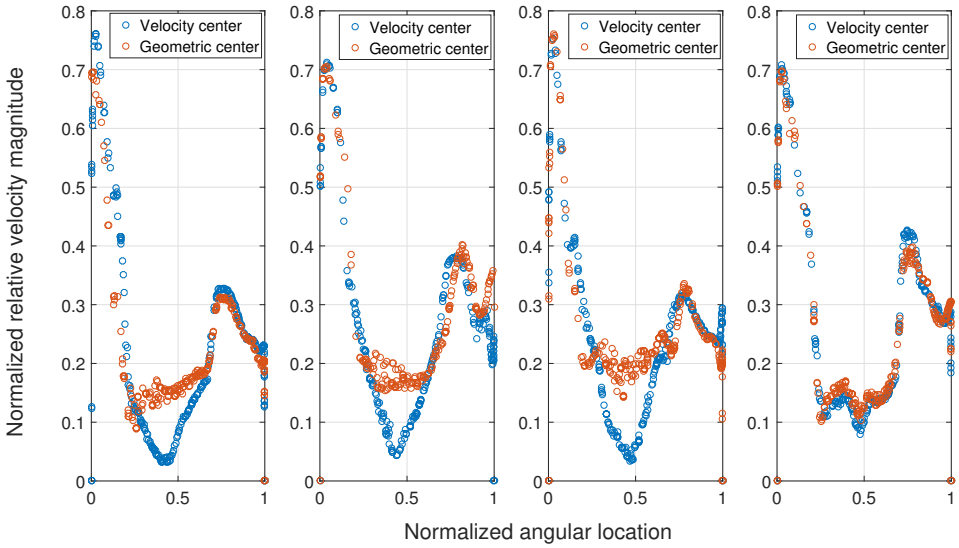

Figure 4.11: Relative velocity magnitude profiles for the selected geometric centered and the velocity centered tangential segments.

In rare cases similar to the last cavity in Figure 4.11, there are no close-to-zero velocity magnitudes in the extracted sampling diagonal plane, or the velocity center is not located on the defined diagonal plane. In a cross comparison with its profiles shown in Figure 4.9, the minimum velocity is located at plane *H1*, or closer to the front of the cavity. For cases similar to the cavity 4 profile, accuracy in the description of the bulk flow characteristics may be compromised if the diagonal plane profiles are used. But if the profiles are only used to define the sizes of the bulk flow parabolas, errors are expected to be negligible since only the very end of the profile's inner decay is missing and the majority of the parabolas are still closely aligned with the flow momentum. Through investigations of all cavities in the endturn region, it is not surprising that the majority of cavities have profiles similar to those of the first three cavities shown in Figure 4.11, which can be easily defined by this plotting method.

Figure 4.12 compares velocity profiles along the radial segments. For these cavities, velocity centers and geometric centers are also found to be between 1 and 2 degrees apart in θ. Therefore, velocity profiles along these two types of segments are expected to be almost identical, even in the *center stagnation region*.

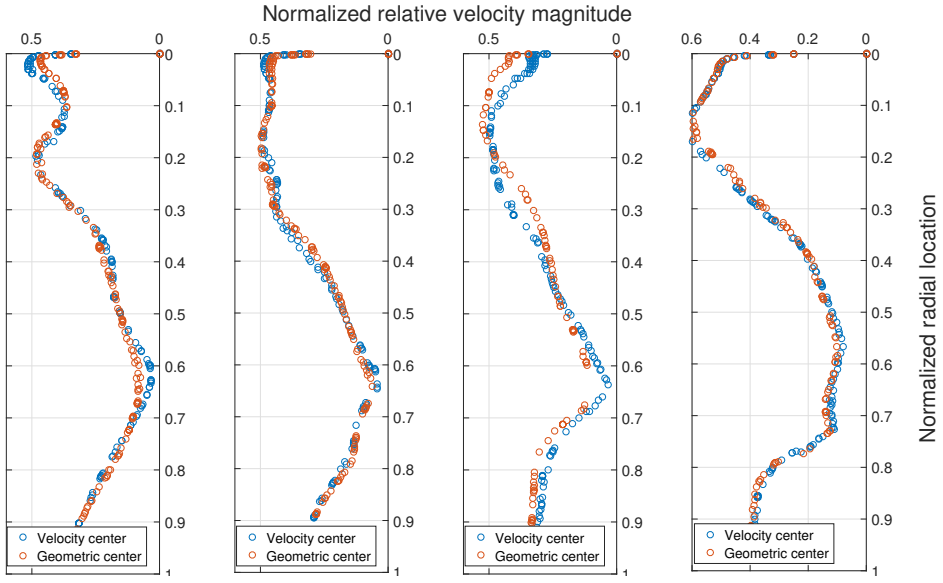

Figure 4.12: Relative velocity magnitude profiles for the selected geometric centered and the velocity centered radial segments.

To sum up, to characterize the local bulk flow sizes, a 'complete' bulk flow velocity profile is needed. The profile must be be able to capture (1) all four identified, distinct bulk flow regions, namely the bulk flow *inlet, top, outlet* and the *center stagnant region*; (2) the transitional regions between the identified four regions, which are either along the bulk flow path or from the individual peripheral bulk flow region moving towards the cavity center, in order to find the locations of flow separations; and (3) the entire in-plane ($r\theta$) widths of the local bulk flow regions. Profiles through the velocity centers on diagonal planes are noticed to have the above desired properties and are therefore chosen for data extraction for all endturn cavities.

4.2.3 Cavity Bulk Flow Study

Before focusing on investigating the peripheral bulk flows only, it is necessary to confirm that the cavity center stagnation size is comparable to that of the peripheral bulk flow such that the volume definitions in Figure 4.3 are reasonable. To do so, five equally spaced radial and tangential segments were extracted to represent regional flow conditions in a representative cavity. These ten slices combined can cover all four regions in the cavity. The goals of this section are to quantitatively identify and confirm flow characteristics in each region and to investigate how the bulk flow changes along the defined cavity 'inlet-top-outlet' flow path. Figure 4.7 shows the segments taken and Figure 4.6 shows the diagonal planes on which the data are extracted.

The five tangential segments were examined first. The profile areas were first categorized and labeled into the named volumes by observing the velocity profile shapes, as shown in Figure 4.13 below. By inspection, the normalized angular locations ranging from 0 to 20% were categorized here as the bulk flow inlet region, 20 to 70% as center region that overlays the expected the center stagnation region, and 70 to 100% as the outlet region. Along the normalized radial location r, R_g^{-2} goes through the cavity back swirl and R_g^2 goes through the bulk flow top region. Each region was examined separately in detail.

First, the inlet parabolas gradually flattened but were seen to decrease in magnitude as locations moved upwards from R_g^{-1} to R_g^1. This was expected as momentum and friction losses occur along the way. On the other side, in the body of the outlet region, or among R_g^{+1} to R_g^{-1}, velocity profiles looked almost identical. These differences are caused by the 'entrance effect' when the annulus flow first enters the cavity. Outlet velocities are also much smaller than inlet velocities, which was expected since loss buildups are significant when the flow reaches the far exit edge. At the velocity slopes at the 0.7 angular location among R_g^{-1} to R_g^1, slopes are flattened as locations move farther away from R_g^{-1}. This was anticipated since the outlet flow just left the *bend transition* region and is still inside the top bulk flow region. But these profiles are no longer useful for the determination of the outlet bulk flow size.

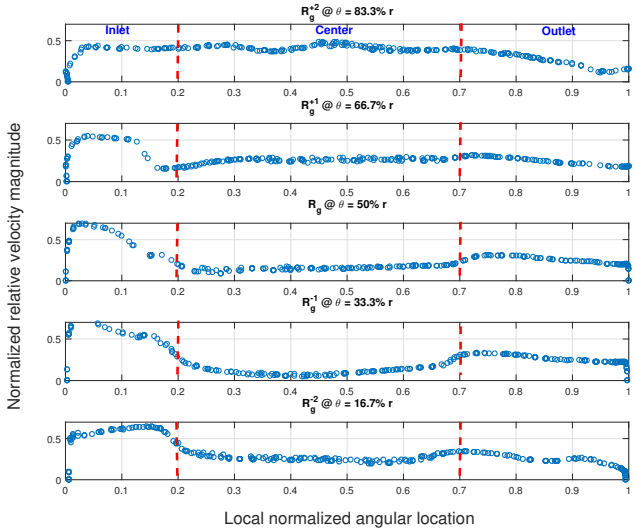

Figure 4.13: Relative velocity magnitude profiles for the selected equally-spaced tangential slices.

It is also noticed that the center of segment R_g^{+2} is located inside the top bulk flow region and that of R_g^{-2} is inside the bottom back swirl region. Data points on these slices follow local streamlines, parallel to the directions of the local flows. Each segment also has an almost constant velocity magnitude. This constant velocity magnitude indicates that the flow is nearly locally hydro-dynamically developed. Relative velocity magnitudes in

the very top and bottom regions are obviously higher than those in the middle, as locations move toward the *center stagnation region*. Last, starting at the minimum velocity segment R_g^{-1} moving upwards to R_g^1, the velocity magnitudes change from almost zero to much higher values that are almost equal to the outlet bulk flow magnitude. This indicates that there exists a swirl-to-stagnant transition area at all bulk flow regions. Based on this separation, the center stagnation region corresponds to a roughly 50% spread in the r direction and is significant for at least 20% of the θ_c length.

Next, five equally spaced radial slices were plotted. By inspection, this cavity can be radially separated into top, center and bottom regions at $0-20\%$, $20-70\%$ and $70-100\%$, respectively. Here, θ_g^{+2} and θ_g^{-2} are inside the bulk flow inlet and outlet regions, parallel to the local bulk flow streamlines. Significant variations in velocity magnitude are observed in θ_g^{+2} along the direction of the flow, and are suspected to be caused by the flow entrance effect. The top region velocity profiles in slices θ_g^{-1} to θ_g^1 have similar parabola shapes. In the center regions, the velocity magnitudes were significantly small in θ_g^{+1} and θ_g, which correspond to about a 40% spread in θ over at least $1/5th$ of the Δr length. Based on velocity magnitudes, it is reasonable to assume that θ_g^{-2} and θ_g^{-1} segments are located inside the bulk flow outlet, whereas only the θ_g^{-2} segment is located inside the inlet, which means the outlet region is bigger in size than the inlet.

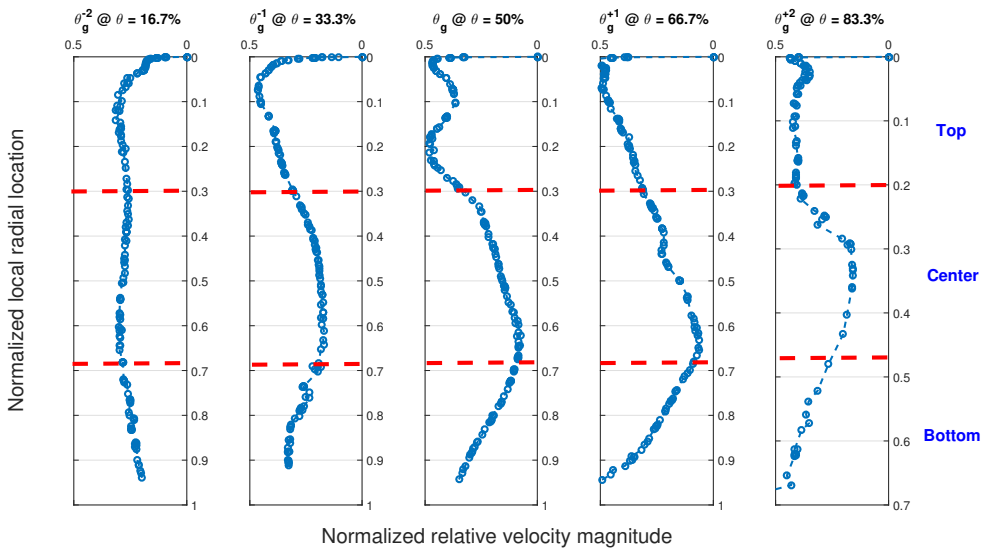

Figure 4.14: Relative velocity magnitude profiles for the selected equally-spaced radial slices.

Thus far, it has been proven that the observed peripheral bulk flow and center stagnation regions are quantitatively distinguishable. And among the three bulk flow regions, the flow conditions are similar but not the same. Therefore, it is necessary to separate the overall cavity volume for a detailed study.

Finally, the velocity profiles solely in the three defined bulk flow volumes, or the dashed regions in Figure 4.3 were studied. Each bulk flow body was studied over a 20% spread centered about the cavity velocity center, sampled at five equally spaced segments at 5% distance each, as shown in Figure 4.15. The 20% spread is taken as the safe distance where the flow is always away from the bend transition regions. Through the refined sampling resolution, the individual bulk flow volume was examined to determine whether the flow was locally hydro-dynamically developed as hypothesized from the previous plots.

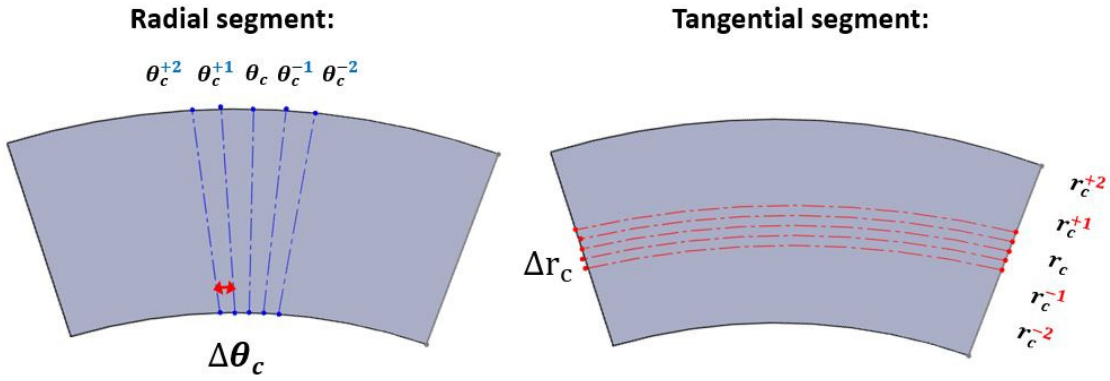

Figure 4.15: Equally spaced data extraction segments centered about the 'bulk flow center'.

Tangential segments were once again compared first, as shown in Figure 4.16 below. The cavity openings θ_c of profiles were separated into inlet, center and outlet regions, by inspection of velocity magnitudes, as before. The focus of this plot is the profiles in the inlet and outlet regions. In both regions, the five segments have almost identical profiles, both in magnitude and shape, except for very small regional fluctuations. From basic flow knowledge, constant upstream velocity profiles indicate a hydro-dynamically developed flow. Therefore, it is safe to assume that away from the *bend transition region*, flows are locally developed in the inlet and outlet. For a hydro-dynamically developed flow, studying one instantaneous response, or in this case the segment through the velocity center location, can be sufficient to represent the regional flow characteristics.

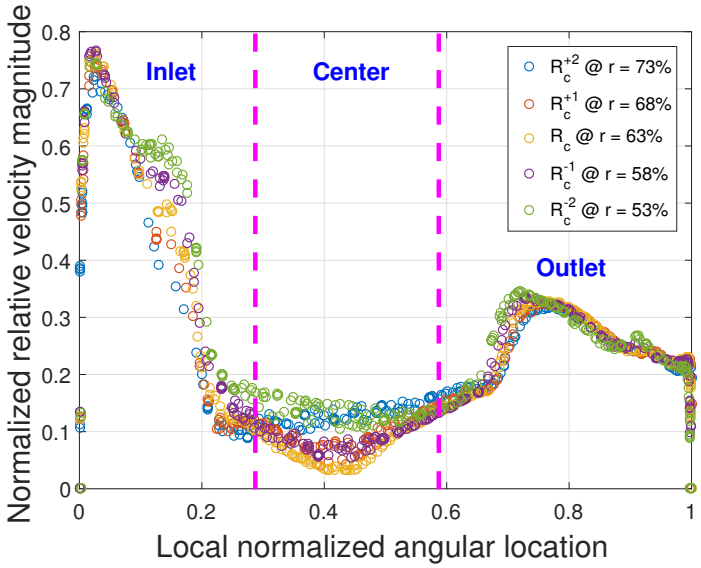

Figure 4.16: Sample inlet and outlet region relative velocity magnitude profiles along the selected tangential segments.

Similar velocity profiles were observed among radial slices. Compared with the profiles across the inlet and outlet regions, fluctuations are noticable, even in the bulk flow top region. The parabola-shaped velocity profiles are no longer smooth, and the differences in upstream magnitudes at the same position are no longer negligible. These differences are most likely caused by the differences in rotational forces ωr that the top bulk flow experiences crossing its spread length in r. In contrast, bulk flows in the inlet and outlet regions are each located at a constant r per slice; therefore this force is not a factor in forming the velocity profiles. Even though the top flow profiles are different, sharper peaks are seen to be compensated by steeper slopes, such as the profile for θ_c^{+1}; whereas flattened parabolas have smaller fluctuations in magnitude, such as the profile for θ_c^{-2}. Therefore, the overall normalized regional velocity magnitudes in the defined length, or between 0 to 20% averaged about 0.45 for all five slices.

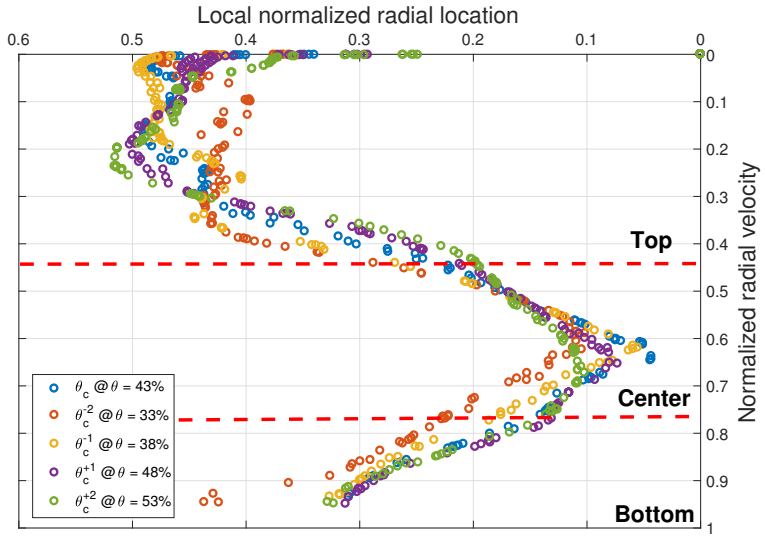

Figure 4.17: Sample top region relative velocity magnitude profiles along the selected radial segments.

4.2.4 Velocity Component Selection

This section determines which velocity component best describes the local bulk flow strength. By inspection of the streamline plots, bulk flow regions appear to be locally one-dimensional, with radial velocity dominating in the inlet and outlet regions and tangential velocity dominating in the top region. If this is true, the three-dimensional cavity bulk flow can be simplified to be regional one-dimensional flow. This section aims to quantitatively investigate whether it is possible to combine these dominant velocity components v, with the previously defined velocity center concept, to develop a universal cavity performance matrix, in the form of $[\theta_c, r_c, v]$.

To determine the characteristic velocity component v, components at the same equally spaced bulk flow segments shown in Figure 4.15 were plotted and compared. Figure 4.18 shows the results for the radial component, Figure 4.19 for the axial component, and Figure 4.20 for the relative tangential component. The radial component has positive values in the inlet region and negative values in the outlet region, as the cavity swirl changed directions. Radial velocity magnitudes are higher in the inlet and much lower in the outlet as well. In

the center region, radial velocity is almost zero.

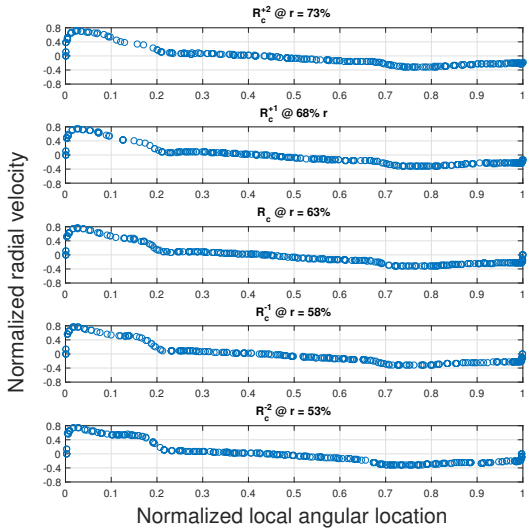

Figure 4.18: Radial velocity comparison for the selected tangential slices.

The axial velocity component magnitudes are negligible, regardless of their locations in space. The velocity profiles are shown in Figure 4.19 below.

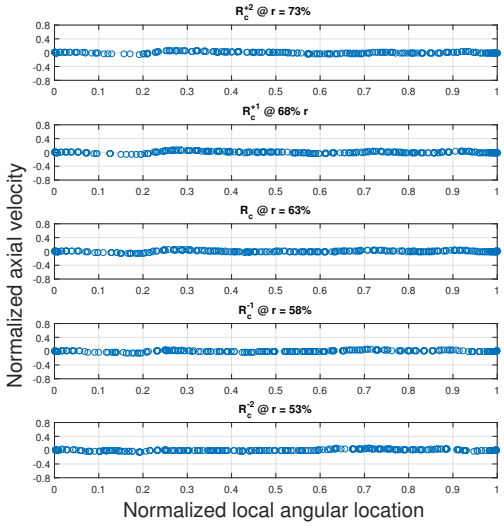

Figure 4.19: Axial velocity comparison for the selected tangential slices.

The relative tangential component is mostly zero over the length of the extracted tangential segments. Small fluctuations off zero are noticed in the inlet region, but they are

still not comparable on order of magnitude with respect to the radial component.

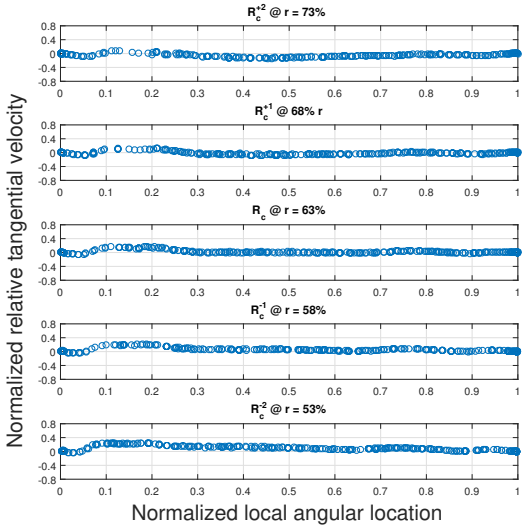

Figure 4.20: Relative tangential velocity comparison for the selected tangential slices.

As a result, the radial velocity component was found to be over-powering in the inlet and outlet regions, and was the characteristic velocity component v in the performance matrix. Next, to study the bulk flow top, components along radial segments were plotted and the results are shown in Figures 4.21 to 4.23.

The radial component is mostly zero over the length of the extracted segments in θ_c^{-1} to θ_c^1. At the same time, very small fluctuations off 'zero' are noticed in the top region, but they are still not comparable on order of magnitude with respect to the relative tangential component in Figure 4.22. At the bottom of segments θ_c^{-2} to θ_c^2, the radial component increased to magnitudes significantly higher, since they were located inside the inlet and outlet, as already shown earlier from the tangential segments.

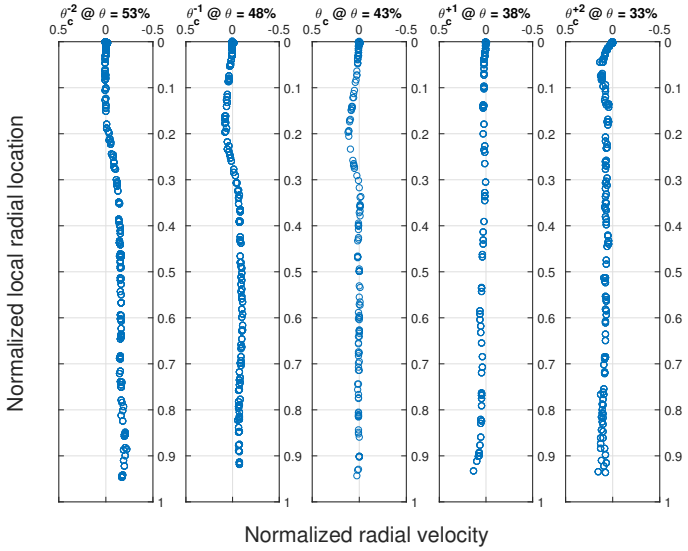

Figure 4.21: Radial velocity comparison for the selected radial slices.

The axial component is once again found to be almost zero and negligible over the entire length of the slices. The results are as shown in Figure 4.22 below.

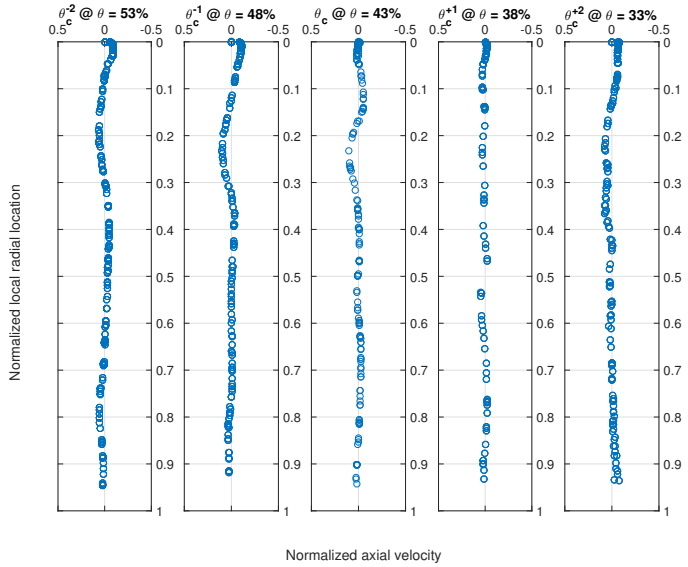

Figure 4.22: Axial velocity comparison for the selected radial slices.

The relative tangential component results are shown below. This component presents the dominant velocity components in the top region. Parabola-shaped velocity profiles are formed in the top of the cavity at significantly higher magnitudes, compared with the other

two components.

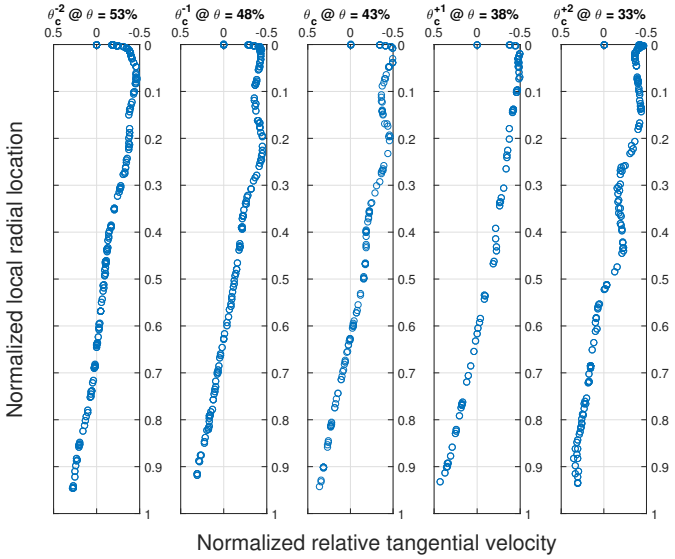

Figure 4.23: Relative tangential velocity comparison for the selected radial slices.

Up till now, the cavity bulk flow is dominated by one component per defined region, which is in the direction along the path passage. In previous single component plots, it can be seen that each dominant component has a profile similar in shape and magnitude, to that of the relative velocity magnitude. Thus it is of interest to investigate whether it was possible to further reduce the rank in velocity components to one, or whether it is possible to use only the relative velocity magnitude to represent flow characteristics in all defined volumes. This simplification is possible since, rather than the actual bulk flow magnitude, only the size of the bulk flow is noteworthy. Component velocity profiles along the velocity center tangential and radial segments were compared. The left plot of Figure 4.24 compares magnitudes in the inlet and outlet regions, while the right plot compares those in the top region. Absolute values of the dominant velocity components were plotted for ease of study, given that both positive and negative values exist in a single cavity. The results showed that the relative velocity magnitudes have profiles that align closely with the profiles of the dominant velocity components. Small differences exist between local points, but these are almost negligible. Due to the similarities in profiles, the

relative velocity magnitude is used instead to capture local bulk flow conditions. This way, the final performance matrix will be consistent and comparable between the three bulk flow regions.

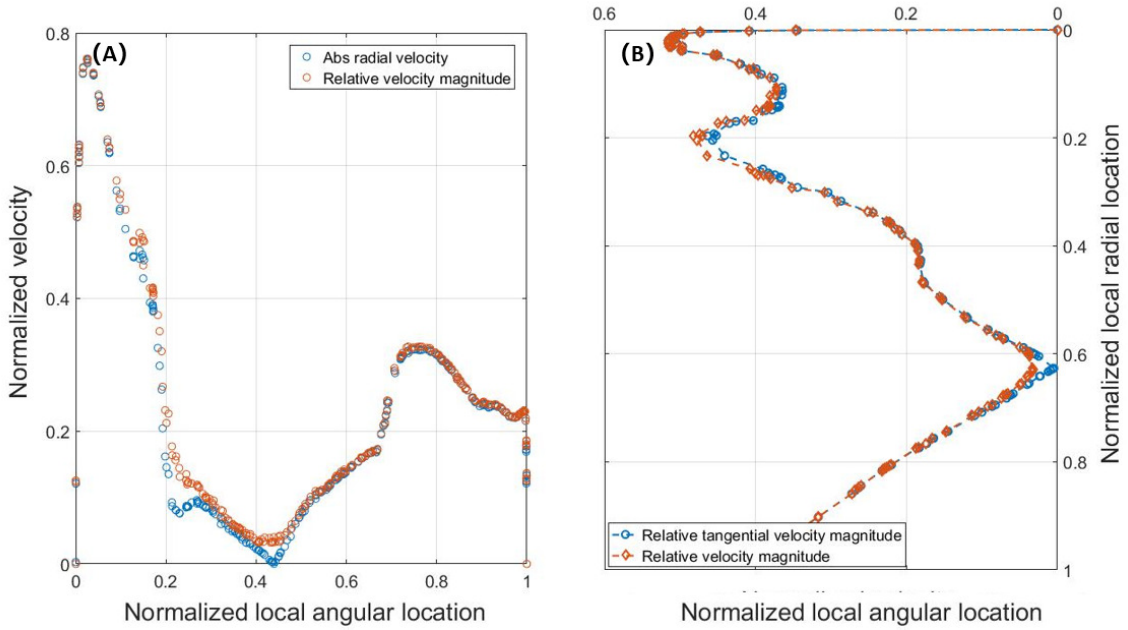

Figure 4.24: Profiles comparison between the dominant velocity component and the relative velocity magnitude for a (A)Tangential segment, and a (B)Radial segment

Thus far, an efficient and systematic data extraction method has been developed for the rotor endturn cavities. The cavity bulk flow can be described with a performance matrix $[\theta_c, r_c, v]$, which identifies the peripheral bulk flow center and captures the flow conditions with the relative velocity magnitude. The massive three dimensional CFD data can be reduced to two segments going through $[\theta_c, r_c]$ locations on a diagonal plane, to represent regional flow characteristics. With this extraction method, all endturn cavities can be studied and compared, to demonstrate their bulk flow phenomena. The overall extraction processes follow the flow chart shown in Figure 4.25 below.

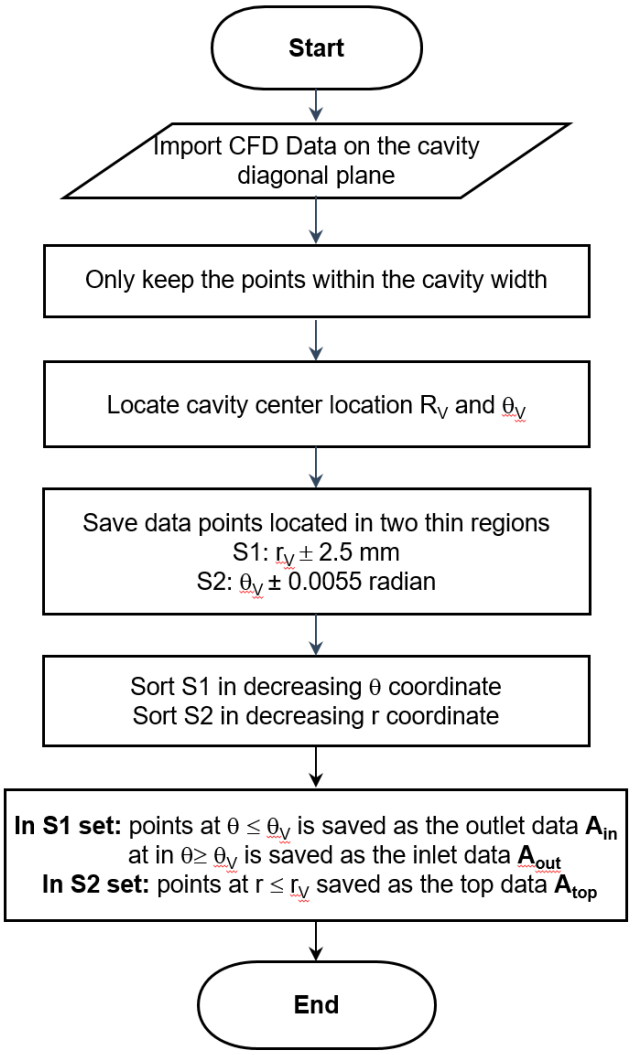

Figure 4.25: Flow chart of the local bulk flow data extraction method.

More specifically, each step is:

Step 1: Import the original diagonal plane CFD data. The diagonal plane crosses the cavity volume as shown in Figure 4.26 left.

Step 2: Keep points located within the cavity width, as shown in Figure 4.26 right.

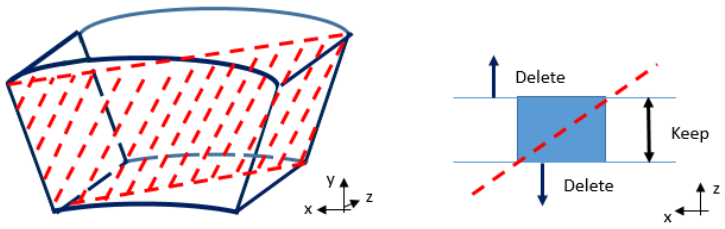

Figure 4.26: Step 2: CFD Data extraction from the cavity diagonal plane.

Step 3: Locate the velocity center P at $[r_v,\ \theta_v]$ by finding the minimum velocity near the center of the cavity, far from the physical walls, as shown in Figure 4.27.

Step 4: Extract data point on a tangential segment ***S1*** in the range of $R \subseteq (r_v \pm 0.0025mm$ and a radial segment ***s2*** in the region $\theta_{center} \pm 0.0025$ radian. The segments are labeled in the two dashed lines in Figure 4.27.

Step 5: Sort the data points in the segment ***S1*** in the decreasing θ direction and sort the segment ***S2*** in the decreasing r direction, following the definition of the bulk flow local coordinates $\hat{r}$ and $\hat{\theta}$ defined in CHAPTER 4 SECTION 4.2.1. The global and local coordinate is labeled in Figure 4.27 as well.

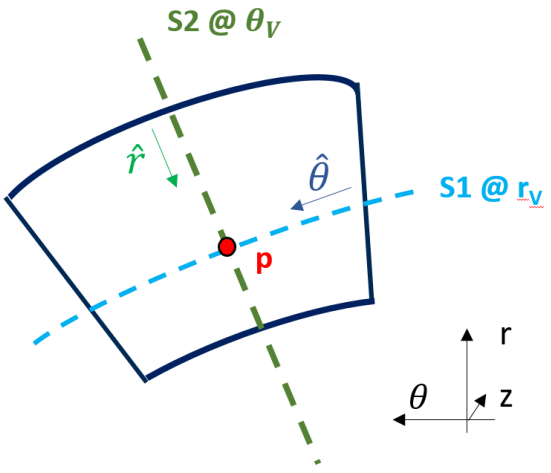

Figure 4.27: Step 4: Locate the cavity velocity center P and its tangential and radial sampling segments $S1$ and $S2$.

Step 5: Divide the segment $S1$ into two groups, where points located at $\theta < \theta_V$ are saved as the outlet data and the rest are saved as the inlet data. Points in $S2$ and are located at $r < r_V$ are saved as the top data. The data locations are as demonstrated in Figure 5.8

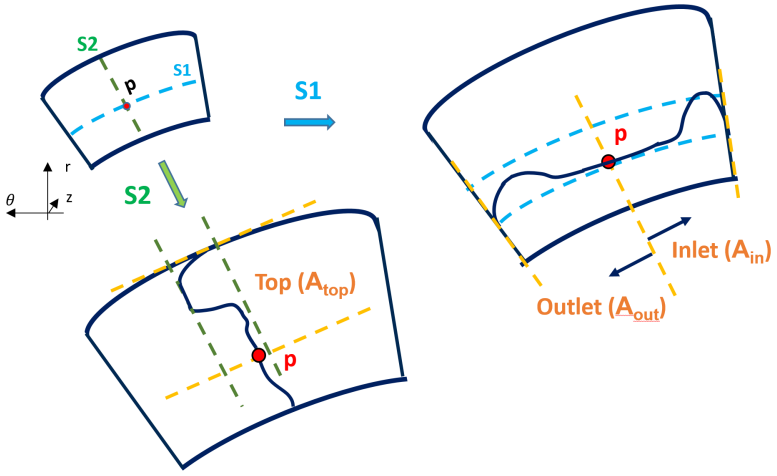

Figure 4.28: Step 5: Divide segments $S1$ and $S2$, save the data points for each identified bulk flow region.

Now that the design parameters are defined, this section here develops a CFD approach to carry out the experiments. The numerical CFD simulations have been demonstarted to successfully and accuractely solve the complex rotor fluid domains before, and here are implemented again to generate a sampling data set to develope the virtual pipe correlations. The CFD study follows the same steps as mentioned in CHAPTER 3, which are *geometry simplification, boundary condition assignment, meshing, and result validation*. Since the principles of each step have been discussed extensively before, only the changes in settings are mentioned in this section.

4.3 Cavity Bulk Flow Summary

The work in the previous section develops a tool to analyze the CFD data, and this section will continue the discussion of the cavity flow phenomenon by implementing this

tool to extend the study over the entire set of the endturn cavities. In this section, the observed cavity peripheral bulk flows in all endturn cavities were quantitatively studied and compared, to investigate whether the flow phenomena are the same. Due to symmetry in geometry, only half of the rotor, or 24 cavities needed to be studied. These cavities are different in the sizes of θ_c, and the locations in the θ direction with respect to the rotor pole, and positions in the z direction with respect to the rotor inlet. At the same row, cavities can also be categorized by leading versus trailing, in terms of their locations relative to the rotating direction. Thus, 1.1 was named the leading cavity and 1.4 was the trailing cavity, and so forth. Four cavities occupy the first five rows, and this later changes to two cavities per row downstream when the bounding coil lengths are significantly shorter. Row 5 has the smallest cavities, and row 7 cavities are located at the end of this nested rotor endturn structure. Cross validations were conducted on the extreme cavity conditions only, and were labeled in cyan in Figure 4.29 below. If the extreme conditions have the same flow phenomenon, then it is safe to assume that the rest of the cavities have the same phenomenon as well. These six cavities represent the extreme leading versus trailing positions, the upstream versus downstream positions, and the smallest versus the biggest cavity sizes. Bulk flow results were also compared at the two extreme expected rotor operating conditions, namely the short circuit 100% and mechanical conditions, which are at a field current ratio of 7.4. If similarities in profiles can be confirmed, then it is safe to conclude that all endturn cavities are phenomenologically the same.

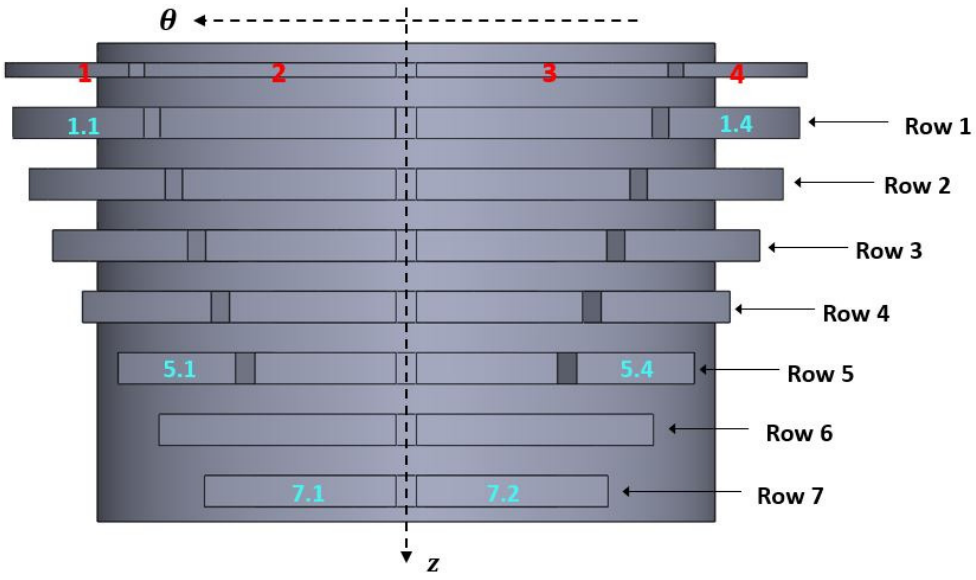

Figure 4.29: Selected endturn cavities for cross validation comparison.

Cross validations were conducted at two levels. The first level was conudcted intuitively by visually examining the diagonal plane vector field plots, and the second was conducted quantitatively by comparing the CFD local velocity profiles. Figure 4.30 below is a set of cavity vector plots for the short circuit operating condition. In all six cavities, the same counter-clockwise, peripheral bulk flow with a stagnant center pattern is observed. Flows have the same phenomena but differ in regional properties. First, comparing the 1^{st} and 4^{th} cavity in a row, the leading side cavities have slightly weaker bulk flows than the trailing sides'. The bulk flow local relative velocity magnitudes are the highest in the first row cavities, and are significantly decreased in the smaller cavities downstream. For example, cavity 1.1 and cavity 7.2 are located at the extreme opposite endturn positions. Cavity 1.1 is closest to the undisturbed rotor inlet flow on the leading side; cavity 7.2 on the opposite side is on the trailing side at the end of the endturn, where the annulus flow condition is expected to differ the most, as a result of upstream loss buildups and flow separation before going into the tapered subslots. Still, the same counterclockwise bulk flow performances are observed in these two cavities. The same flow phenomenon is also observed between the biggest and smallest cavities 1.1 and 5.1, even though the bulk flow strengths are signif-

icantly decreased at row 5. In short, based on visual inspection, cavities are found to have bulk flow phenomena that are similar but not identical. It is then important to determine whether the above differences affect the descriptions of the local bulk flow sizes. Next, next bulk flows are quantitatively studied using the previously developed extraction method.

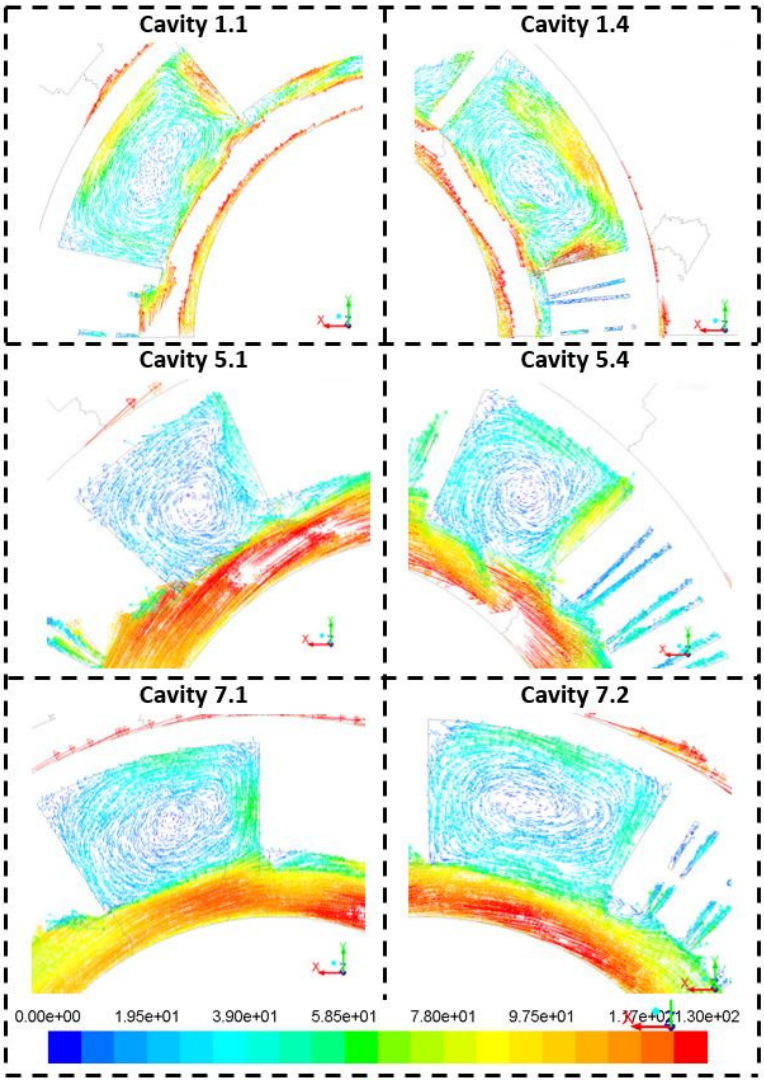

Figure 4.30: Relative velocity vectors colored by the relative velocity magnitude for the selected endturn cross validation cavities, for the simulation case of the short circuit 100 % operating condition.

The relative velocity magnitude velocity profiles were compared with the identified local dominant velocity components on the extreme case, cavity 7.1, as a quick first check of applicability of the developed extraction method. Figures 4.31 plotted along a radial and

a tangential segment, which both go through the calculated velocity center. The velocity magnitudes shown were normalized based on the rotor's average rotational speed $\bar{u}_{avg}$. In both cases, the dominant component has magnitudes nearly identical to those of the relative velocity magnitudes, in the bulk flow regions. Therefore, the performance matrix is confirmed to be universally applicable to all endturn cavities.

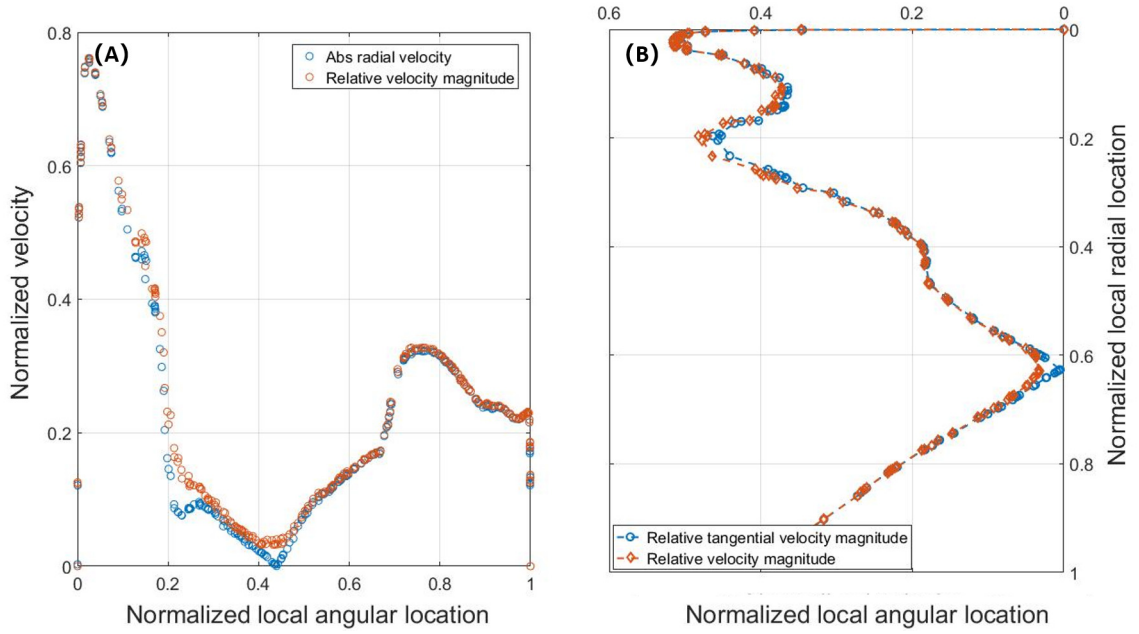

Figure 4.31: Sample validation case velocity profiles comparison for (A) radial versus relative velocity magnitude components for the radial segment, and (B) tangential versus relative velocity magnitude components for the radial segment (row 7 cavity 1).

Next velocity profiles crossing cavity bulk flow regions for all six cavities were extracted, plotted, and compared next. First of all, the velocity centers $[\theta_c\,|_i, r_c\,|_i]$ for each cavity are located to find the center radial and tangential segment's locations. Per inspection of the vector field plots, the chosen extreme cavity cases are significantly different in size and flow momentum compared with the same row cavity comparisons in the previous sections. Therefore, it is no longer reasonable to normalize these diverse velocity profiles based on the universal values $[\hat{\theta}, \hat{r}, \hat{u}_{avg}]$. As a result, the bulk flow profiles were normalized with respect to the characteristics of their enclosure cavities instead. This means, that

global angular locations need to be normalized based on the local cavity opening size $\overline{\theta_c}\big|_i$, and the relative velocity magnitudes need to be normalized based on the local maximum value $\overline{V}_{max}\big|_i$ of the extracted local segment. As a result, the spread in spatial θ and the range of relative velocity magnitudes are both transformed into the same bounded range of $[0, 1]$. Therefore, the resulting profiles are resized to overlay, as shown in Figure 4.32, which makes the comparison to a percentage cavity volume basis. These plots only aim to compare the sizes and shapes of the inlet/outlet parabola areas, in order to determine the phenomenological conditions of the studied cavities. In fact, the relative velocity magnitudes shown are not to scale, and are thus not comparable among profiles because they are normalized based on their own local maximum velocity magnitudes, which are known to vary significantly for different cavities. A solid red line was generated for each segment type, by averaging results of the six representative cavities; therefore this average value is treated as the expected, typical cavity bulk flow profile for the variety of the entire set of endturn cavities. Comparing these two profiles, the individual cavity profiles are noticed to align closely with each other and with the red mean profile line. In addition, the 'stretched' parabola areas are seen to occupy about the same percentage of the local spatial spread $\hat{\theta}/\hat{r}$, which means bulk flows occupy about the same percentage volume of their corresponding cavities, regardless of cavity's location and size.

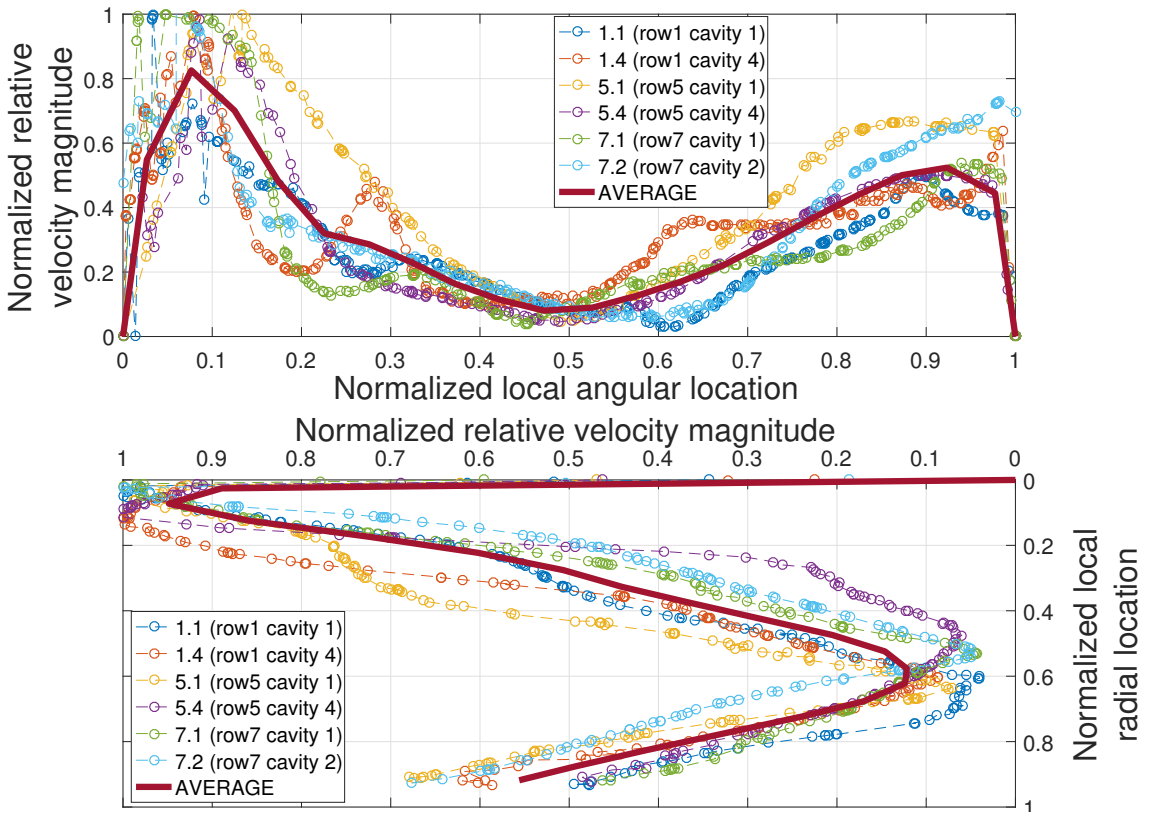

Figure 4.32: Locally normalized relative velocity profiles comparison between the (Top) tangential and (Bottom) radial segments at the short circuit 100% operating condition

The above observations confirmed the flow similarities among various cavity conditions under the same expected operating conditions. Next, cavity bulk flow phenomena are compared for two different rotor operating conditions, which are at a field current ratio of 7.4. This is a significant change in the cavity thermal boundary since the internal volumetric heat generation, or the I^2R loss varies quadratically. As a result, while other conditions, such as the endturn inlet temperature and rotor geometry are maintained the same, a change in cavities' thermal boundary conditions directly results in changes in the bulk flow temperature and in turn changes in flow density and viscosity. These eventually affect the internal flow phenomena and thus need to be investigated.

Following the same procedure, cavity diagonal plane vector field plots under expected mechanical operating condition were extracted as before. Three representative cav-

ities were then chosen for both operating conditions for comparison, as shown in Figure 4.33 below. Velocity vector plots for the rest of the chosen extreme cavities at mechanical loading are shown in Appendix C. The three cavities chosen here are cavities 1.1, 5.4 and 7.1, for a comparison between the first versus last (with respect to rotor inlet), the leading versus trailing location, and the biggest versus smallest cavities. Here, similar peripheral counter-clockwise swirl phenomena is observed for both conditions.

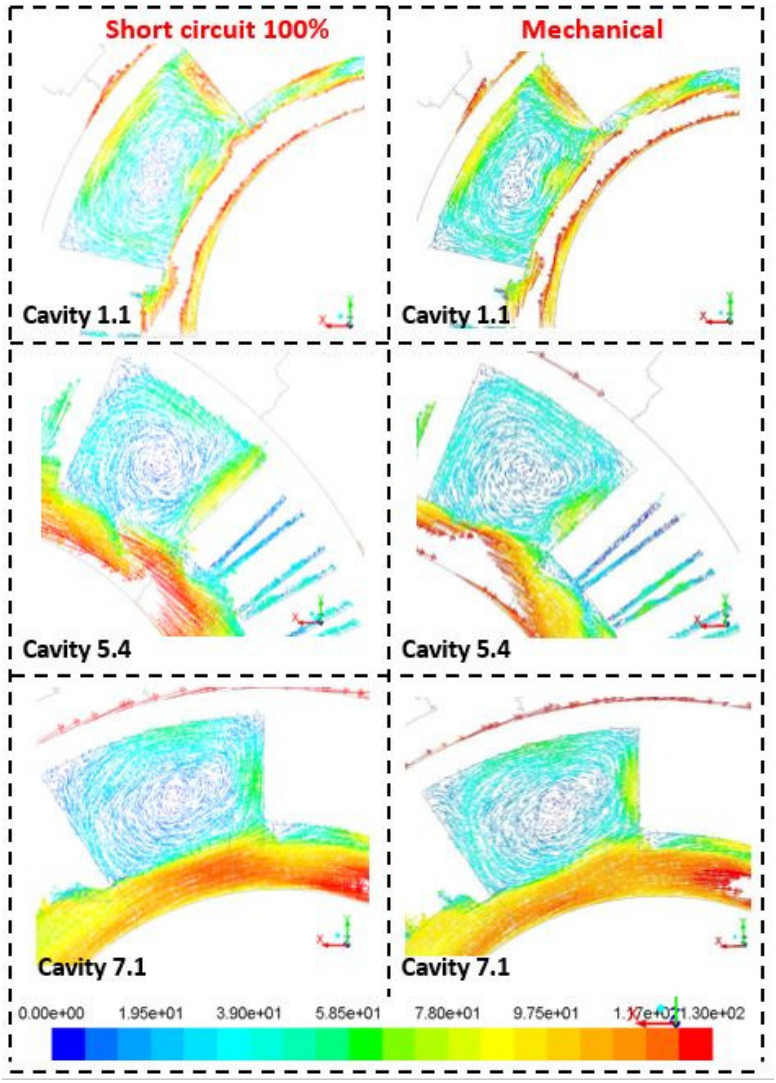

Figure 4.33: Relative velocity vectors colored by the relative velocity magnitude for the selected endturn cross validation cavities, for the comparison between the chosen simulation cases between the mechanical and the SC 100% operating conditions.

Next, normalized velocity profiles were used to quantify bulk flows. Averaged veloc-

ity profiles are developed for mechanical conditions as well, and are the solid blue lines in Figure 4.34 below. Note, each velocity profile is locally normalized such that the velocity magnitudes shown in this figure are not comparable. Comparing the expected average bulk flow performances between the two operating conditions, or the solid red and blue lines, the same shapes with negligible differences are concluded for both tangential and radial segments. In all three bulk flow regions, the local peak values coincide at the same normalized local angular location, but differences in peak velocity magnitude ΔV between inlet and outlet regions (in the top plot) is higher at the short circuit condition (red line), which is suspected to be the result of higher viscous heating losses from the heated bounding walls. For the same reason, in the top region (bottom plot) or along the radial segment, velocity decay is faster at the short circuit condition. But in sum, similarities in the flow phenomena can be confirmed, and the local bulk flow sizes are insensitive to their thermal boundary conditions.

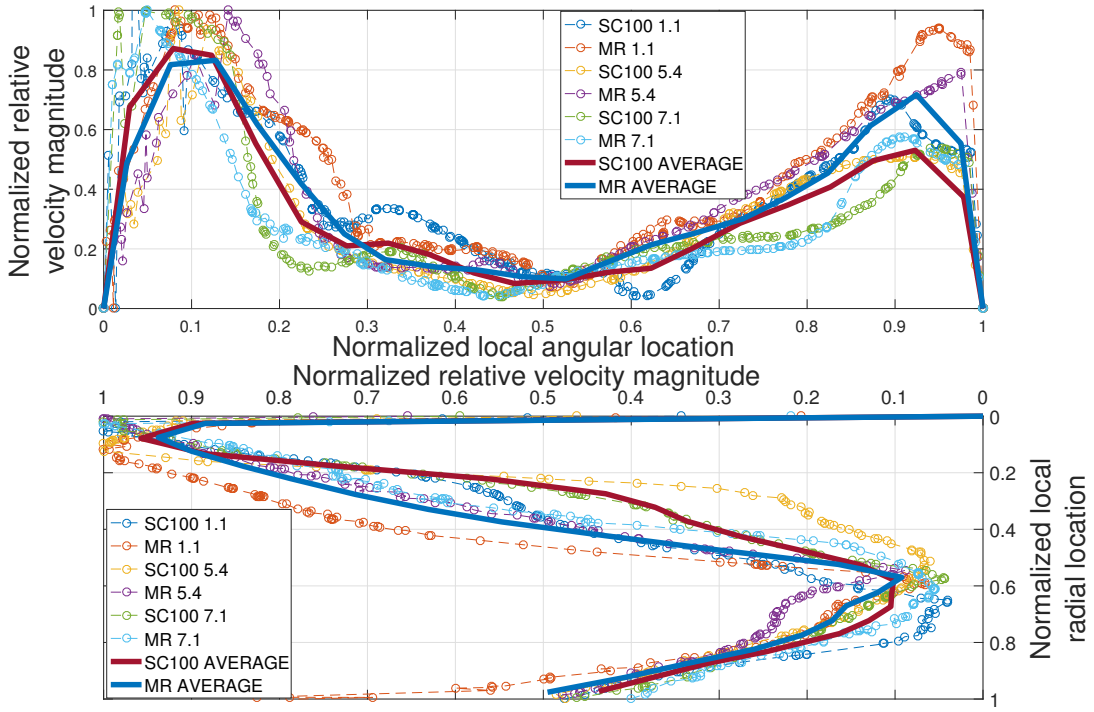

Figure 4.34: Locally normalized relative velocity profiles comparison between the (Top) tangential and (Bottom) radial segments, between the mechanical and the SC 100% **operating conditions.**

In conclusion, the results from the cross validation cases have confirmed that all endturn cavities are phenomenologically the same. Local bulk flows are noticed to occupy roughly the same percentage volume regardless of the cavity conditions. In fact, if the bulk flow 'inner boundaries' are defined at locations where the bulk flows magnitudes decay to less than 0.1 of the local maximum value, all cases are found to occupy roughly the 0.3 inlet and outlet regions in the $\hat{\theta}$ and about 0.45 in the $\hat{r}$ in the top region. These observations in flow phenomena are important since thereafter, if one cavity bulk flow can be quantitatively described and analytically calculated, the rest of the cavities can be applied with the exact same methodologies. As a result, this presented rotor endturn ventilation study can be focused on describing a single cavity instead of all 24. Initial investigation of all endturn cavities, on average, there is about 35% of cavity volume occupied by swirl and center 65% fits the stagnate description Swirl and stagnate separation is defined by the location of the flow where are less than 10% of the maximum velocity in the corresponding cavity

Table 4.1: Summary of the row-averaged cavity bulk flow versus stagnant region percentage volume occupancy estimations for the SC 100% cavities

Row No.	**Leading Cavity**	**Trailing Cavity**	**Leading Cavity**	**Trailing Cavity**
	Stagnant Region		**Swirl Region**	
2	65.04%	70.79%	34.96%	29.21%
3	63.81%	69.72%	36.19%	30.28%
4	62.25%	68.38%	37.75%	31.62%
5	60.27%	66.67%	39.73%	33.33%
6	57.64%	64.40%	42.36%	35.60%
7	65.17%	70.90%	34.83%	29.10%
Mean	62.36%	68.48%	37.64%	31.52%
Standard Deviation	2.96%	2.56%	2.96%	2.56%

4.4 Discussion

Now that the endturn cavity bulk flows have been demonstrated to be phenomenonlogically the same, this section completes the discussion by verifying and summarizing the unique flow properties observed so far, as a preparation for the development of a analytically representation of the cavity thermo-fluidic transport next. During the velocity rank reduction study, it is noticed that the local velocity profiles are nearly identical inside the individual bulk flow body, as demonstrated in Figures 4.31. This property allows the local bulk flow regions to be described with properties of hydro-dynamically developed flows. Thereafter, well-developed empirical correlations, as well as commonly accepted assumptions and simplifications can be applied, when later developing the fluid network for the copper analytical predictor. In this section, the regional bulk flow profiles parallel to the flow directions were investigated, to verify the efficacy of this hydro-dynamically developed flow assumption.

From basic internal flow knowledge, if the time-averaged velocity profiles remain unchanged, the flow is considered to be hydro-dynamically fully developed. For example, for an internal pipe flow, a hydro-dynamically fully developed flow has a profile similar to the one in Figure 5.6 left for laminar flow, or the one on the right for turbulent flow. These internal pipe flow profiles are referenced here, since an analogy in profile can be made between the observed cavity bulk flow and the internal pipe flow. This approximation is possible because it is proven that the bulk flows can be approximated to be regional one-dimensional, and to have parabola-shaped velocity profiles. Here, in order to fit the 'internal pipe flow' analogy, a 'pseudo wall' is defined at the end of the parabola inner decay, or the line between the regional *bulk flows* and the *stagnant center*.

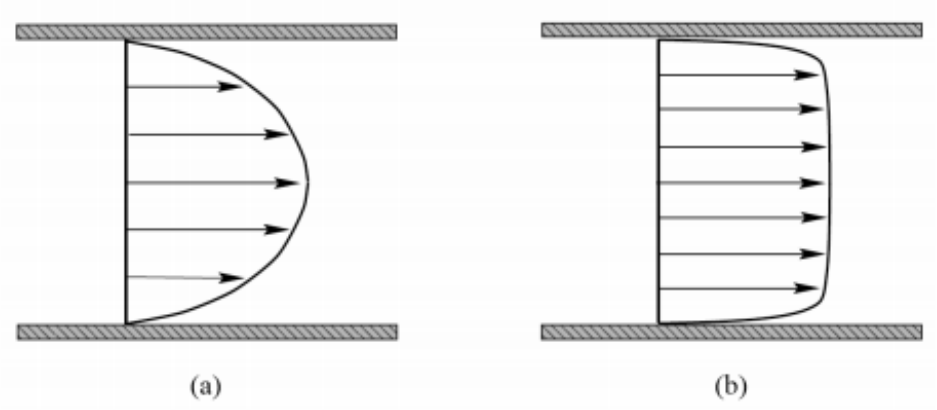

Figure 4.35: Hydrodynamic fully developed laminar (a) versus turbulent (b) pipe flow velocity profile [90]

For a hydro-dynamically fully developed flow, the velocity profiles do not change downstream, and the velocity magnitudes only vary in the direction normal to the flow. Therefore, this flow property can also be mathematically defined as

$$\frac{\partial u(r,x)}{\partial x} = 0 \quad or \quad u = u(r) \tag{4.8}$$

here, u is the velocity magnitude, r and x are the spatial directions normal and parallel to the flow direction. The velocity profiles perpendicular to the local bulk flow directions have already been presented, in Figure 4.34 and 4.32. Therefore, the velocity profiles parallel to the local bulk flow directions were investigated here.

The cavity bulk flow inlet and outlet regions, which have profiles as shown in Figure 4.36 were first studied. This figure has three parts: (left) the CFD vector field plot with the extra radial data extraction segments labeled; (top right) the tangential segment's velocity profile through the cavity velocity center, and normal to the inlet-outlet flow directions (along the $'r'$ direction in the pipe flow analogy); and (bottom right) the labeled radial segments' velocity profiles that are parallel to the flow directions and inside the local bulk flow regions (along the $'x'$ direction in the pipe flow analogy). These four radial slices are

equally spaced at 10% distance in local $\hat{\theta}$ each, away from the adjacent cavity side walls, given that they appear to be located inside the bulk flow per inspection of the vector field plot. In the inlet area, the velocity magnitudes are found to be almost constant along $S1$, but to slightly fluctuate along $S2$. Cross compared with flow performance normal to the 'S' segments along the tangential slice, $S2$ is found to be near the line between the *inlet* and the *stagnant center*, since the velocity magnitudes have already decreased to less than 20% of the local maximum value. Therefore, the fluctuations are reasonable and expected. In the outlet area, velocity magnitudes are found to be almost constant along both flow path segments $S3$ and $S4$. Referenced to the tangential segment plot, the outlet region is wider, and $S3$ and $S4$ are both still located inside the bulk flow body around the 'centerline'. In short, these three plots indicate that along the flow path, in the 'center' of the local bulk flow away from the bulk flow 'side walls', the velocity magnitudes are constant downstream, which corresponds to the description of a hydro-dynamically fully developed flow.

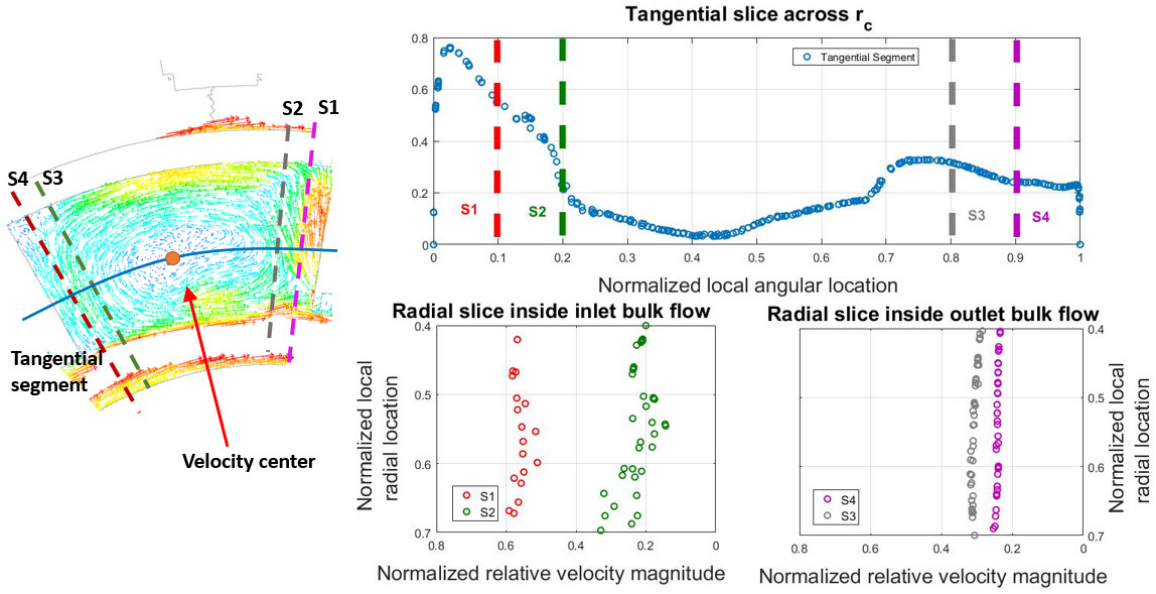

Figure 4.36: Inlet and outlet bulk flow velocity profiles comparison along radial slices parallel to the bulk flow directions.

Similarly, the bulk flow top region was studied, and the results are shown in Figure 4.37. This figure also has three parts: (left) the CFD vector field plot with the extra tangen-

tial data extraction segments labeled; (middle) the radial segment velocity profile through the cavity velocity center, and normal to the flow direction (along the $'r'$ direction in the pipe flow analogy); and (right) the velocity profile along the labeled tangential segments that are parallel to the top flow direction and inside the bulk flow region (along the $'x'$ direction in the pipe flow analogy). The two tangential segments are 10% and 20% away in space from the cavity top arc. On inspection, segment $S1$ is for sure located inside the bulk flow body, whereas $S2$ appears to be closer to the bulk flow inner pseudo-wall since the decrease in velocity magnitude is significant. Velocity profiles on the right show $S1$ having almost constant velocity magnitudes, with very little fluctuation between the points. On the contrary, since $S2$ is closer to the end of top flow decay area going into the stagnant center, the velocity magnitudes vary significantly along the flow path.

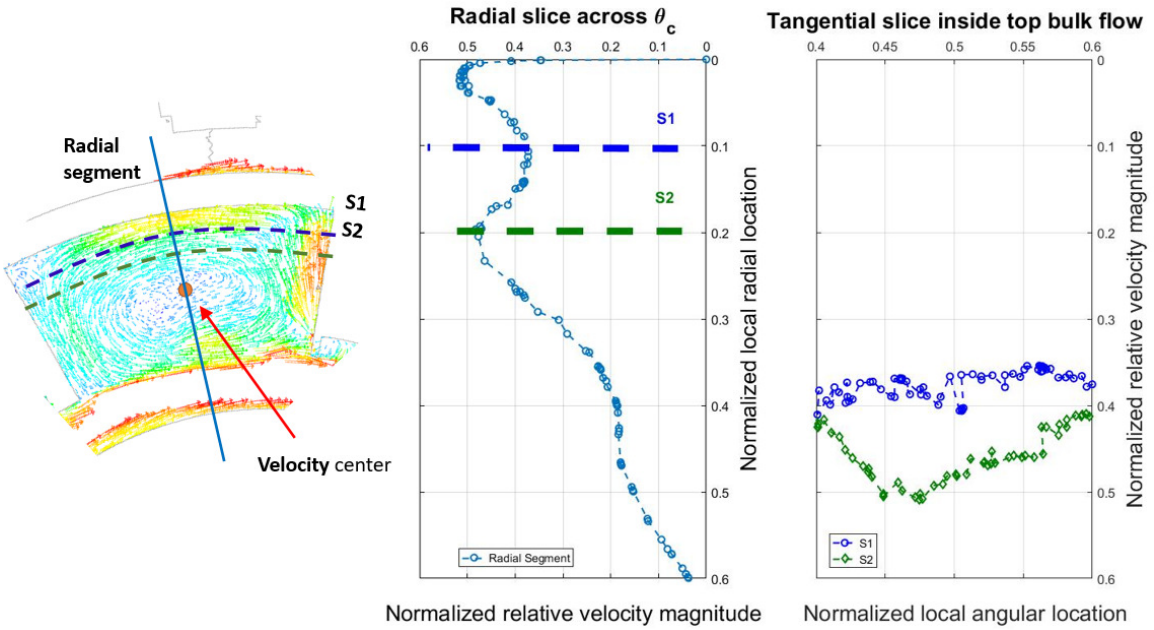

Figure 4.37: Top bulk flow velocity profiles comparison along tangential slices parallel to the bulk flow direction.

In sum, if the locations are inside the bulk flow body away from the pseudo-wall, the velocity magnitudes parallel to the flow direction are almost constant. But as the locations move towards the cavity center, the fluctuations in magnitudes downstream increase and become significant. Therefore, when the location of the pseudo-wall is carefully defined,

the local bulk flow can be approximated as hydro-dynamically fully developed flow. This fluid property builds up the foundation for simplifications taken when determining node locations in the thermal-fluidic network. As already mentioned in Chapter 3, rotor coils are stacks of high conductivity copper straps which are separated by very thin and low thermal conductivity insulation; it is reasonable to assume that there is no heat transfer between the straps in the radial direction r with small temperature gradients along each strap length in the angular direction θ. Therefore, based on the coil structure and material properties, together with the locally hydro-dynamically fully developed flow simplification, it is acceptable to assume that the straps neighboring the velocity center, are cooled by local bulk flows having the same velocity profile. In this way, a regional cavity wall temperature can be reasonably approximated by one point as long as it is located inside the bulk flow body. In addition, the desired copper temperature predictor intended to predict temperature for the suspected high temperature regions, to evaluate the thermal feasibility of the rotor design. Therefore, the lower portion of the cavity, or the *entrance*, *back swirl* and *exit* regions are not studied, since they are just above the annulus flow and are expected to be the coolest locations in each coil.

Up to this point, the local bulk flow regions have been demonstrated to have the following characteristics

1. Can be approximated to be locally one-dimensional.
2. Can be considered to be hydro-dynamically developed in the 'body' of each flow.
3. Can be compared to internal pipe flows for having parabola-shaped velocity profiles.

Therefore, it is suspected it might be possible to model the local bulk flows with known flow physics of the internal pipe flows. But the differences in flow geometries and conditions need to be addressed before applying this idea. First, even though velocity profiles

are parabola-shaped and correspond to flow domains with bounded walls at both ends, cavity bulk flow regions are in reality only bounded by three physical walls. Therefore, the location of this inner pseudo-wall boundary needs to be determined. Second, parabolas are noticed to decay at slow and unpredictable speeds as they move into the cavity center, and this results in local velocity profiles that are asymmetric and skewed toward the physical walls. Therefore, how to 'match' the bulk flow profiles to the symmetric, theoretical profiles such that they capture the same amount of flow momentum needs to be investigated as well.

4.5 Conclusion

The study in CHAPTER 3 developed a CFD modeling technique for large complex domains, offering an introductory view of the endturn cavity flow conditions. This chapter analyzes the CFD results to the problem of a description of the cavity bulk flow phenomenon. Through a series of comparisons, preliminary observations and assumptions can be quantitatively verified. A number of conclusions can be made which will be used in later studies.

1. The bulk flows have visually and quantitatively demonstrated that all cavities have the same flow phenomenon.

2. The cavity swirl can be described by a performance matrix in the form of $[\theta_c, r_c, V_{mag}]$, which defines the peripheral 'center' $[\theta_c, r_c]$ and simplifies the three-dimensional peripheral bulk as locally one-dimensional flows, using the relative velocity magnitude V_{mag}.

3. The bulk flow inlet and outlet regions are found to be locally hydro-dynamically developed. Hydrodynamic effects significantly overpower heating effects from adjacent coils; therefore changes in loading conditions have negligible effects on local bulk flow sizes when the rotating speed remains constant.

4. The identified bulk flow regions have velocity profiles similar to these of the internal pipe flows.

5. It is possible to quantify the bulk flow sizes and the associated heat transfer with known empirical correlations of fundamental pipe flows.

CHAPTER 5

VIRTUAL PIPE HYDRAULIC DIAMETER CALCULATION

5.1 Introduction

This chapter develops an analytical algorithm to calculate the characteristics length D_h based on the shapes of the extracted CFD profiles by proposing a corresponding theoretical profile in accordance with the proposed virtual pipe concept. CHAPTER 4 demonstrated that the complete cavity swirls can be divided to three regional one-dimensional flows to allow the use of the fast-solving analytical lumped circuit method to calculate their related thermal-fluidic transports. In order to use the circuit method, the bulk flow characteristic length, or in this case is the virtual pipe hydraulic diameter D_h is required in order to use the empirical correlations in the networks; but a description for this parameter is not yet available for the unique flow conditions presented in the endturn circumferential cavities. A quantitative description of the bulk flow characteristic length was developed as opposed to the heat transfer coefficient, in order to obtain a generic description of the bulk flow phenomenon. This was pursued in order to allow for the calculation of the location specific coil temperature anywhere along the endturn winding, on any coil in the rotor endturn region. It is also noticed that the regional velocity profiles are parabola-shaped, similar to those of the internal pipe flows; therefore, flow dimensions can be approximated by forcing the pipe flow analogy in the bulk flow regions.

This section has two parts. First, a quasi-analytical process was developed, which defines the sizes of the parabolas by drawing a theoretical velocity profile that captures the equivalent momentum of the CFD results. The theoretical curve is generated under the as-

sumption that it represents the flow response if the pseudo-wall is replaced with a physical wall, which forms the actual internal pipe environment. Second, numerical design studies were performed using the cavity endturn model developed in CHAPTER 3, to provide additional cavity flow results at various inlet or geometric settings, in an attempt to investigate the endturn rotor ventilation design scenarios and to test the performance of the developed calculation method.

5.2 Local Virtual Pipe Hydraulic Diameter Calculation

This section develops a quasi-analytical method to determine the flow length D_h of the observed cavity internal bulk flows by using extracted CFD data. The local velocity profiles were obtained using the data extraction method developed in CHAPTER 4. The normalized cavity velocity profiles are similar to the one shown in Figure 5.1 below, where each local parabola is always bounded by a solid wall on one side, such as the green solid lines; the dashed red lines represent the unknown virtual pipe pseudo-walls.

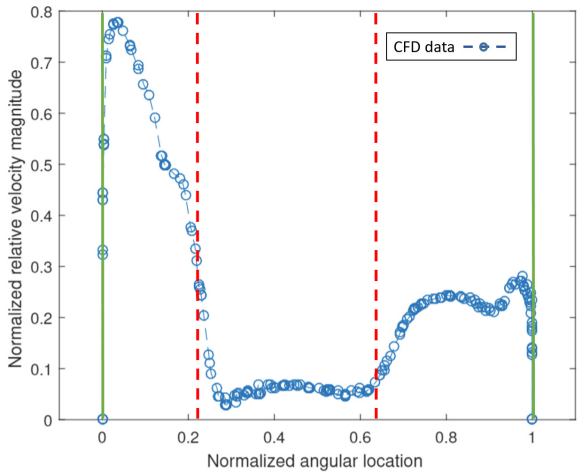

Figure 5.1: Sample velocity profile in proposed virtual pipe regions.

To determine D_h, three approaches were proposed and compared, following two paths:

1. The bulk flow and stagnant center regions have distinct slopes, and therefore the inflection point at the end of the parabola is the location of the pseudo-wall.

2. Assuming that the parabola is not symmetrical because of the missing fourth wall, then the expected symmetrical theoretical flow response can be determined by matching the averaged velocity magnitude. Two additional approaches were developed based on this assumption; each imposes a turbulent profile to create the corresponding 'theoretical' bulk flow profile:

    (a) Create a symmetrical parabola profile by going through 3 points, two of which are the locations of the physical wall and the local maximum velocity. The third point is the location where the CFD velocity magnitude decreases to 50% of the maximum value.

    (b) Create the theoretical profile by implementing a textbook empirical expression that best describes the flow conditions observed. The pseudo-wall location is located by iteratively searching for the distance to the wall that results in a match between the averaged velocity magnitudes under the two profiles.

5.2.1 Method 1: Inflection Point

The first method proposed is based on the fact that distinctive profile shapes are observed in the bulk flow and the stagnant region. In general, the velocity profiles are noticed to have negative slopes that continuously decrease the velocity magnitudes in the bulk flow regions; profiles are almost flat and fluctuating in the center stagnant region. Therefore, the pseudo-wall location is the inflection point $'dV/dx = 0'$ that separates the bulk flow and stagnant center profile slopes, as shown in Figure 5.2. The point crossing zero is located, and therefore the region to the left is the inside bulk flow whereas the region to the right is in the stagnant center.

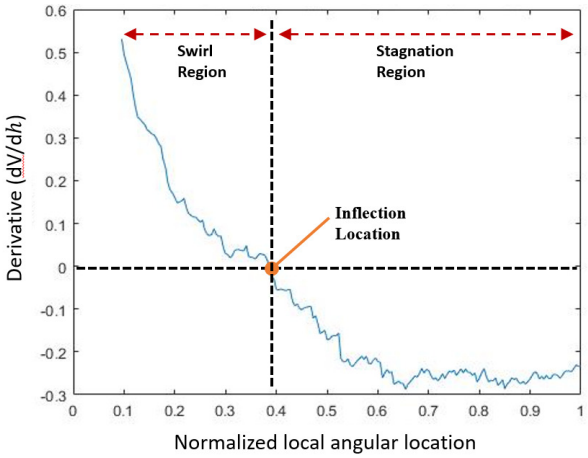

Figure 5.2: Sample flow region definition by the inflection point method.

Even though this method is mathematically feasible, it performed poorly in practice. This method was realized to work only for smooth and continuous profiles; otherwise many cross-zero values were found, and the *'correct'* inflection location could not be defined. Figure 5.3 presents a 'noisy' profile, where multiple zero derivatives are located, as shown on the top right plot of Figure 5.3.

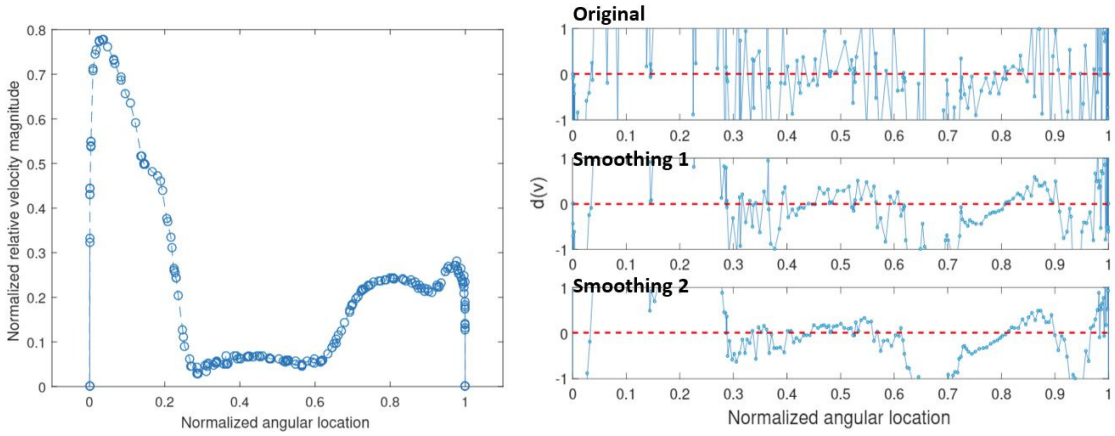

Figure 5.3: Sample velocity profile with hard to define inflection locations (Left): Velocity profile; (Right): Velocity derivative plots with and without profile smoothing.

In this case, there is not an automatic way to identify the correct location, since zero derivatives can happen anywhere along the velocity profile; therefore, manual manipulation is required. The fluctuations are assumed to occur as a result of a highly dense but

non-uniformly distributed, modified FLUENT mesh. Nodal points may be located at close proximity, and therefore have nearly identical velocity magnitudes and almost zero slopes, even at high velocity magnitudes obviously within the bulk flow region. To fix the uneven data distributions, the moving average method is applied to the original CFD data set. The bottom right plots in Figure 5.3 show two smoothing steps applied to this cavity, where *Smoothing 1* was averaged at every 3 points and *Smoothing 2* at every 6 points. The 2nd smoothing arrived at the inspected desired position, judging by the velocity profile on the left. Smoothing can be useful but does introduce new problems. First, the smoothing intensity is expected to vary case by case and is hard to define unless the designer visually inspects the smoothed result between trials. Over-smoothing risks losing the inflection point, while under-smoothing cannot useful to filter out the noises in the data set. Second, smoothing introduces errors in prediction as the result of location averaging, which is not possible to remedy. Overall, this method is quickly ruled out for its inconsistent and unreliable performance.

5.2.2 Method 2: Three Point Curve Fitting

The second method for determining D_h is proposed based on the mathematical definition that three points can define a curve. The first point chosen is the fixed location of the physical wall P_{wall}, and is available at each bulk flow region. Two methods are used to derive the second point that defines the center of the parabola. The first method is to directly use the absolute maximum velocity loation $[P_{max}, V_{max}]$, which automatically defines the third point by forcing the fitted parabola to be symmetric. The second method constrains the allowable minimum bulk flow velocity magnitude to define the inner-wall location, and shifts the peak location to maintain symmetry in the profile shape. Both approaches are tested on various cavity profiles and a representative result is shown in Figure 5.4.

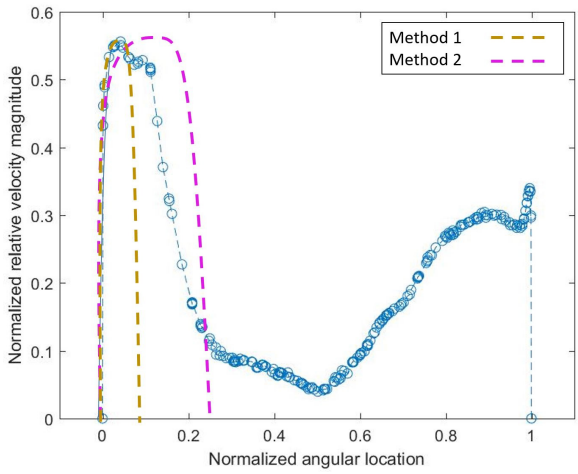

Figure 5.4: Three point curve fitting result demonstration.

For the profile presented in Figure 5.4, Method 1 leads to an under-predicted pipe size, and Method 2 appears to capture the profile shape properly. Method 2 is first found to be superior to Method 1 at skewed profiles for being able to capture the slower inner transition performances. But there is not a clear definition of the cut-off velocity magnitude that would form the proper symmetric profile in Method 2. For very skewed profiles, the 50% value is no longer appropriate, such as the example shown in Figure 5.5. In this case, the differences in size to the left and right of the peak are so large that the 50% cut off location arrives only about half way through the decay length, and a portion of the flow that needs to be included in the bulk flow parabola is missed. This means that the cutoff velocity magnitude value needs to be individually defined based on the properties of the local velocity profiles. In sum, these two methods are both found to fail to describe the profile characteristics.

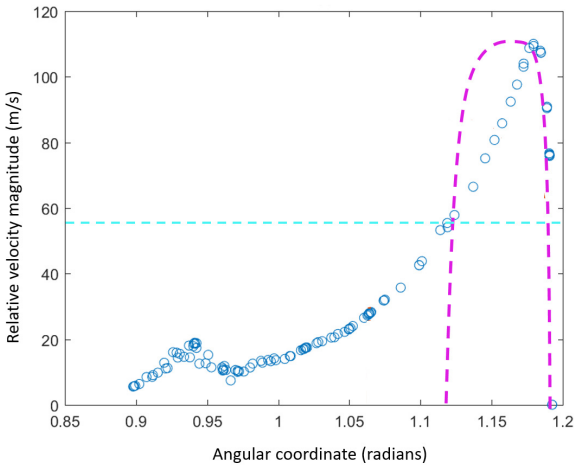

Figure 5.5: Example of skewed CFD profile and its fitted curve by the 50% cutoff velocity.

5.2.3 Method 3: Fitted versus Bulk Flow Error

The last method for finding D_h uses an iterative process to track the flow properties under the curves to find the location of the pseudo-wall. The regional averaged velocity magnitude is used as the reference to compare the difference between the experimental CFD result, and the super-imposed theoretical pipe flow profile until a match is achieved. The process starts by assuming the pseudo-wall is at the cavity velocity center $[r_v,\ \theta_v]$, and moves outwards to the physical bounded wall, which focuses on compensating for the unpredictable inner decay shapes. This method is developed under the assumption that the bulk flow distribution is skewed and stretched wider than its corresponding symmetric and smooth theoretical curve because of the missing fourth wall; but neither the overall regional flow strength, nor the average velocity magnitude should be significantly affected.

In order to make the comparison in velocity magnitudes, a theoretical description of the flow needs to be obtained first. The cavity bulk flow presents properties similar to the internal pipe flows, which can be either laminar with profiles similar to those in Figure 5.6 (a), or turbulent like those in Figure 5.6 (b). The major difference between these two profiles is that the center of the profile for the turbulent flow is flat, whereas that of the

laminar flow is sharp and curvy instead.

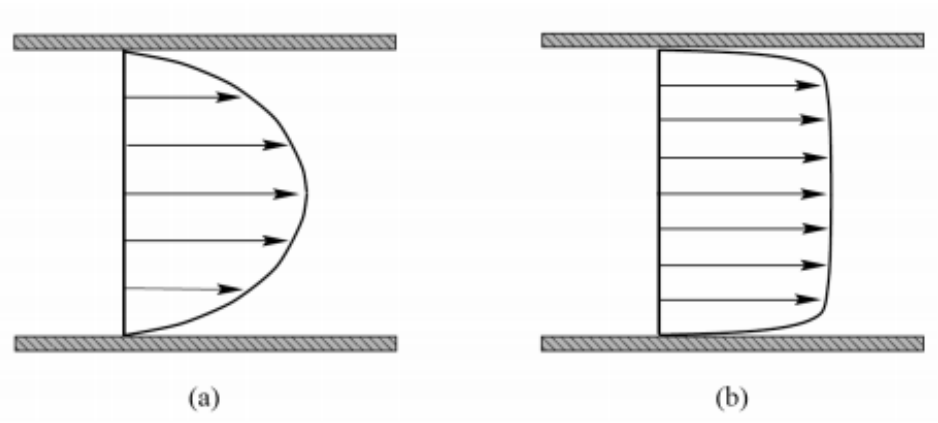

Figure 5.6: Pipe flow velocity profiles for (a) Laminar, (b) turbulent regions [90].

Both shapes in Figure 5.6 have been observed in the endturn cavities. Type (a) often occurs in the bulk flow inlets; type (b) has been seen more often in the outlet regions; and both types exist in the top regions. The cavity bulk flow profiles are also asymmetric, which makes it difficult to find a pattern based on direct inspection. It is known that the laminar and turbulent properties are often-time characterized by the non-dimensionalized *averaged Reynolds number,* Re_{D_h}. For the traditional internal pipe flows, the cutoff Re_{D_h} values are [90]

- Laminar: $Re < 2300$
- Transition: $2300 < Re < 4000$
- Turbulent: $Re > 4000$

A preliminary estimate of the regional Reynolds number $Re_{D_h}\,|_{vp}$ can be obtained by applying a global definition by where the location where the velocity magnitude first decreased below 10% defines the location of the fourth cavity pseudo-wall; therefore the sizes of the bulk flows are 30% for the inlet and top regions and 40% for the outlet regions, based on the averaged generator cavity flow results shown in Figure 4.34. Note that the Reynolds

number $Re_{D_h}\,|_{vp}$ here is a local value and is valid only under the proposed virtual pipe assumption. Preliminary calculations indicate that the Reynolds numbers for all bulk flow regions are much greater than 4000. Thus, the bulk flows are interpreted as turbulent pipe flows with an expected ideal velocity profile similar to that in Figure 5.6 (b). Later, once the bulk flow sizes are mathematically quantified, the Reynolds number can be accurately calculated if needed, but it will not affect the turbulent definition of the flow type.

The turbulent flow has many empirical correlations available to enable approximation of the local velocity profiles. The simple yet the most effective form is the power-law profile, which has been implemented and has proven to successfully capture the internal turbulent flow characteristics in many studies. Its form is shown in Equation.

$$\frac{\overline{U}}{U_{max}} = (1 - \frac{r}{R})^{\frac{1}{n}} \tag{5.1}$$

Here, the exponent n is a whole number that depends on the Reynolds number. The higher the Reynolds number, the higher this n value is, and the more flattened the velocity profile is. In practice, the $1/7^{th}$ order ($n = 7$) can reasonably approximate many flows and is chosen in this study for a more general and universal representation.

The iterative algorithm is therefore developed. The inlet and outlet local hydraulic diameters D_h are analytically calculated following the flowchart in Figure 5.7; the top bulk flow region follows the exact same steps, except that the distance d_i in ***Step 8*** simply equals to $(R_o - R_{min})$. In the iterative loop, the overall process includes two parts: (1) CFD data averaging and (2) power-law calculation. It is common that an exact match can not be found between the experimental and theoretical results; therefore this study allows a $\pm\, 5m/s$ difference in magnitudes as the convergence criterion, which is later tested to be a reasonable range that eliminates exceptions.

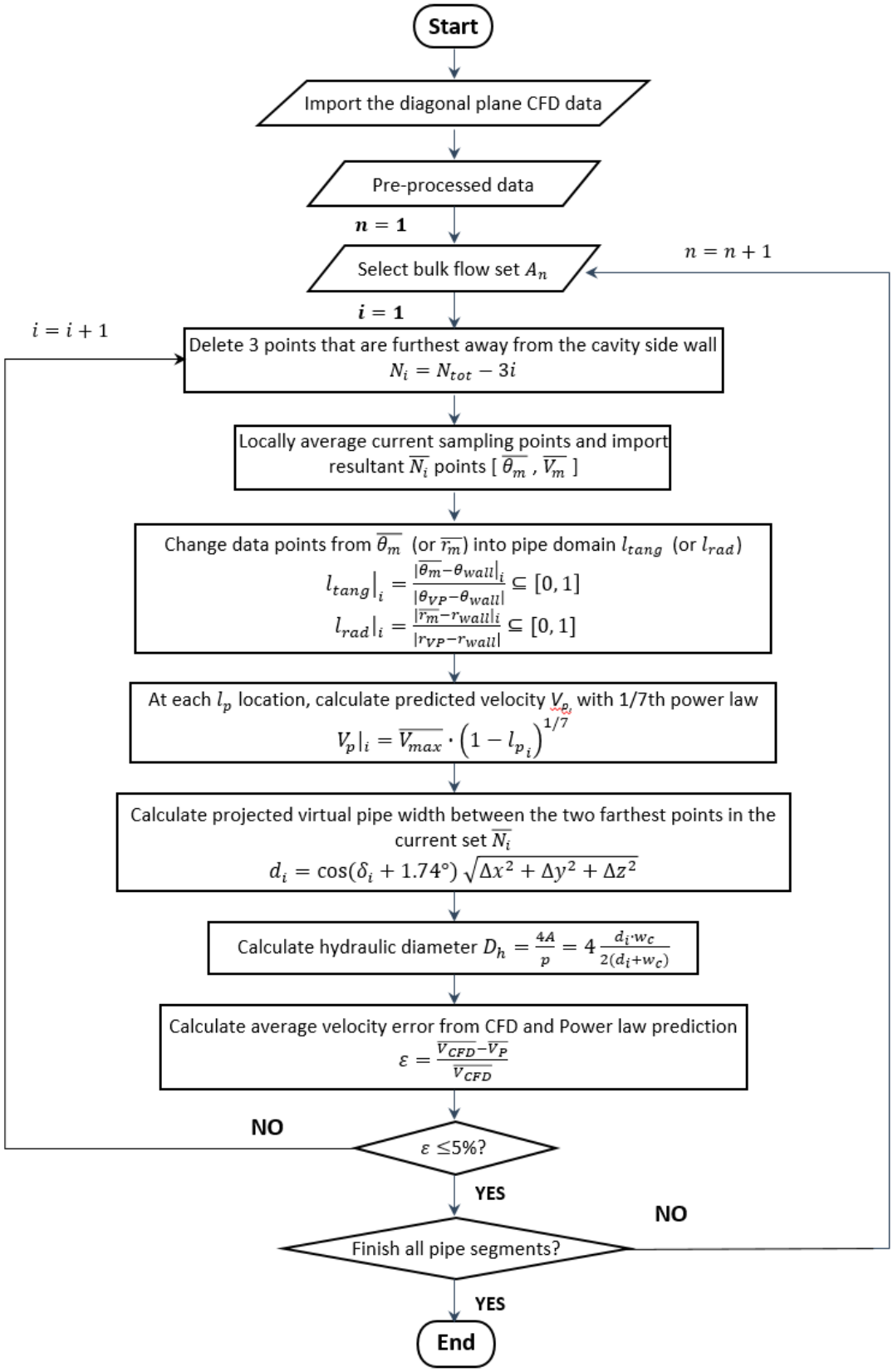

Figure 5.7: Iterative virtual pipe height calculation

Step 1 in the algorithm is to organize the CFD data based on the definition of the bulk flow locations, or separately for the inlet, the top and outlet regions.

Step 1: Import the extracted diagonal plane CFD data ***S1*** and ***S2***, as shown in the top left of Figure 5.8.

Step 2: Separate the original CFD data to three bulk flow sets, such that points in ***S1*** and to the left of ***P*** are saved in the outlet data set A_{out}; the rest are saved as the inlet data set A_{in}. Points in the segment ***S2*** and located above ***P*** are saved in the top data set A_{top}. The three sets are labeled in Figure 5.8.

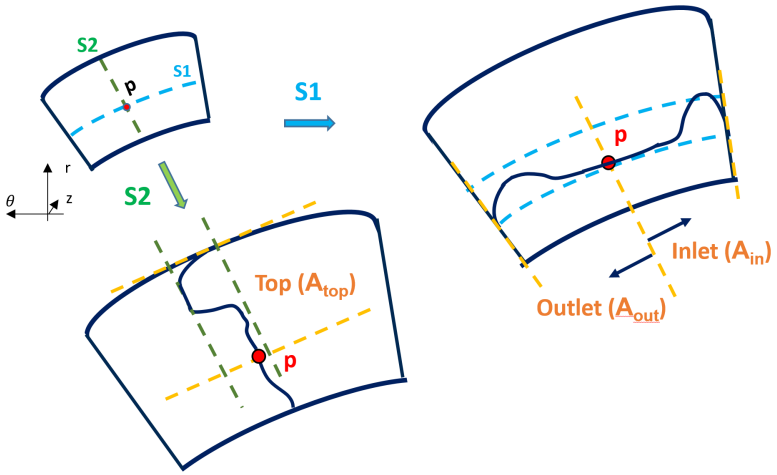

Figure 5.8: Located and saved data points for each bulk flow region

Step 2 is the power-law curve fitting process, which has two loops, during which the original data set is modified such that the pseudo-wall location is moved until convergence is achieved. The detailed steps are discussed below.

[$\Longrightarrow$ Loop 1]: Take the inlet data $n = 1$ and start the outer loop ($n = 2$ for the top and $n = 3$ for the outlet)

Step 3: Pick the n^{th} bulk flow data set A_n

[$\Longrightarrow$ Loop 2]: Start the inner loop, and initialize loop counting $i = 1$

Step 4: Delete $3i$ points counted from the cavity center P such that the size of the sampling data changes to N_i for the current iteration. In this way, the inner bound of the current data set, or the pseudo-wall location is moved away from the center.

Step 5: Locally average the current data set A_n, following the flow chart in Figure 5.9, such that the modified points are evenly distributed in the coordinates. The new set has $\bar{N}_i = j$ points with the form of $[\bar{\theta}_m, \bar{v}_m]$ for the inlet and outlets sets, and as $[\bar{r}_m, \bar{v}_m]$ for the top set. The detailed processes, explanations and justifications are discussed next.

Step 6: Normalize the current data points from the global cylindrical coordinates $[r, \theta, z]$ into the local pipe domain $[\bar{s}, \bar{\theta}, \bar{z}]$, following Equations 5.2 to 5.3. This transforms $\theta_p \mid_i \subseteq [\theta_{wall}, \theta_{vp} \mid_i]$ to $l_{tang} \subseteq [0, 1]$, for the inlet and the outlet sets, or $r_p \mid_i \subseteq [r_{wall}, r_{vp} \mid_i]$ to $l_{rad} \subseteq$ [0, 1] for the top segment. Here, l_{tang} and l_{rad} are the local pipe coordinates; $\theta_{vp} \mid_i$ and $r_{vp} \mid_i$ are the current pseudo-wall locations, which vary for each iteration following the decreased bulk flow sampling sizes, where the subscript i is the iteration number.

$$l_{tang} \mid_i = \frac{|\bar{\theta}_m - \theta_{wall}| \mid_i}{|\theta_{VP} - \theta_{wall}|} \tag{5.2}$$

or

$$l_{rad} \mid_i = \frac{|\bar{r}_m - r_{wall}| \mid_i}{|r_{VP} - r_{wall}|} \tag{5.3}$$

Step 7: Calculate the power law velocity at each local pipe coordinate, following

$$V_p|_i = \overline{V}_{max} \cdot (1 - l_p)^{1/7} \tag{5.4}$$

here, l_p is the normalized local pipe coordinate from Step 6, and $\overline{V}_{max}$ is the normalized local averaged maximum velocity magnitude for the

corresponding pipe region being processed.

Step 8: Calculate the size of the theoretical velocity curve in the $r\theta$ direction, which equals the direct absolute distance between the two farther points in the current set and is calculated as

$$\Delta d_i = \sqrt{\Delta x^2 + \Delta y^2 + \Delta z^2} \tag{5.5}$$

The actual bulk flow size is the projection of this 3D line onto the side edge, to which it should be perpendicular. It is calculated using Equation 5.6, where an additional 1.74 degrees are added to adjust for the distance shifted from the global coordinate system as a result of the center blocking.

$$d_i = cos(\delta_i + 1.74^\circ)\sqrt{\Delta x^2 + \Delta y^2 + \Delta z^2} \tag{5.6}$$

Here δ_i is the angular distance between the two farther points in the sample; x, y, z are their locations in the global Cartesian coordinates.

$$\delta_i = \theta_{max} - \theta_{min} \tag{5.7}$$

Step 9: Calculate the local hydraulic diameter, which is the ratio between the channel's cross-sectional area of the flow to its perimeter, using Equation 5.8.

$$D_h|_i = \frac{4A}{p} = \frac{4(d_i \cdot w_c)}{2(d_i + w_c)} \tag{5.8}$$

where w_c is the width of the cavity and d_i is the calculated bulk flow size from the previous step.

Step 10: Last, calculate the percentage difference ε_i between the CFD and the

power-law velocity profile

$$\varepsilon_i = \sum_{j=1}^{m} \frac{\overline{V_{CFD}} - \overline{V_p}}{\overline{V_{CFD}}} \mid_j \tag{5.9}$$

Here, $\overline{V_{CFD}}$ and $\overline{V_p}$ are the velocity magnitudes of the current, evenly distributed data set $\bar{N}_i$.

Step 11: Compare the error ε_i with respect to the stopping criteria: if the error is less than 5%, stop the iteration and store the current hydraulic diameter $D_h|_i$; otherwise, update $i = i + 1$ and repeat Steps 4 to 11.

Step 12: Save the results for data set A_n. If $n < 3$, $n = n + 1$ and repeat Steps 3 to 11; otherwise, stop the process.

This algorithm implements two data modifications based on the observations from the previous two failed methods, which are locally averaging the original data for uniform distributions and using the regionally representative maximum velocity magnitude at the center of the theoretical curve. First, uneven data distribution in the coordinate can lead to an 'unfair' profile description whereby the errors in the denser mesh locations are weighted more heavily. Note that the variation in the local mesh density is common in the cavity profiles and can be caused by the use of the advanced wall functions method in the original mesher, or the y-plus mesh adaptation applied in FLEUNT, which are both inherently unpredictable. Denser mesh distributions are oftentimes observed near the walls or in the inlet, to satisfy the turbulence near wall requirements and to capture the more diverse geometric features. As a result, if a repeated high prediction error occurs near physical walls, the power-law curve has to move towards the walls, leaving out more of the inner decay region in order to reach the convergence criteria. Therefore, a local averaging of the original data points in Step 5 before the curve fitting in Step 7 is performed, following the steps in the flow chart in Figure 5.9.

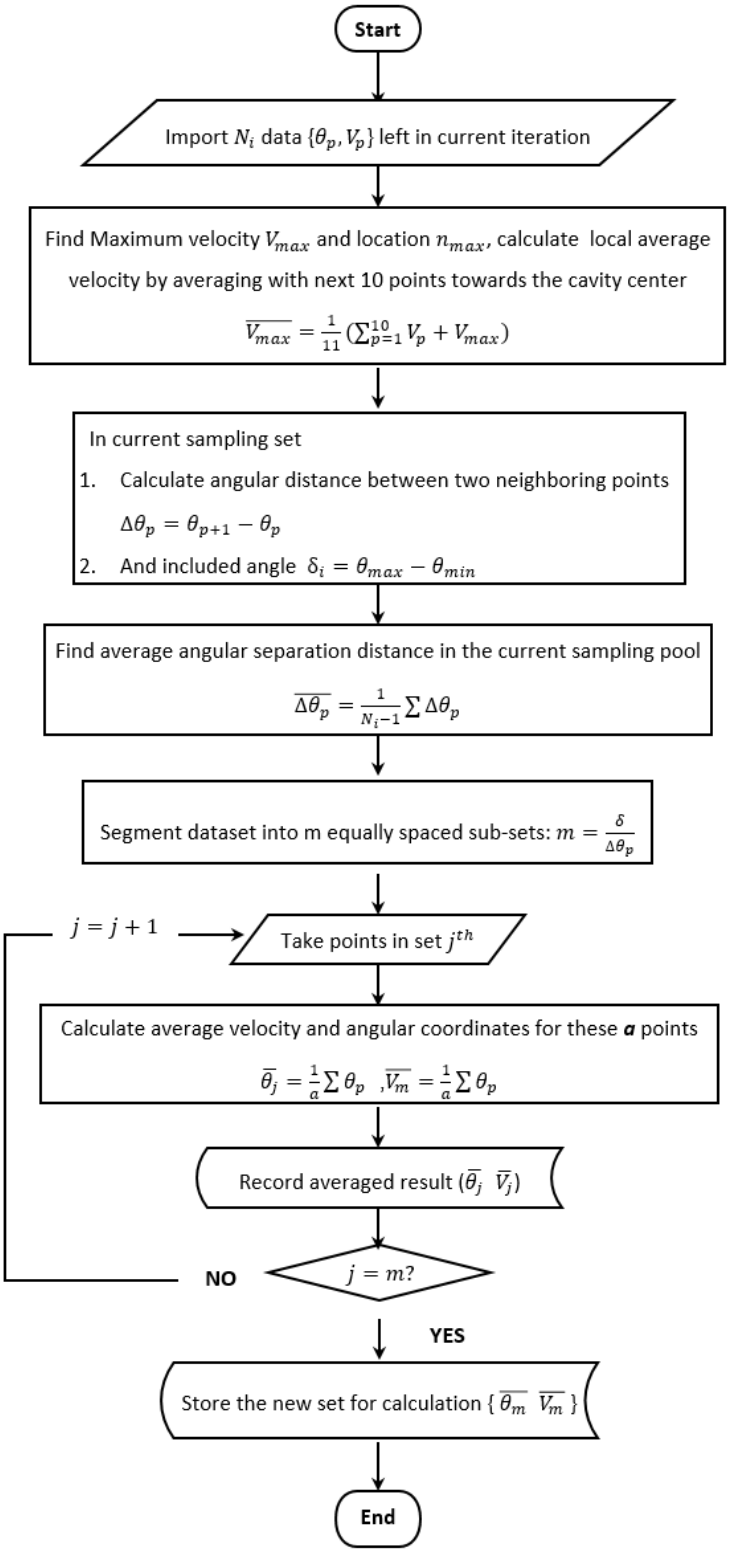

Figure 5.9: Local average process for evenly distributed data

Step 1: Import the j points data set in Step 4 of the overall algorithm.

Step 2: Locate the absolute maximum velocity $[\theta_{vm}, V_{max}]$ (or $[r_{vm}, V_{max}]$ for the top region), which is the n^{th} point in the current sampling pool of j points. Next, the maximum value is averaged with the next 10 points towards the cavity center to $\overline{V_{max}}$.

$$\overline{V_{max}} = \frac{1}{11}(V_{max} + \sum_{n}^{n-10} V_{CFD}) \tag{5.10}$$

This step is explained in detail next.

Step 3: Find the angular distance between the farthest two points in the current set as

$$\delta_i = \theta_{max} - \theta_{min} \tag{5.11}$$

and the local angular distances between two neighboring points in the inlet and outlet set as

$$\Delta\theta_j = \theta_{k+1} - \theta_k \tag{5.12}$$

or in the top set become

$$\Delta r_j = r_{k+1} - r_k \tag{5.13}$$

where, *k* is the index indicating the location of the point, and $k \subseteq [1, j]$.

Step 4: Find the average data distance in the inlet and outlet sets as

$$\overline{\Delta\theta_j}\big|_i = \frac{1}{N_i - 1}\sum \Delta\theta_p \tag{5.14}$$

or in the top set as

$$\overline{r_j}\big|_i = \frac{1}{N_i - 1}\sum \Delta r_p \tag{5.15}$$

Step 5: Segment the current data set to q equally spaced sub-sets, spaced at the averaged separation distance $\overline{\Delta\theta_p}\big|_i$, as illustrated in Figure 5.10.

$$q = \frac{\delta_i}{\overline{\Delta\theta_p}\big|_i} \tag{5.16}$$

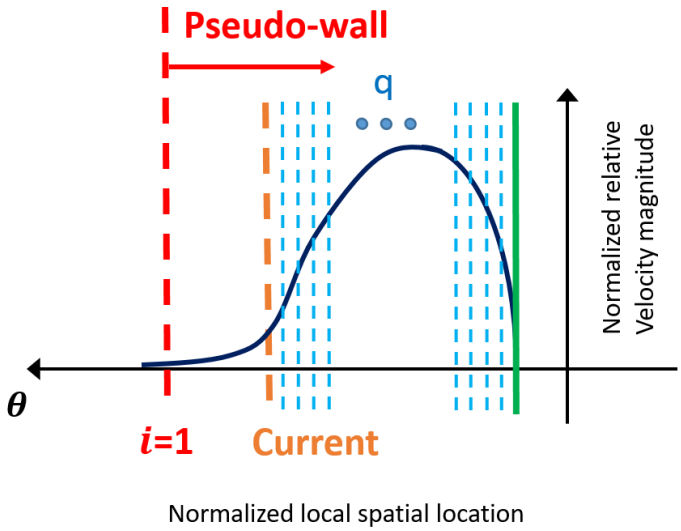

Figure 5.10: Profile length division.

Step 6: Inside each subset, calculate the average coordinate location and the average velocity magnitude, 5.17

$$\overline{\theta_q} = \frac{1}{a}\sum \theta_p \quad ; \quad \overline{V_q} = \frac{1}{a}\sum \theta_p \tag{5.17}$$

The averaged velocities and angular coordinates are stored in a new set $\overline{N}_i$. Figure 5.11 compares the original data and the processed, evenly distributed data. Note that not all P subsets have a velocity value, which is assumed because the diagonal plane cut through the element at that location. Therefore, the velocity magnitude comparison between the experimental and theoretical results should be performed at the existing

locations only.

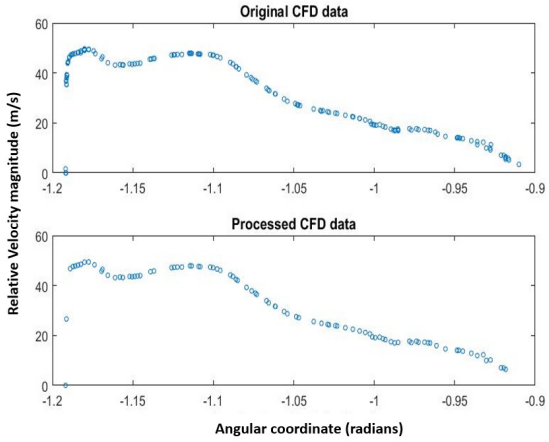

Figure 5.11: Velocity profiles comparison between the (top) original and (bottom) locally averaged result.

Step 7: Store these q data points $(\overline{\theta_q}, \overline{V_q})$ to apply in STEP 5 in Figure 5.7

The second data modification is to apply a regionally average maximum velocity magnitude in the power-law profile calculation to account for the cases where abrupt decay in velocity occurs inside of the peak. Figure 5.12 below is presented as an example to demonstrate the importance of the maximum velocity averaging. For this profile shape, because the maximum speed that the flow reaches at the side wall is so much faster than the speed which the flow decreases towards the stagnant center, the error with respect to the theoretical curve is increased.

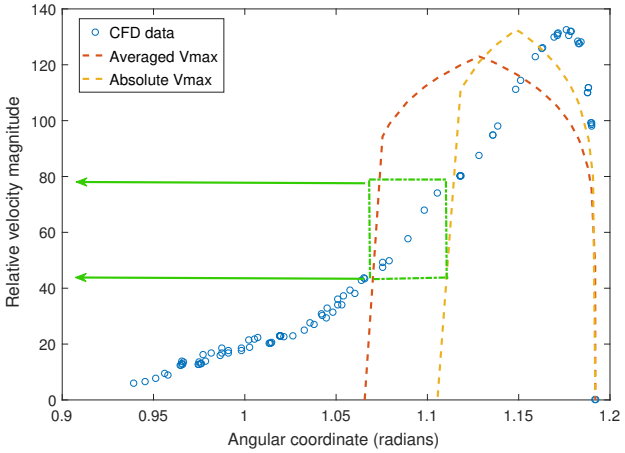

Figure 5.12: Power-law predicted profile comparison before and after maximum velocity averaging.

If simply using the absolute maximum velocity V_{max} as the reference value in Equation 5.4, the resultant power-law profile ends up being very narrow, which is the dashed orange curve. But after decreasing the maximum velocity by averaging ($\bar{V}_{max}$ is smaller than V_{max}), the new power-law profile is the red dashed curve, which is 30% wider. This would bring down the 'cutoff' velocity magnitude at the pseudo-wall by roughly 25% and captures an additional amount of flow in the green boxed region, which has high velocity magnitudes and cannot be assumed to be negligible. The absolute maximum velocity magnitude results in an under-estimate of pipe size and therefore of the characteristic length and an over-estimated regional flow strength. Judging from the heat transfer perspective, this results in a higher Reynolds number, then a higher Nusselt number, and finally a higher heat transfer rate. The over-estimated heat transfer rate will underestimate the local wall temperature and is a useful prediction tool. Therefore, averaging in the maximum velocity magnitude is important.

Following the algorithm, a power-law profile is plotted on top of the CFD data, and the equivalent bulk flow size is determined. Figure 5.13 presents the first and last iterations, where the initial iteration used all the data points saved from the original bulk flow data set and resulted in an over-estimation of the virtual pipe size. The proposed algorithm keeps

iterating, which makes the yellow dashed line keep moving towards the left in this case, until the power-law approximated velocity profile can represent the same bulk flow strength calculated from the CFD data, ending at the stop criteria at the red dashed line.

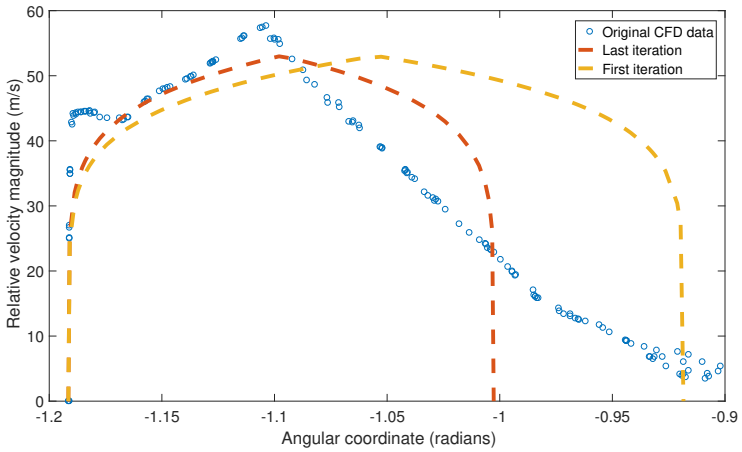

Figure 5.13: Sample iteration comparison plot

5.3 Design of Parametric Cases

The previous chapter demonstrates the similarities in the cavity bulk flow phenomenon and proposes a description of the flow named the virtual pipe; and the previous section develops a mathematical algorithm to quantify the sizes of the bulk flows. But both are conducted using data extracted from two design scenarios only. This section continues the cavity bulk flow study by introducing additional design cases, to (1) verify and validate the feasibility and applicability of the developed descriptions and analysis methods, and (2) investigate the possible design scenarios for the current class rotor. A parametric experimental study is conducted in this section that uses the previously developed partial endturn cavity CFD model, which focuses on the parameters that are identified to directly contribute to the formation of the bulk flow phenomenon.

5.3.1 Definition of Parameters

This section discusses the cavity parameters that are evaluated from the endturn ventilation design perspectives. Note that this study is interested in only two aspects of the velocity profiles; their shapes and sizes. The velocity magnitudes are inspected but not studied in detail. Based on the thorough investigations in CHAPTER 4, it was realized that the above two bulk flow aspects are generally affected by (1) the cavity geometry, and (2) the annulus flow conditions; and are generally not affected by the rotor loading conditions. Therefore, the relevant rotor endturn parameters can be categorized into the controllable design parameters and the uncontrollable design constraints, which are both informed by the literature and the previous CFD studies.

The identified parameters are summarized in Table 5.1 below. The design parameters need to be defined, which includes their names, parametric ranges, and parametric resolutions; the design constraints only needs to be identified. The design parameters investigated here are the cavity geometries and the rotor endturn inlet conditions. The cavity geometries vary as a result of the rotor coil designs, while the inlet conditions are affected by the rotor fan blade designs. Each endturn cavity can be described by three dimensions: width w_c, height Δr, and cavity opening θ_c. Together, they influence the amount of bulk flow that can enter the cavity, and the flow lengths of the 'inlet-top-outlet' virtual pipe path. The velocity inlet conditions include the inlet velocity magnitude V_{in} and the inlet velocity angle θ_{in}. They determine the strength of the initial 'pumping' momentum in the annular region underneath the cavity.

Table 5.1: Summary of experimental design factors.

Design Parameter		**Design Constraint**	
Geometric	Cavity width w_c	**Operating condition**	Cold gas temperature T_{in}
	Cavity opening θ_c		Inlet gauge pressure P_{in}
	Cavity height Δr		Rotating speed ω
Inlet	Inlet velocity magnitude V_{in}		Field current I
	Inlet velocity angle θ_{in}	**Rotor dimensions**	Rotor diameter D_i, D_o
	Radial velocity V_{rad}		Insulation blocking w_b, h_b
	Tangential velocity V_{tang}		Shaft diameter D_{shaft}

Among the above design parameters, the cavity height Δr was excluded from the parametric study set, since changes in the rotor diameters D_o and D_i involve much more complex electromagnetic and mechanical coupled physics beyond the ventilation design, which require detailed investigation since inappropriate values may easily lead to a complete rotor redesign. The rotor outer diameter D_o is mechanically limited by the rotor body and the retaining centrifugal forces [4], and is especially strictly restricted due to the limitations of the airgap sizes of electric machines; therefore it is kept constant in this study. The rotor inner diameter D_i can be varied but will change the amp-turn output value; therefore it is not studied here. Figure 5.14 presents the remaining four parameters. These are studied to develop a more comprehensive understanding of the cavity internal bulk flow performances.

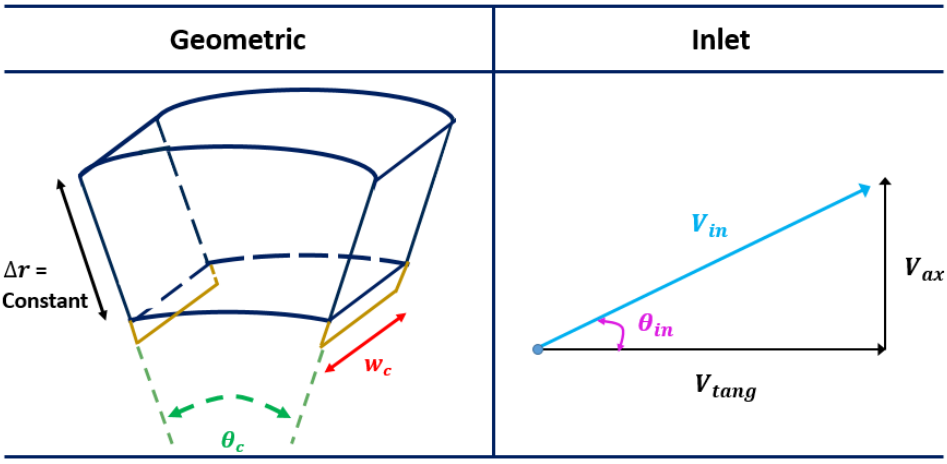

Figure 5.14: Parametric parameters of interest for the cavity geometry and the fluid inlet conditions.

The nominal condition is taken as the reference condition, which is the 350 MVA machine operating under the short-circuit condition, with values summarized in Table 5.2. The parametric cases are designed to search for optimized endturn cavity designs to improve ventilation performance; therefore the identified design parameters are discussed from the design perspective in this section in order to determine their corresponding useful parametric ranges.

Table 5.2: Summary of cavity design variables nominal values

Parameter		**Value**
Geometric	Width $\widetilde{w_c}$	40 mm
	Row 2 cavity opening $\widetilde{\theta_c}$ [b]	35.28 degree[a]
	Coil outlet radius $\widetilde{R_o}$	515 mm
	Coil inner radius $\widetilde{R_c}$	393 mm
	Blocking inner radius $\widetilde{R_i}$	373 mm
	Row to row cavity opening ratio	1.1
Inlet	Inlet velocity angle $\widetilde{\theta_{in}}$	30 degree
	Axial velocity $\widetilde{V_{ax}}$	37 m/s

[a] Value measured with respect to cavity two side walls; the global coordinate system has an additional 1.74 degree offset because of the center blocking.

[b] Row of interest.

The design constraints include the machine operating conditions (rotating speed, rotor capacity etc.), and the number of fixed rotor dimensions, which must be kept constant to maintain the same class machine designation. The design constraints limit the variations in the design parameters, while the design parameters assure the applicability of the design constraint settings. The cavity's geometric parameters are constrained by the constructional pattern of the rotor coils and the insulation, as shown in Figure 5.15. Therefore, the parametric cases are designed conservatively such that no major change in the overall rotor electro-magnetic and mechanical design would be required in order to reflect the changes in cavity dimensions. Here, the annulus thickness is further separated into two parts; the top *Mixing zone* and the bottom *Bypass zone*, based on the locations with respect to the insulation blocks. The length $(R_c - R_i)$ between the bottom of the stacked coil and the blocking is named the *mixing zone*, inside which highly disturbed flow exists, as a result

of the bypassing flow streams that enter and leave the cavity. The length underneath the blocking is named the *bypass zone*, where the forced rotor inlet flows are noticed to mostly travel further into the rotor undisturbed, with only minor losses contributing to changes in flow properties.

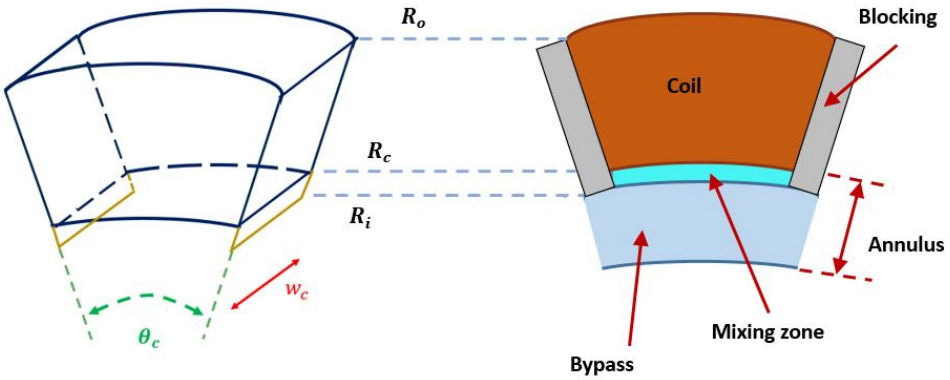

Figure 5.15: Single cavity geometry separation.

The applicable ranges for the geometric parameters need to follow the principles of the current rotor coil designs:

1. The coil and insulation patterns are symmetric about both the quadrature axis 'q' (coil) and the direct axis 'd' (pole), as shown in Figure 3.2

2. The rotor coil end-arc lengths are 'linearly decreased', as the z position moves into the rotor, as labeled in the green dashed lines in Figure 3.6; all coils also have the same width w_{cu}, height h_{cu}, and are equally spaced at a designated distance w_c

3. The cavities in the same row (z position) have the same shape and are equally separated by the blocking at a distance w_b

4. There are four cavities per row surrounding the first five, longer coils and two per row surrounding the last two short coils

All of the above design principles are kept the same throughout the parametric cases to keep the endturn construction pattern consistent. Note, the insulation blocks are kept of the exact same length and height (only varying in width following w_c) to maintain cavity separation distance, since they are specifically designed to maintain the alignment of the end winding coils during operation [8], and will require additional mechanical analysis in order to make any changes.

With the design principle details specified, the two geometric parameters can be defined next. First, changes in the cavity width w_c, or the rotor coil spacing directly affect the length of the rotor. The rotor length affects the rigidity of the rotor and the need to attain normal running through the first critical speed [4]. Thicker cavities, or a longer rotor result in (1) higher mechanical loadings, and (2) higher length-to-diameter ratios which cause balancing issues [91]. In contrast, a thinner cavity results in: (1) lower volumetric flow rates, thus lower heat transfer rates and higher rotor coil temperatures, when running at the same field current, which eventually limits generator power capacity; (2) less magnetic material to carry the designed level of flux for the generator and less materials to accommodate all the stresses and loads the rotor experiences during rotation [91]; (3) a higher risk of winding arcing between two adjacent shorted turns. Therefore, this investigation was conducted within a range of $\pm 25\%$ off the nominal $\widetilde{w_c}$ value only, which results in a roughly 10% change in the endturn length and a 2% change in the overall rotor length.

The cavity opening θ_c is strictly limited by the rotor's symmetry constraint. For a two-pole machine, the sum of the biggest four cavities plus the blocking cannot exceed 180 degrees per rotor winding region, which makes the current biggest cavity openings (39 degrees) already the maximum allowable value. But, the smallest cavity can be even smaller if the end-arc length of the adjacent two coils is shortened at a higher ratio. Per inspection of the vector field plots of the row 5 cavities in Figures 4.33 and 4.30, an additional decrease in θ_c may not be realistic, since the bulk flow is already noticeably weak in the current smallest cavity. An even smaller cavity opening would only further weaken the

rotor ventilation performance, and therefore is not considered. As a result, the parametric experiments will cover the current ranges, or from 39 to 23 degrees. To provide a rich yet feasible number of experiments, each design parameter is determined to study at five equally spaced levels, as summarized in Table 5.3 below.

Table 5.3: Geometric parameter case summary.

Parameter	Value
Cavity width w_c (m)	0.03, 0. 35, 0.04, 0.045, 0.05
Cavity opening θ_c (Degree)	23, 27, 31, 35, 39

The rotor inlet stream condition involves highly complex flow physics and is also one of the three streams leaving the front axial cooling fans. The inlet stream is affected by the pressure distribution of the overall machine, and the construction of the stator end winding, and the airgap. In the generator CFD study, the rotor inlet is inside the near-field volume such that no boundary condition needs to apply; but it is a separate boundary that needs to be defined in the parametric partial endturn CFD model. Here, for the purpose of serving the design study, the rotor inlet is defined to be *velocity inlet* type, with constant components to allow for flexible parametric designs. This definition is applied since it is given that less aggressive fan blades are designed for this generator, which normally have big and thick shapes and result in small stall and camber effects during operation. Under these circumstances, the flow streams exiting the axial fans have relatively uniform distribution and can be reasonably approximated using the *velocity triangle*. In addition, a clear and smooth flow passage is present between the fan and the rotor inlet, and therefore the flow reaching the front of the rotor is expected to maintain the same exit properties. Note that by this assumption, for any velocity inlet components combination, the corresponding fan blade can be determined by 'reverse engineering' using the velocity triangle; this therefore guarantees the feasibility of building an axial fan based on the expected rotor inlet flow conditions.

Based on the provided fan blade design dimensions, it is first noticed that the radial velocity off the blade is zero. Therefore, the inlet velocity components were varied in two ways only, as shown in Figure 5.16, which either changes the tangential velocity at a constant axial velocity, or vise versa. The fixed tangential velocity cases study the flow responses to the changes in the annulus flow rate, while the constant axial velocity cases investigate the impacts of the annulus 'pumping' momentum.

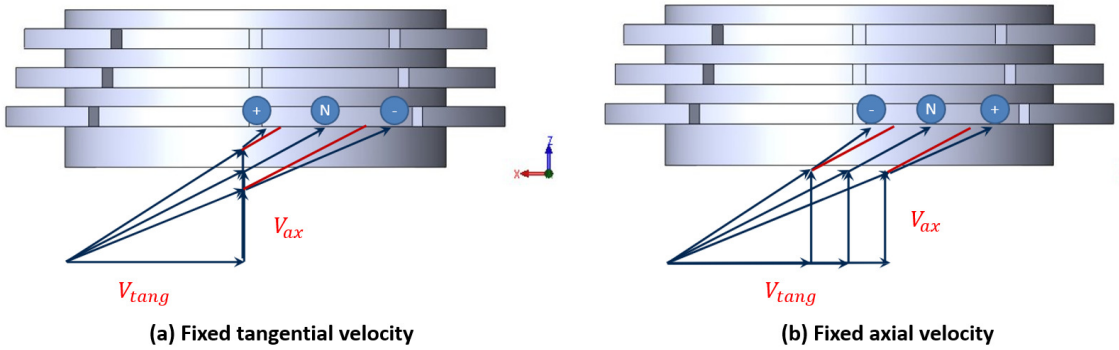

Figure 5.16: Endturn velocity input component variation diagrams.

It is also given that the typical resultant rotor inlet velocity components are angled from 30 to 45 degrees. Therefore, the parametric experiments were designed to vary from 28 to 48 degrees to cover these popular designs. The axial velocity defines the rotor mass flow rate, where in general, less flow means less effective ventilation performance in the rotor body. As a result, this study is interested only in increasing the axial velocity component from the nominal value $\widetilde{V_{ax}}$, in an attempt to improve the ventilation performance. With the inlet angle and the axial velocity component defined, the tangential velocity component is calculated based on the inlet velocity vector diagram in Figure 5.14, or following Equation 5.18 below.

$$v_{tang} = \frac{v_{ax}}{tan(\theta_{in})} \tag{5.18}$$

Here, v_{ax} and θ_{in} are the values set for each experimental case. These parameters are studied at five levels again, as shown in Table 5.4 to keep consistent with the geometric

parameters.

Table 5.4: Inlet parameter case summary

Parameter	Value
Inlet angle θ_{in} (m/s)	28, 33, 38, 43, 48
Inlet axial velocity V_{ax} (m/s)	37, 40, 43, 46, 49

Note that the radial and tangential velocity components are inlet inputs defined in the absolute reference frame. But the rotor flow domains are defined in both the absolute and the relative (rotating) reference frames; therefore, the velocity vectors in both frames need to be addressed. The overall velocity vector diagram is as shown in Figure 5.17 below, where the smaller triangle on the right side is the inlet design parameters; and on the opposite side, u_r is the relative tangential velocity from the rotating motion. Adding them together is the relative velocity magnitude in annulus v_r, which arrives at the bottom of the blocking at an angle of attack θ_{attack}, before being 'pumped' into the cavity. The relative velocity magnitude is useful when designing the virtual pipe correlations later in this chapter, and also the thermal-fluidic networks in CHAPTER 7.

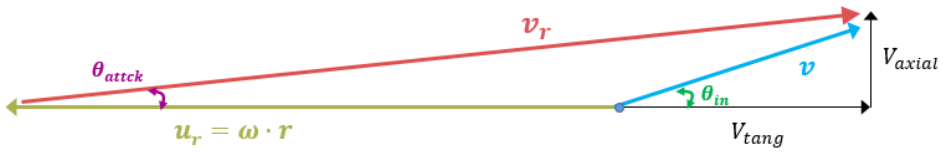

Figure 5.17: Absolute versus relative reference frame endturn velocity vectors.

The design constraints include operating constraints and geometry constraints, and all of them are kept constant for all parametric experimental cases. The operating constraints related to this cavity study are (1) the inlet 'cold gas' temperature and gauge pressure that are defined by the overall ventilation design and (2) the rotating speed and the field current that are defined by the machine class definition. These two constraints are

applied in the parametric CFD study as boundary conditions. The geometry constraints are the rotor inner and outer diameters, and the shaft diameter that are all concerned regarding the additional mechanical and electrical considerations mentioned in CHAPTERs 1 and 2.

5.3.2 Experimental Design

Now that the design parameters were specified, and a CFD model was specifically designed to meet the research objectives, the parametric cases were designed as part of the rotor ventilation investigation, and to validate the feasibility of the developed flow characteristic D_h calculation algorithm. The cases were constructed using the *factorial design* method that is commonly used for a traditional design of experiment (DOE) study. For a full rank factorial study, the number of cases needed is calculated using Equation 5.19 [92]

$$\# \; case = level^{factor} \tag{5.19}$$

In the current study, each design parameter type has five levels and two factors, which results in 25 cases each (5^2) and two uniformly distributed, two-factor full-rank 'orthogonal' data sets. These full-rank cases aim to provide comprehensive insights to understand the effects of each type of parameter, while constructing a uniform data layout at a fine resolution. Note that for the geometric cases, the inlet velocity components are maintained at the nominal values $\widetilde{w_c}$ and $\widetilde{\theta}_c$; whereas for the inlet cases, the cavity dimensions w_c and θ_c are kept at the nominal values $\widetilde{V}_{ax}$ and $\widetilde{V}_{tang}$.

In sum, a total number of 50 parametric experiment cases are prepared for the bulk flow study of two types of design parameters. These cases are carried out using a three-dimensional, partial parametric endturn cavity model. CFD results are later inspected for the interest of studying the local bulk flow performances, while testing the performances of the analytical virtual pipe D_h calculation algorithm in the previous section.

5.3.3 Parametric Study Results Summary

This section examines the applicability of the parametric cases on the current machine, by verifying the cavity bulk flow phenomenon. Since the ranges of the design parameters are intuitively defined based on textbook background knowledge, provided factory data, and simplifications and assumptions taken based on experiences, the design results need to be evaluated. The following aspects are examined: (1) the goodness of the experimental parametric cases, (2) the phenomenon similarities of the experiment's cavity bulk flows, (3) and the applicability and reliability of the CFD profile basis D_h calculation algorithm. The cases that present flow phenomena that differ from the nominal conditions are discarded; only the qualified cases are kept for further study.

Preliminary inspection has indicated that all parametric cases have the expected bulk flow phenomena, except for the two biggest cavity cases, or the geometric design cases $\#49$ and $\#50$ in Table D.2. These two cases failed because the feeding flow momentum is not enough for the extra volume added. Take Case $\#49$ as an example; it maintains the nominal inlet inputs, while increasing the cavity width w_c by 12.5 $\%$ and the cavity opening θ_c by 11.4 $\%$. Overall it increases the cavity volume by 25.6 $\%$, with respect to that of the nominal cavity design. The vector field plots in Figure 5.18 show that the leading cavity 1 and 2 have significantly smaller swirls that cannot reach the far left sides of their cavity walls, leaving considerable portions of the right side cavity volume empty with no bulk flows. This means the bulk flow strength is not strong enough, either in magnitude or in volumetric flow rate, in order to form a complete swirl that travels along the entire cavity perimeter and spreads over the entire cavity width at the same time. These swirls no longer possess the flow characteristics pursued and therefore fall outside the scope of this study. Thus, they are excluded from the sampling set.

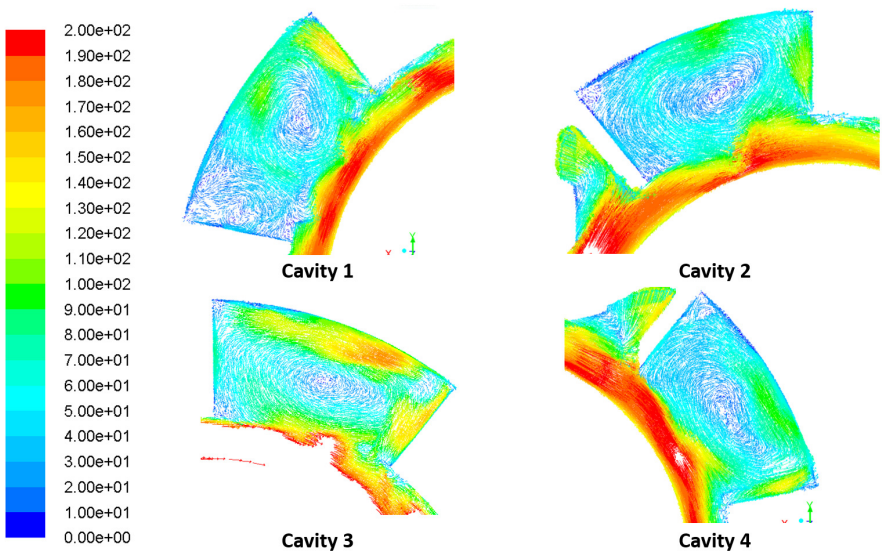

Figure 5.18: CFD results for geometric design case 24.

Velocity profiles of the remaining 48 experimental design cases are investigated, with the vector field plots and the local velocity profiles. The results of the most representative extreme four cases are presented. The extreme cases have design parameter settings summarized in Table 5.5.

Table 5.5: Parametric study validation case summary.

Case		**Parametric Case ID (Tables D.2, D.1)**	**Values**	
1	Geo min	#26	$w_c = 30\ mm$	$\theta_c = 23\ degree$
2	Geo max [a]	#48	$w_c = 40\ mm$	$\theta_c = 39\ degree$
3	Inlet min	#21	$\theta_{in} = 48\ degree$	$V_{tot} = 50\ m/s$
4	Inlet max	#5	$\theta_{in} = 28\ degree$	$V_{tot} = 104\ m/s$

[a] Maximum among the valid cases

Vector field plots of the 3rd cavity for each case are shown in Figure 5.19. These four figures are plotted on the same legend to compare velocity magnitudes; their dimensions are also at scale in order to compare sizes.

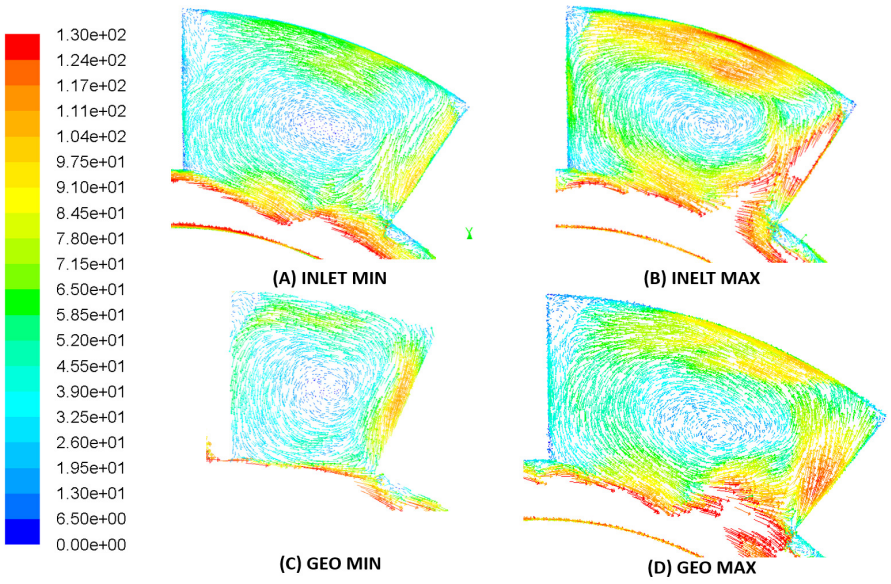

Figure 5.19: Cavity 3 vector plots comparison for the extreme cases in the parametric study.

Among these four cases, all vector plots show the expected, complete counter-clockwise bulk flows, even though flows are at different strengths. More specifically, cavity (A) and (B) are at the nominal geometric dimensions while the annulus inlet flow in case (B) enters at a shallower angle with a higher axial flow than (A). This results in a significantly stronger bulk flow inside cavity (B), where the relative velocity magnitudes are noticed to be much higher even in the outlet region. Cases (C) and (D) are under the same inlet conditions, while case (C) is designed at the minimum cavity angle and width combination, and case (D) is the valid maximum cavity. Case (D) has a stronger bulk flow than the Case (C), and it is suspected that at the same inlet conditions, bigger cavities increase the changes for the annulus flow to enter the cavity and therefore improve the ventilation performance. In sum, these four cavities all show the desired bulk flow pattern and can be categorized together with the nominal case cavity flows.

Next, the velocity profiles along the same tangential and radial segments introduced in CHAPTER 4 are plotted. The expected one-dimensional, one-component dominating, parabola-shaped flow properties need to be verified. Figure 5.20 below is a representative plot, which compares the velocity components of the leading cavity 1 for the minimum

inlet flow rate parametric case (#5 in Table D.1). For this cavity, radial velocity dominates in the tangential slice, and tangential velocity dominates in the radial slice, and both can be substituted with the velocity magnitude curve. All of these match the observations mentioned in CHAPTER 4. The same conclusions are achieved for the other parametric cases.

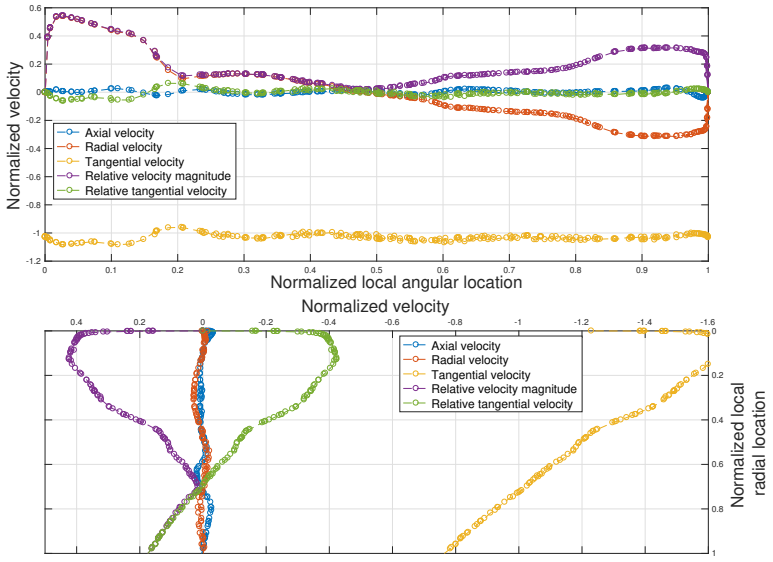

Figure 5.20: Bulk flow velocity component comparison along (top) tangential segment, and (bottom) radial segment (cavity 1 of inlet case 5).

Locally normalized relative velocity magnitude profiles of these four cavities are plotted and shown in Figure 5.21. Parabola-shaped velocity profiles are noticed for all three bulk flow locations for all four cavities. Differences in the sizes of the parabolas exist, as expected. For example, in the outlet region, the velocity growth from the velocity center for case *InMaX C2* is much faster than that of *InMin C2*; therefore different pseudo-wall cutoff locations are expected. On the other hand, in the top region, *InMax C2* has a flattened profile that matches the description of the turbulent pipe flow, whereas *GeoMin C2* has a sharp profile similar to that of laminar pipe flows instead.

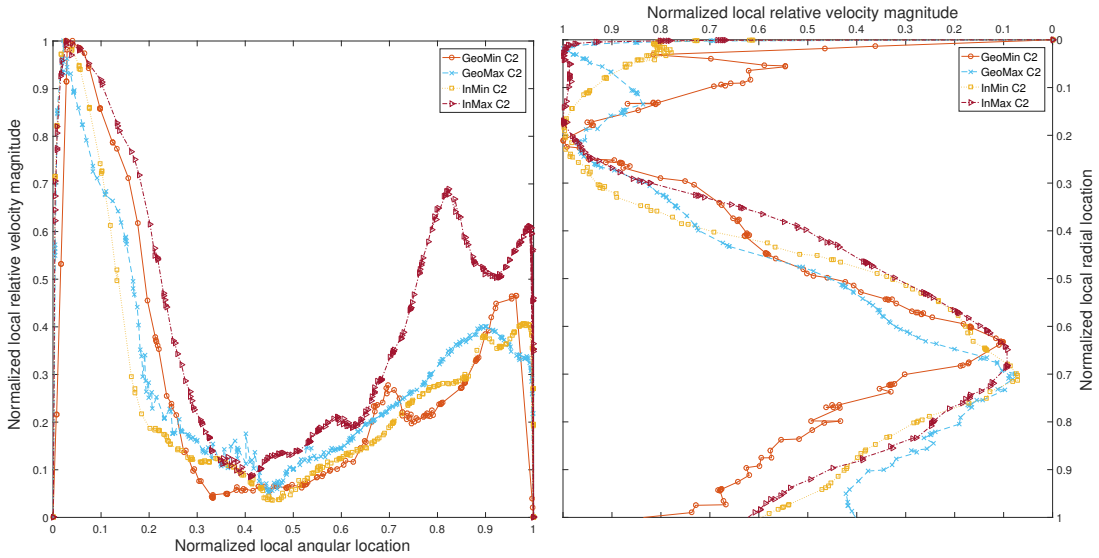

Figure 5.21: Parametric study bulk flow velocity profile cross validation for same cavity in (Left) Inlet and outlet region; (Right) Top region.

For an even more rigorous comparison, all 16 cavities in the four extreme cases are compared. Figure 5.22 presents the locally normalized velocity profiles of these cavities, where the left plot is plotted along the tangential segments and the right plot is plotted along the radial segment.

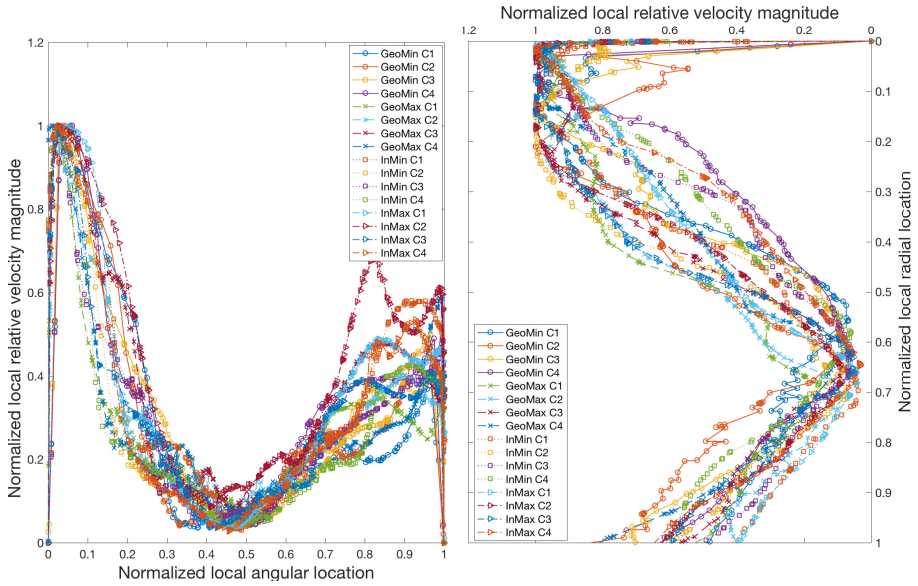

Figure 5.22: Cross validation of velocity profiles of all cavities in the parametric extreme cases for (Left) Inlet and outlet region; and (Right) Top region.

At first glance, it is obvious that for both segments profiles are closely aligned and follow the same layout, as expected. But nontrivial differences are present as well. Except for the differences in the parabola shapes, differences in the velocity decay are substantial. In the virtual pipe inlet (0 to 50% on the left plot) and top regions (0 to 50% on the right plot), the speeds of the velocity decays are significantly different. If taking the normalized velocity magnitude of 40% as reference, the locations at which the profiles reach this magnitude differ by roughly 10% in the inlet and 20% in the top. In the outlet regions, the shapes of the velocity profiles become even more diverse, which also have significantly different local maximum velocities with parabolas that are more or less skewed towards the physical wall at different spatial locations. All of the above differences need to be taken into consideration when developing a description of the virtual pipe flows, and therefore the visually inspected percentage values in CHAPTER 4 SECTION 4.3 are no longer appropriate, but rather a more comprehensive, systematic, generic and most importantly, a justifiable virtual pipe size calculation method needs to be developed.

In sum, 48 experimental cases are verified to serve the research objective and are used to verify the performance of the D_h algorithm. It is also noticed that these four parameters contribute significantly to the formation of cavity bulk flows, and their importance is presented in this study in terms of their flow characteristic lengths D_h.

5.3.4 Virtual Pipe Size Calculation Summary

The local D_h values are calculated for all 48 design cases, or a total of 576 calculations were performed. A representative set of results is shown in Figure 5.23, which presents normalized velocity profiles for the defined three virtual pipe locations for the geometric maximum condition (Case $\#48$). Note that the velocity magnitudes and spatial locations are locally normalized to show the general trends only. The proposed method is shown to be able to capture the regions of strong bulk flow, and cut-off the length of the transition regions into the stagnant center when defining the sizes of the local bulk flows.

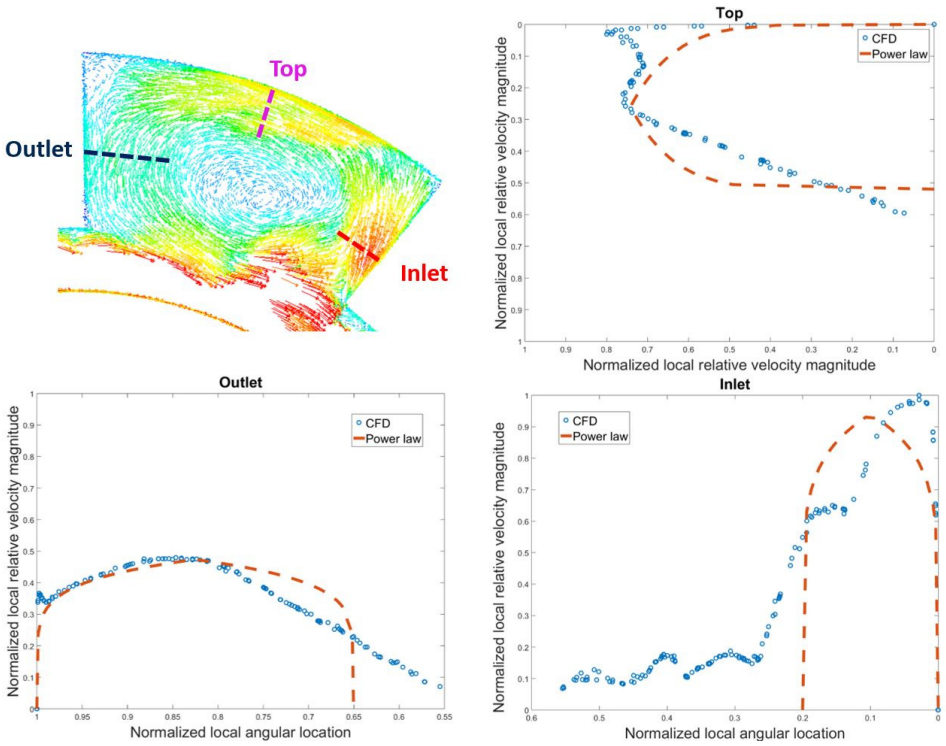

Figure 5.23: D_h calculation example for the three virtual pipe locations (Geometric maximum case $\#48$).

Comparing the results from all 192 cavities examined, the inlet bulk flows are found to be generally the narrowest of the three, whereas the opposite outlet sides are much wider. The inlet flows are much higher in magnitude while the outlet flows are weaker, corresponding to the principle of conservation of mass. The majority of the cases have profiles similar to the ones shown in the above figures, which can be successfully and automatically calculated using the developed method. All calculations can be completed by following the convergence criteria, but 3% of the results are visually inspected to be 'wrong'.

The failed cases have profile shapes similar to the one shown in Figure 5.24 below. A near-wall, localized high velocity peak occurs that occupies less than 10% in space; a second, wider 'peak' presents with velocity magnitudes that are 20% lower but are still strong enough to match the bulk flow requirement. Because of the big differences in magnitude between the two peaks, the V_{max} averaging method can no longer correct for the near wall

singular value. This results in a narrow fitted profile, or the labeled yellow dashed line that obviously fails to cover a major portion of the swirl. These 'two peak' profiles are not unexpected since the extraction diagonal planes coincide with the corners of the cavities at the inlet and outlet regions, likely causing localized strong flow streams. The algorithm under-predicts the local virtual pipe size for these profiles and were corrected here.

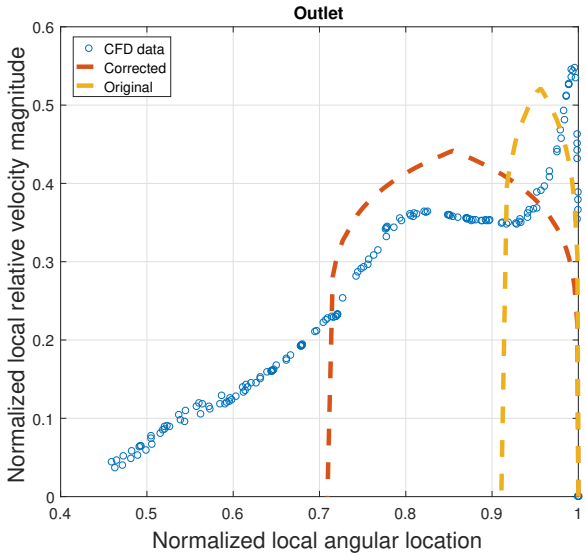

Figure 5.24: Representative bulk flow profile for failed calculation cases.

The remedy applied here is to manually replace the averaged maximum velocity used in equation 5.4 with the average of the first and second 'peaks', which in this case is the average of 0.56 and 0.35. After the second averaging, the peak magnitude is lowered and stretches out the fitted parabola to the red, dashed line. The correct profile is able to account for both the strong flow at the corners and the body of the bulk flow away from the walls, providing more practical results. Averaging here has to be manually applied since the second peak has to be visually identified and located.

5.3.5 Study of the Cavity Design Parameters versus the Cavity Internal Bulk Flow

Now that the experimental cases are visually and quantitatively inspected, and the failed cases are identified and filtered from the sampling set, this section explores the impacts of the identified parameters. To do so, the vector field plots were used, and comparisons were performed separately for each identified design parameter.

Figure 5.25 first compares the vector field plots of the two types inlet cases, which are either at the same axial velocity (mass flow rate) or the same inlet velocity angle (cavity inlet angle of attack). Cavity 3 are used for demonstration again and all cases shown have the nominal cavity geometry. The axial velocity is constant along the left column, but the inlet velocity angles θ_{in} increase accompanied by a decrease in absolute tangential velocity, from Case $\#3$ to $\#23$. The decrease in the tangential velocities resulted in weakened cavity bulk flows, in terms of both the flow magnitudes and sizes. This indicates that the annulus tangential velocity directly contributes to the 'pumping momentum' into the cavity, just as it was previously assumed. On the right column, increasing the axial velocity magnitude at a constant inlet angle, or when maintaining the same relative component ratio between the axial and tangential velocity results in a stronger bulk flow when gradually increasing the axial velocity, especially in the bulk flow inlet area.

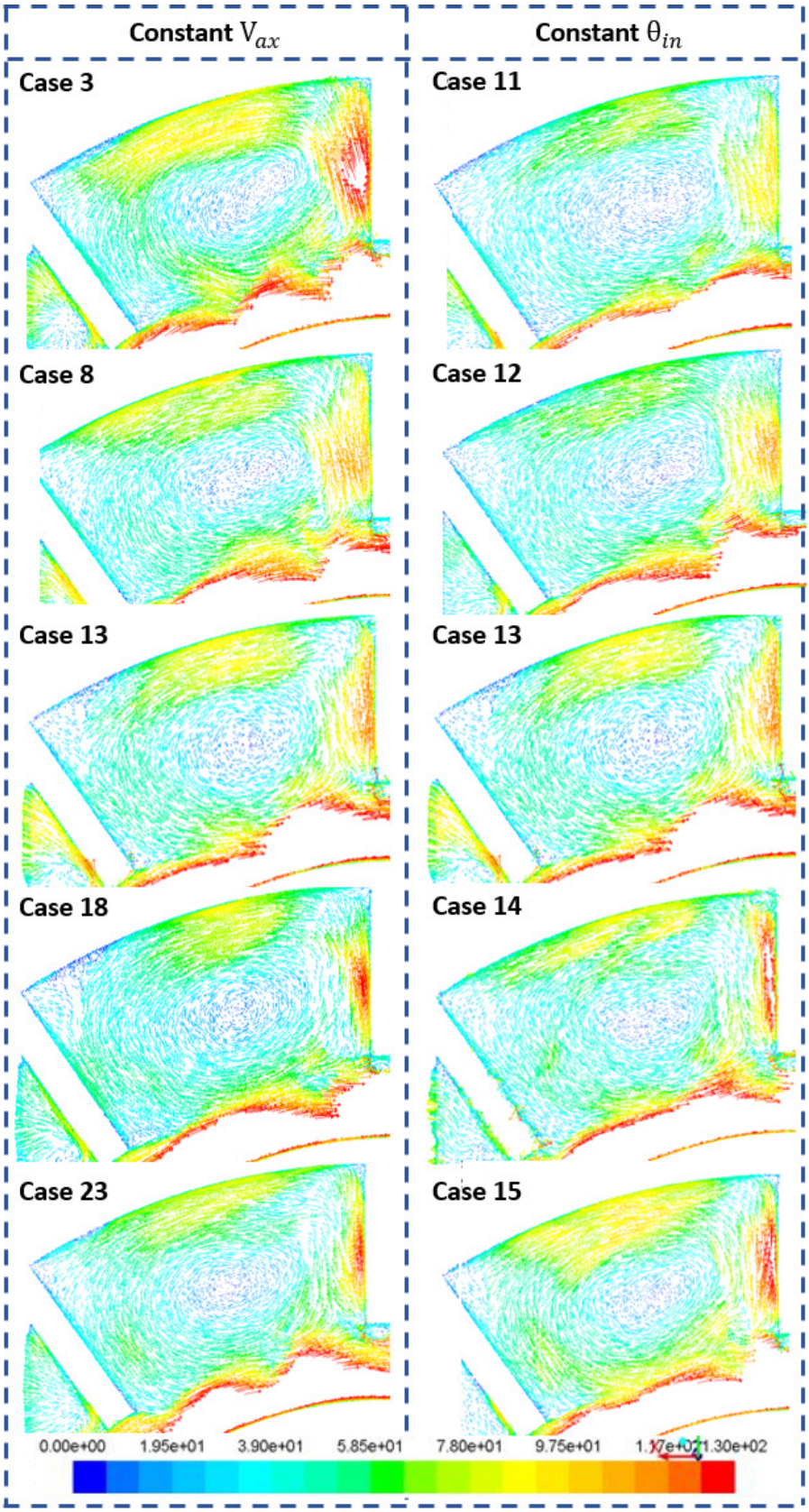

Figure 5.25: Cavity 2 vector plots comparison for (Left) Constant axial velocity; (Right) Constant velocity inlet angle.

Figure 5.26 compares vector plots of cavities operating at the same cavity width versus at the same cavity opening, while both maintained at the nominal inlet condition. All figures are plotted at scale in order to compare their relate sizes. The cavity width is constant along the left column, while the cavity opening θ_c increases from Case $\#27$ to $\#47$. As cavities become bigger, increases in the bulk flow strength are observed; at the same time, the center stagnant regions are also noticed to slightly decrease in size. The bulk flow top regions gradually increase in strength and are able to drive the swirls to reach the far left-side cavity wall at higher magnitudes. On the right column, the cavity opening is constant but the cavity width gradually increases from Case $\#36$ to $\#40$. This time, wider cavities are observed to have weaker bulk flows. In sum, comparing these two cases, increasing the cavity opening enhances cavity bulk flow momentum while increasing the cavity width does the opposite, when maintaining the other cavity dimension constant.

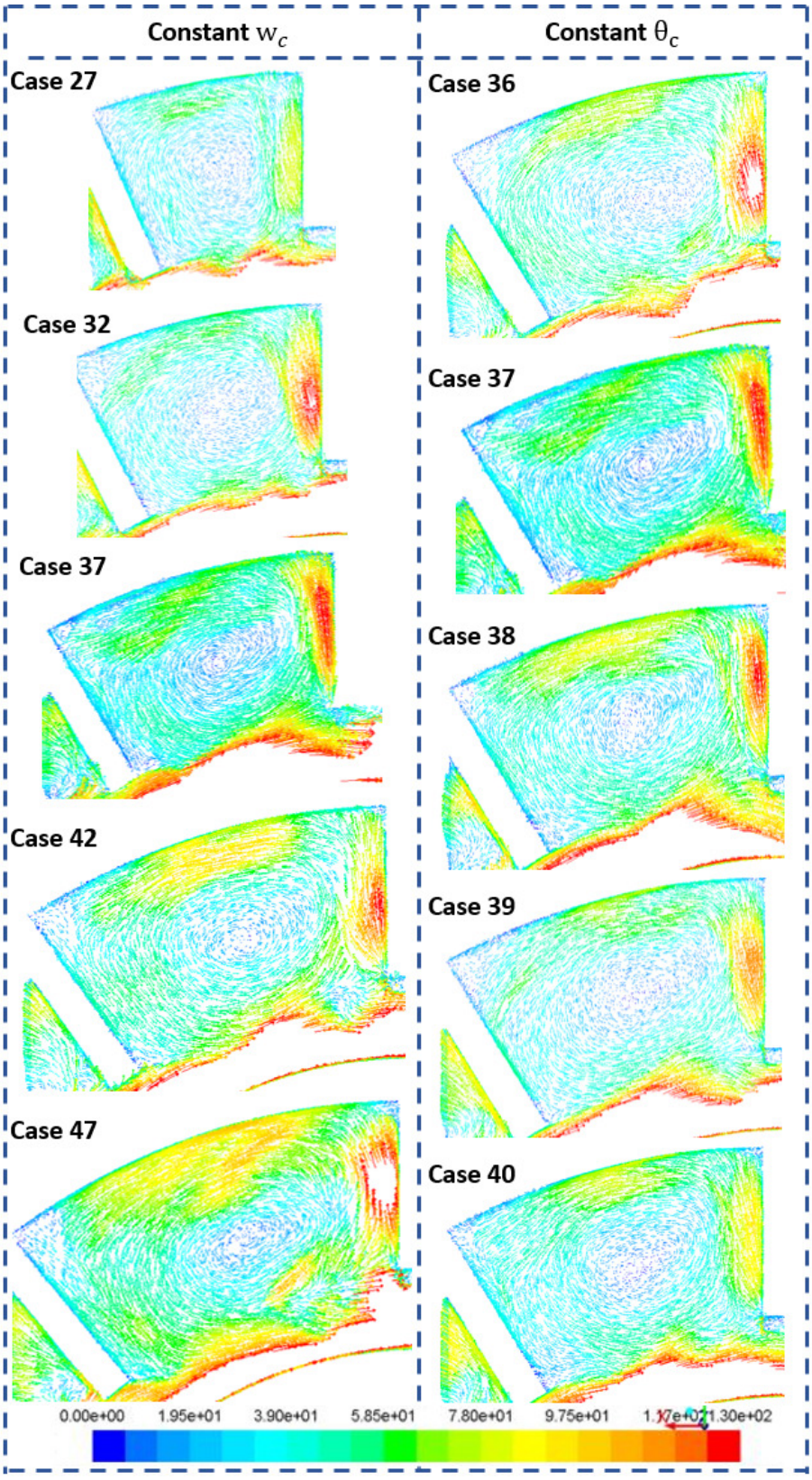

Figure 5.26: Cavity 2 vector plots comparison for (Left) Constant cavity width; (Right) Constant constant cavity opening.

5.4 Conclusion

An analytical algorithm was developed, which offers estimations of the local hydraulic diameter D_h in the defined cavity virtual pipe regions. The method was developed in accordance with the previously proposed virtual pipe description, such that the D_h values are calculated by matching flow characteristics of those of the turbulent internal pipe flows. The method also implemented data processing steps that take the conditions of the raw CFD data into consideration, therefore issues such as uneven element distribution and local outlier values would not lead to unfair comparisons between the experimental and theoretical velocity magnitudes, when used to determine the theoretically 'correct' local bulk flow sizes. Using the analytical algorithm, the cavity flow results are able to reduced to three hydraulic diameters that can be used to represent the regional flow properties.

For the purpose of validating the applicability and the calculation performance of the developed D_h algorithm, two sets of parametric studies were conducted to provide additional cases for investigation. Two types of design parameters were identified and defined, based on the requirements and constraints of large turbo-generator rotor design, which together made the two parametric sets orthogonally related. The parametric cases also offer additional insights on the flow conditions at various design scenarios, to broaden the study of the circumferential cavity for more generic descriptions.

CHAPTER 6

VIRTUAL PIPE HYDRAULIC DIAMETER CORRELATION DEVELOPMENT

6.1 Introduction

This chapter develops an generic, analytical representation of the cavity bulk flow characteristic length D_h, through a parametric experimental study. The work presented in CHAPTER 4 has demonstrated that the cavity bulk flow characteristics correspond to a internal pipe flow analogy. Therefore, this chapter implements this idea to quantify the observed regional bulk flows to the problem of the lack of a characteristic length in order to apply the lumped circuit method for the overreaching goal of an analytical endturn coil temperature predictor. A parametric set of cavity design experiments are constructed, to extend the applicability of the later developed D_h correlations. A quasi-analytical method is proposed, since an exact solution involves solving the three-dimensional Navier-Stokes equations by hand, which is not possible. Thus, the parametric cases are first conducted through CFD simulations and then analytically studied by applying the internal pipe flow analogy.

The proposed quasi-analytically method has three parts. First, the endturn cavities are numerically and parametrically investigated, to explore the change in the cavity bulk flow in respect to the cavity inlet and geometric conditions. Second, local bulk flow length D_h is mathematically calculated by 'matching' extracted CFD velocity profile to that of the fully developed turbulent internal pipe flow. The parametric cases now provide a well-constructed sampling pool in preparation of correlation development. Last, calculated local D_h values are mathematically fitted in terms of the identified design parameters for a

generic, analytically description of the local bulk flow sizes.

6.2 Parametric Study for Rotating Sectors

This section constructs the sampling data set that is gonna to be used for the D_h correlations development. Four design parameters of interest have been identified and 48 experimental cases have been completed, which forms two orthogonal data sets for the inlet and geometric conditions separately as summarized in Tables D.1 and D.2. Additional information is needed here between the two planes, for descriptions of the interactive effects of the design parameters. The overall experimental design break-down follows Figure 6.1.

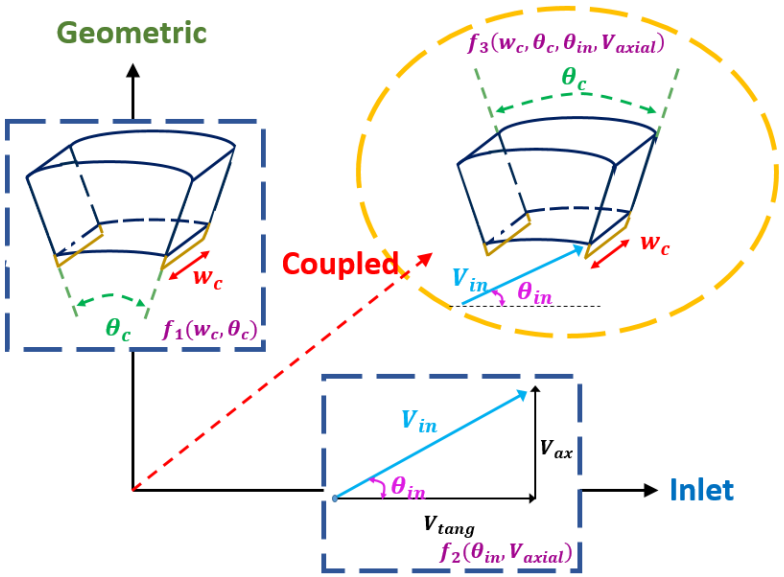

Figure 6.1: Parametric study rank reduction.

The four cavity design parameters are five levels each, which end up with 5^4, or total of 625 cases for the full rank factorial design. It is unrealistic to complete all interactions using the numerical model, even just use the partial endturn model. It takes about 5 hours to complete one simulation, not to mention the additional time would be required to inspect, process, compare and validate the overwhelming data set. Therefore, the coupled cases are designed by using the *fractional factorial design method*, which is developed based on the

'sparsity-of-effects principle'; it states that a system is normally dominated by the main effects and the lower-level interactions, whereas the higher-level interactions are considered confounding/aliasing [93]. Here, the alias structure is developed by using a two-level fractional factorial design at the resolution IV with 2^{k-1} cases [94]. This provides a full three-factor factorial design for the parameters w_c, θ_c, and V_{ax}, while confounding the remaining factor θ_{in} with interactions generated by the relationship $D = ABC$. This method results in the main effects being only confounded with the three-factor interactions to maximize the data resolution. The two-level method is implemented by dividing the five-level parameters into two groups for the fractional factorial study, where *group 1* is at $\pm p$ distance off the nominal value, and *group 2* is at $\pm 2p$ distance off the nominal value. Each group ends up with data located on one 'surface' crossing the two orthogonal planes, and the two surfaces are equally spaced about the centering nominal point $[\widetilde{w_c}, \widetilde{\theta_c}, \widetilde{V}_{ax}, \widetilde{V}_{tang}]$. Now, any scenarios located in-between the sample points can be easily interpolated using this four-dimensional data structure. These extra 16 cases for the circumferential cavities are summarized in Table D.3.

For the purpose of developing a set of experimental data for the development of empirical correlations of the cavity virtual pipe D_h, a total of 66 parametric design cases were conducted for two types, four different parameters at five levels each; the cases were designed to form two orthogonal data set for each type separately, then considered the possibility of interactive reactions by additional coupled cases. The design cases are carried out numerically using ANSYS FLUENT, with the partial parametric endturn cavity model developed in CHAPTER 3 SECTION 3.4. The simulation results were inspected and data were extracted using the extraction method developed in CHAPTER 4; the corresponding local virtual pipe characteristics lengths D_h were calculated with the CFD data using the quasi-analytical method developed in CHAPTER 5. The cavities that present the desired bulk flow properties were recorded and their local D_h values are saved for the next correlation development.

6.3 Virtual Pipe Hydraulic Diameter Correlation Development

This section develops generic, empirical correlations for the virtual pipe local D_h values, in terms of the identified endturn ventilation design parameters [w_c, s_c, v_{ax}, v_{tang}]. The correlations were developed following two paths, namely the *data driven* and the *physics informed* methods. The data driven methods uses the design parameters directly; the physics based methods are different for converting the parameters in terms of pipe flow related thermal-fluidic terms, such as pressure and flow length. Both linear and non-linear models were investigated for these two methods in an attempt to find the most accurate set of correlations that serves the design requirement of being suitable to implement in a fast-solving rotor end-arc temperature predictor.

A general simplification was made before starting the process. The goal of the temperature predictor is to provide estimations of the averaged cooling performance per end-arc coil. Therefore, the averaged hydraulic diameters cross all fours same row cavities were used as the representative flow characteristics D_h when developing the correlations.

$$\overline{D_h} = \frac{1}{n} \sum D_h \mid_i \tag{6.1}$$

The design parameters are transferred to dimensionless format to keep consistent with the common heat transfer terminologies. The normalization processes are different for the data drive and physics informed methods, and are discussed separately later.

A virtual pipe coordinate system s is defined, which travels along the cavity perimeter and follows the directions of the local bulk flows, as shown in Figure 6.2 below. It is assumed that positions at the middle of each edge are the representative local bulk flow locations, and the local flow lengths s_i are the distances that the flow travels until reach these locations, calculated with Equation set 6.2. Since the coil stack height Δr is kept

constant in the design studies, the inlet lengths s_{in} are always constant, but the top and outlet lengths s_{top} and s_{out} vary for the geometric cases and the coupled cases, as the cavity top arc lengths vary with the θ_c values. The flow lengths are constant for the inlet parametric cases.

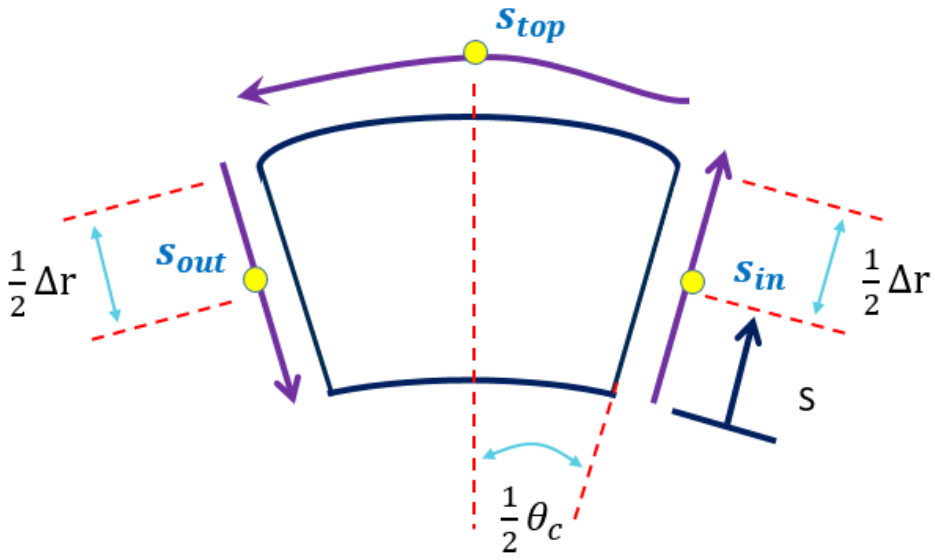

Figure 6.2: Definition of virtual pipe bulk flow flow lengths.

$$
\begin{aligned}
S_i &= \frac{1}{2}\Delta r \\
S_t &= S_i + \Delta S_t = S_i + (\frac{1}{2}\Delta r + \frac{1}{2}\theta_c(R_o - D_h\,|_t) - \frac{1}{2}\,D_h\,|_i) \\
S_o &= S_t + \Delta S_o = S_t + \frac{1}{2}\theta_c(R_o - D_h\,|_t) + \frac{1}{2}\Delta r - \frac{1}{2}\,D_h\,|_o \\
L_{path} &= S_o
\end{aligned}
\tag{6.2}
$$

In addition, changes in the cavity width and cavity opening can be reflected in changes in

the cavity volume, therefore the volume of the defined virtual pipe regions V_i.

$$
\begin{aligned}
V_{in} &= w_c \cdot \Delta S_i \\
V_{top} &= V_{in} + \Delta V_t = V_{in} + (\frac{1}{2}\Delta r - \frac{1}{2}\ D_h\ |_i) + \frac{1}{2}\theta_c(R_o - \ D_h\ |_t) \\
S_{in} &= S_{top} + \Delta S_{out} = S_{top} + (\frac{1}{2}\theta_c R_o + \frac{1}{2}\Delta r) \\
S_c &= L_{path} = 2\Delta r + \theta_c R_o\ V_{vp}\ |_i = \sum\ (w_c \Delta S_i)\ |_i
\end{aligned}
\tag{6.3}
$$

with ΔS_i being the length traveled between the defined virtual locations in Equation 6.2. This has the advantage of eliminating one parameter to simplify the overall equation. *Method 2* correlations have a form of

$$y \sim 1 + x1 + x2 + x3 \tag{6.4}$$

here $x1$ is the combined cavity geometric term, or the bulk flow volume V_i; $x2$ and $x3$ are the flow terms β_{Δ_P} and β_v.

Linear and non-linear relationships were both investigated. The linear correlations are developed using the MATLAB linear regression models *'fitlm'* which outputs functions as a combination of polynomials at the defined order n, in the format shown in Equation 6.5.

$$y = \sum_{n=1}^{n+1} p_i x^{n+1-1} \tag{6.5}$$

where $n + 1$ is the order of the polynomial or number of coefficients to be fit, and n is the degree of polynomial or the degree that gives the highest power of the predictor variable x [95]. The non-linear models available in many forms, but only exponential forms were investigated in this study. For example, for a three variable case, the nonlinear model is expected in the form of

$$y \sim x^a y^b z^b \tag{6.6}$$

where x, y, and z represents the variable of interest, where each has a exponent of a, b, and

c, respectively. The fastest way to determine the exponents is to linearlize the exponential equation by taking the natural-log of both sides of the equation, or as shown in Equation 6.7

$$\begin{aligned} ln(y) &\sim ln(x^a y^b z^b) \\ &\sim a \cdot x + b \cdot y + c \cdot z + constant \end{aligned} \tag{6.7}$$

the linearlized equations is a first order polynomial, which can be easily calculated in MATLAB to find the corresponding coefficients for each parameter.

6.3.1 Mathematically Fitted Method

The first method is to directly fit the experimentally calculated D_h values in terms of the values of the design parameters. The overall process follows the steps shown in Figure 6.3. This method non-dimensionlize the design parameters with respect to the parameter values at the nominal design condition $[R_o, \widetilde{V_{ax}}, \widetilde{\theta_{in}}]$ in Table 5.2.

Two types of correlations are developed following the four steps below, assuming that the design parameters are linearly correlated on the 2nd or the 3rd order.

Step 1: Import the table of the quasi-analytically calculated sampling cases hydraulic diameters D_h and the corresponding design parameter settings, which are in the form shown as below.

$$\overline{D_h} \sim [w_c, \theta_c, V_{ax}, \theta_{in}] \tag{6.8}$$

Step 2: For each bulk flow location, find the average local hydraulic diameters using Equation 6.1 to obtain the set of representative virtual pipe description $[\overline{D_h}\,|_{in}, \overline{D_h}\,|_{top}, \overline{D_h}\,|_{out}]$ for each parametric case. Non-dimensionalize the design parameters to

$$\overline{D_h} \sim [\frac{w_c}{R_o}, \frac{s_c}{R_o}, \frac{V_{ax}}{\widetilde{V_{ax}}}, \frac{\theta_{in}}{\widetilde{\theta_{in}}}] \tag{6.9}$$

where s_c is the cavity arc length, which is the product of the rotor outer diameter R_o and the cavity opening θ_c

$$s_c = \theta_c \cdot R_o \tag{6.10}$$

Step 3: Use the MATLAB command *fitlm* to generate linear polynomial fitting models for D_h, in the form of

$$D_h = f(w_c, s_c, V_{ax}, \theta_{in}) \tag{6.11}$$

Here, the first order linear model is not considered because it cannot capture any interaction between the parameters; the 2nd and 3rd order models are all tested, in the form as Equation 6.13 and 6.12, respectively. For the case of 64 data points, the highest order available is the 3rd order, as a result of the limitation of the degree of freedom.

- Third order linear model:

$$\begin{aligned} y \sim 1 + x_1 + x_2 + x_3 + x_4 + {x_1}^2 + x_1x_2 + {x_2}^2 + \\ x_1x_3 + x_2x_3 + {x_3}^2 + x_1x_4 + x_2x_4 + x_3x_4 + \\ {x_4}^2 + {x_1}^3 + {x_1}^2x_2 + x_1{x_2}^2 + {x_2}^3 + {x_1}^2x_3 \\ + x_1x_2x_3 + {x_2}^2x_3 + x_1{x_3}^2 + x_2{x_3}^2 + {x_3}^3 + \\ {x_1}^2x_4 + x_1x_2x_4 + {x_2}^2x_4 + x_1x_3x_4 + x_2x_3x_4 + \\ {x_3}^2x_4 + x_1{x_4}^2 + x_2{x_4}^2 + x_3{x_4}^2 + {x_4}^3 \end{aligned} \tag{6.12}$$

- Second order linear model:

$$y \sim 1 + x_1 + x_2 + x_3 + x_4 + {x_1}^2 + x_1x_2 + {x_2}^2 + x_1x_3 + x_2x_3 + {x_3}^2 + x_1x_4 + x_2x_4 + x_3x_4 + {x_4}^2 \quad (6.13)$$

Theoretically, the 3rd order model is able to capture higher level interactions than the 2nd order, but at the same time constrains the flexibility of the fitted models, adds more terms and therefore the complexity of the models at the same time.

Step 4: Save the equations and generate the model plots. The plots are generated by MATLAB which create scatter plots of the data along with fitted curves and the corresponding confidence bounds [96].

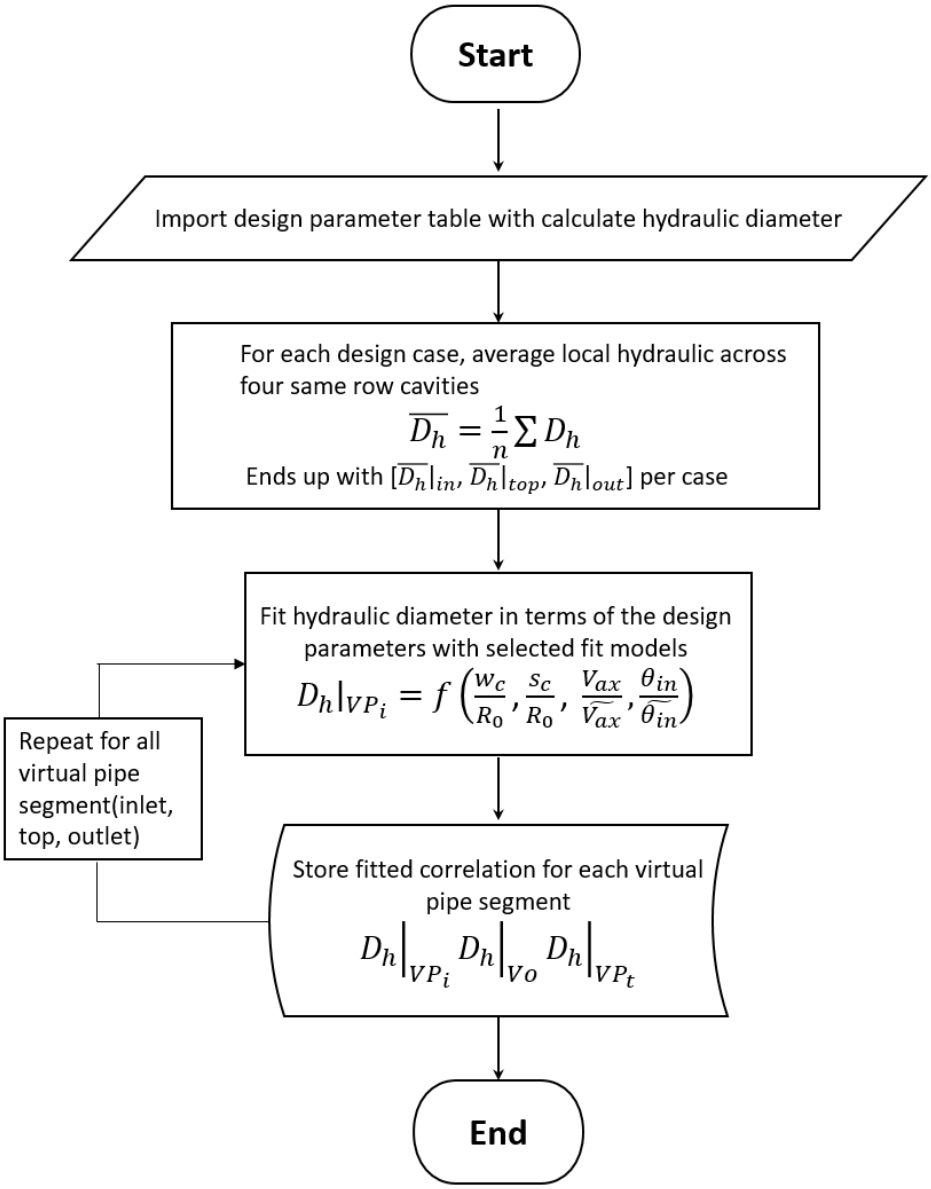

Figure 6.3: Data driven correlation development process

The nonlinear relationships considered here is the exponential format, which is in the general form of

$$\begin{aligned} y \sim & A \cdot {x_1}^{a1} \cdot {x_2}^{a2} \cdot {x_3}^{a3} \cdot {x_4}^{a4} \\ \Rightarrow & ln(y) \sim 1 + a1 \cdot ln(x_1) + a2 \cdot ln(x_2) + a3 \cdot ln(x_3) + a4 \cdot ln(x_4) \end{aligned} \tag{6.14}$$

in this case, $x1$ to $x4$ are the four cavity design parameters, where $a1$ to $a4$ are their coeffi-

cients, respectively. The coefficients are determined by the MATLAB *fitlm* function at the order of $n = 1$. The correlations ar developed following the same process shown in Figure 6.3, except for normalization in STEP 2 needs to take the natural-log the input design parameters and convert them to

$$ln(\overline{D_h}) \sim f_3(ln(\frac{w_c}{R_o}, ln(\frac{s_c}{R_o}), ln(\frac{V_{ax}}{\widetilde{V_{ax}}}), ln(\frac{\theta_{in}}{\widetilde{\theta_{in}}})) \tag{6.15}$$

these new input and output values are then used in STEP 3 at order of 1. This results in the D_h correlations

$$D_h \mid_{predicted} = exp(f_3) \tag{6.16}$$

The three data driven methods discussed above are plotted and shown in Figure 6.4.

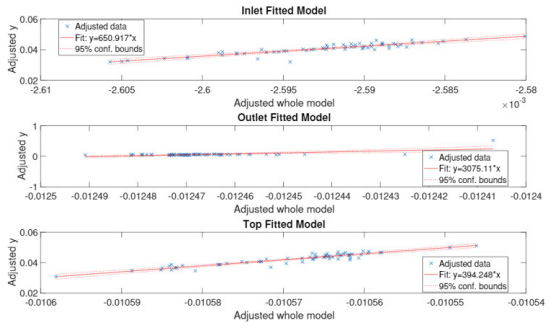

(1) Third-order linear data driven method correlations

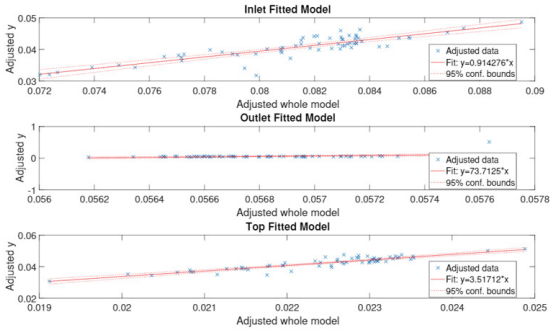

(2) Second-order linear data driven method correlations

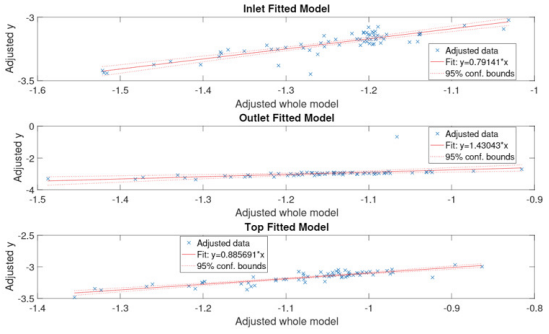

(3) Non-linear data driven method correlations

Figure 6.4: Data driven methods correlations summary.

6.3.2 Physics Based Fitted Methods

The physics based methods are differed from the data driven methods by expressing the original design parameters in the form of physics terms that describe the hydrodynamic effects of the turbulent internal pipe flows. The physics based parameters are defined first. The geometric parameters are modified based on two concepts, which are the definition of hydraulic diameter, and the definition of pipe flow length. The former affects the Reynolds number whereas the latter affects the associated major and minor losses along the defined cavity virtual pipe system. The definition of the hydraulic diameter is the ratio between the area and the wetted perimeter of the flow channel, which both relate to the dimensions of the cavity, as shown in Equation 6.17 below,

$$D_h = \frac{4A}{P} \tag{6.17}$$

For this virtual pipe system, the hydraulic diameter D_h is expressed as the product of flow length s and cavity width w_c, or has a form of as in shown Equation 6.19.

$$D_h = \frac{4(w_c \cdot d)}{2(w_c + d)} \sim {w_c}^p {s_c}^q \tag{6.18}$$

here, d is the size of the parabola in the $r\theta$ plane, which is calculated in the previous power-law fitting process in Equation 5.6. This equation is linearlized by taking the natural-log on both sides to change it to the linear form again, as shown Equation 6.19

$$ln(D_h) = p \cdot ln(w_c) + q \cdot ln(s_c) + constant \tag{6.19}$$

s_c in this equation can be either the local or overall virtual pipe flow lengths, depend on the definition of the individual model.

The inlet parameters are converted to pressure terms. It is known from the basic flow

knowledge that in any pipe system, flow distributions are driven by the pressure terms. Following this concept, the changes in the inlet conditions can be expressed as the result of changes in the annulus flow momentum, as shown in Equation 6.22

$$\beta_{dP} = \frac{\Delta P_r}{\widetilde{\Delta P_r}} = \frac{(p_{tot} - p_{tang})_i}{(p_{tot} - p_{tang})_{nom}} \tag{6.20}$$

where pressure is related to the local velocities as

$$P_i = \frac{1}{2}\rho V^2 \tag{6.21}$$

here, P_{tang} is proportional to the tangential velocity V_{tang}, and P_{tot} is proportional to the relative velocity magnitude V_{mag}.

Last, the strength of the tangential velocity reaches the bottom of insulation blocking determines the pumping power available to enter the cavity, which is similar to that of the axial fan blade and affects the virtual pipe inlet region and thereafter. Therefore, the relative momentum strength between the available pumping power and the available overall dynamic head in the annulus is also important, which is calculated as

$$\beta_v = \frac{P_{tang}}{P_{tot}} \tag{6.22}$$

In sum, the physics based parameters are summarized in Table 6.1 below.

Table 6.1: Summary of proposed physics based design parameters

Definition		Symbol
Geometric	Cavity width	w_c
	Bulk flow length	s_i
	Virtual pipe width	d_i
Inlet	Change in difference in pressure	β_{dP}
	Pressure ratio	β_v

Now that the physics based parameters are defined, they are fitted following two methods. *Method 1* considers the formation of the virtual pipe as the combined effects of the cavity width and flow length, in the form shown in Equation 6.23; *Method 2* considers the geometric and inlet conditions as successive reactions, where the cavity dimensions first build the foundation of the virtual pipes, then the inlet conditions make further adjustments on the properties of the local virtual pipe regions, in the form shown in Equation 6.24.

Method 1:

$$D_h = f(w_c, s_c, V_{ax}, \theta_{in}) \tag{6.23}$$

Method 2:

$$D_h = f(w_c, s_c) \cdot g(V_{ax}, \theta_{in}) \tag{6.24}$$

The method 1 correlations are developed following the process shown in Figure 6.5; the four steps are similar to the ones discussed for the *data driven method* in the previous section, except for the non-dimensionlization process in STEP 2. Two types of correlations are developed, where Type 1 uses all four identified design parameters and Type 2 are three-parameter correlations that employ the concept of local bulk flow volume V_i. Since the hydraulic diameter is defined to be the product of w_c and s_c terms in all physics based methods, the correlations have to use the nonlinear relationships. The case values are

therefore non-dimensionlized as shown in Equations 6.25.

$$\begin{aligned} &\textbf{Type 1: } ln(\overline{D_h}) \sim f\left(ln(\frac{w_c}{R_o}), ln(\frac{S_i}{\tilde{S}_i}), ln(\beta_{\Delta_P}), ln(\beta_v)\right) \\ &\textbf{Type 2: } ln(\overline{D_h}) \sim f\left(ln(\frac{V_i}{\tilde{V}_i}), ln(\beta_{\Delta_P}), ln(\beta_v)\right) \end{aligned} \tag{6.25}$$

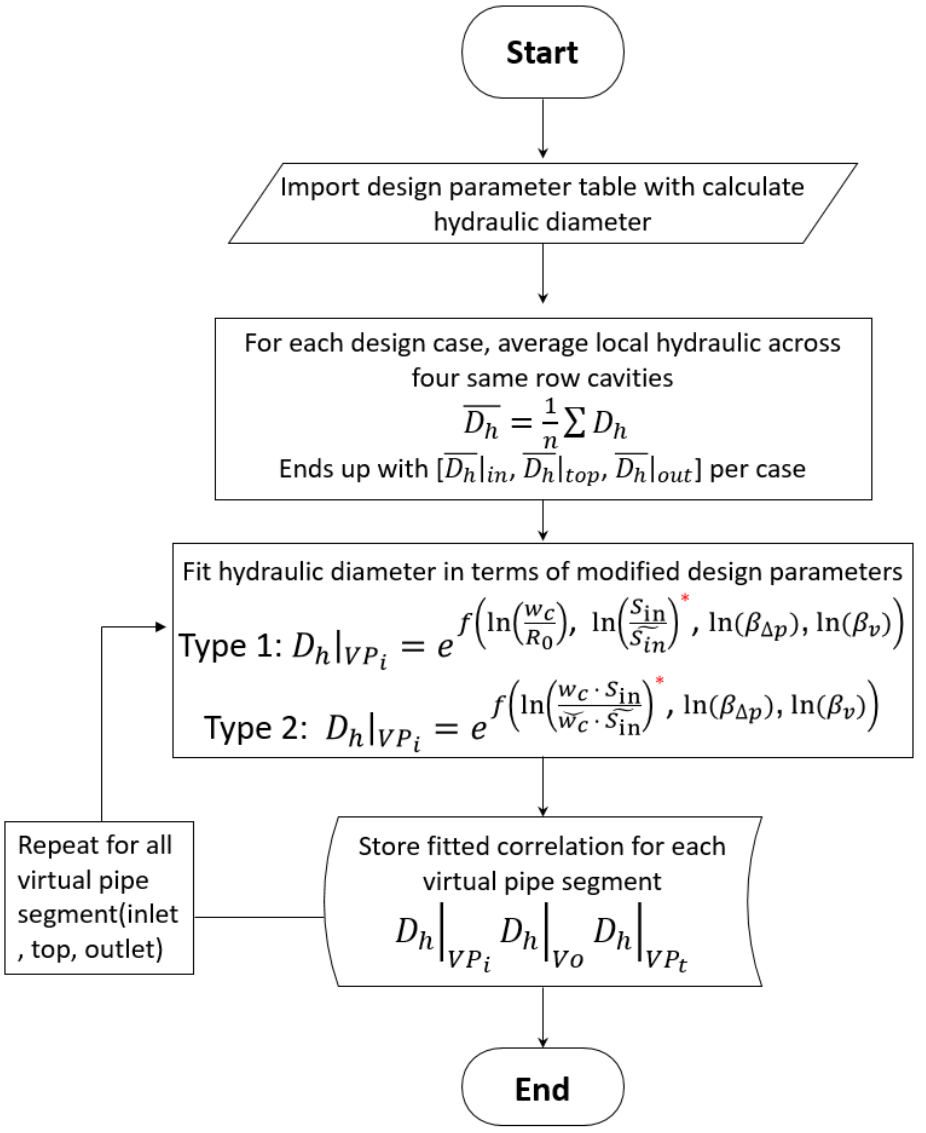

Figure 6.5: Physics based method 1 correlation develop process.

Method 2 considers the orthogonal effects of the inlet and geometric parameters as separate contributing factors, therefore the correlations are developed separately, following the six steps shown in Figure 6.6, which ends up with one correlation that predicts a $D_h\mid_{geo}$ based on the cavity geometry first, and another correlation $\delta\mid_i$ for the inlet parameters. The second term will only be applied if and only if there is a change in the inlet condition, with respect to the nominal condition. The steps are repeated for all three virtual pipe locations.

Step 1: Import the table of the quasi-analytically calculated sampling cases hydraulic diameters D_h and the corresponding design parameter settings, which are in the form shown as below.

$$\overline{D_h} \sim [w_c, \theta_c, V_{ax}, \theta_{in}] \tag{6.26}$$

Step 2: For each bulk flow location, find the average local hydraulic diameters, $\overline{D_h}$, using Equation 6.27

$$\overline{D_h} = \frac{1}{4}\sum \overline{D_h}\mid_i \tag{6.27}$$

here, $\overline{D_h}\mid_i$ is the calculated value for each cavity to obtain the set of representative virtual pipe description $[\overline{D_h}\mid_{in}, \overline{D_h}\mid_{top}, \overline{D_h}\mid_{out}]$. Non-dimensionlize the parameters uses Equation 6.25.

$\Rightarrow$ **Develop** $D_h\mid_{geo}$

Step 3: The first part of this method uses the 23 valid geometric cases only, to develop an equation in a form of

$$\begin{aligned} D_h\mid_{geo} &= e^{f(ln(\frac{w_c}{R_o}),ln(\frac{s_i}{s_i}))} \\ &\sim 1 + x_1 + x_2 + x_1x_2 + x_1^2 + x_2^2 \end{aligned} \tag{6.28}$$

the function f is developed using the first order linear model. The geometrically determined local hydraulic diameter is therefore

$$D_h \mid_{geo} = e^{\left(ln(\frac{w_c}{R_o}), ln(\frac{s_i}{\bar{s}_i})\right)} \tag{6.29}$$

$\Rightarrow$ **Develop** $\delta \mid_{in}$

Step 4: The second part uses the remaining 41 cases to develop the correction factor δ which is designed to capture the additional changes in flow that are caused by the changes in the inlet parameters. This δ is the ratio between the experimentally calculated 'correct' values, and the geometrically predicted values from the correlation $D_h \mid_{geo}$ in step 3.

$$\delta = \frac{\overline{D_h} \mid_{CFD}}{\widetilde{D_h} \mid_{geo}} \tag{6.30}$$

The correlation is developed using the linear model and is in the form of

$$\begin{aligned} ln(\delta) =& g(ln(\beta_{\Delta_p}), ln(\beta_v)) \\ & \sim 1 + x_1 + x_2 + x_1 x_2 + x_1^2 + x_2^2 \end{aligned} \tag{6.31}$$

and the ratio is calculated as

$$\delta = e^{g\left(ln(\beta_{\Delta_p}), ln(\beta_v)\right)} \tag{6.32}$$

Step 5: The overall prediction correlation is the product of the geometric and inlet correlations, in the form of

$$D_h = D_h \mid_{geo} \cdot \delta \mid_{in} \tag{6.33}$$

Step 6: Repeat step 3 to 5 for the top and outlet regions, and save the correlation and generate the model plots.

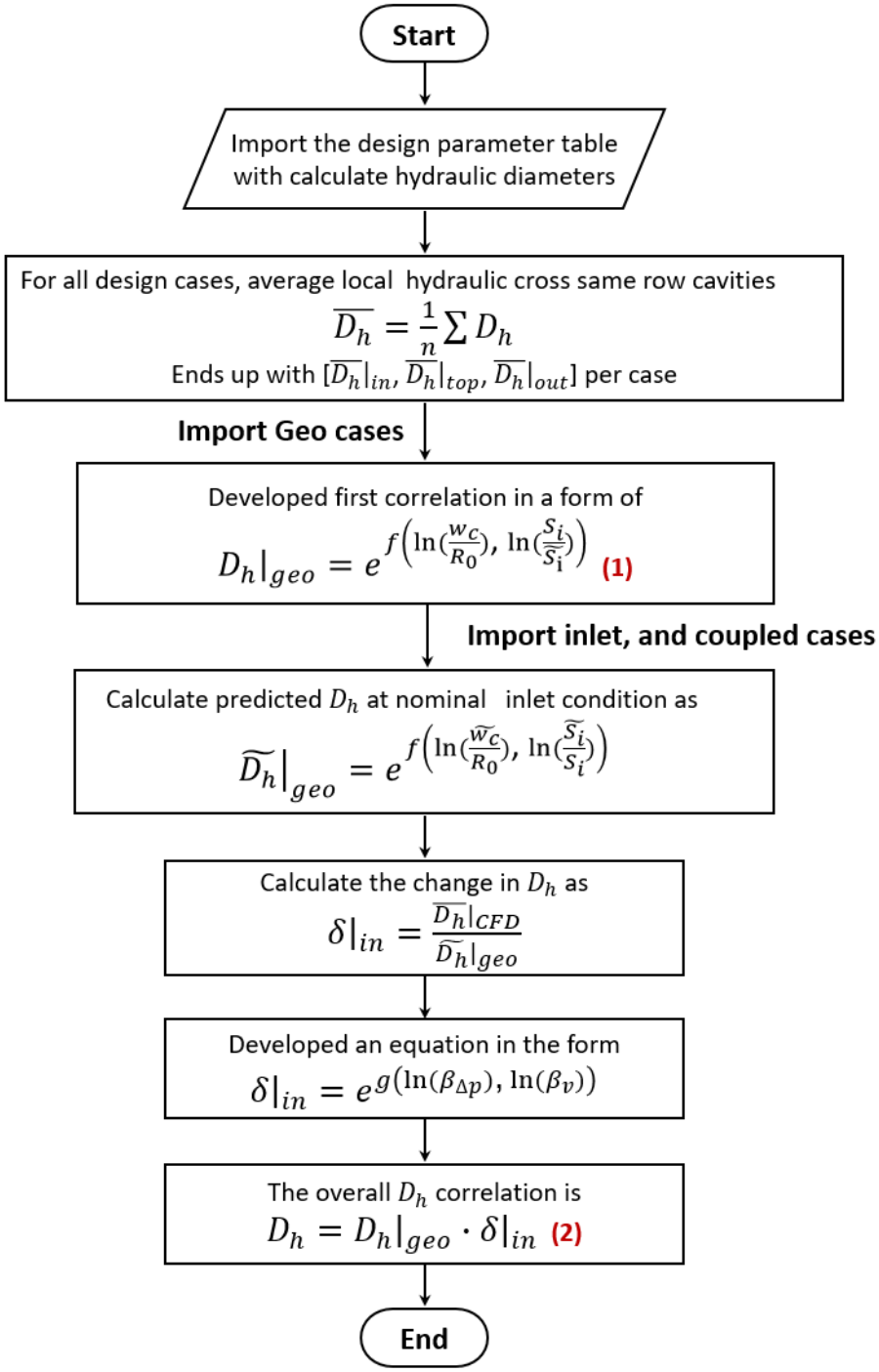

Figure 6.6: Physics based method 2 correlation development process.

The correlations are plotted and shown in Figure 6.7 below.

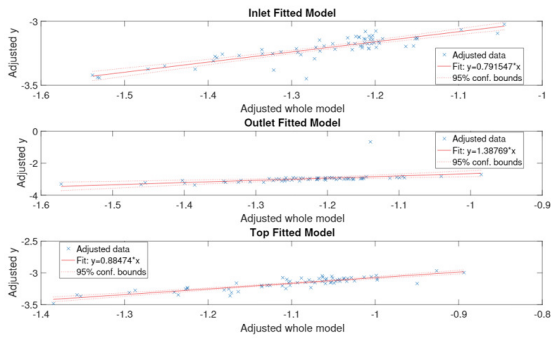

(1) Physics based method 1.1 correlations

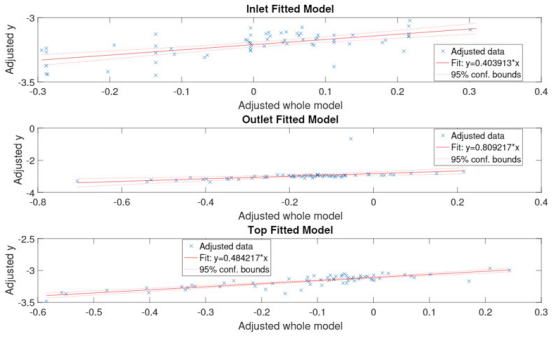

(2) Physics based method 1.2 correlations

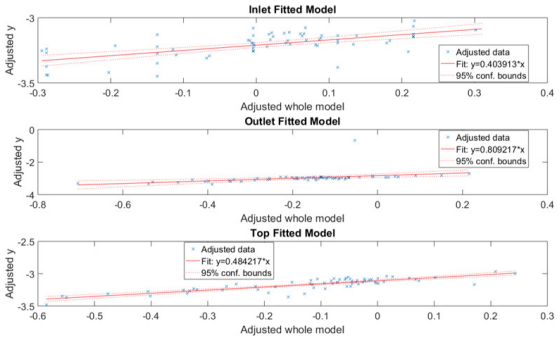

(3) Physics based method 2.1 correlations

Figure 6.7: Physics based methods correlations summary.

Up to here, six types of equations are developed that can be used to predict the local hydraulic diameters for the proposed cavity virtual pipe flow system. Their performances are tested using additional validation cases and is discussed in the next section. The most accurate and yet practical correlation method that satisfies the design requirements for the copper temperature predictor is chosen.

6.3.3 Validation Experiments

Now that empirical D_h correlations are developed, validation cases are needed to test their efficacy and accuracy, and to determine the set of correlations that provide the desired predictions that best serve the design requirements of the final rotor end-arc coil temperature predictor. The validation cases are designed following the same case break down

scheme as is shown in Figure 6.1, which ends up with 5 geometric only cases, 5 inlet only cases and 7 coupled cases. This 17 cases were given random parameter values that were within the defined parameter ranges. These cases were experimentally studied using the three-row endturn cavity model developed in CHAPTER 3 SECTION 3.4. The CFD results were extracted following the extraction method in CHAPTER 4 Figure 4.25, and the local bulk flow hydraulic diameters D_h were calculated using the quasi-analytical method developed in CHAPTER 5.

6.4 Results

The previous section develops mathematical correlations for the cavity local bulk flow characteristic lengths D_h. This section continues the correlation development study by comparing their prediction accuracy using the validation cases, to determine the goodness of the correlations. The most accurate and reasonable correlation type is chosen to use in the thermal-fluidic network in the next Chapter.

In addition, this section also introduces a preliminary experimental investigation of the possible effects of the changes in cavity height on the cavity local bulk flow conditions, only to provide insights on how the changes in rotor coil construction may affect the rotor ventilation design, and to address the applicability of the proposed virtual pipe method on different coil stack heights.

6.4.1 Correlation Comparison and Validation

The previous section introduces six different possible expressions to predict the local D_h values. This section determines the most appropriate method by evaluating the goodness of the predictions. The predictions are evaluated by a set of performance parameters, which are quantifiable values that demonstrate how the errors in D_h predictions reflect the thermal-fluidic network calculations of the corresponding local flow properties, such as the

Reynolds number and the Nusselt number. These performance parameters are calculated for the prediction results of the 17 validation cases. The method that has the superior overall performances is chosen to use in the final rotor coil temperature predictor.

The most commonly used and practical performance parameter is accuracy. In this case, prediction accuracy is the error between the correlation predicted values and the experimentally determined values that are calculated using the proposed, iterative power-law curve fitting algorithm. Prediction error is calculated following Equation 6.34.

$$\varepsilon = \frac{\overline{D_h}\mid_{CFD} - \hat{D}_h\mid_p}{\overline{D_h}\mid_{CFD}} \cdot 100\% \tag{6.34}$$

note that $\overline{D_h}\mid_{CFD}$ is the averaged CFD hydraulic diameter cross all of the four mid-row cavities in the segmented parametric CFD model; $\hat{D}_h\mid_p$ is the correlation predicted value. The allowable range of ε is defined in terms of the resulting error in the final temperature prediction networks.

The accuracy of the hydraulic diameter prediction is especially important because it is directly applied in the thermo-fluidic calculations that determines the flow properties and the associated heat transfer rate. For the internal pipe flow at constant flow rate Q, D_h determines to the Reynolds number Re_D

$$Re_D = \frac{\rho V D_h}{\mu} = \frac{Q}{A}\frac{D_h}{\mu} \tag{6.35}$$

here, ρ and μ is the local air density and kinematic viscosity, respectively, which are based on the local air temperature. The averaged velocity V is calculated as the ratio between the mass flow rate Q and the cross-sectional area A. The Reynolds number determines the Nusselt number, as calculated in Equation 6.36, which is the key factor that determines the heat transfer rate.

$$Nu_D = 0.023{Re_D}^{4/5}Pr^n \tag{6.36}$$

here, as a preliminary estimation of the virtual pipe Nusselt number, Dittus-Boelter correlation for fully developed internal turbulent pipe flow is used. Pr is the Prandtl number, which is also temperature dependent. Finally, the Nusselt number determines the heat transfer coefficient h, as

$$h = \frac{q''}{T_w - T_\infty} = \frac{Nu_D k}{D_h} \tag{6.37}$$

where k is the thermal conductivity. Heat transfer coefficient h can also be calculated based on the Fourier's law, which is the ratio between the surface heat flux q'' and the temperature difference between the wall T_w and the cooling air T_∞. Combine and rearrange Equations 6.35, 6.36 and 6.38, the targeted wall temperatures T_w can be calculated in the form of shown in Equation 6.38, which is in terms of the bulk flow size D_h.

$$T_w = \left(\frac{q'' \cdot {w_c}^2}{0.046(\frac{Q}{\nu})^{4/5} Pr^n k}\right)\left(\frac{{D_h}^{6/5}}{(w_c - \frac{D_h}{2})}\right) + T_\infty \tag{6.38}$$

here, in order to demonstrate the relationship between the error in D_h and the error in T_w, it is assumed that at each virtual pipe location of interest, all the terms except for D_h in Equation 6.38 above are pre-determined, constant values that are independent of the D_h value. More specifically, the local flow properties, T_∞, Pr, k, ν and rho are solely dependent on the four design parameters $[w_c, \theta_c, V_{ax}, V_{in}$. It is also assumed that the volumetric flow rate $\dot{V}$ of bulk flow in the studied cavity internal virtual pipe system is solely dependent on the annulus flow conditions; therefore the virtual pipe mass flow rate $Q = \rho\dot{V}$ is always conserved, regardless of the size of the local pipes. In addition, w_c is the cavity geometry and q'' is the cavity surface heat flux, and are both constant for all parametric cases. Therefore, the changes in wall temperature prediction is strictly restricted by the accuracy of the bulk flow characteristic length D_h. Thus, Equation 6.38 above can be rearranged as

$$\Delta T_w = A \cdot \frac{\Delta {D_h}^{6/5}}{(w_c - \frac{\Delta D_h}{2})} + B \tag{6.39}$$

here A and B are dummy variables representing two constants. Therefore, the errors in the wall temperature calculations ΔT_w are estimated based on the percentage error prediction in the virtual pipe ΔD_h, using Equation 6.39, on an $\pm 5\%$ interval basis as shown in 6.8 below.

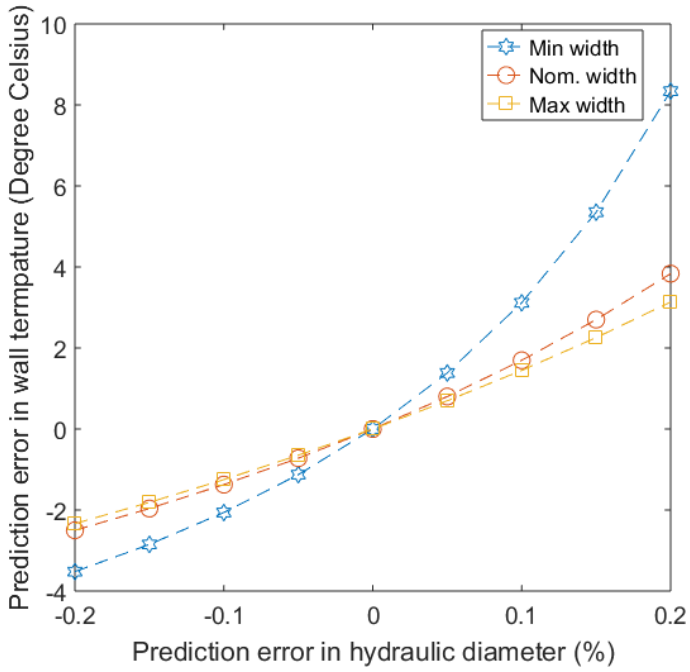

Figure 6.8: Error in wall temperature with respect to percentage error in hydraulic diameter calculation

This plot presents the estimated errors in the wall temperature prediction for three different widths w_c. At the same cavity width, over-predicting in local D_h results in over-predicting in wall temperature, and vise versa; over-predicting D_h also results in higher absolute T_w errors than under-predicting. At the same percentage D_h error, the thinnest cavity has shown the highest prediction errors; the T_w errors also grow exponentially as the cavity width decreases. Therefore, theoretically increasing the width of the cavity helps to lower the resulting error in wall temperature prediction at the same D_h prediction. In addition, this plots indicates that in order to achieve desired wall temperature errors within $\pm$ 5 degrees Celsius, errors in the D_h predictions should be restricted within 10%. 10% is taken to allow additional error propagation that may occur in the thermal-fludic networks, as the

result of the simplifications and assumptions taken in the endturn nested cavity system. In addition, judging from the service perspective, a temperature predictor that over-predicts the wall temperature is more practical in order to avoid over-loading the rotor or imposing high safety factors, therefore is preferred. Taken all of above into consideration, the following performance parameters are used in this study to address the goodness of the correlations:

1. **Accuracy:** To ensure accuracy in overall rotor coil temperature predictions, errors of D_h predictions are limited to $\pm 10\%$.

2. **Success rate:** The probability that correlation predicted D_h values have errors within $\pm 10\%$ (or $P_\varepsilon|\varepsilon < 10\%$).

3. **In-bound prediction performances:** (1) The smaller the prediction errors, the better the correlations are. Here is judged by the mean error $\bar{\varepsilon}$ and the maximum absolute error $|\varepsilon|_{max}$. (2) The probability of over-predicting vs. under-predicting in wall temperature $P_\varepsilon|\varepsilon < 0\%$: For the wall temperature predictions to be informative, over-estimating is preferred and so does D_h.

Now that the expected D_h prediction performances are specified, the six fitting methods can be compared and discussed by comparing results from 17 validation cases as summarized in Table D.3. The three virtual pipe D_h values are calculated using the analytical algorithm presented in CHAPTER 5, and the values are treated as the correct hydraulic diameter values. Local hydraulic diameters are also estimated using the developed correlations and the prediction errors are calculated and plotted, for the inlet, top and outlet regions separately, as shown in Figure 6.9.

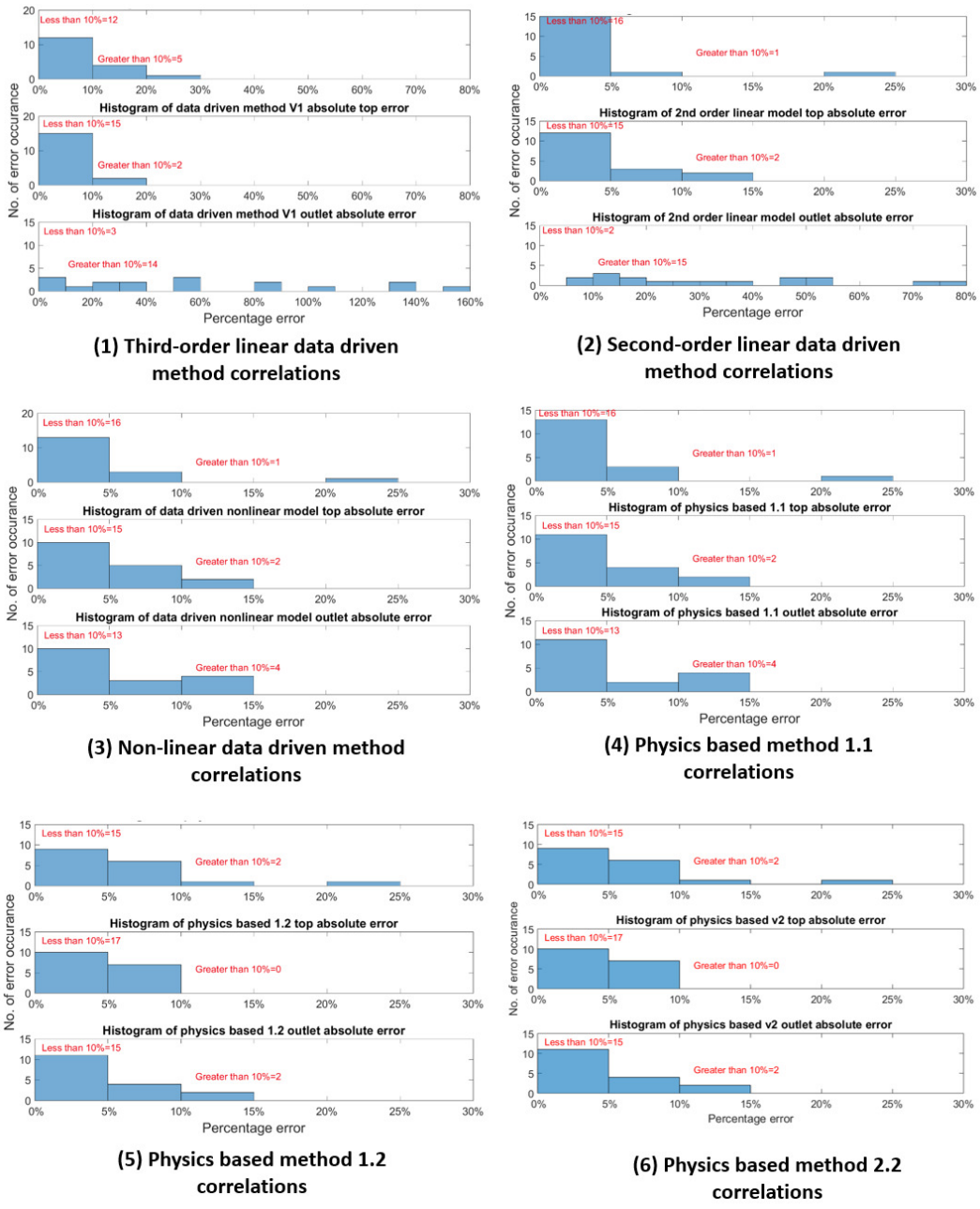

Figure 6.9: Summary of fitting models histograms.

The correlation prediction performance parameters are summarized in Table 6.2 below. Here, N_t is the number of validation cases; N_s is the number of success cases (or within $\pm 10\%$; $|\varepsilon|_{max}$ is the absolute maximum error; $P_\varepsilon|\varepsilon < \pm 10\%$ is the probability of correlation to achieve $\pm 10\%$; $P_\varepsilon|\varepsilon < 0\%$ is the probability of over-predicting; and $\bar{\varepsilon}$ is the mean of the prediction errors of the success cases N_s.

Table 6.2: Summary of correlation prediction performances

Location	Method		N_t	N_s	Max error $\|\varepsilon\|_{max}$ [%]	$P_\varepsilon\|\varepsilon < \pm 10\%$	$P_\varepsilon\|\varepsilon > 0\%$	Mean error $\bar{\varepsilon}$ [%]
Inlet	**Data**	**3rd order**	17	12	21.7	70.6	41.2	3.7
		2nd order	17	16	22.6	94.1	52.9	2.6
		Nonlinear	17	16	22.1	94.1	29.4	2.7
	Physics	**Method 1-1**	17	16	22.1	94.1	35.3	2.7
		Method 1-2	17	15	21.4	88.2	35.3	3.7
		Method 2	17	16	22.1	94.1	35.3	2.7
Top	**Data**	**3rd order**	17	15	14.4	88.2	0	4.2
		2nd order	17	15	12.2	88.2	0	2.9
		Nonlinear	17	15	12.5	88.2	0	3.9
	Physics	**Method 1-1**	17	15	12.1	88.2	0	3.9
		Method 1-2	17	17	9.7	100	0	4.5
		Method 2	17	15	12.1	88.2	0	3.9
Outlet	**Data**	**3rd order**	17	3	153	17.7	11.8	5.5
		2nd order	17	2	77.1	11.8	0	5.9
		Nonlinear	17	13	12.5	76.5	29.4	3.8
	Physics	**Method 1-1**	17	13	13.9	76.5	29.4	3.6
		Method 1-2	17	15	11.8	88.2	29.4	3.9
		Method 2	17	13	13.9	76.5	29.4	3.6

The *max* $\%$ *error* value first rules out the *3rd order* and *2nd order* data driven method for both having absolutely unacceptable prediction errors of 153% and 77.1% in the outlet region. These two methods happens to have the maximum absolute in-bound average error as well. Among the remaining correlations, the *physics based method 1-2* is chosen for having an superior combined performance matrices and the simplest format, and the correlations are shown in Equation 6.3. The applicable range of the equations are summarized in Table 6.3, and note that the regional Reynolds number applies to values calculated using

the proposed virtual pipe method.

$$\begin{aligned}
\text{Inlet}: \quad & D_{h,in} = 0.111(\frac{w_c}{R_o})^{0.411}(\frac{s_i}{R_o})^{0.675}(\beta_{\Delta P})^{0.0349}(\beta_v)^{0.0229} \\
\text{Top}: \quad & D_{h,top} = 0.112(\frac{w_c}{R_o})^{0.401}(\frac{s_i}{R_o})^{0.784}(\beta_{\Delta P})^{0.0810}(\beta_v)^{0.0284} \\
\text{Outlet}: \quad & D_{h,out} = 0.282(\frac{w_c}{R_o})^{0.673}(\frac{s_i}{R_o})^{1.19}(\beta_{\Delta P})^{0.187}(\beta_v)^{-1.058}
\end{aligned} \tag{6.40}$$

Table 6.3: Applicable range of D_h correlations

Parameter	**Applicable Range**
Cavity Width w_c (mm)	30$\leq w_c \leq$50
Cavity opening θ_c (degree)	23$\leq \theta_c \leq$39
Inlet axial velocity V_{ax} (m/s)	37$\leq V_{ax} \leq$49
Inlet angle θ_{in}	28$\leq \theta_{in} \leq$48
Virtual pipe Reynolds number Re_{VP}	8E4$\leq Re_{VP} \leq$5E5

Even though *physics based 1-2* can achieve the level of accuracy and prediction requirements specified, the R-squared values of this method are found to be approximately 80% for the inlet, top and outlet regions, respectively. This indicates that not all of the 4th order interactions between the parameters are negligible in the mathematical descriptions of the local virtual pipes. Therefore, the performances of the correlation can be further improved by increasing the size of the sampling set, to allow for higher degree of freedoms, and expanding the correlation formats to the 4th order. But it is not required for the presented study since the current model already meets the design requirements of ± 5 Celsius in the wall temperature error.

6.4.2 Cavity Height Study

Now that the flexible design parameters are studied and mathematical descriptions of the bulk flow characteristic lengths D_h have been developed and validated, this last section

broaden the study of the endturn circumferential cavity to the previously identified, more strictly constrained cavity height Δr. This section only interests in variations applied at the coil inner diameter R_c, while keeping the height of the insulation blocking Δr_b and rotor outer diameter R_o constant. Figure 6.10 below presents the change in geometry that is an example of increasing the coil inner diameter from R_c to R'_c, to decrease the coil height and increase the extrusion thickness.

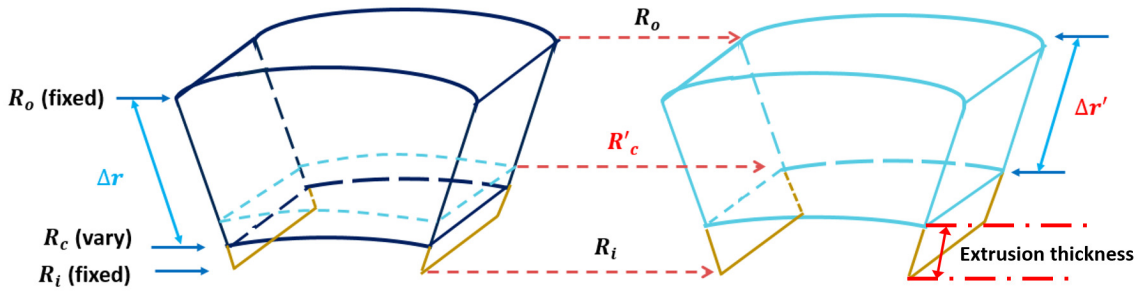

Figure 6.10: Demonstration of change of coil stack height

Changes in the cavity height Δr are of interest since it is expected to affect the cavity bulk flow conditions by changing the amount of pumping momentum at the inlet of the cavity. It is suspected that the blocking in annulus performs similar to that of a radial blade fan, which generates local pressure build-up and additional pumping force into the cavities. Therefore, even though longer 'blades' results in smaller cavity cooling volume, but at the same time are expected to obtain higher pumping power that may result in stronger virtual pipe inlet flows. The extrusion thickness is also another major difference in flow conditions comparing to that discussed by Hayase, et al. [89], where the annulus flow enters the cavity is only the result of the rotational motion. The effects of this pumping length are not studied yet due to the limitations on rotor coil design discussed in CHAPTER 1, but it is still interested to test this 'radial blade fan' theory and to investigate the possibility of improving cavity cooling performances by varying the lengths of coil stack heights.

To study this blocking pumping effect, the previously failed geometric case (case # 49) is used for demonstration, where changes in the bulk flow conditions are expected to

be more obvious. If the pumping theory is valid, evident improvements in the bulk flows should present when the extrusion thicknesses are increased. It is expected that eventually at some point, the bulk flow is able to reaches the defined outlet edge and obtain the desired cavity bulk flow characteristics. To do so, five cases were compared that includes the nominal case at the pumping length of $10\ mm$, with an additional four cases with the extended extrusion lengths at an increment of $3\ mm$ each, up to a maximum length of $22\ mm$. Note that at the same field current condition, changes in the coil heights result in changes in the surface heat fluxes, which are adjusted accordingly for the extra four cases, as listed in Table 6.4. The original four cavity design parameters, namely the width w_c, cavity opening θ, inlet angle θ_{in} and inlet axial velocity V_{ax} are all kept at the nominal values. The parametric three-row endturn CFD model developed in SECTION 3.4.1 is used to conduct the simulations.

Table 6.4: Summary of heat conditions for the cavity height cases.

Type	R_in	Nominal q"
Nominal (Geo DP24)	0.383	1.000
Case 1	0.386	1.023
Case 2	0.389	1.048
Case 3	0.392	1.073
Case 4	0.395	1.100

vector field plots of leading cavity 1 for the above five cases are compared, since they are expected to have the most significant changes in the bulk flow phenomenon, as shown in Figure 6.11. As pumping lengthes increase from the nominal case of $10mm$ to the maximum of $3mm$ at case 4, the outlet bulk flows are significantly improved in both magnitudes and distribution. The bulk flow is able to reach the defined outlet side of the cavity once the pumping lengths are increased, and the local velocity magnitudes increase at the same time. This indicates that increasing the pumping length improves the initial

bulk flow momentum and therefore the cavity bulk flow strengths.

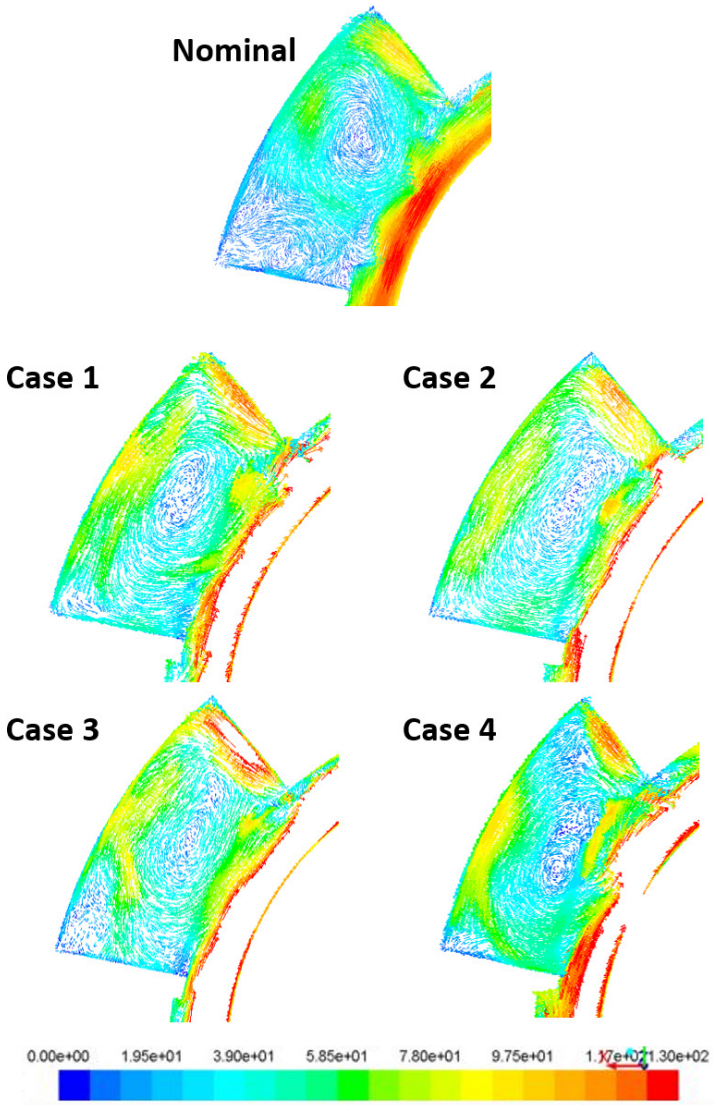

Figure 6.11: Vector field plots comparison

The averaged cavity bulk flows performances were studied with the normalized velocity profiles. The four-cavity averaged profiles are compared and are as shown in Figure 6.12. These velocity profiles still present the flow characteristics required to meet the cavity virtual pipe descriptions. With the required flow phenomenon and properties, the CFD results can be extracted and process with the extraction method; local flow characteristics lengths can be both experimentally and analytically determined using the calculation algorithms developed before. Therefore, for cases with small variations in the coil stack

heights, it is still possible to use the D_h correlations to quantify the sizes for the virtual pipe regions.

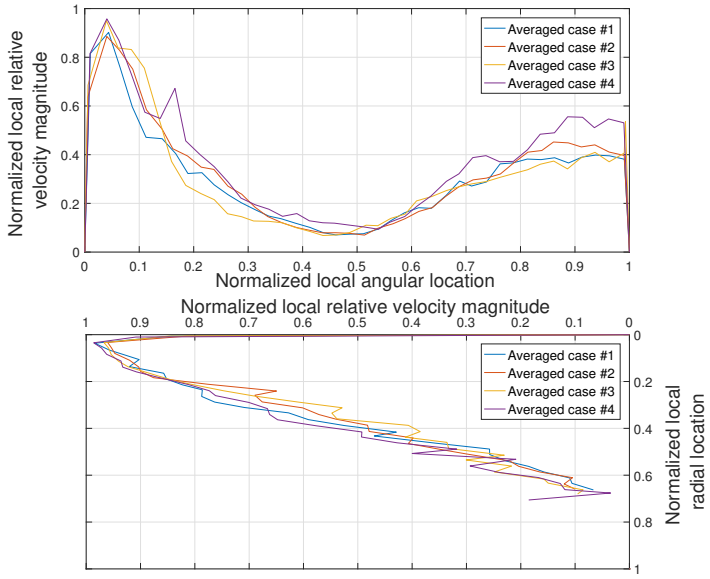

Figure 6.12: Averaged velocity profile comparison

6.5 Conclusion

Empirical correlations were developed for the three identified virtual pipe locations, to calculate their hydraulic diameters D_h, using a set of sampling data obtained from a parametric study. The experimental data consisted of two sets (25 cases each) that vary in each type of parameter individually; an additional set that consisted of coupled design cases that provides information on the inter-related relationships between the two types of parameters. Initially, six correlations were developed, which considered linear versus nonlinear relationships between the parameters, for either direct mathematical data fit of the sampling points, or physics informed methods that reconstruct the forms of the design parameters before mathematical fitting. The correlations were evaluated by four prediction performance parameters, which indicated that the physics based method 1.2 is the superior choice. The selected correlations create the most consistent and desirable performance, that

best satisfy the requirements of the final endturn temperature predictor. With these correlations, the sizes of the bulk flows can be quickly quantified to allow the use of textbook empirical correlations to construct thermal-fluidic networks, and therefore to implement the fast-solving analytical lumped circuit method for the development of the final temperature predictor in the next chapter.

During the parametric study, it was noticed when cavity size becomes too big, the nominal rotor inlet design can no longer provide enough strength in flow to form complete peripheral swirls in the cavities, therefore the flow phenomenon is no longer qualified to be described with the concept of virtual pipe. Aside from manipulating the inlet flow, another possible remedy is to increase the initial cavity pumping momentum by increasing the length of the annulus blocking. The blocking is suspected to work similar to a fan blade that creates more radial flow momentum at a higher length. A preliminary investigation had validated this idea, which presented fixed cavity swirls at shorten coil stack heights δr, or lengthen 'blade length' (at the fixed outer diameter value). The coil height cases tested only vary within $\sim 8\%$ of the original coil stack height, of which the flow results present the bulk flow properties needed in order to use the previously developed extraction method and quasi-analytical D_h algorithm; therefore, it is reasonable to conclude that at design variations within this δr range, the correlations are still valid.

CHAPTER 7

ENDTURN COPPER TEMPERATURE PREDICTOR

7.1 Introduction

This chapter develops a generic, fast-solving analytical temperature predictor to calculate the rotor end-arc temperatures. The rotor coils generate high heat during operation and need to be effectively cooled; temperature management of the end-arc length of the coils is especially important to prevent rotor failure. The lack of a fast-solving and accurate temperature predictor in the past has limited the rotor's ability to perform at its highest potential; this study aims to solve this problem. The previous chapters have developed a description of the observed cavity bulk flows, namely the virtual pipe method, which is comparable to the turbulent internal pipe flows; mathematical representations of the cavity bulk flow parameters D_h were also developed. The knowledge of the cavity's internal flows has enabled us to develop the design analytical predictor by using the analytical lumped-circuit method, and constructing thermal-fluidic networks that follow the descriptions of the proposed virtual pipes' cavity bulk flow and obtain textbook empirical correlations.

This chapter first describes a thermal-fluidic network, for the single cavity virtual pipe and for the overall nested endturn pipe system. This network was tested on the *SC100*, *SC2* and *MR* conditions for the 60Hz machine, by comparing temperature predictions with the factory provided temperature readings and with results obtained from CHT simulations. The efficacy and accuracy of the proposed predictor were assessed. Next, the predictor was used on a hydrogen machine and a 50Hz machine that has similar ventilation designs and class designations, in order to investigate the physical similarities of the endturn flow physics, and the applicability of this generic temperature predictor. Last, the predictor was used to estimate end-arc coil temperatures of the previously studied endturn parametric

cases, to offer design insights on possible improvements to the current rotor ventilation system.

7.2 Thermal-fluidic Network Development

Now that an analytical description of the local bulk flows in the endturn circumferential cavities have been developed, the associated regional hydrodynamic and thermodynamic flow properties can be captured with textbook empirical correlations. This fulfills the objective of this research of implementing the fast-solving lumped-circuit analytically method in the temperature predictor, which can provide end-arc temperature predictions quickly and accurately. This section sets up the endturn cavity networks, where the assumptions, simplifications and the use of thermal-fluidic correlations are discussed and justified.

7.2.1 Assumptions and Simplifications

The two design goals of the analytical temperature predictor are to: (1) calculate end-arc coil temperatures at the given operating and design parameters, within a 5 degrees Celsius error; and (2) achieve temperature predictions in minutes, compared to the hours or days needed for the CFD simulations. To achieve these goals, a couple of simplifications and assumptions are made, which set up the fundamental design frame of the overall network.

The cavity internal flow is the vector sum of the relative bulk flow and the rotational flow as shown in Equation 7.1.

$$\overrightarrow{V} = \overrightarrow{v_r} + \overrightarrow{\omega r} \tag{7.1}$$

The relative flow can be described and quantified with the virtual pipe method; the rotational flow can be approximated with properties of natural convection between parallel plates. The flow separation is able to simplify the complicated flow phenomena in the cav-

ity such that the convective heat transfer is treated as the propagated effects from these two types of flows that are shown in Figure 7.1 (A) and (B), and calculated with Equation 7.2.

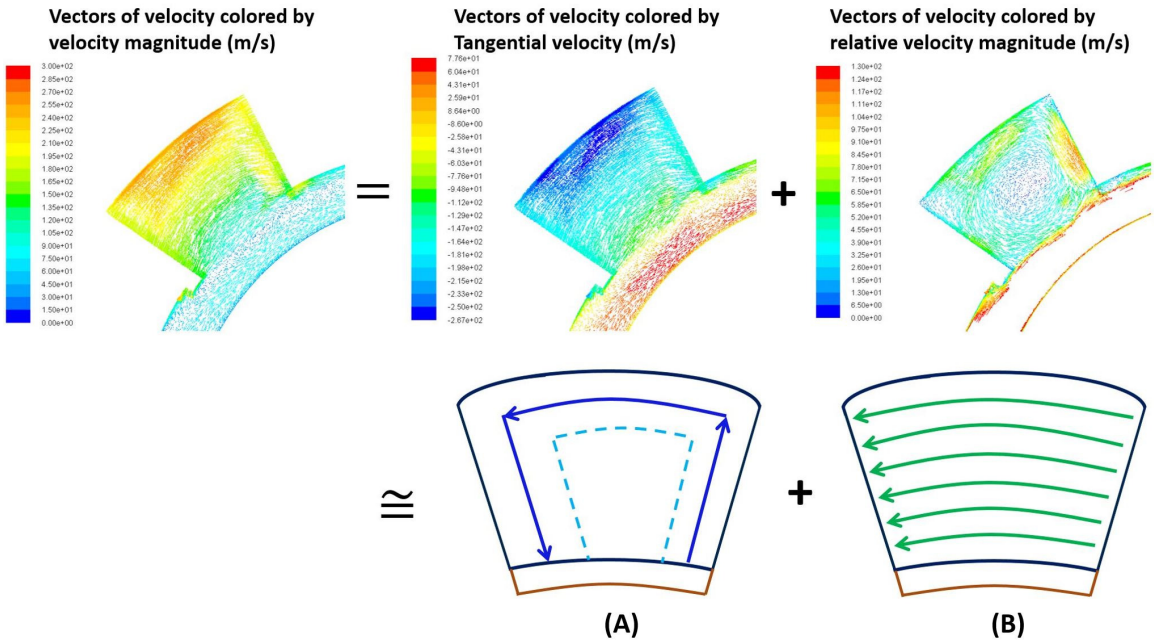

Figure 7.1: Proposed single cavity convective heat transfer propagation.

$$\bar{h} = \bar{h}_{VP} + \bar{h}_{\omega} \tag{7.2}$$

where $\bar{h}_{VP}$ and $\bar{h}_{\omega}$ are the regional heat transfer coefficients from the virtual pipe and the parallel flows that are shown in Figure 7.1 (A) and (B), respectively.

The same row cavities are assumed to have identical flow properties, ignoring the small differences between the leading and trailing sides. This assumption also applies to the annulus flow such that the inlet flow rates $\dot{m}_{in}$ are evenly distributed. Therefore, the amount of flow in each mixing zone has an amount m_{mz} that equals

$$\dot{m}_{mz} \mid_i = \frac{A_{mz}}{A_{annulus}} \dot{m}_{in} \tag{7.3}$$

In addition, the upstream and downstream cavities are related through the *mixing zone* by correcting for the changes in the flow temperatures and velocity magnitudes. The

gravitational effects are negligible and are not specifically addressed in the networks, since the gravitational acceleration g is so small compared to the centrifugal acceleration ωr.

7.2.2 Fluid Network

The predictor is constructed with two networks, namely the fluid network and the thermal network. Both networks are constructed on the unit-cavity basis and the nested-endturn system basis, as demonstrated in (A) and (B) in Figure 7.2 below, respectively. The circumferential cavity is defined to be the volume bounded by the rotor coils; the blocking extrusion thickness into the annulus is part of the annulus, as defined in CHAPTER 5 and shown in Figure 5.15. Therefore, within a single cavity, one complete virtual pipe is defined to start and end at the bottom right and left of the rotor coils, labeled as 1 and 2 in Figure 5.15, respectively. The nested endturn system starts at the bottom right of the first row cavity and ends at the exit of the 8^{th} row cavity. Between two adjacent cavities, the *exit* flow from the front cavity is assumed to travel directly towards the *entrance* of the back cavity through the cavity mixing zone, as shown in Figure 7.2 (B).

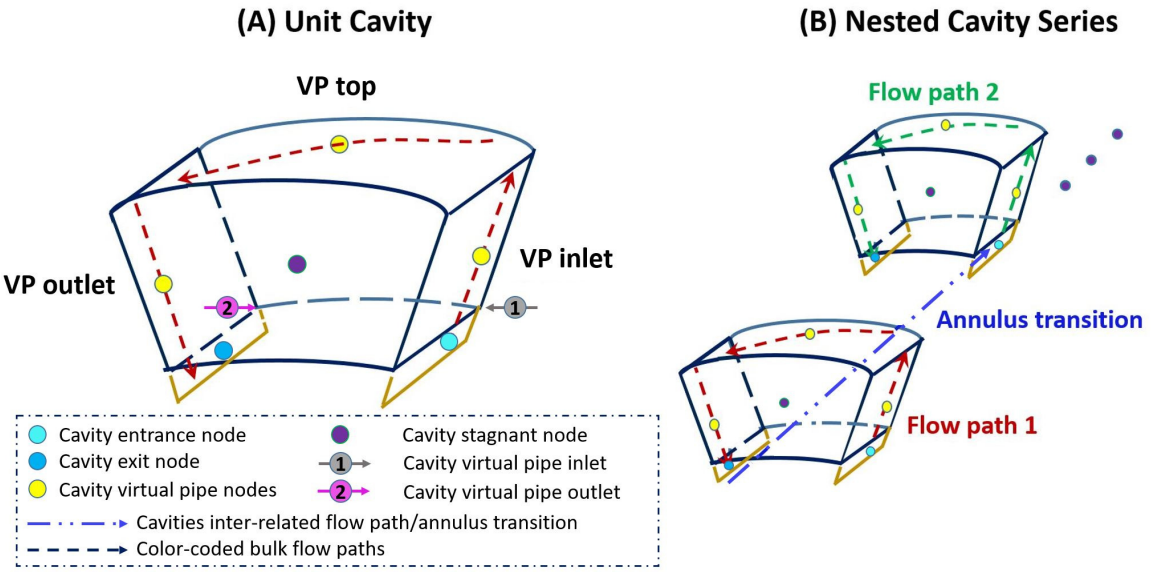

Figure 7.2: Network comparison for: (A) unit-cavity, (B) nested-endturn.

The fluid network is first developed for the individual cavity to obtain the local flow

properties. Four nodes are defined for each cavity, as demonstrated in Figure 7.2 (A); three nodes are inside the virtual peripheral pipe region (one per segment), and the fourth node is defined at the center of the stagnant region. These network nodes are located at the center of each region, in order to represent the averaged regional bulk flow conditions. The peripheral bulk flow is treated as a rotated, one-dimensional continuous pipe, along the pipe coordinate S that follows the sides of the cavity. At each node, the local bulk flow velocity magnitude, pressure and temperature are calculated in the fluid network.

In order to develop the cavity network, input parameters that are required to setup and initialize the algorithm are identified; these are listed in Table 7.1 below. These parameters are known values that can be obtained from the manufacturer.

Table 7.1: Summary of cavity network input parameters

Rotor parameter	**Detail**	
Rotor inlet	Inlet mass flow rate: $\dot{m}_{in}$	
	Inlet velocity angle: define V_{ax}, V_{tang}	
	Inlet air temperature: T_{cold}	
Coil dimension	Copper strap	height: h_{insul}
	Insulation	height: h_{strap}
	Stacked coil	arc length: l_{strap}
		width: w_c
		inner diameter: r_i
		Outer diameter: r_o
Rotor shaft	Radius: r_{shaft}	
Material properties	Solid	coil conductivity: K_{cu}
		insulation conductivity: K_{insul}
	Air	temperature dependent
Operating Condition	Rotational speed: ω	
	Field current: I	

The geometry and flow dimensions are defined for the four segments, or the virtual pipe *inlet*, *top*, and *outlet* regions, and the *center stagnant* region. The three virtual pipe nodes are located at the middle of each cavity edge and the center of the pipe width d. They are summarized in Table 7.2 and presented in Figure 7.3 below. The left of Figure 7.3 labels the local virtual pipe flow dimensions, and the right of this figure labels the dimensions of each virtual pipe segment, where the segment separations are color-coded as well.

Table 7.2: Summary of virtual pipe flow parameters.

Flow Parameter	**Source**
Local hydraulic diameter D_h	Virtual pipe correlations
Stagnant region height L_{stag}	$L_{stag} = \Delta r - D_h \mid_{top}$
Virtual pipe flow path lengths	$S_{in}, S_{top}, S_{out}, S_c$
Local virtual pipe cross-sectional area $A_c \mid_i$	$A_c \mid_i = D_h \mid_i \cdot w_c$
Mixing zone length t_{mz}	$t_{mz} = L_{blocking} - \Delta r$
Individual virtual pipe length	$l_{in}, l_{top}, l_{out}, l_c$
Local pipe width	d_i, d_o, d_t

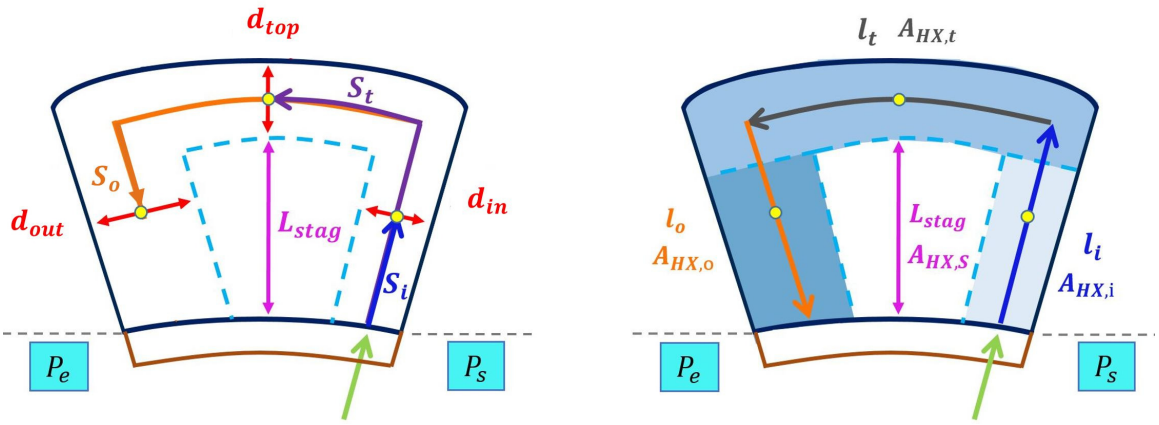

Figure 7.3: Virtual pipe flow dimension definition.

The local and overall pipe length balues l and s are calculated using the Equation set 7.4 below. The flow lengths s are traced along the center of each virtual pipe segment (or

at $\frac{1}{2}d$) as labeled in Figure 7.3 left. The virtual pipe length l_{VP} is therefore the sum of the individual pipe lengths.

$$\begin{aligned}
S_i &= \frac{1}{2}\Delta r = \frac{1}{2}l_i \\
S_t &= S_i + \frac{1}{2}\Delta r + \frac{1}{2}\theta_c(R_o - D_h\,|_t) - \frac{1}{2}\,D_h\,|_i = l_i + \frac{1}{2}l_t \\
S_o &= S_t + \frac{1}{2}\theta_c(R_o - D_h\,|_t) + \frac{1}{2}\Delta r - \frac{1}{2}\,D_h\,|_o = l_i + l_t + \frac{1}{2}l_o \\
l_{VP} &= l_i + l_t + l_o
\end{aligned} \tag{7.4}$$

the heat transfer surface areas (color-coded areas in Figure 7.3 right) are calculated with the Equation set 7.5 below. The factor 2 in the equations accounts both the front and the back cavity walls.

$$\begin{aligned}
A_{HX,i} &= 2 \cdot L_i \cdot D_h\,|_i = 2 \cdot (\Delta r - D_h\,|_t) \cdot D_h\,|_i \\
A_{HX,t} &= 2 \cdot \left((\frac{1}{2}\frac{\theta_c}{360}) \cdot R_o^2 - (R_0 - D_h\,|_t)^2 \right) \\
A_{HX,o} &= 2 \cdot L_o \cdot D_h\,|_o = 2 \cdot (\Delta r - D_h\,|_t) \cdot D_h\,|_o \\
A_{HX,VP} &= A_{HX,i} + A_{HX,t} + A_{HX,o} \\
A_{HX,s} &= 2 \cdot \left(A_c - A_{HX,i} - A_{HX,t} - A_{HX,o} \right)
\end{aligned} \tag{7.5}$$

the virtual pipe cross-sectional areas that are normal to these heat transfer surfaces are calculated in Equation 7.6, where d is the width of the local bulk flow (perpendicular to the cavity).

$$\begin{aligned}
A_{C_{in}} &= w_c \cdot d_{in} \\
A_{C_{top}} &= w_c \cdot d_{top} \\
A_{C_{out}} &= w_c \cdot d_{out} \\
A_{C,stag} &= A_c - A_{C_{in}} - A_{C_{top}} - A_{C_{out}}
\end{aligned} \tag{7.6}$$

The annulus area is separated into the mixing areas that is underneath the cavity, and the

bypass area that is underneath the blocking, as shown in Figure 7.4.

$$A_{annulus} = \pi(r_o^2 - r_{shaft}^2) - \sum A_{blocking} = A_{bypass} + N \cdot A_{mz} \tag{7.7}$$

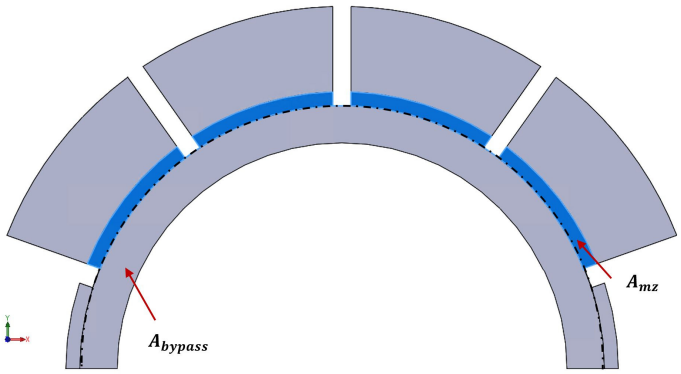

Figure 7.4: Annulus area separation demonstration.

The fluid network is developed to calculate the local flow properties, or the virtual pipe velocity magnitudes and temperatures. The flow temperatures define the material properties, such as the viscosity $nu\,[m^2/s]$, density $\rho\,[kg/m^3]$, specific heat capacity $C_p\,[J/Kg-K]$ and thermal conductivity $k\,[W/m-K]$ etc. Just like any other lumped-circuit network, this cavity network also involves iterative calculations.The iterative calculation processes are performed within the local virtual pipes, where the flow properties and the material properties are continuously updated until convergence in the inlet virtual pipe velocity magnitude is achieved. The iterative flow calculations are based on an equivalent flow resistance network, as shown in Figure 7.5 below. The entrance and the exit of the virtual pipe are at pressure values P_s and P_e, respectively. Pressure losses and gains along the flow passage include the *major* and *minor losses*, the *dynamic pressure* or the pumping momentum from the blocking extrusion effect, and the *centrifugal pressure* from the rotational motion. Two types of minor losses are accounted for at the two top corners, which are losses from the changes in pipe cross-sectional areas, and the losses for changes in the flow directions.

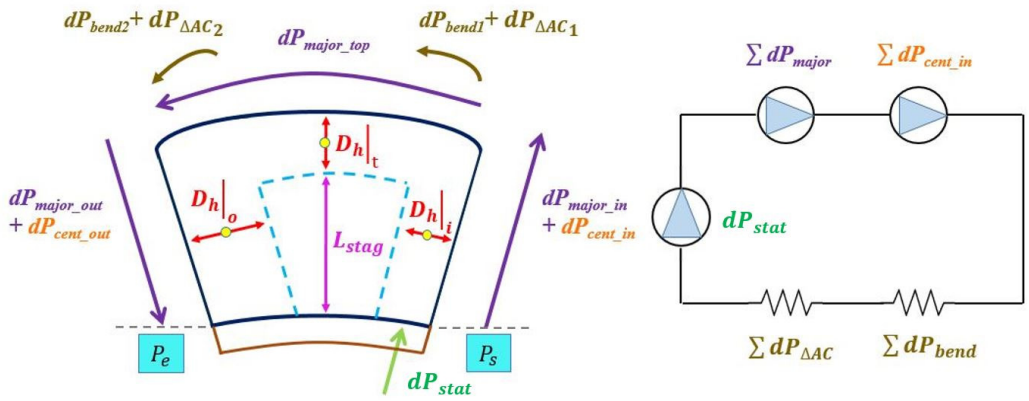

Figure 7.5: Cavity bulk flow region fluid network demonstration

This network is developed under the assumption that the gauge pressures in the annulus underneath the cavity are uniform, such that the pressure values at P_s and P_e are equal. Therefore, the sum of the pressure losses and gains is balanced between the entrance and the exit of the virtual pipe, using Equation set 7.8 below. The definition of each pressure term is discussed and explained next.

$$
\begin{aligned}
dP_{loss} &= dP_{gain} \\
dP_{gain} &= \sum dP_{cent} + dP_{stat} \\
&= dP_{cent}\,|_{in} + dP_{out}\,|_{in} \\
dP_{loss} &= \sum dP_{major} + \sum dP_{minor} \\
&= dP_{major}\,|_{in} + dP_{major}\,|_{top} + dP_{major}\,|_{top} + dP_{minor}\,|_{bend1} \\
&+ dP_{minor}\,|_{bend2} + dP_{minor}\,|_{\Delta AC1} + dP_{minor}\,|_{\Delta AC2}
\end{aligned}
\tag{7.8}
$$

Two types of pressure gains occur in the virtual pipe. The first gain dP_{cent} originates from the rotor's rotational motion, which adds the centrifugal force to the bulk flow. Changes in the centrifugal pressures along the virtual pipe are the result of the changes in the radial locations and the local air density, as shown in Equation 7.9. Therefore, a pressure gain is obtained in the virtual pipe inlet and a pressure loss occurs in the virtual pipe outlet region; no change is expected in the virtual pipe top region since the flow travels in

the tangential direction at a constant radial height.

$$
\begin{aligned}
dP_{cent}|_{in} &= \frac{1}{2}\bar{\rho}_{in}\omega^2({R_o}^2 - {R_i}^2) \\
dP_{cent}|_{out} &= \frac{1}{2}\bar{\rho}_{out}\omega^2({R_i}^2 - {R_o}^2)
\end{aligned}
\tag{7.9}
$$

the rotational speed Ω, the inner and outer diameters of the rotor coils R_i and R_o are constant values. The density of air, ρ, changes between the inlet and outlet locations, and therefore causes a net centrifugal pressure in the virtual pipe. The varying densities of air here are evaluated at the regional mean fluid temperature $\overline{T}_m$. The bulk flow temperatures increase along the virtual pipe, as a result of the heat transfer between the adjacent heated rotor coils. The fluid temperatures for the three virtual pipe locations are calculated using the 1^{st} law, or as in Equation 7.10

$$
T_m\ |_i = T_{air}|_{i-1} + \alpha_{q,i}\frac{Q}{\dot{m}C_p} \tag{7.10}
$$

Q and $\dot{m}$ are the mass flow rate, and surface heat. $T_m|_i$ is the fluid temperature at the current node; $T_{air}|_{i-1}$ is the value at the previous node. The heat Q values depend on: (1) the areas of the virtual pipe heat transfer surfaces; and (2) the surface heat flux q''. Recall that two turns of rotor coils bound one row of the circumferential cavities, and each coil is assumed to operate under a constant and uniform surface heat flux ${q''}_{c_i}$. Therefore, the amount of heat that dissipates to the cavity Q_c, to the peripheral virtual pipe Q_{VP}, and to each separated cavity region Q_i is calculated as

$$
\begin{aligned}
Q_c &= 2q_c^{''} \cdot A_c \\
Q_{VP} &= Q_c \cdot \frac{A_{HX,VP}}{A_c} \\
Q_i &= Q_c \cdot \frac{A_{HX,i}}{A_c}
\end{aligned}
\tag{7.11}
$$

The exit temperatures can therefore be calculated as

$$T_e = T_s + \frac{Q_{VP}}{\dot{m} C_p} \tag{7.12}$$

here T_s and T_e are the virtual pipe entrance and exit air temperatures (locations labeled in Figure 7.5), respectively. The exit air temperature rise is caused by the amount of heat Q_{VP} that needs to be dissipated in the virtual pipe region; the inlet temperature needs to account for the flow mixing between the cavity exit flow and the annulus bypass flow, calculated as Equation 7.13.

$$T_s|_i = \begin{cases} T_{cold} & \text{if } n = 1 \\ \frac{T_e|_i \cdot \dot{m}_{mz} + T_e|_{i-1} \cdot \dot{m}_{VP}}{\dot{m}_{mz} + \dot{m}_{VP}} & \text{if } n > 1 \end{cases} \tag{7.13}$$

here $\dot{m}_{VP}$ and $\dot{m}_{mz}$ are the virtual pipe flow rate and the mixing zone mass flow rate, respectively. The mixing zone flow rate is calculated by assuming evenly distributed inlet flow over annulus area $A_{annulus}$. Therefore, the amount of flow in each mixing zone is

$$\dot{m}_{mz} = \dot{m}_{in} \cdot \frac{A_{mz}}{A_{annulus}} \tag{7.14}$$

As the entrance and exit air temperatures are calculated, the inlet and outlet air temperatures are calculated as

$$\begin{aligned} T_{m,in} &= T_e - x_2 \left(\frac{Q_{VP}}{\dot{m} C_p}\right) \\ T_{m,out} &= T_e - x_1 \left(\frac{Q_{VP}}{\dot{m} C_p}\right) \\ x_1 &= \frac{S_i}{l_{VP}} \\ x_2 &= 1 - x_1 \end{aligned} \tag{7.15}$$

here $T_{m,in}$ and $T_{m,out}$ are the the virtual pipe inlet and outlet air temperatures, respectively; they are calculated based on the fraction of heat present in the local volume. The top and

stagnant air temperatures are calculated as

$$T_{m,t} = \frac{T_{m,in} + T_{m,out}}{2} \tag{7.16}$$

where the top node is located half-way through the virtual pipe l_{VP}, and therefore the air temperature $T_{m,t}$ is the average of the inlet and outlet temperatures. The center stagnant region has a gas temperature of

$$\begin{aligned} T_{m,stag} &= T_s + (\frac{Q_{stag}}{\dot{m}_{stag} C_p}) \\ \dot{m}_{stag} &= (\omega \cdot r_{stag}) \cdot A_{C,stag} \end{aligned} \tag{7.17}$$

Based on the coil height study discussed in the previous chapter, an additional pressure gain is introduced to the local virtual pipe, which is the result of the *radial blade fan effect* of the annulus blocking extrusion thickness. A portion of the annulus flow is stopped by the blocking at the bottom of the cavity; this converts the dynamic pressure into a static pressure, and creates a local pressure buildup that adds to the centrifugal pressure dP_{cent}. This effect is calculated as

$$dP_{stat,nom} = \frac{1}{2} \rho {V_{tan}}^2 \tag{7.18}$$

note that this pressure term is evaluated by the properties of the annulus bypass flow, which has a tangential velocity component of V_{tang} at a temperature of T_{cold}. It is assumed that the bypass region is isolated from the cavity flow and therefore the temperature is assumed to be maintained at T_{cold}. Previous studies have also found that the strengths of the virtual pipe inlet flows gradually decrease as the cavity locations move downstream. Therefore, the amount of local static pressure that is being converted at each cavity location is adjusted based on the cavity opening θ, under the assumption that the bigger the cavity opening is,

the higher the conversion rate.

$$dP_{stat,i} = dP_{stat,nom} \cdot \frac{\theta_i}{\theta_1} \tag{7.19}$$

Major losses and minor losses occur between the virtual pipe nodes. The major losses are the result of the differences in the velocity magnitudes along the flow length between the nodes, and are calculated as shown in Equation 7.20. The friction factor f is calculated using the Colebrook-White equation [90] for open channel flow.

$$\begin{aligned} dP_{maj} = \frac{\Delta P_L}{\rho g} = \frac{1}{2}\rho f \frac{L}{D_h}(\Delta V_{mag}^2) \\ \text{with } \frac{1}{\sqrt{f}} = -2log_{10}(\frac{\varepsilon}{12R_D} + \frac{2.51}{Re_D\sqrt{f}}) \end{aligned} \tag{7.20}$$

where ε is the coil surface roughness and equals to $4.5e^{-7}mm$; R_D is the bulk flow hydraulic radius that is the ratio between the cross-sectional area and the wetted perimeter, as shown in Equation 7.21 below

$$R_h \mid_i = \frac{A_c}{P_w} = \frac{w_c l_i}{2l_i + w_c} \tag{7.21}$$

where l_i is the length of each virtual pipe segment, shown in Figure 7.3. V is the local virtual pipe velocity magnitude, which is an unknown value that defines the convergence criteria and is to be iterated in the fluid network. The mass flow rate in the virtual pipe is conserved; therefore, the local velocity magnitudes $V_{mag}|_i$ can be expressed in terms of the constant mass flow rate $\dot{m}_{VP}$, as shown in Equation 7.22 below

$$\dot{m}_{VP} = A_C \cdot \rho \cdot V \tag{7.22}$$

where A_C is the local virtual pipe cross-sectional area that is calculated in Equation 7.6. This substitution is able to express the three velocity variables by one variable $\dot{m}_{VP}$ only,

which simplifies the network and therefore the computation time.

Minor losses include effects from the changes in flow directions at the cavity top corners, and expansion or subtraction in the pipe cross-sectional area between the pipe segments. They are calculated using Equation set 7.23 [90] below.

$$\begin{aligned} dP_{minor} =& \frac{1}{2} K_L \rho V^2 \\ & \text{with: } K_L \mid_{90bend} = 0.3 \\ & \qquad K_L \mid_{\Delta A_c}: \text{ interpolate from table} \end{aligned} \tag{7.23}$$

K_L is the loss factor and is different for each loss phenomenon; the 90 degree bend in flow direction has a constant loss factor of 0.3, where the loss from the change in the size of the flow channel is interpolated from a table.

To sum up, the iterative fluid network calculations follow the process shown in Figure 7.6. The convergence criterion is the virtual pipe inlet velocity, and the iteration ends when the change in the velocity magnitude between iterations is less than 0.1 m/s.

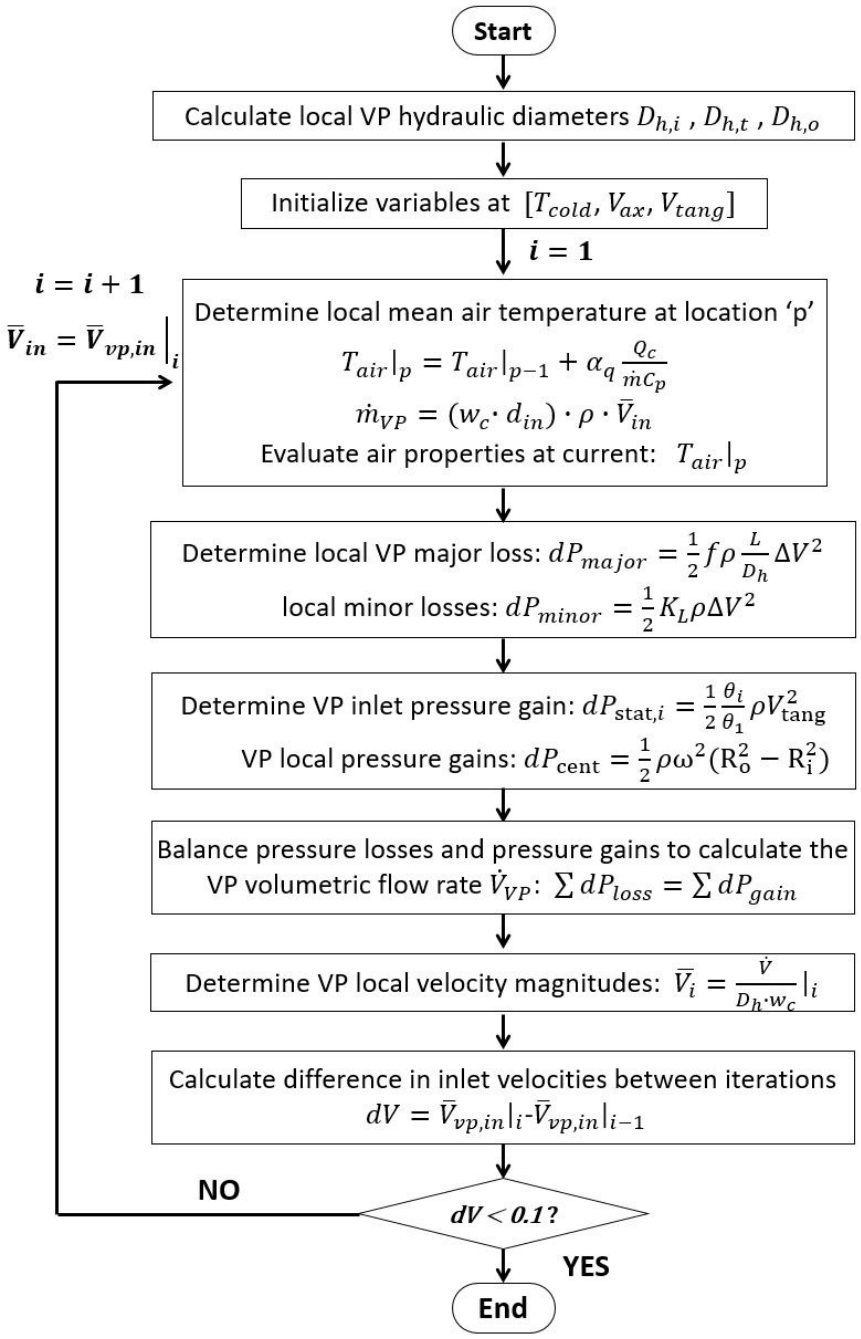

Figure 7.6: Single cavity virtual pipe fluid network calculation overview.

7.2.3 Thermal Network

Once the virtual pipe flow velocities and temperatures are determined, the values are used in the thermal network to calculate the associated local heat transfer, in order to es-

timate the adjacent coil temperatures. The thermal network consists of conduction and convection heat transfers; the radiation heat transfer is known to be negligible in magnitude from literature [7], and therefore is not included.

To quantify the convective heat transfer, the convective heat transfer coefficient h needs to be determined. h can be first calculated based on Newton's law of cooling, as shown in Equation 7.24.

$$T_w = T_{air} + \frac{q_c''}{h} \tag{7.24}$$

where q_c'' is the cavity surface heat flux that comes from the two adjacent rotor coils; T_w is the wall temperature to be determined. h is also related to the thermal conductivity of air k, the hydraulic diameter D_h, and the regional Nusselt number Nu_D, calculated as in Equation 7.25.

$$h = \frac{\overline{Nu}_D \cdot k}{D_h} \tag{7.25}$$

in the virtual pipe region, the Nusselt number can be calculated with either the Dittus-Boelter correlation for heating as shown in Equation 7.26,

$$\overline{Nu}_D = 0.023 {Re_D}^{0.8} Pr^{0.4} \tag{7.26}$$

or the Gnielinski correlation as shown in Equation 7.27 [90]

$$\overline{Nu}_D = \frac{(f/8)(Re_D - 1000)Pr}{1 + 12.7(f/8)^{1/2}(Pr^{2/3} - 1)} \tag{7.27}$$

The Dittus-Boelter correlation has the advantage of being a simple and effective approximation when the temperature difference cross a fluid is small; but it is also known to introduce errors for rough wall surfaces. The Gnielinski correlation is considered because it captures the effects of wall roughness and the transitional flow conditions by adding the friction factor f to the relationship [90]. The prediction performances of these two correlations are compared and discussed. The friction factor f is the same as those obtained from

the fluid network in Equation 7.20.

The pipe flow *entrance effect* is accounted in the virtual pipe as well, with the relationship shown in Equation 7.28 below. The entrance length l is taken as 10 times the pipe hydraulic diameter D_h[90]

$$x_{ent} = \frac{\overline{Nu_D}}{Nu_{fd,D}} = 1 + \frac{C}{(\frac{l}{D})^n} = 1.49$$
$$l = 10D_h \tag{7.28}$$

here, C and n equal 2.0152 and 0.614, respectively. The entrance effect is implemented in two ways. If the virtual pipe is considered as one continuously rotating pipe, then the entrance effect is applied only within the 10 $D_h|_{in}$ pipe length. But taking the changes in flow condition at the cavity top corners between the virtual pipe locations into consideration, the entrance effect needs to be implemented individually for all three virtual pipe segments, based on values calculated using the local hydraulic diameters $D_h|_i$ instead.

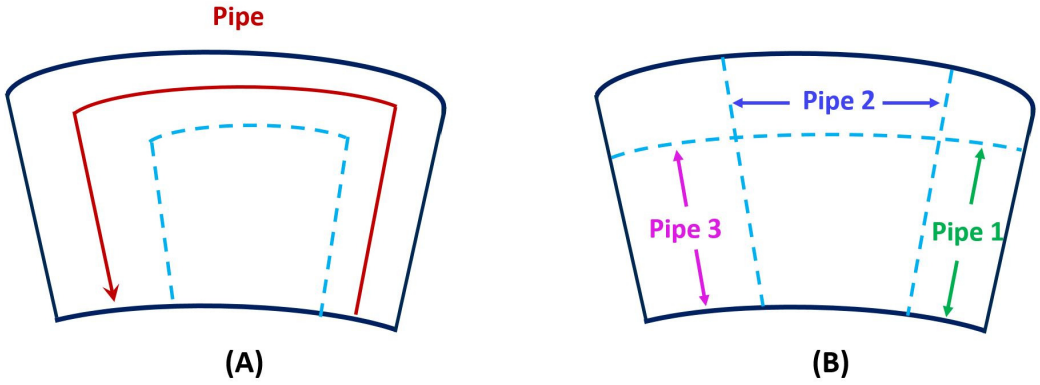

Figure 7.7: Entrance length calculation: (A) one complete pipe per cavity, and (B) separate pipe per virtual pipe location.

$$\text{Case A:} \begin{cases} Nu_{in} = Nu_{in} \cdot x_{ent} \\ Nu_{top} = \begin{cases} Nu_{top} \cdot \left(\frac{x_{ent}-l_i}{l_t} \cdot x_{ent} + (1 - \frac{x_{ent}-l_i}{l_t}) \right), & \frac{x_{ent}-l_i}{l_t} < 1 \\ Nu_{top} \cdot x_{ent}, \text{ else} \end{cases} \\ Nu_{out} = \begin{cases} Nu_{top} \cdot \left(\frac{x_{ent}-l_i-l_t}{l_o} \cdot x_{ent} + (1 - \frac{x_{ent}-l_i-l_t}{l_o}) \right), & \frac{x_{ent}-l_i}{l_t} > 1 \\ Nu_{out}, \text{ else} \end{cases} \end{cases} \tag{7.29}$$

$$\text{Case B:} \begin{cases} Nu_{in} = Nu_{in} \cdot x_{ent} \\ Nu_{top} = Nu_{top} \cdot x_{ent} \\ Nu_{out} = Nu_{out} \cdot x_{ent} \end{cases} \tag{7.30}$$

The rotational flow V_{rot} in Figure 7.1 B is approximated with flow phenomena for natural convection between two vertical parallel plates. The hydraulic diameter of the channel is twice the width of the channel [90].

$$D_{h,stag} = 2w_c \tag{7.31}$$

The Nusselt number is calculated using the correlation developed by Bar-Cohen and Rohsenow, as shown in Equation 7.32 [90] for isothermal plates. The isothermal plate assumption is taken for the fact that the temperature differences within an end-arc copper strap are expected to be small, due to its high thermal conductivity.

$$\begin{gathered} \overline{Nu_L} = [\frac{C_1}{(\frac{Ra_s S}{L})^2} + \frac{C_2}{(\frac{Ra_L S}{L})^{1/2}}]^{-1/2} \\ with\ Ra_s = \frac{g\beta(T_w - T_\infty)S^3}{\alpha\nu} \\ g \sim a_t = \frac{v^2}{r} = \omega^2 r \end{gathered} \tag{7.32}$$

here, $C1$ and $C2$ equal 576 and 2.87, respectively. S is the spacing between the plates, which equals to the cavity width w_c in this case. L is the dimension of the plate that is parallel to the direction of the body force, or in this case is parallel to the centrifugal force ωr and is equal to the height of the stagnant region L_{stag}. β is the thermal expansion coefficient and has a value equals the inverse of the absolute fluid temperature $1/T$, under the ideal gas assumption. The gravitational acceleration g in the natural convection is replaced by the overpowering centrifugal acceleration a_t. Fluid properties are evaluated at the film temperature, which is the average temperature of the bounding plates T_{cu} and the reference fluid temperature T_{cold}.

$$T_f = \frac{T_{cu} + T_{cold}}{2} \tag{7.33}$$

Using Equations 7.26, 7.27, and 7.32, the local Nusselt numbers $\overline{Nu}$ can be determined. The heat transfer coefficients h are calculated using Equation 7.25. The local heat transfer coefficients are the sum of the h values from the virtual pipe and the parallel flows, as

$$h = h_{VP} + h_{stag} \tag{7.34}$$

The corresponding wall temperatures are calculated last $[T_w|_{in}, T_w|_{stag}, T_w|_{out}]$ using Equation 7.24. Up till now, the wall temperatures have been calculated solely based on convection heat transfer, where a heat flux boundary condition is applied that has a constant and uniform value over the entire cavity surface A_c; the separated cavity volumes are assumed to be cooled independently. But based on the previous studies, the local velocity magnitudes vary significantly among the four cavity nodes, such that the resultant heat transfer rates are expected to vary significantly among the four locations. Therefore, the temperature differences between the inlet, stagnant and the outlet regions are expected to be significant. But copper is known to have a high thermal conductivity, such that the temperature gradients along a strap of short distance should be negligible. Therefore, conduction heat

transfer within the straps is calculated last to capture the heat flows within the straps that are the result of the differences in the regional convective heat dissipation rates.

The rotor coils are stacks of copper straps that are thermally insulated with insulation layers. The end-arc strap is much longer in the tangential direction than in the axial or radial directions. Therefore, the three-dimensional conduction in the copper strap is simplified to one-dimensional, in the tangential direction only. Conduction heat transfer calculations are performed among the *inlet*, *stagnant* and *outlet* nodes; the *top* node is located in a separate strap, and therefore is not thermally related to the other nodes. The in-plane tangential conduction is calculated by balancing the heat between the cooler, outer nodes and the hotter center stagnant node; the conduction paths Q_{cond} are demonstrated in Figure 7.8 below.

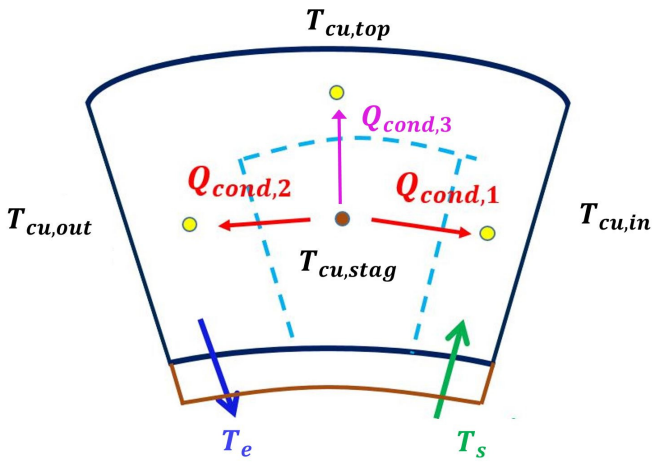

Figure 7.8: In-plane conduction

In reality, the rotor straps are expected to operate under an almost uniform regional temperature distribution under steady state. Therefore, the different regional convective heat transfer coefficients h_i within the cavity would result in high temperature differences between the cavity nodes, under the constant heat flux q''_c boundary, which contradicts with the observed results. Therefore, in-plane conduction is modeled last, which is initialized with the wall temperatures predictions $[T_w|_{in}, T_w|_{stag}, T_w|_{out}]$ calculated based on the convection calculations discussed before (Equations 7.24 to 7.32). The differences in the

convection rates result in a higher amount of heat remaining in the stagnant region; this results in heat flow from the stagnant region outwards to the inlet and outlet regions. In the algorithm, the heat in the stagnant region is being gradually added to the cooler regions, until the time when the local temperatures between the three nodes are within 1 C difference. The overall in-plane conduction algorithm follows the processes shown in Figure 7.9, and the steps are:

1. Initialize conduction algorithm with the heat transfer coefficients calculated from the convective heat transfer network $[h_{in}, h_{top}, h_{out}, h_{stag}]_{@j=0}$, and the corresponding nodal wall temperatures $[T_{cu,in}, T_{cu,top}, T_{cu,out}, T_{cu,stag}]_{@j=0}$

2. Determine the amount of heat in the virtual pipe inlet and outlet regions, and in the center stagnant region.

$$Q_{HX} = q''_{HX} \mid_{i-1} \cdot A_c \tag{7.35}$$

where q''_c is the initial homogeneous surface heat flux, and A_c is the total cavity heat transfer surface areas.

3. Determine the amount of heat flow between nodes that is the result of the difference in the node temperatures, based on Newton's law of cooling relationship.

$$\begin{aligned} Q_{cond,1} &= \frac{T_{cu,stag} - T_{cu,in}}{R_{cond,1}} \qquad Q_{cond,2} = \frac{T_{cu,stag} - T_{cu,out}}{R_{cond,2}} \\ Q_{cond,3} &= \frac{T_{cu,stag} - T_{cu,top}}{R_{cond,3}} \end{aligned} \tag{7.36}$$

where $R_{cond,i}$ is the conductive thermal resistance for the conduction paths between: (1) the inlet and stagnation, (2) the stagnation and outlet regions, or (3) the stagnation and top regions, respectively. It is calculated using Equation 7.38, based on the dimensions that are parallel and perpendicular to the heat transfer direction, which are the conduction length l_{cond} and the cross-sectional

area A_c, respectively.

$$R_{cond} = \frac{l_{cond}}{k_{cu} A_c} \tag{7.37}$$

note that the stacked coils have cyl-orthotropic thermal conductivity that the values in the tangential and radial directions are 387 and 6.7 W/m-K, respectively. The conduction dimensions among nodes *inlet*, *stagnant*, and *outlet* in the tangential direction are calculated per strap basis as

$$\begin{aligned} l_{cond,1} &= \frac{1}{2}\theta_c(R_i + R_0 - d_t) - d_0 - \frac{1}{2}d_i \\ l_{cond,2} &= \frac{1}{2}\theta_c(R_i + R_0 - d_t) - d_i - \frac{1}{2}d_o \\ A_{c,t} &= w_{strap} \cdot h_{strap} \end{aligned} \tag{7.38}$$

The conduction dimensions in the radial direction between the nodes *stagnant*, and *top* in the tangential direction are calculated

$$\begin{aligned} l_{cond,3} &= \frac{1}{2}(R_i + R_0) - \frac{1}{2}d_t \\ A_{c,r} &= l_t \cdot w_c \end{aligned} \tag{7.39}$$

4. The local heats Q_{HX} are re-organized among the *stagnant*, and the cooler *inlet* and *outlet* areas, such that a portion of the heat is moved from the hotter areas to the outer cooler virtual pipe regions, as shown in Equation 7.40.

$$\begin{aligned} Q_{HX,1} &= Q_{HX,1} + \delta Q_{cond,1} \\ Q_{HX,2} &= Q_{HX,2} + \delta Q_{cond,3} \\ Q_{HX,3} &= Q_{HX,3} + \delta Q_{cond,2} \\ Q_{HX,4} &= Q_{HX,4} - \delta Q_{cond,1} - \delta Q_{cond,3} - \delta Q_{cond,2} \end{aligned} \tag{7.40}$$

The differences in heat between the nodes are gradually decreased during iterations, and it is assumed that the conduction rate in the θ direction ($\delta Q_{cond,1}$,

$\delta Q_{cond,3}$) is faster than the r ($\delta Q_{cond,2}$) direction.

5. Determine the new local surface heat fluxes at the i^{th} iteration

$$q''_{HX,i} = \frac{Q_{HX,i}}{A_s, i} \tag{7.41}$$

6. Update the wall temperatures for the i^{th} iteration

$$\begin{aligned} T_{cu,stag} \mid_i &= T_{m,stag} + \frac{q''_{HX,4}}{h_{stag}} \\ T_{cu,in} \mid_i &= T_{m,2} + \frac{q''_{HX,1}}{h_{in}} \\ T_{cu,out} \mid_i &= T_{m,2} + \frac{q''_{HX,3}}{h_{out}} \\ T_{cu,top} \mid_i &= T_{top} + \frac{q''_{HX,2}}{h_{top}} \end{aligned} \tag{7.42}$$

7. Calculate the difference in the heat transfer rates between the three nodes.

$$\text{Isothermal strap: } \varphi_i = \frac{T_{w,stag} - T_{w,in}}{l_{cond,1}} - \frac{T_{w,stag} - T_{w,out}}{l_{cond,2}} \tag{7.43}$$

8. If φ_i is greater than 0.1, repeat steps 2 to 7; otherwise, end iteration and save the wall temperatures.

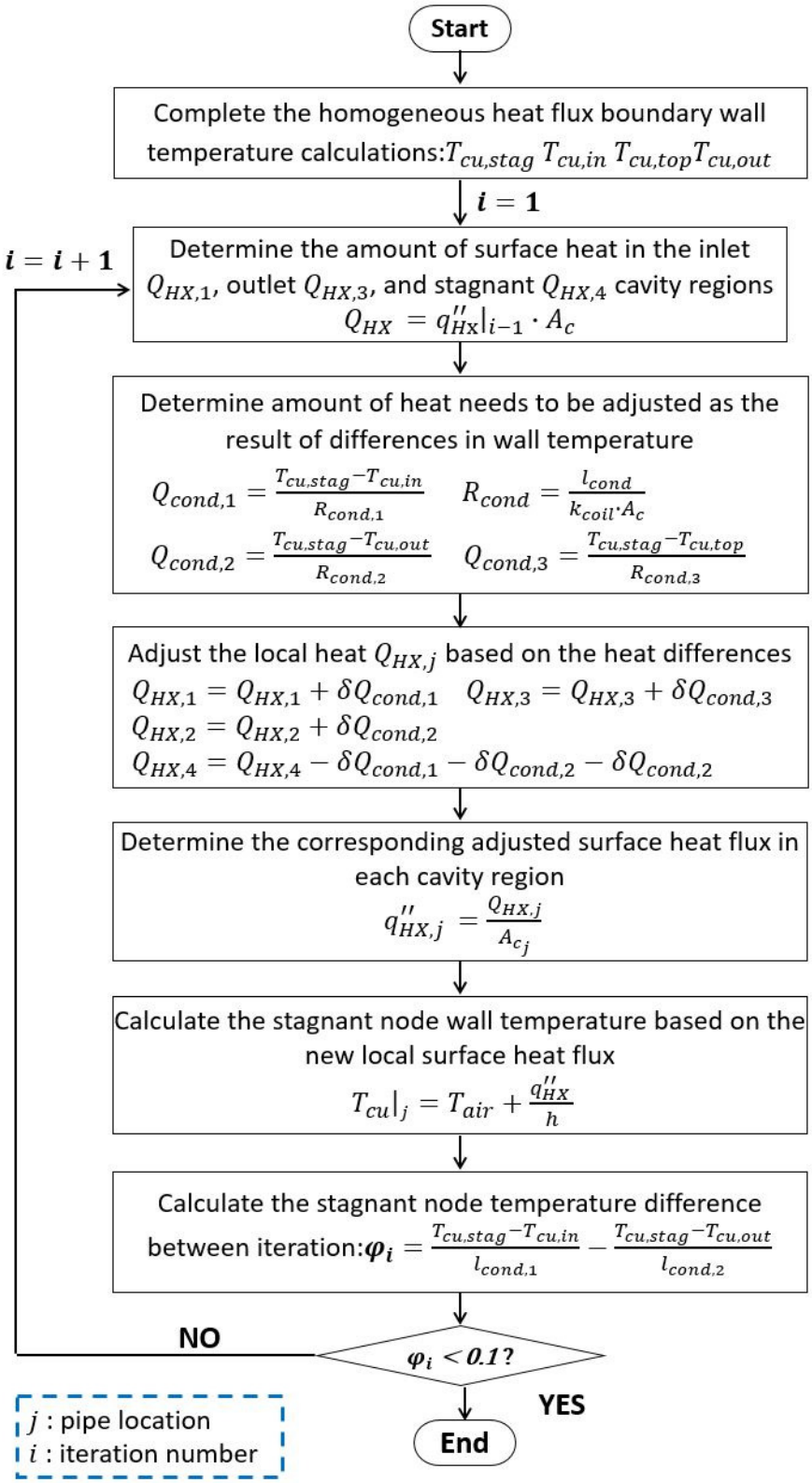

Figure 7.9: Strap tangential conduction process overview.

The overall thermal-fludic processes inside a single cavity are shown in Figure 7.10. In order to calculate the coil temperatures, the fluid properties are determined first in order to calculate the heat removal rate, or the local convective heat transfer coefficient h_i. Conduction heat transfer is then performed, including tangential conduction heat transfer within the coil by applying the isothermal strap assumption, and radial direction conduction to account for the imperfection of the insulation layers.

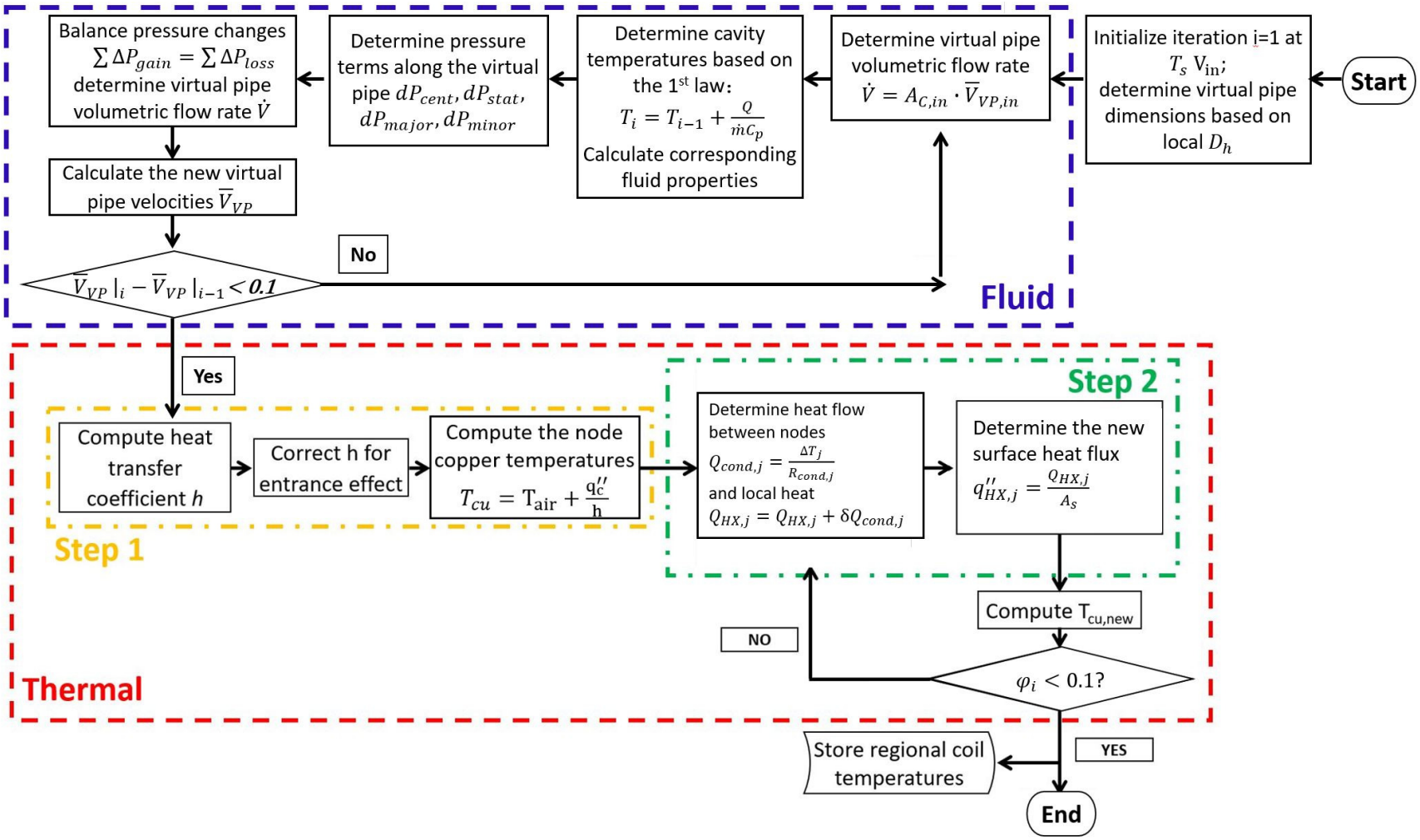

Figure 7.10: Iterative thermal-fluidic network for a unit cavity.

7.3 Predictor Verification

The previous section has developed an analytical method that can quickly calculate end-arc coil temperature under the given operating conditions. This section evaluates and discusses its efficacy and accuracy. To do so, the analytically predicted temperatures were compared with provided factory sensor readings, and with results from endturn CHT simulations. Both comparison methods have limitations and uncertainties, and therefore they were used together to validate the performance of the thermal-fluidic network. The number of factory sensor available for comparison is very limited, not to mention that the sensors themselves present manufacture uncertainties during operation and measurements. Conjugated heat transfer (CHT) simulations are able to provide temperature readings along the entire arc-length of the rotor turns of *coil B* though *coil H*, which allows for detailed, point-to-point temperature comparisons. But simplifications and assumptions were implemented during the CHT model setup, where errors were introduced at the same time. The temperature comparisons were also conducted in order to determine the more appropriate approach for the following virtual pipe calculations:

1. Virtual pipe Nusselt number calculation that can be accomplished with either the Dittus-Boelter correlation or the Gineilinski correlation.

2. The entrance length correction for the virtual pipe Nusselt numbers, which can be applied either at each virtual pipe location, or once only when treating the pipe as one continuous pipe.

7.3.1 Prediction Overview

The proposed virtual pipe Nusselt correlations and thermal entrance correction methods were compared first to determine the final predictor construction. The Nusselt correlation comparisons were conducted between the Gnielinski and Dittus-Boelter relationships.

The SC100 condition was taken as the representative case, considering that when the rotor operates at the highest measurable heat load condition, the associated coil temperature calculations are expected to be the most sensitive to the performances of the correlation chosen. The predicted temperatures are presented in Figure 7.11 below.

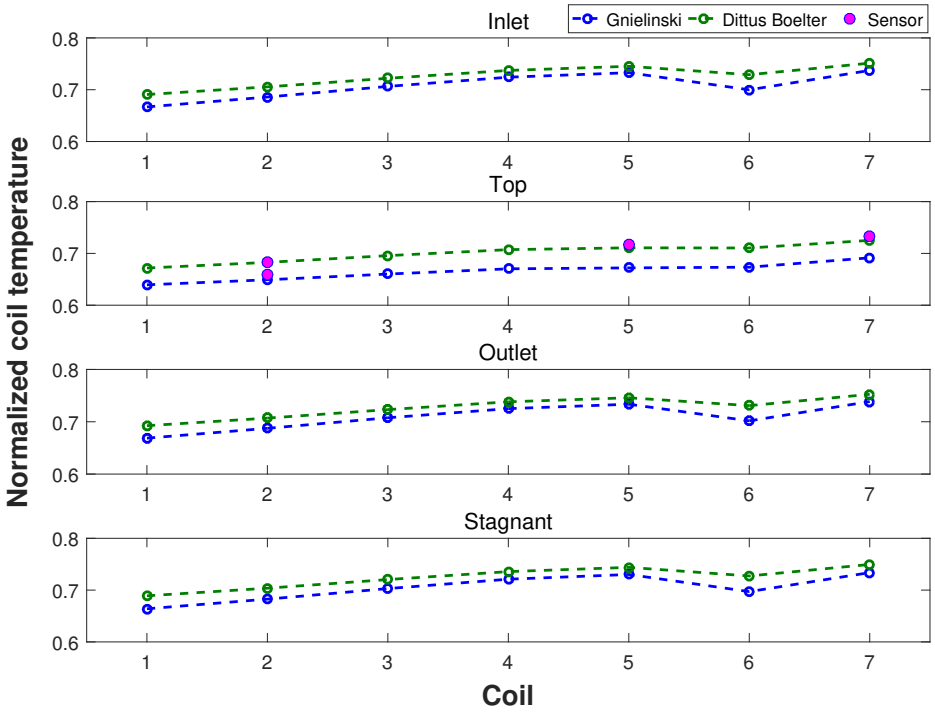

Figure 7.11: Prediction comparison between Dittus-Boelter and Gnielinski correlations.

At all four cavity nodes, the Dittus-Boelter predictions were higher than those from the Gnielinski correlation. The leading sensor agreed with the Gnielinski calculation while the center sensors agreed with the Dittus-Boelter predictions better. The predictor was designed under the assumption that one cavity represents the cooling performances of all cavities along the end-arc; therefore, the predictions closer to the sensor readings are preferred, or the Dittus-Boleter correlation is chosen.

The pipe flow entrance effect was designed to apply in the virtual pipe regions in two ways, as shown in Figure 7.7 before. The results of each method that were generated with

the Dittus-Boelter correlation are presented in Figure 7.13 below. The local temperatures were noticed to be less sensitive to the two entrance corrections, but the *Entrance A* method always predicted higher temperatures than the *Entrance B* method. The center stagnant region was affected by the entrance effect, as the result of the conduction calculations in the predictor. The stagnant region was more sensitive to the entrance methods and *Entrance A* predicted higher temperatures. *Entrance A* method was chosen for being close to the sensor readings, and for the fact that over-predicting in temperature is preferred for the predictor. In sum, the Dittus-Boelter correlation and the *Entrance A* method combination was chosen to quantify the virtual pipe local Nusselt numbers.

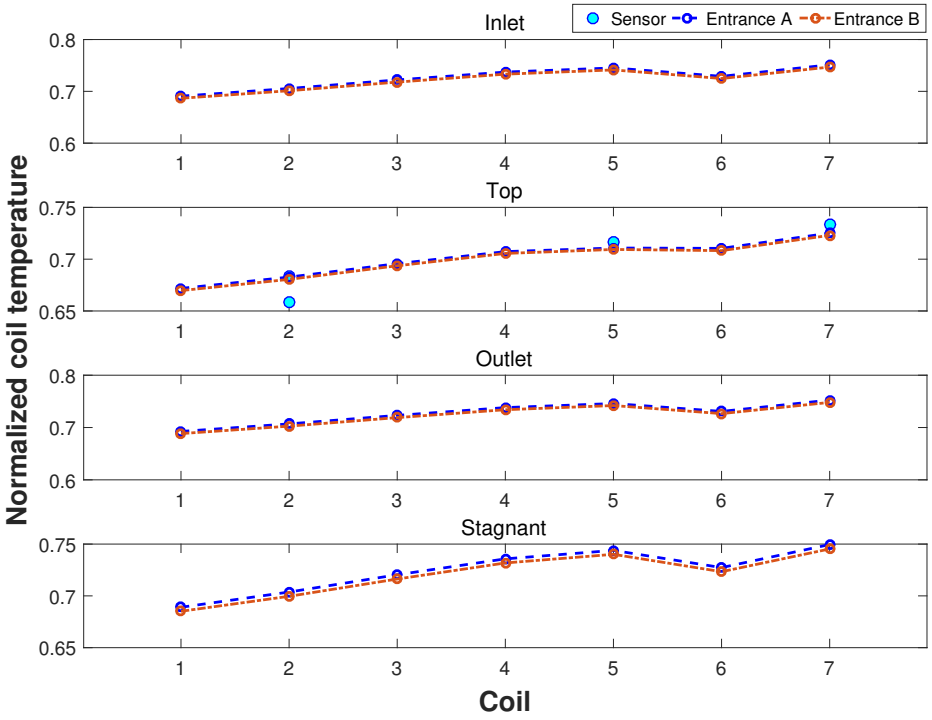

Figure 7.12: Prediction comparison between entrance effect methods

The predictor was then used to calculate temperatures under three given operating conditions, namely the mechanical condition (*MR* at 9.9% I_{rated}), half-load short-circuit 50% (*SC2* at 37.2% I_{rated}), and full-load short-circuit 100% (*SC100* at 72.9% I_{rated}) conditions, which have distinct heat loads. Even though predictor performances at the me-

chanical cold run and the low heat SC2 conditions are not targeted in this study, but it was of interest to study the predictor performances under different heat loads. The results are presented in Figure 7.12 below. It was noticed that the temperature differences between the top strap (*Top* calculations) and the center strap (*Inlet*,*Outlet*, and *Stagnant* calculations) increased as the field current increases. The differences between the straps are nearly zero at the MR condition, but were increased to ∼5 degrees at the SC100 condition.

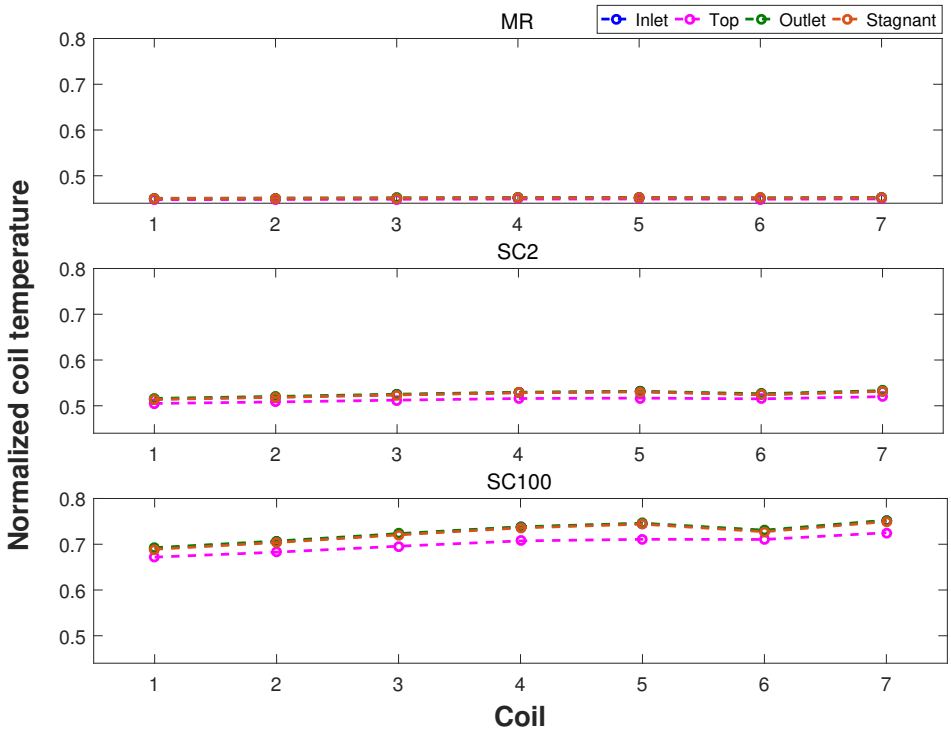

Figure 7.13: Virtual pipe entrance effect correction methods comparison.

The observed trends in temperature distributions between the top and center straps, under various heat loads were cross compared with the reported sensor readings and with the CHT simulation results next.

7.3.2 Factory Sensor Reading Comparison

Thermocouples were embedded inside the rotor straps for temperature monitoring. Those inside the rotor endturn region that were comparable to the applicable range of the

analytical predictor are shown in Figure 7.14 below. Sensors are installed inside the second top strap, at coil G, D and B only, and are at the same locations at both poles. Therefore, the sensors values are only comparable to the temperatures predicted for the cavity *Top* node. Sensors #1, #2, #5, and #7 are inside the end-arc length comparable to the predictor values; the rest are located at the corner of the coil surrounded by insulation. Three of the comparable sensors are placed at the middle of the arc and behind the center blocking; the fourth one is located one cavity opening θ_c away from the center, towards the leading direction inside the *coil G* only. The two sensors at the same location are reported to have a maximum of 1 degree Celsius between the north and south poles, and therefore the negligible differences between the poles were not discussed. The rest of the discussions in this section were conducted with the north pole sensors only.

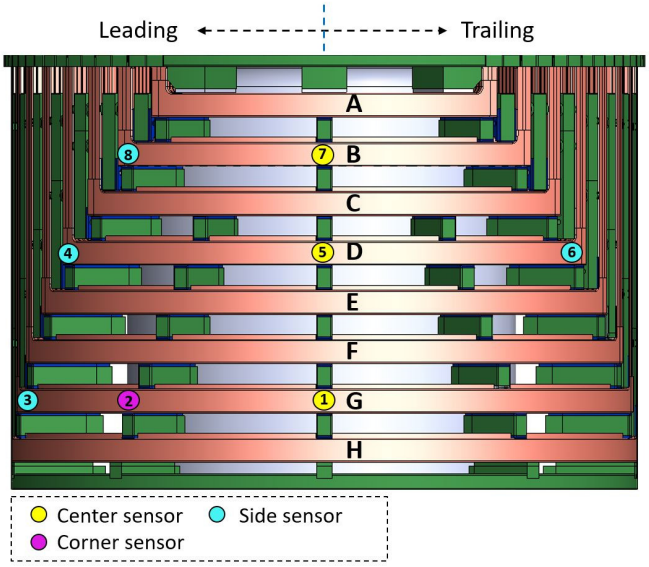

Figure 7.14: End-arc factory sensor locations.

The four corner sensors are inside the same strap as the other four sensors but are located between the *end-arc* and *straight length* heat transfer regions, and are outside the applicable range of the temperature predictor. The cooling conditions are less effective at the corners, since they are tightly constrained by insulation and little space is available for the coolant to pass through. Therefore, the corners would have slightly higher temperatures

than the regions directly adjacent to the circumferential cavities. These sensors were used here to estimate the temperature difference cross the length of the end-arc, between the leading and trailing sides. The temperature differences between the sensors are summarized in Table 7.3 below.

Table 7.3: Temperature difference between same strap embedded sensors.

Location	Temperature Difference (C)		
	SC100	**SC2**	**MR**
B (8 vs. 7)	1.6	0.1	0.1
D (4 vs. 5)	3	0.2	-0.3
D (5 vs. 6)	-5.1	0.3	-1.1
G (2 vs 1)	-2.9	-1	-0.4
G (3 vs 2)	8.9	1.7	-0.1

The comparisons between the sensors indicates that at lower heat conditions, or the SC2 and the MR, temperature variation along the end-arc lengths are negligible; but the temperature variations were significant at the high heat SC100 condition. Under high heat, temperature variation increases as the length of the end-arc increases. A maximum of 8.9 degrees temperature difference was concluded cross half length of the end-arc. In reality, as the result of the lower heat transfer rates at the coil corners, heat would conduct from the corner towards the cooler end-arc regions. This is not accounted for in the predictor, and therefore the end-arc sensors are expected to report higher temperatures than the predictor outputs. This condition is recognized during temperature comparisons. At all cases, sensor #2 reported lower coil temperature than sensor #1, and therefore partially verified the previous observations that the leading side cavities remove heat more efficiently than the trailing side ones.

The accuracy of the predictor is evaluated by then temperature difference calculated with Equation 7.44 below, which is compare with the desired ± 5 degrees Celsius error

tolerance.

$$\varepsilon = T_t - T_{correct} \tag{7.44}$$

Here, T_t is the predictor output value; $T_{correct}$ is the 'correct' strap temperature, or the reported sensor reading. Figure 7.15 below presents the comparison results between the north pole four sensors and the predictor top results, for the three provided 60Hz cases. Temperatures are normalized based on the given maximum allowable temperature of this the machine. The overall results have shown good agreements between the predicted values and the sensor readings, within the allowable 5 degrees Celsius tolerance. The predictor estimations slightly underestimated the wall temperature for the MR and $SC2$ conditions, and the estimations were much improved at the $SC100$ condition.

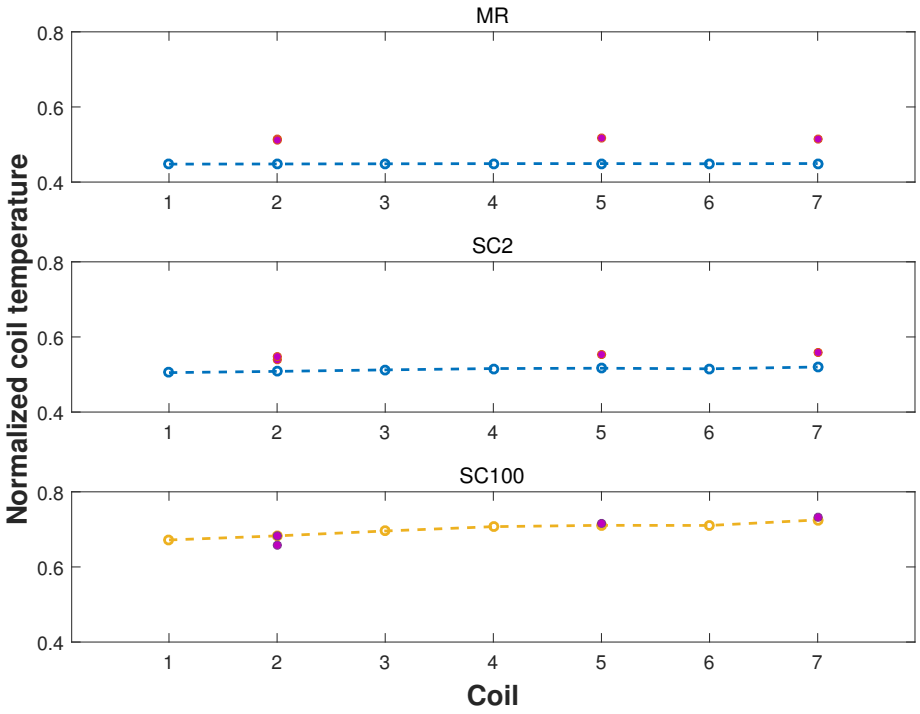

Figure 7.15: Temperature prediction comparison with sensors for all available 60HZ cases.

The prediction errors (compared to the sensor readings) are summarized in Table 7.4. Note that it is expected that the predictor will underestimate the coil temperatures at the top

straps, since the conduction from the rotor corner is not included in the predictor. Among the three presented representative cases, the predictor accuracy was improved as the coil heat load increased. The maximum error was observed at the MR condition, which has the lowest internal heat generation rate of 2% of the SC100 condition. The MR predictions exceed the error tolerance, and the predictor cannot achieve the desired performance at this low heat condition. It was suspected that at low heat, the hydrodynamic effects such as viscous heating dominate inside the cavities, which are heat sources that were not specifically accounted for in the proposed analytical predictor. The low heat conditions do not present risks of overheating, and was not targeted when designing the predictor; therefore, the rest of the discussion would no longer include the MR condition.

Table 7.4: Temperature comparison between predictor output and sensor reading at the reported locations.

Sensor Location		**Temperature Difference (C)**		
		MR	SC2	SC100
Center	Coil B	-8.1	-3.6	0.8
	Coil D	-8.1	-4.5	-0.7
	Coil G	-7.8	-4.5	-1.0
Side	Coil B	-7.7	-4.6	2.9

Figure 7.16 below presents predictions for all four cavity nodes, under the targeted SC100 condition. Coil $\#1$ (Coil H) through $\#7$ (Coil B) are going from the longest to the shortest coils. Coil temperatures gradually increase as the locations move downstream towards the coil $\#7$. A slight decrease in temperature in the center strap was noticed at coil $\#6$. This coil is unique for adjacent to smallest, four-row cavities on front and two-row cavity on the back, where front cavity θ_c is 40% smaller in size compared the back cavity. The cavity bulk flow strengths are different, and therefore the convective heat transfer conditions. Sensor readings are not available at this location, and therefore

this temperature decrease can not be justified yet; this observation was compared with the CHT results later. From coil #1 to #7, an approximately 6 degrees Celsius increase in temperatures was observed in the center strap, and a 8 degrees Celsius increase in the top strap. The top and the center of the coil was estimated to have a temperature difference of 3 degree Celsius. The predicted top node temperature is close to the side sensor that is located in the leading side; and the predictor still under-predict at the top node.

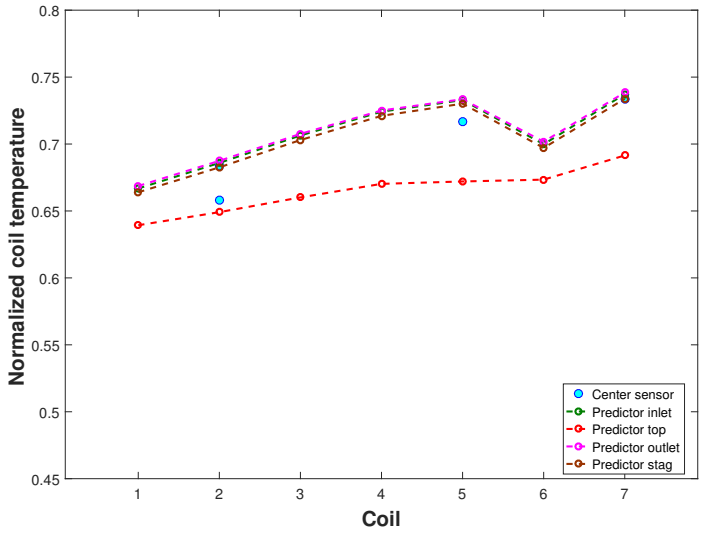

Figure 7.16: Temperature prediction for SC100 at cavity node locations.

In sum, the above comparisons indicated that the predictor was able to estimate temperatures at the top of the coil within the desired error range, and the temperature distributions within straps and between coils are both as expected. But only four locations can be verified in the entire end-arc region, and are not enough to conclude the accuracy of the predictor. For detailed comparisons, the conjugated heat transfer (CHT) simulations were conducted, of which the temperature results were extracted and used to verify prediction accuracy at both the top and the center of the coils, for all seven coils of interest.

7.3.3 Conjugated Heat Transfer Simulation Comparison

The conjugated heat transfer (CHT) studies were designed and conducted to provide additional temperature data in order to validate the accuracy of the proposed temperature predictor. The CHT model was developed based on the flow results obtained from the generator model; only the endturn circumferential cavities were included in the CHT *fluid* domain; the length of the end-arc rotor coils were modeled as *solid* and were added in the geometry. The coil cut-off locations follow the rotor coil heat transfer definition shown in Figure 3.18. The model detail is discussed in CHAPTER 3.4.1 SECTION 3.4.

CHT simulations were set up and carried out, and each simulation took about two days to complete, compared to less than 30 seconds taken with the analytical predictor. CHT simulations were computationally difficult and require more run-time since the solid volumes and the fluid volumes need to be solved iteratively, in order to capture the coupled heat transfer effects. Figure 7.17 below present contour plots of the coil temperatures for the *SC100* conditions. The plots are taken at the center of the coils, where embedded sensors were located, to allow point to point comparisons.

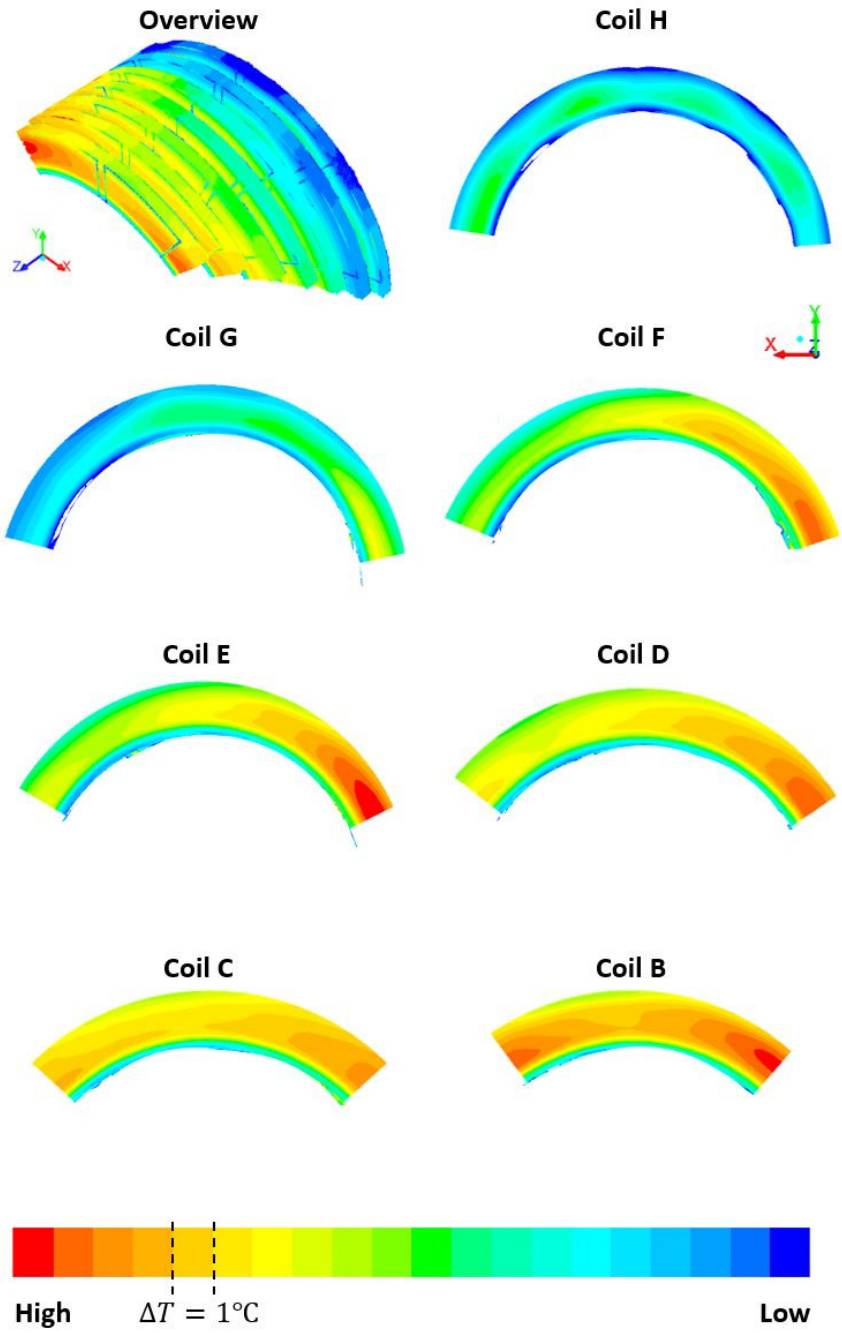

Figure 7.17: 60HZ generator endturn CHT wall temperature results under SC100 condition.

The contour plots were shown to investigate temperature distributions only. From *Coil G* downstream to *Coil A*, the arc-lengths l gradually decrease; but the coil temperatures gradually increase, which reflects the previously observed losses in the endturn flow mo-

mentum downstream from the rotor inlet. The bottom straps of the coils were the coolest, and the center of the coils are the hottest. The temperature variations cross the end-arcs at the SC100 condition are significant; a maximum of 7 degrees Celsius temperature difference between the leading and trailing side was noticed, which agreed with the provided sensor readings. A maximum of 15 degrees temperature increase was observed between the longest (coil H) and the shortest coil (Coil B). Hot spots were located at trailing side, around to the middle strap of the stacked coil. The absolute temperature differences between the leading and trailing sides were the lowest at the longest, upstream *coil G*, and the highest along the *coil E*. A slight temperature decrease was shown from *coil D* to *coil C*, and therefore the temperature drop predicted in the predictor results were not unreasonable.

CHT temperature readings were extracted at the same nodal locations in the thermal-fluidic network, as labeled in Figure 7.18 below. Since the predictor was designed by assuming no flow differences between the same row cavities, the extracted local CHT temperatures were averaged first to obtain the representative strap temperature, before comparing with the analytical predictor.

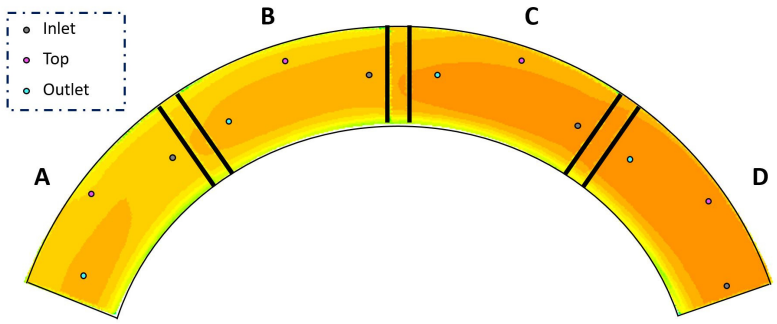

Figure 7.18: CHT temperature extraction locations.

Temperature comparison results are summarized in Table 7.5 below, errors were calculated using Equation 7.45. The negative values means the predictor under-predicts, and vice versa. Two comparisons were conducted, which are: (1) predictor versus strap aver-

age, and (2) predictor versus strap maximum.

$$\varepsilon = T_p - \overline{T}_{CHT} \tag{7.45}$$

Table 7.5: Summary of temperature comparisons between CHT and analytical predictor under the SC100 condition.

Coil	Temperature Difference (C)			
	Center avg	Center max	Top avg	Top max
B	-2.9	-1.9	-2.9	-3.4
C	-3.7	-2.5	-3.7	-4.1
D	-3.7	-1.6	-3.7	-4.5
E	-4.1	-3.6	-4.1	-4.1
F	-3.5	-4.4	-3.5	-4.7
G	-2.1	-4.4	-2.1	-3.8
H	-2.4	-3.1	-2.4	-2.0

The predictor under-predicted the coil temperature, but both the average and the maximum temperature differences were within the desired error tolerance. The predicted temperature were plotted and shown in Figure 7.19 below, which verified that the temperature distributions had similar trends between the CHT and the predictor as well.

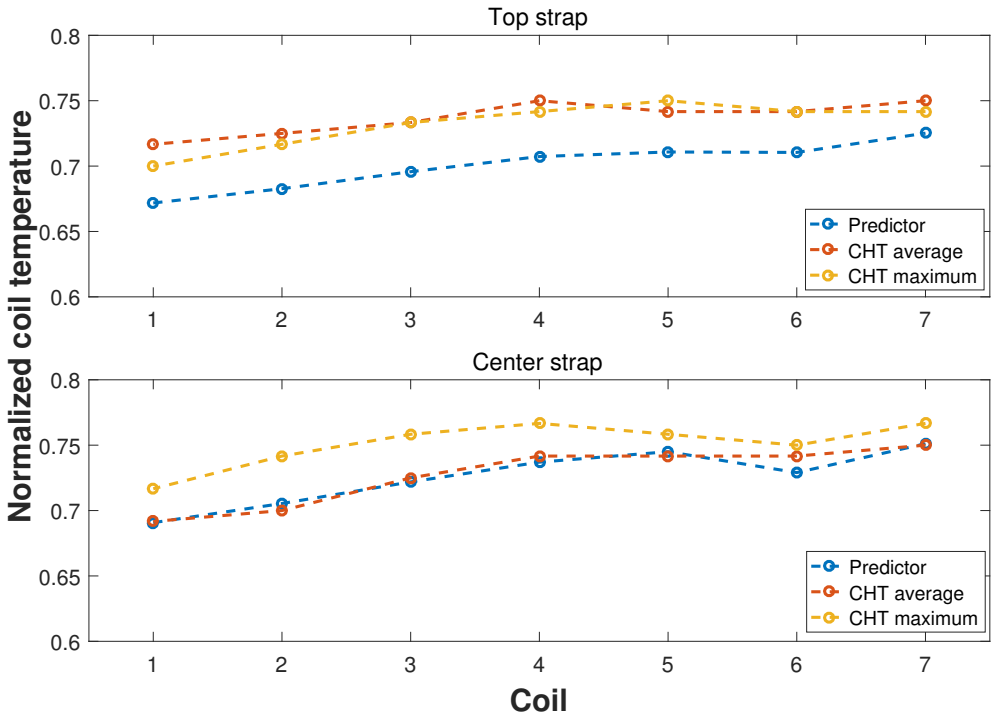

Figure 7.19: Predictor temperature versus CHT temperature for SC100 condition.

In sum, the comparisons with the sensor reading were able to verify the ability of the predictor to estimate temperatures along the top of the coils, while the comparisons with the CHT results verify the predictions at the center of the coils. Both the CHT model and the analytical predictor are demonstrated to be valid to quantify end-arc coil temperatures.

The temperatures for the *rated* condition were investigated last. Factory testing is not possible at this condition, and therefore the rotor coil temperatures have to be estimated through either CHT simulation or the proposed analytical predictor. The temperatures at the center of the coils by the CHT simulations are shown in Figure 7.20 and the predictor calculations are plotted and shown in Figure 7.21. Similar temperature distributions were presented, comparing to the SC100 results. Coil temperatures spread over a higher range, where an approximately 20 degrees increase in temperature was observed between the two furthest coils. The temperature difference between the leading and trailing side along the same coil was increased as well. The maximum temperature was still smaller than the

maximum allowable insulation temperature.

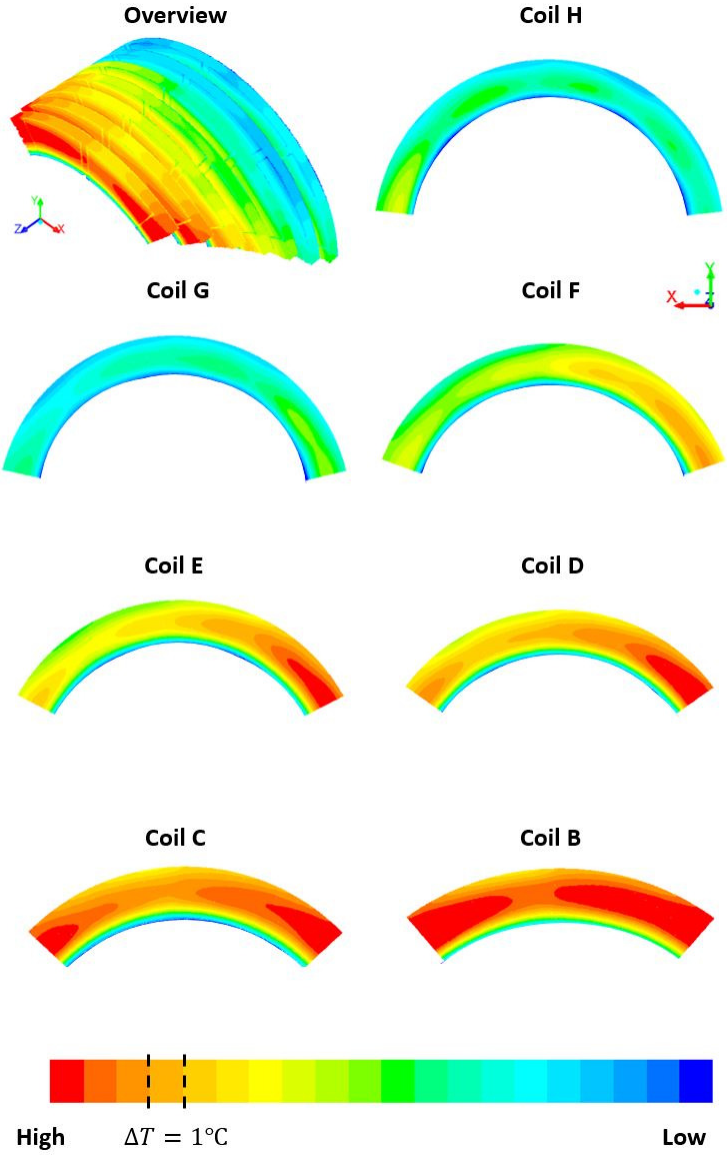

Figure 7.20: Contour plots of CHT coil temperatures.

The temperature results are shown in Figure 7.21 below. The top plot compared predictor calculated temperatures with the CHT predicted strap average temperatures, and the bottom compared with the local strap maximum temperatures.

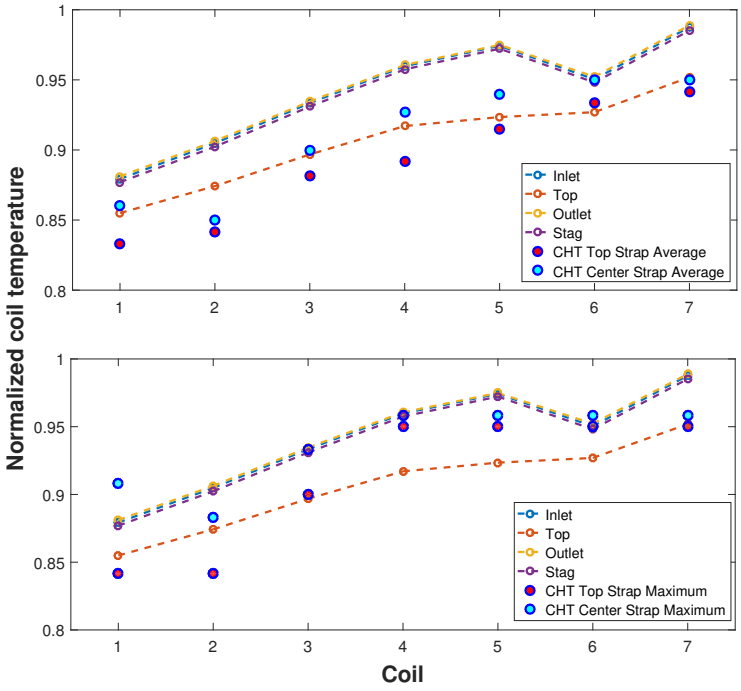

Figure 7.21: Predicted rated condition coil temperatures.

The temperature differences were calculated and presented in Figure 7.22, between the CHT results and the predictor estimations. The blue dashed lines present the averaged strap temperature; and out of the 14 predictions, one value is out of the ± 5 degrees tolerance, and 12 are over-predicting. The purple diamond points present the temperature differences between the absolute strap maximum strap temperatures and the predicted temperatures, where one prediction exceeds the desired tolerance and 11 coils are under-predicted.

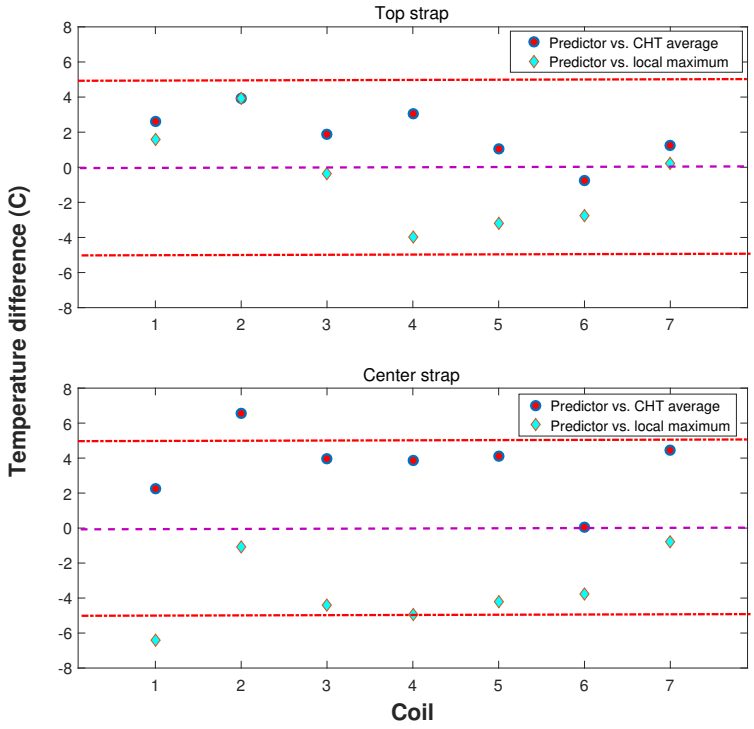

Figure 7.22: Prediction comparison at the rated condition.

7.3.4 Predictor Summary and Discussion

The previous section performed temperature calculations with the proposed analytical temperature predictor. Through the comparison with both the reported sensor readings and the CHT results, the predictor has been demonstrated to be feasible to estimate end-arc coil temperature at the desired accuracy. The following predictor performances can be concluded based on the comparisons:

1. The predictor is sensitive to the heat load q_c. The current predictor is unable to capture the coil temperatures under the cold runs such as low heat MR conditions; but is able to perform well for the heat runs that with heat above the SC2 load.

2. The predictor is prone to under-predict the strap temperatures, according to the

comparisons with reported factory sensors. The predictions may be improved by accurately quantifying the rate of conduction: (1) from the hotter rotor corners that is adjacent to the end-arc, and (2) between the stacked straps within the coil. Both would require separate studies in order to quantify the rates.

3. The predictor is able to estimate coil temperatures within the desired ± 5 degree of Celsius for the heat runs, in less than 30 seconds as desired.

4. The predictor was design to capture the coil temperature by applying isothermal strap assumption. But it was realized from both the reported sensors and the CHT simulations that at high heat conditions, the temperature variation along the strap between the leading and the trailing sides are significant. The current highest loading condition, or the rated condition results in a maximum of 6.3 degrees under-estimated highest temperature, and 93% prediction within the prediction tolerance. They local hot spots can be reasonably assumed to be *5 degrees* higher than the predictor values, but future detailed studies might be necessary to accurately quantify the local hot spots temeraptures, on a coil by coil basis.

7.4 Discussion

7.4.1 Predictor Error Analysis

There are two main sources of errors that are recognized in the temperature predictor, which are the uncertainties in the inlet condition, and the propagated error from the virtual pipe hydraulic diameter calculations. The associated errors in temperature prediction were demonstrated with the highest heat condition, or the heated condition, where the errors were expected to be the highest. The inlet angle in this study was estimated based on the given rotor fan conditions, and therefore introduced uncertainties in the temperature

predictor. Therefore, it was of interest to investigate the associated prediction errors, as the results of uncertainties in the inlet velocity components. A $\pm 10\%$ confidence interval was investigated for the inlet angle with the constant nominal axial velocity magnitude. The axial velocity is considered to be accurate since flow rate can be directly measured during factory testing, and the reported values were verified by separate studies. Therefore, the inlet tangential velocity magnitudes were adjusted, which affects the pumping momentum dP_{stat} in the fluid network. The corresponding temperature predictions at each node location are presented in Figure 7.23. Decreasing the inlet angle, or increasing the tangential velocity resulted in lower temperatures, and vice versa. The 10% difference in the inlet angle resulted in a temperature difference of 3 degrees with respect to the nominal results. Therefore, additional ± 3 degrees Celsius error would be expected if the inlet condition can not be accurately determined.

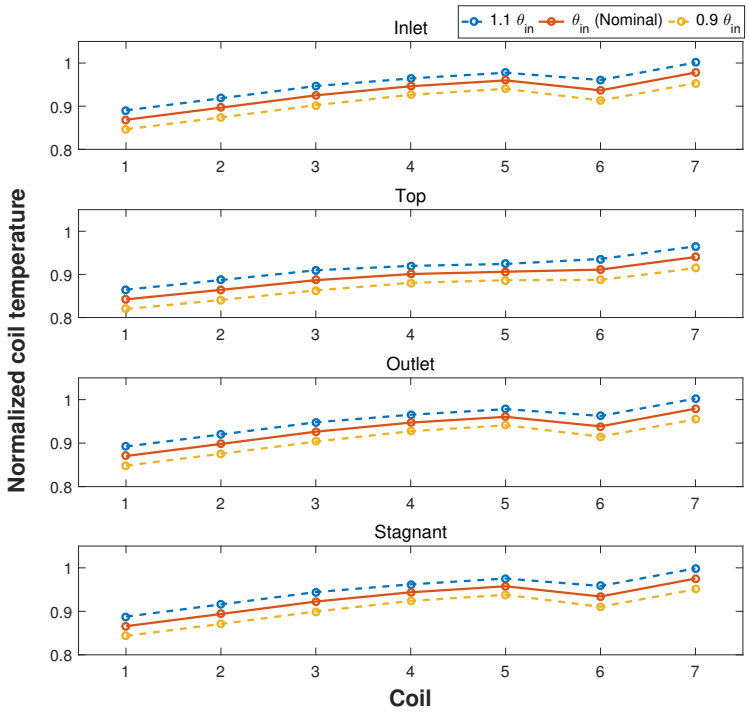

Figure 7.23: Temperature prediction comparison for inlet angle accuracy at $\pm 10\%$ variation under the rated condition.

As it was discussed in the previous chapter, error in D_h calculation directly affects the heat transfer rates, and therefore the wall temperature prediction. Here, $\pm$ 10% error in D_h prediction was inspected, and the results are shown in Figure 7.24.

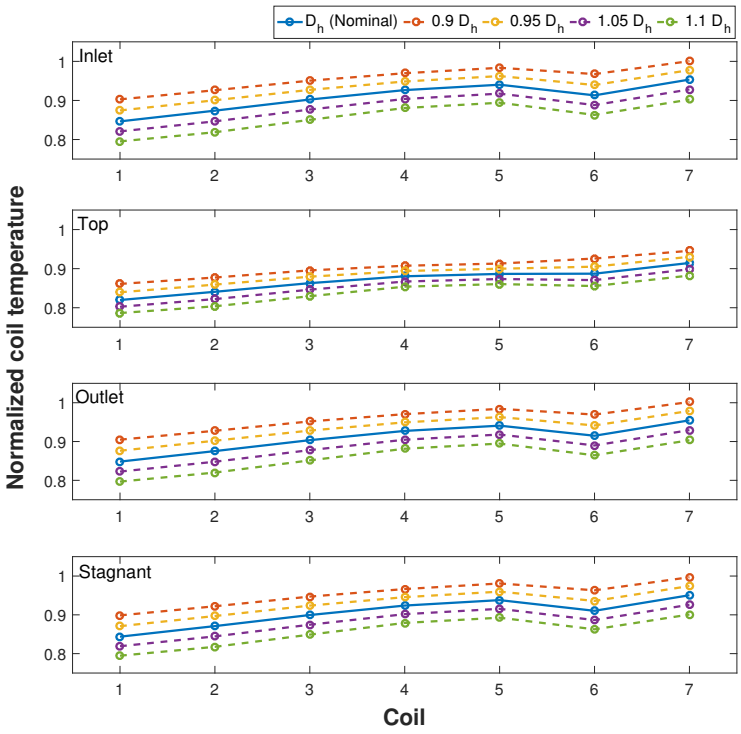

Figure 7.24: Temperature prediction comparison for local virtual pipe hydraulic diameter accuracy at $\pm 5\%$ and $\pm 10\%$ variations, under the rated condition.

The predicted wall temperatures are more sensitive to the hydraulic diameters. A -10% and $+10\%$ error in D_h results in a +6 and -5 degree Celsius errors with respect to the nominal prediction, respectively. The validations cases had an average of $\pm 5\%$ error in D_h results, which caused a A -5% and $+5\%$ error in D_h results in a +3 and -2 degree Celsius errors with respect to the nominal prediction, respectively. They are both acceptable and therefore the 10% error in D_h calculation defined in the previous chapter is verified. And it is noticed that under-predicting the hydraulic diameter affects the coil temperature slightly more than over-predicting.

7.4.2 Endturn Ventilation Design Inspection

The predictor was implemented to estimate the wall temperatures of the possible parametric design scenarios discussed in CHAPTER 5. Two types of designs were investigated, which were geometric cases and inlet cases at constant inlet flow rates. The geometric conditions of interest are: (1) constant width at decreased cavity opening, and (2) constant cavity angle with varied cavity widths. The estimated coil temperatures are shown in Figure 7.25 below.

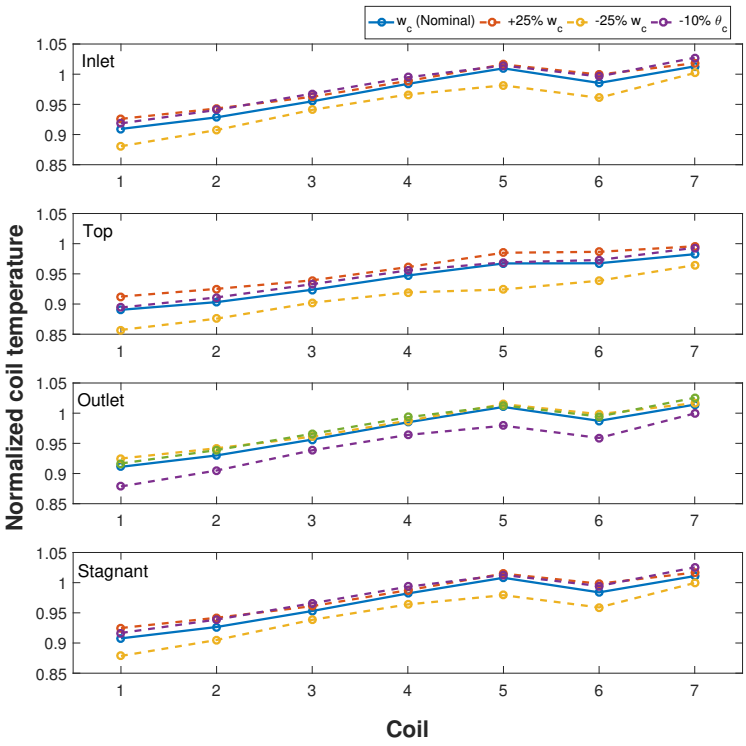

Figure 7.25: Predicted wall temperatures for the parametric geometric cases.

The prediction indicated that the coil temperatures are not sensitive to the changes in cavity geometry. The general patterns in coil temperatures observed are: (1) a smaller cavity opening pattern under the same width resulted in higher coil temperatures in the center strap but lower at the top strap, which corresponds to the observation that smaller cavity constrains the annulus flow pumping availability and therefore the virtual pipe velocities;

(2) a smaller cavity width at the same cavity openings resulted in lower coil temperatures, as the result of higher virtual pipe velocities. Next, coil temperature at different inlet conditions were compared and shown in Figure 7.26 below. The comparisons were conducted at the nominal axial velocity when changing the inlet angle, and therefore the inlet tangential velocity. The results indicated that the inlet conditions significantly affects the cooling efficiency of the circumferential cavities, where a 10 degree change in the inlet angle can result in a 10 degrees change in the coil temperatures.

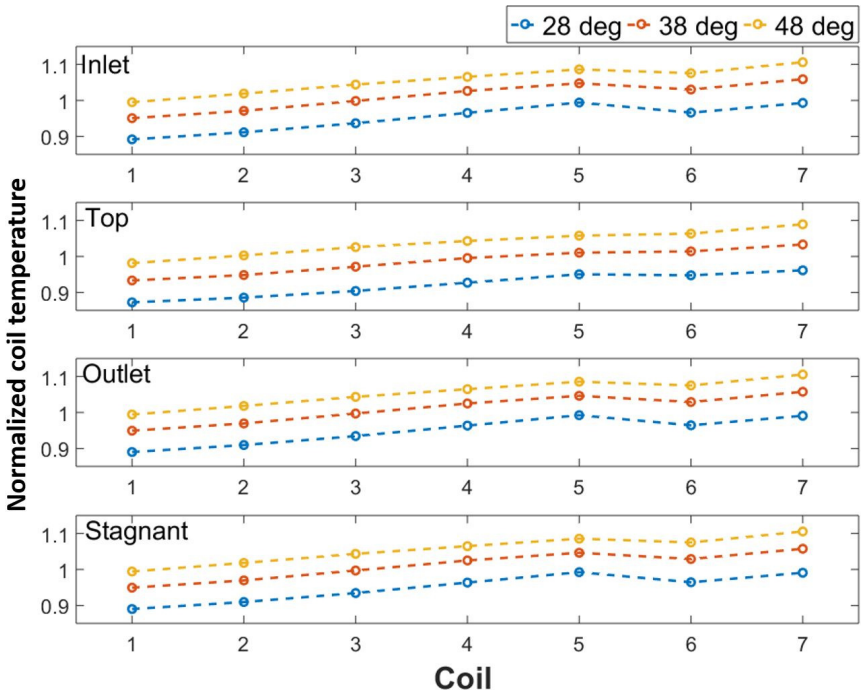

Figure 7.26: Predicted wall temperatures for the parametric inlet cases.

7.4.3 Application on 50Hz Machines

The applicability of the temperature predictor was also demonstrated by applying on the air-cooled, 50 Hz machines. This machine has a similar ventilation design, where the flow physics are expected to be similar. They 50 Hz machine is different from the 60 Hz model for (1) rotating at a slower speed, (2) having inner and outer rotor diameters that are approximately 1.06 time larger, (3) consisting of rotor coils that are 10% thicker but 12.5 % closer, (4) having the same cavity pattern but are slightly smaller than the 60 Hz, (5)

having a resultant inlet angle of 40 degrees.

The prediction results are shown in Figure 7.27. The sensors shown are located at the same places as the 60 Hz machine. Prediction upstream is still as expected and within the tolerance, but the predictor failed to capture the downstream flow conditions properly in order to capture the correct amount of heat transfer. A maximum of 11 degrees error occurred at the shortest, coil #5 and the prediction can no longer achieve the desired level of accuracy. Therefore, it is realized that additional studies are necessary in order to characterize, and quantify the coupled effects of the above design differences on the resulting cavity flows, in order to improve the prediction accuracy for the 50 Hz machine.

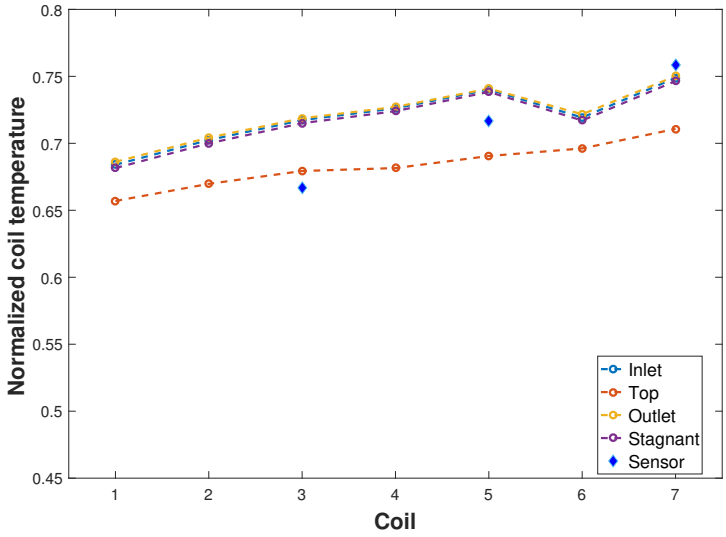

Figure 7.27: Predicted wall temperatures for 50 Hz machine.

7.5 Conclusion

An analytical temperature predictor was developed that is constructed following the lumped-circuit network method, to quickly estimate the coil temperatures under the given operating condition. The predictor has two levels, or the cavity level and nested cavity system level. A thermal-fluidic network is developed that iteratively calculate the adjacent coil temperature, where two neighboring cavities are related by mixing the fluid tempera-

ture. The cavity heat transfer was calculated as the propagated result from the virtual pipe bulk flow and the rotational flow. Convection and conduction heat transfer calculations are performed, where convection removes heat from the coil, and conduction accounts for the imbalance in local heat as the result of different in heat transfer rates to correct for the localized high temperature.

The predictor is able to achieve the objective of the research, which is able to provide accurate temperature estimation in less than 30 seconds within the desired $\pm$5 degree Celsius error. The predictor was verified with the reported factory testing sensor readings, and with endturn CHT simulation results. Both comparisons demonstrated the efficacy and accuracy of the predictor. The predictor was also used to calculate coil temperature at the highest heat condition, or the rated condition; the results were compared with CHT result and showed good agreement. The predictor over-predicts the local tempreatures at the rated condition, as desired. Therefore, the predictor was valid to apply on the 60 Hz machine. The inlet condition and the local virtual pipe hydraulic diameter D_h are the two main sources of error when using the predictor; the predictor was noticed to be more sensitive to the accuracy of the virtual pipe hydraulic diameters than the inlet angle. Temperature variation along the strap was realized and based on the rated condition results, it is also concluded that a +5 degree Celsius can be applied on the predictor result in order to estimate the maximum strap temperature. The predictor was tested on the 50 Hz machine that has a similar ventilation design; higher prediction errors was observed but the prediction follows the trends of the reported sensor readings. Therefore, once detailed fluid studies is performed and the differences in flow between the two ventilation designs are captured, the predictor can be adjusted to apply on the 50Hz machine at the desired accuracy.

CHAPTER 8

CONCLUSION

8.1 Summary and Conclusion

The increasing demand for more electricity have brought about the need for improved rotor ventilation performances of the large industrial turbo-generators. Overheating in the rotor endturn region under the expected operating conditions is one of the major ventilation concern for the air-cooled machines, but a fast and accurate temperature monitoring method is not yet available. The rotor endturn coil temperature evaluations are currently heavily relied on the time-consuming computational fluid dynamics simulations, which posses difficulties in the rotor ventilation design. This presented work develops a fast-solving analytical predictor, which can estimate the rotor end-arc coil temperatures at the expected high load operating conditions. The predictor is developed using the lumped-circuit method, which has been implemented by many researchers to successfully apply for many electric machines. To do so, the fluid properties in the nested cavities adjacent to the heated coils are first numerically captured with detailed CFD simulations. The cavity flow phenomenon is inspected and a virtual pipe method is proposed to describe and quantify the observed internal bulk flow characteristics. The virtual pipe hydraulic diameters are quasi-analytically determined, by mathematically matching the CFD extracted velocity profile with the expected theoretical profile for the internal turbulent pipe flow. Generic correlations of the defined local virtual pipe segments are developed in terms of the identified design parameters, as a tool to estimate the D_h values for any design scenarios within the applicable ranges of the design parameters. A set of CFD parametric studies are conducted to provide a reasonable sampling set to use for the correlation development. Finally, a thermal-fluidic network is developed by implementing the virtual pipe description of the

cavity internal bulk flow, which accounts for convective and conductive heat transfers at the coils to calculate the coil temperatures under different heat loads. The predictor is verified with both the reported factory sensor readings and CHT simulation, and is concluded to be able to achieve the desired ± 5 degrees of Celsius error.

Pursuant to the research presented in this thesis and summarized above, the following conclusions are drawn:

- *Endturn circumferential cavity phenomenological study*

  The observed peripheral bulk flow in all endturn rotating circumferential cavities were studied, and the following conclusion are drawn:

  - The circumferential cavity in the rotor endturn region has an internal counter-clockwise peripheral bulk flow, which occupies approximately 35% of the cavity volume.
  - The cavity bulk flow can be separated into three local components, namely the inlet, top and outlet components, in the direction of the flow along the edges of the cavity.
  - The inlet bulk flow is the strongest among the three components, whereas the outlet bulk flow is the weakest. The outlet bulk flow velocity magnitude is typically 25% to 45% lower compared to the inlet velocity magnitude. Increasing the cavity opening θ_c introduces greater velocity differences between the inlet and the outlet.
  - All three bulk flow components have parabola-shaped velocity profiles, similar to those of the traditional internal pipe flows. The proposed virtual pipe method provides a good description of the local bulk flow.
  - The characteristics bulk flow is in the circumferential cavity is dominated by pressure driven flow. The heat conditions have negligible

impact on the sizes of the bulk flows. The contribution of the heating condition is negligible as demonstrated by only 3% difference in the local bulk flow sizes, between the heat ratio of 45:1.

  - The cavity peripheral bulk flow can be described as three hydrodynamically fully developed one-dimensional local bulk flows, in which the flow properties are described by the local relative velocity magnitude. Axial velocity within the cavity present less than 6% of the relative velocity magnitude.

- *Parametric study of the endturn circumferential cavity*

  A set of parametric experiments were conducted to pursue quantitative understanding of the bulk flows of the circumferential cavities. The following conclusions are obtained:

  - The characteristic flow pattern of the cavity bulk flow collapses as the cavity width is increased beyond 125% of the nominal cavity width.

  - Increasing the inlet tangential velocity increases the inlet momentum flux into the cavity, supporting the characteristic flow in wider cavities.

  - The equivalent local hydraulic diameter D_h is calculated using a quasi-analytical method, based on matching the velocity profile with the $1/7^{th}$ power-law velocity profile for turbulent pipe flow. A 97% success rate was achieved across the 576 D_h calculations performed.

  - The inlet and outlet components of the characteristic bulk flow pattern occupy approximately 22% and 33% of the cavity opening θ_c, respectively; the top component occupies approximately 30% of

the cavity height Δr, for all flow condition studied.

  - A correlation for the equivalent hydraulic diameter D_h is expressed in terms of the cavity dimensions and the rotor inlet condition. The developed local D_h correlations are verified to have an average of $\pm 4\%$ prediction error.

- *Thermal-fluidic network of the nested endturn circumferential cavity cooling system*

  In pursuant to the study of the analytical prediction of the end-arc coil temperatures presented in CHAPTER 7, the following conclusions are drawn:

  - The analytical predictor is able to calculate coil temperatures in less than 30 seconds, compared to the weeks needed for CHT simulations. The predictions were able to achieve the desired $\pm$ 5 degrees Celsius error.
  - A $\pm 10\%$ error in the inlet velocity angle θ_{in} results in an approximately $\pm$ 3 degrees Celsius error in the temperature prediction.
  - A $\pm 5\%$ error in the local hydraulic diameter estimation D_h results in an approximately $\pm$ 3 degrees Celsius error in the temperature prediction.
  - The analytical predictor over-predicts coil temperatures by an average of 3 degrees Celsius, for characteristic flows described by the Reynolds number between $8E^4$ and $5E^5$.

8.2 Contributions

The main contributions of the work presented in this thesis are:

- *Development of generator rotor CFD model*

  In accordance to the literature survey, the CFD modeling presented in this thesis is the first reported study using a large scale CFD model to solve the rotor ventilation in large scale turbo-generators.

- *Development of quantifiable description of the cavity internal flow*

  - This is the first time the virtual pipe description is implemented on rotating circumferential cavities, in order to estimate adjacent heated coil temperatures.
  - The proposed virtual pipe method is able to effectively describe the observed unique counter-clockwise peripheral cavity bulk flow. The method simplifies the complex three-dimensional flow into three one-dimensional local pipe flows, which are hydro-dynamically fully developed and can be described with known empirical pipe flow correlations. The virtual pipe method is able to capture the flow properties quickly without the need of either solving the three-dimensional Navier Stokes equation, or using the time consuming CFD simulations; it also provide means to incorporate the fast-solving lumped-circuit method to develop the target coil temperature predictor.
  - A systematic method has been developed to extract and process the cavity CFD results, such that the massive data can be effectively and efficiently analyzed in order to capture the dominating flow characteristics.
  - An analytical method was developed to calculate the size of the local bulk flows in accordance to the proposed virtual pipe descriptions, such that the hydraulic diameter D_h calculations are physics

tractable, where the results match the flow characteristics of those for the traditional turbulent internal pipe flows.

  - Mathematical correlations of the hydraulic diameters are quasi-analytically developed, which are presented in terms of the identified design parameter. The correlations are generic such that it is able to calculate bulk flow sizes for various design cases of interest.

- *Development of endturn thermal-fluidic network*

  - A thermal-fluidic network is developed for the nested endturn circumferential cavity system, by calculating the hydrodynamic and heat transfer resistances. The endturn cavities were treated as one continuous pipe system, where the fluid and thermal conditions of cavities are inter-related.

  - The convective heat transfer within the cavities are captured as the propagated heat transfer rates of the virtual pipe flows and the rotational flow. The cavity volume was separated into four regions based on the local flow properties, where their corresponding heat transfer rates were individually determined.

  - The parallel flow from the fast rotational motion can be approximated with natural convection between vertical parallel plates, for the fact that the rotational acceleration resembles the effect of the gravitational acceleration.

Publication of these results in archival is delayed pending the filing of intellectual property protection as the request of the sponsor. Manuscripts are in preparation and will be submitted at the completion of the one year publication embargo.

8.3 Recommendation for Future Work

During the course of this study, additions and extensions to the work were recognized, which are the following

- *Virtual pipe hydraulic diameter correlation improvement*

  The hydraulic diameter correlations developed in this study were able to perform at the desired level of accuracy; but improvements can be made by conducing parametric cases at higher resolutions.

- *Predictor improvement*

  - Prediction can be further improved by accounting the additional heat source from the corner of the rotor turns, which were verified to be hotter based on the readings of the reported factory sensors.
  - Strap conduction can be improved by quantify the actual rate of conduction in the radial direction, through the insulation layers.
  - The predictor can be modified to focus on capturing the hydrodynamic effects, such as the viscous heating on the heated walls, in order to predict wall temperature under cold conditions such as the mechanical condition.
  - Additional flow investigations of the air-cooled 50 Hz machine, and possibly the hydrogen-cooled machines can be performed, to capture the differences in the flow phenomenon between the ventilation design, for an accurate predictor specifically for the target machine.

- *On-line rotor temperature monitoring and prognostics*

  - Application of the fast-solving temperature predictor to on-line monitoring and predictive maintenance of electric machines.

– Application of fast-solving temperature predictor to on-line monitoring of thermal stresses under start condition and thereby enable analytical estimation of useful remaining starts for large medium-voltage (MV) and high-voltage (HV) machines.

Appendices

APPENDIX A

CFD THEORIES

A.1 FLUENT Governing Equations

1. **Conservation of mass**

$$\frac{\partial \rho}{\partial t} + \bigtriangledown \cdot \rho \vec{v_r} = 0 \tag{A.1}$$

2. **Conservation of momentum**

$$\frac{\partial}{\partial t}(\rho \vec{v_r}) + \bigtriangledown \cdot (\rho \vec{v_r} \vec{v_r}) + \rho(2\vec{\omega} \times \vec{v_r} + \vec{\omega} \times \vec{\omega} \times \vec{r}) = - \bigtriangledown p + \bigtriangledown \cdot \bar{\bar{\tau}}_r + \vec{F} \tag{A.2}$$

where p is the static pressure; two additional acceleration terms are added to momentum equation, which are Coriolis acceleration $2\vec{\omega} \times \vec{v_r}$ and centripetal acceleration $\vec{\omega} \times \vec{\omega} \times \vec{r}$; $\bar{\bar{\tau}}_r$ is stress tensor is calculated as the sum of unit tensor and effect of volume dilation, as shown in Euqation A.3; ρg is gravitational body force and $\vec{F}$ is external forces along with other model-dependent source terms such as porous media and additional user-defined sources.

$$\bar{\bar{\tau}}_r = \mu[(\bigtriangledown \vec{v_r} + \bigtriangledown \vec{v_r}^T) - \frac{2}{3} \bigtriangledown \cdot \vec{v_r} I] \tag{A.3}$$

where I is the unit tensor, and the first term $\bigtriangledown \vec{v_r} + \bigtriangledown \vec{v_r}^T$ is to capture the effect of volume dilation.

3. **Conservation of energy**

$$\frac{\partial}{\partial t}(\rho\vec{E_r}) + \bigtriangledown \cdot (\rho\vec{v_r}H_r) = \bigtriangledown \cdot (k \bigtriangledown T + \bar{\bar{\tau}}_r \cdot \vec{v_r}) + S_h \tag{A.4}$$

energy equation is written in terms of relative terms, namely relative internal energy $\vec{E_r}$and relative total enthalpy H_r.

$$E_r = h - \frac{p}{\rho} + \frac{1}{2}({v_r}^2 - {u_r}^2) \tag{A.5}$$

$$H_r = E_r + \frac{p}{\rho} \tag{A.6}$$

A.2 Near wall calculations

Friction or shear velocity is calculated as [80]

$$U_\tau = \sqrt{\frac{\tau_w}{\rho}} \tag{A.7}$$

where τ_w is wall shear stress. Dimensionless length and velocity is calculated as

$$y_+ = \frac{yU_\tau}{\nu} \tag{A.8}$$

And the dimensionless velocity, and is the ratio between velocity u parallel to the wall as a function of distance y from the wall, divided by the friction velocity u_τ

$$u_+ = \frac{u}{U_\tau} \tag{A.9}$$

and y is normal distance from the wall. Equation A.8 and A.9 are commonly used together to estimate the placement of first grid point.

APPENDIX B

CFD MODEL SUMMARY

B.1 Generator Geometries

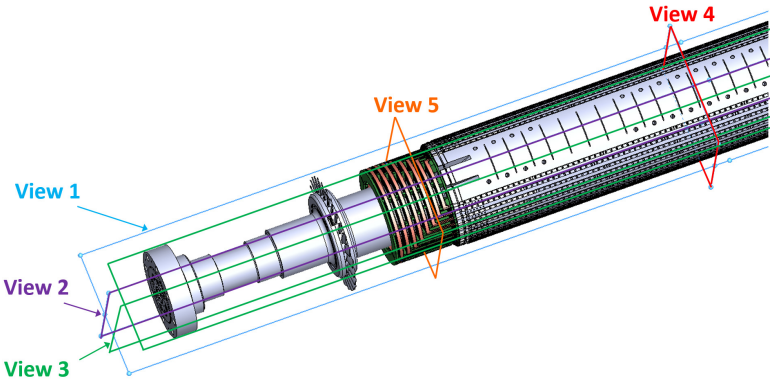

Figure B.1: Rotor cutout view planes

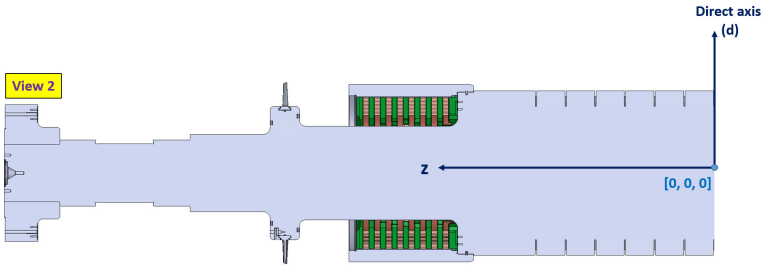

Figure B.2: Rotor cutout view planes

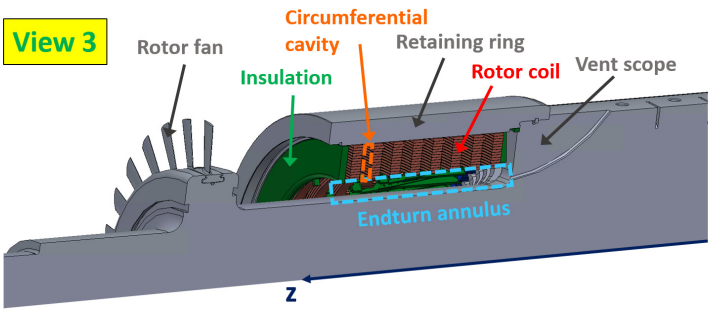

Figure B.3: Rotor cutout view planes

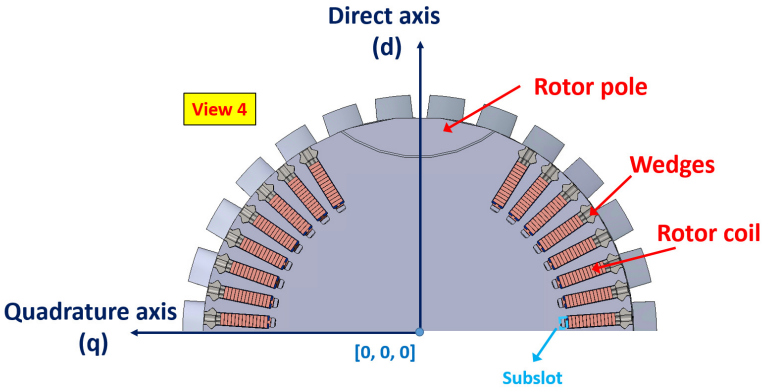

Figure B.4: Rotor cutout view planes

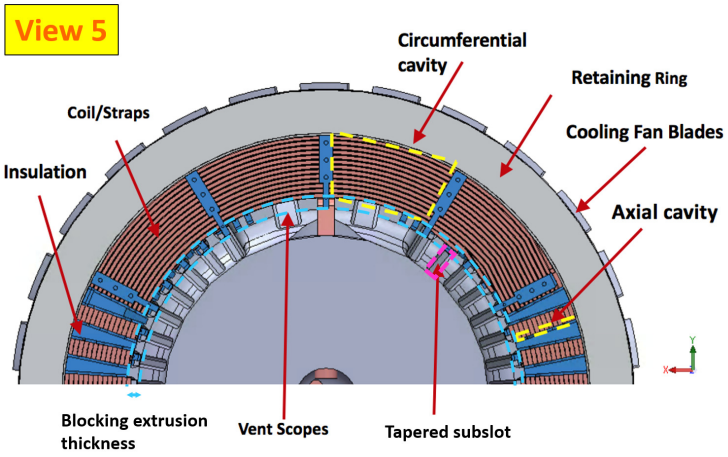

Figure B.5: Rotor cutout view planes

B.2 Generator CFD Model Boundary Condition Summary

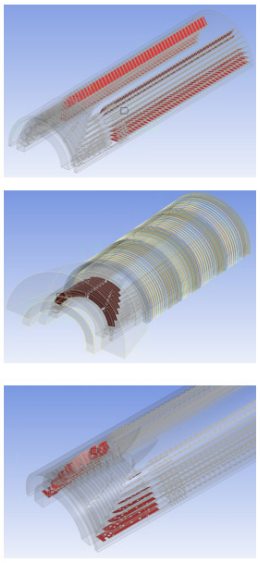

Current loading affected surfaces
- Surfaces adjacent to copper coils
  - Can be unloaded or loaded with different Ohmic losses depending on the expected operating condition tested
- Material: copper
- Inputs
  - Heat flux

Figure B.6: Loading condition affected boundaries

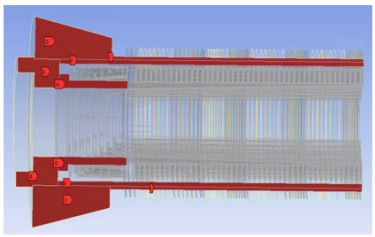	Half rotor surfaces: ○ Periodic boundary
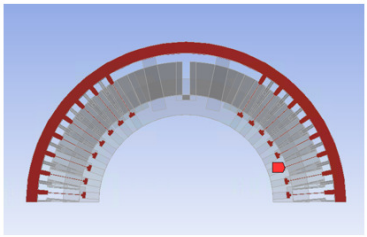	Rotor Center: Symmetry

Figure B.7: Additional boundary conditions

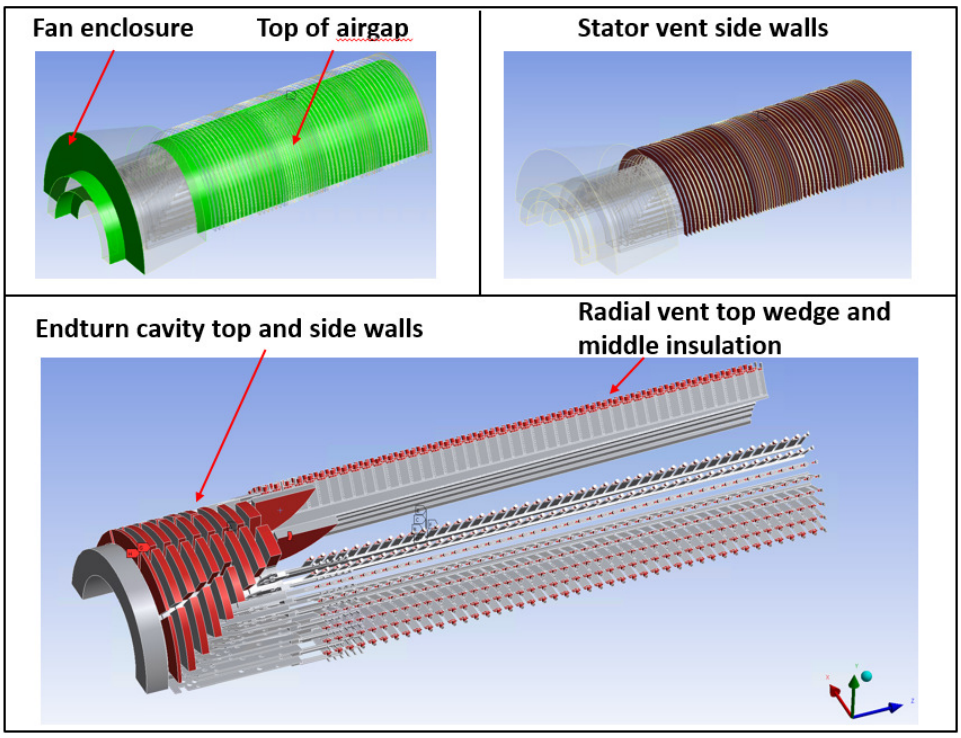

Figure B.8: Adiabatic surfaces

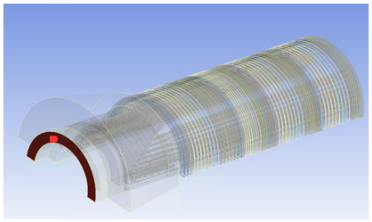	**Front fan inlet:** ○ Pressure inlet ○ Inputs ▪ Gauge pressure ▪ Temperature ▪ Velocity components vector
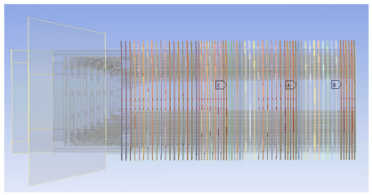	**Stator outlet zone** ○ Pressure outlet ○ Inputs ▪ Temperature ▪ Gauge pressure ▪ Target mass flow rate
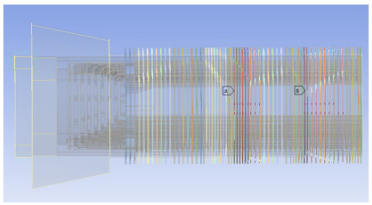	**Stator inlet zone** ○ Pressure inlet ○ Inputs ▪ Gauge pressure ▪ Target mass flow rate
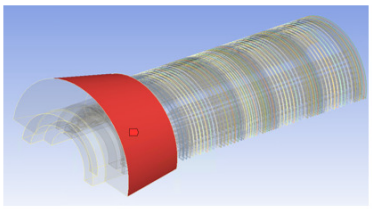	**Endturn Stator winding** ○ Pressure outlet ○ Inputs ▪ Gauge pressure ▪ Target mass flow rate

Figure B.9: Inlet and outlet boundaries

APPENDIX C

ENDTURN CAVITY FLOW RESULTS SUMMARY

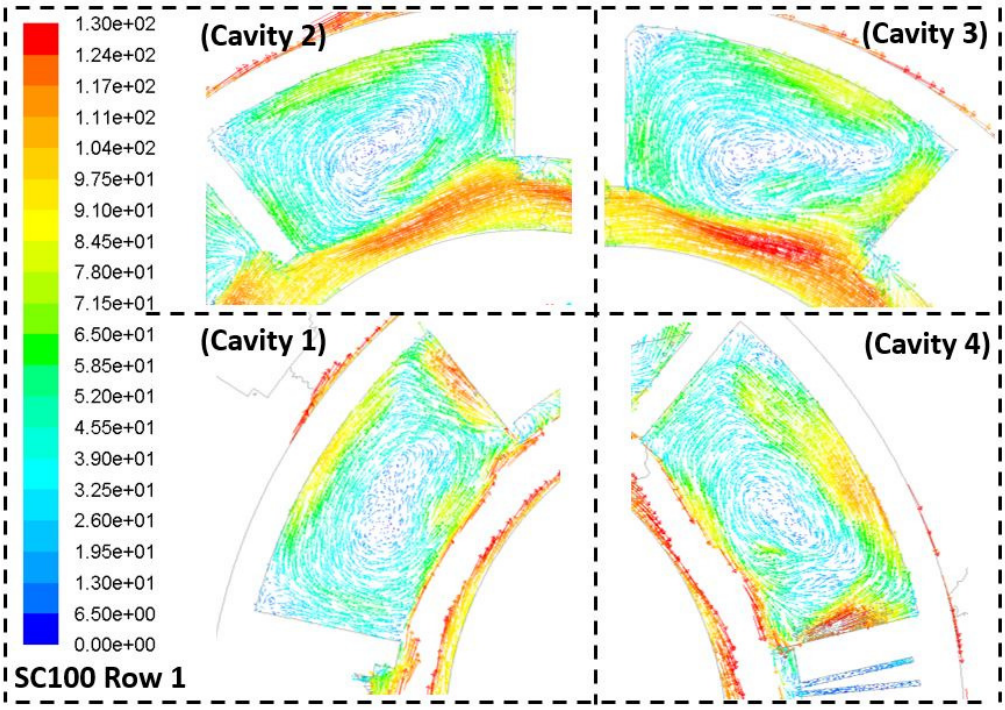

Figure C.1: Relative velocity vectors colored by relative velocity magnitude on diagonal planes for row 1 cavities

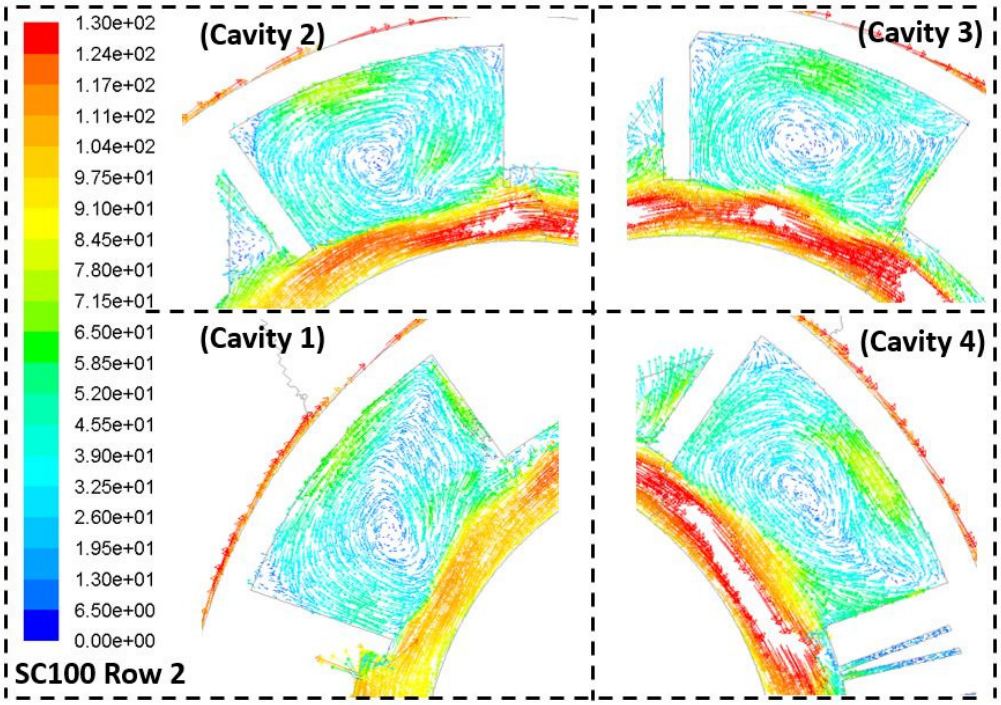

Figure C.2: Relative velocity vectors colored by relative velocity magnitude on diagonal planes for row 2 cavities

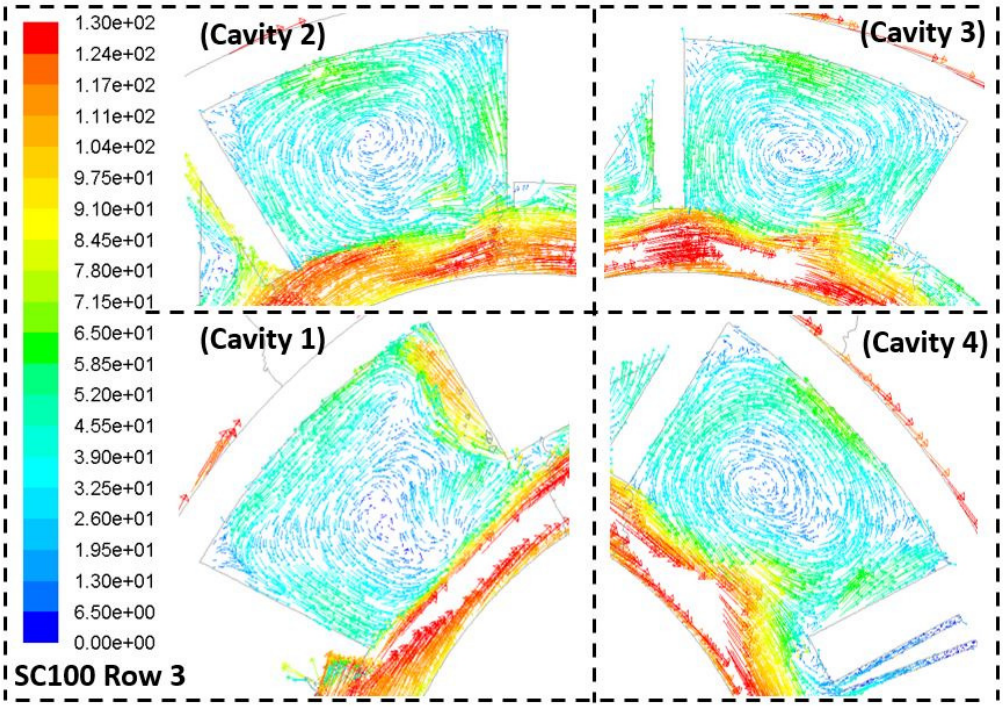

Figure C.3: Relative velocity vectors colored by relative velocity magnitude on diagonal planes for row 3 cavities

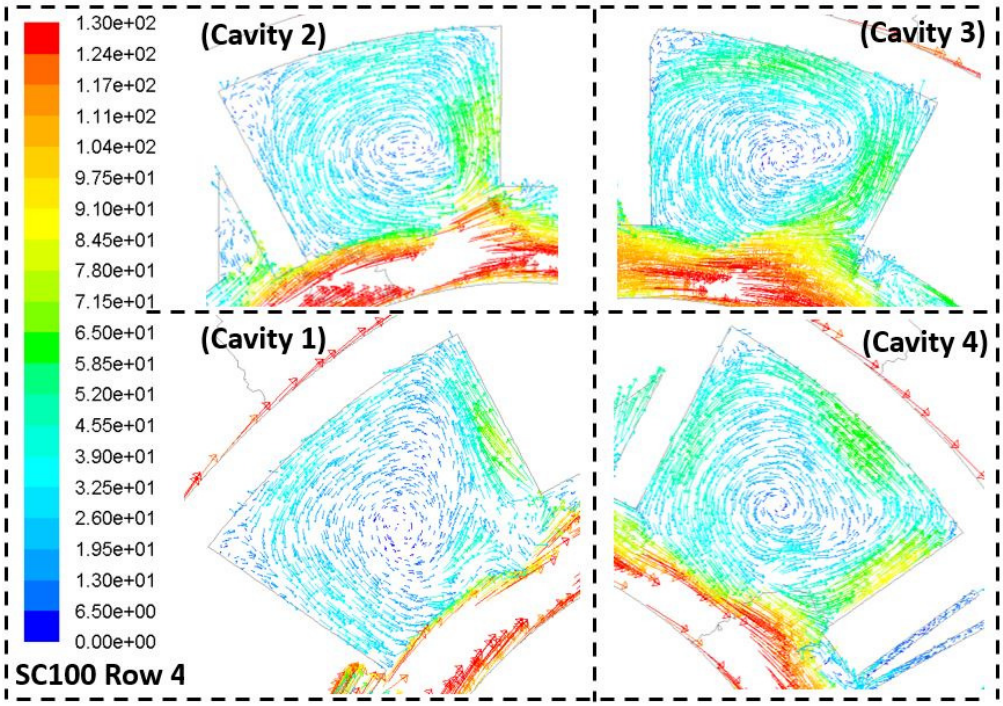

Figure C.4: Relative velocity vectors colored by relative velocity magnitude on diagonal planes for row 4 cavities

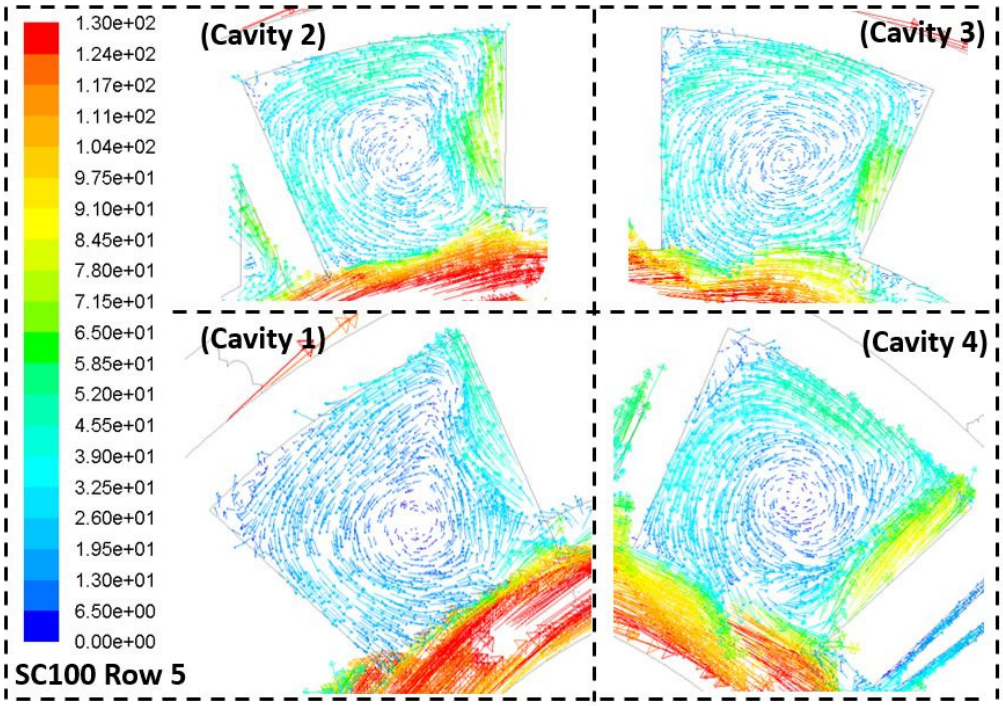

Figure C.5: Relative velocity vectors colored by relative velocity magnitude on diagonal planes for row 5 cavities

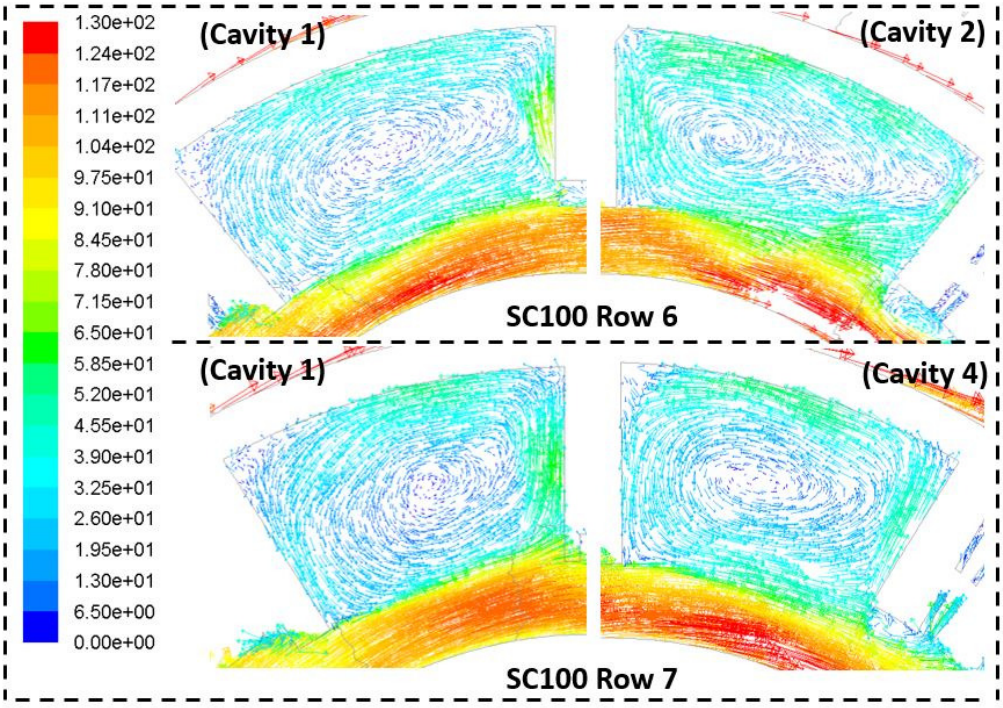

Figure C.6: Relative velocity vectors colored by relative velocity magnitude on diagonal planes for row 6 and row 7 cavities

APPENDIX D

PARAMETRIC CASES

Table D.1: Inlet parametric cases

Case	Inlet angle (degree)	Total Velocity (m/s)
1	28	79
2	28	85
3	28	92
4	28	98
5	28	104
6	33	68
7	33	73
8	33	79
9	33	84
10	33	90
11	38	60
12	38	65
13	38	70
14	38	75
15	38	80
16	43	54
17	43	59
18	43	63
19	43	67

20	43	72
21	48	50
22	48	54
23	48	58
24	48	62
25	48	66

Table D.2: Geometric parametric cases

Case	Width (m)	Cavity Opening (degree)
26	0.03	23
26	0.035	
26	0.04	
26	0.045	
26	0.05	
26	0.03	27
26	0.035	
26	0.04	
26	0.045	
26	0.05	
26	0.03	31
26	0.035	
26	0.04	
26	0.045	
26	0.05	
26	0.03	35
26	0.035	

Table D.2: Geometric parametric cases

Case	Width (m)	Cavity Opening (degree)
26	0.04	
26	0.045	
26	0.05	
26	0.03	39
26	0.035	
26	0.04	
26	0.045	
26	0.05	

Table D.3: Validation Cases

Case		Geometric Parameter		Inlet parameter			
		Width (m)	**Cavity Opening (degree)**	**Inlet angle (degree)**	**V_ax (m/s)**	**V_tot (m/s)**	**V_tang (m/s)**
Coupled	**1**	0.043	37.00	30.00	39.00	78.00	67.55
	2	0.047	23.00	35.00	45.00	78.46	64.27
	3	0.038	28.00	41.00	48.00	73.16	55.22
	4	0.032	38.00	44.00	41.00	59.02	42.46
	5	0.042	33.00	30.00	44.00	88.00	76.21
	6	0.037	26.00	33.00	40.00	73.44	61.59
	7	0.044	30.00	38.00	42.00	68.22	53.76
GEO ONLY	**8**	0.036	29.00	30.00	37.00	74.00	64.09
	9	0.039	26.00	30.00	37.00	74.00	64.09
	10	0.041	32.00	30.00	37.00	74.00	64.09
	11	0.043	27.00	30.00	37.00	74.00	64.09

	12	0.037	34.00	30.00	37.00	74.00	64.09
Inlet ONLY	**13**	0.040	35.00	36.00	38.00	64.65	52.30
	14	0.040	35.00	32.00	42.00	79.26	67.21
	15	0.040	35.00	43.00	46.00	67.45	49.33
	16	0.040	35.00	39.00	43.00	68.33	53.10
	17	0.040	35.00	34.00	47.00	84.05	69.68

REFERENCES

[1] *Basic ac generators*, http://www.asope.org/pdfs/AC_Electrical_Generators_ASOPE.pdf, Accessed: 2016-01-20.

[2] K Hattori, K Ide, F Goto, A Semba, and T Watanaba, "Sophisticated design of turbine generator with inner cooler ventilation system",

[3] *Siemens inc., cutout view of aircooled turbo-generator*, www.energy.siemens.comhqenfossil-power-generationgeneratorssgen-1000a-series.html, Accessed: 2017-09-25.

[4] M. Say, *The Performance and Design of Alternating Current Machines*. 1936.

[5] H Jamshidi, "Ventilation of a Model Hydro-Generator", 2015.

[6] G. S. Porepp, "Characteristics of ventilation circuits applied to cylindrical rotor synchronous machines", no. June, 2013.

[7] Aldo Boglietti, Andrea Cavagnino, David Staton, Martin Shanel, Markus Mueller, and Carlos Mejuto, "Evolution and Modern Approaches for Thermal Analysis of Electrical Machines", *IEEE Transactions on Industrial Electronics*, vol. 56, no. 3, pp. 871–882, 2009.

[8] I. AGT Services, "Generator field winding shorted turns: Observed conditions and causes",

[9] R. J. Zawoysky and K. C. Tornroos, "Ge generator rotor design, operational issues, and refurbishment options",

[10] C. J. Mozina, "Power plant "horror stories"",

[11] C. V. aughan, "Premature failure of modern generators",

[12] D. A. Howey, P. R. Childs, and A. S. Holmes, "Air-gap convection in rotating electrical machines", *IEEE Transactions on Industrial Electronics*, vol. 59, no. 3, pp. 1367–1375, 2012.

[13] A. Boglietti, "Special Section on Thermal Issues in Electrical Machines and Drives - Guest editorial", *IEEE Transactions on Industrial Electronics*, vol. 55, no. 10, pp. 3498–3499, 2008.

[14] M. W. Blackwell, O. R. Tutty, E. Rogers, and R. D. Sandberg, "Computational fluid dynamics based iterative learning control for smart rotor enabled fatigue load reduction in wind turbines", *2014 American Control Conference*, no. Ilc, pp. 4446–4451, 2014.

[15] Y. Lu, W. Yin, J. Han, W. Li, and P. Chen, "Effect of insulation property and distribution of turbo generator rotor on temperature field", in *2008 World Automation Congress*, 2008, pp. 1–5.

[16] A. Ben Nachouane, A. Abdelli, G. Friedrich, and S. Vivier, "Numerical approach for thermal analysis of heat transfer into a very narrow air gap of a totally enclosed permanent magnet integrated starter generator", *2015 IEEE Energy Conversion Congress and Exposition, ECCE 2015*, pp. 1749–1756, 2015.

[17] Y. J. Guo, P. Jin, Y. Yuan, H. Y. Lin, Z. F. Chen, B. C. Guo, and J. N. Dong, "Thermal analysis of 3MW permanent magnet embedded salient pole wind generator", *2015 18th International Conference on Electrical Machines and Systems, ICEMS 2015*, vol. 30, pp. 1005–1009, 2016.

[18] S. J. Pickering, D. Lampard, and M. Shanel, "Modelling ventilation and cooling of the rotors of salient pole machines", *IEMDC 2001 - IEEE International Electric Machines and Drives Conference*, pp. 806–808, 2001.

[19] D. Camilleri and R. Rolston, "Rotor Radial Vent Pumping in Large Synchronous Electrical Machines", pp. 1–6, 2016.

[20] Y. L. Y. Lu, W. Y. W. Yin, P. C. P. Chen, and W. L. W. Li, "Mechanism research on air mass flow rate distribution in rotor radial ducts of turbo generator with sub-slot ventilation", *2008 World Automation Congress*, 2008.

[21] R. A. Baudry and F. E. I. King, "Improved Cooling for Generators of Large Rating", 1965.

[22] F. D. Newbury, "Present limits of speed and output of single-shaft turbo generators", *Proceedings of the American Institute of Electrical Engineers*, vol. 38, no. 11, pp. 1233–1242, 1919.

[23] D. Harrington and J. E. McElligott, "New developments in armature winding arrangements for large turbine generators [includes discussion]", *Transactions of the American Institute of Electrical Engineers. Part III: Power Apparatus and Systems*, vol. 73, no. 1, 1954.

[24] T Bpckstrom, C Sadarangani, and S Ostlund, "New development in diesel driven generators", no. 444, pp. 239–243, 1997.

[25] S. L. Henderson and C. R. Soderberg, "Recent improvements in turbine generators", *Transactions of the American Institute of Electrical Engineers*, vol. 47, no. 2, pp. 549–570, 1928.

[26] M. H.J. J. RYAN, "Some Factors in the Mechanical Design of High-Speed Turbogenerators", vol. 59, no. January, pp. 51–56, 1940.

[27] H. D. Taylor, "Design Features and Characteristics or Large Steam Turbine Generators", pp. 1335–1346, 1958.

[28] C. Guan, W. Li, and P. Zheng, "Coupled analysis on multi-physics of turbo-generator used in IGCC power station", *2010 International Conference on Power System Technology: Technological Innovations Making Power Grid Smarter, POWERCON2010*, pp. 1–6, 2010.

[29] W. Fei, P. C. K. Luk, D. Wu, and B. Xia, "Approximate three-dimensional finite element analysis of large permanent magnet sychronous generators with stator radial ventilating ducts", *IECON Proceedings (Industrial Electronics Conference)*, pp. 7313–7318, 2013.

[30] H. Ansari, M. Mohammadi, and A. A. Kharamani, "Mathematical Modelling of the Ventilation System of Large Turbo Generators : Using Lumped-Parameter Model", no. 3, pp. 3–7,

[31] E. M. Johnson and C. P. Holder, "The design of high-speed salient-pole a.c. generators for water-power plants", *Electrical Engineers, Journal of the Institution of*, vol. 1952, no. 10, pp. 253–254, 1952.

[32] S. Ding, Z. Sun, and D. Deng Lei, "Calculation and analysis of fluid flow and heat transfer for large doubly-fed wind generator", *Proceedings of 2011 6th International Forum on Strategic Technology*, vol. 1, no. 1, pp. 619–623, 2011.

[33] J. J. Simond, M. T. Xuan, and R. Wetter, "An innovative inductive air-gap monitoring for large low speed hydro-generators", *Proceedings of the 2008 International Conference on Electrical Machines, ICEM'08*, pp. 1–5, 2008.

[34] M. Kimura, D. Kori, a. Komura, H. Mikami, K. Ide, T. Fujigaki, M. Iizuka, and M. Fukaya, "A study of permanent magnet rotor for large scale wind turbine generator system", *2012 XXth International Conference on Electrical Machines*, pp. 1161–1171, 2012.

[35] W. Li, D. Li, J. Li, and X. Zhang, "Influence of rotor radial ventilation ducts number on temperature distribution of rotor excitation winding and fluid flow state between two poles of a fully air-cooled hydro-generator", *IEEE Transactions on Industrial Electronics*, vol. 64, no. 5, pp. 3767–3775, 2017.

[36] L. Weili, G. Chunwei, and C. Yuhong, "Influence of rotation on rotor fluid and temperature distribution in a large air-cooled hydrogenerator", *IEEE Transactions on Energy Conversion*, vol. 28, no. 1, pp. 117–124, 2013.

[37] W. J. Gilson, "Field Preheating ror Large Turbine Generators", 1954.

[38] J. C. Adamowski, A. T. Souza, N. Perez, A. A. Lima, P. D. Oda, and H. H. Tiba, "Ultrasonic dynamic air-gap monitoring system for large hydro-generators", *IEEE International Ultrasonics Symposium, IUS*, pp. 1311–1314, 2013.

[39] A. Hong-wen, M. Zhi-yong, L. Zhuang, Z. Cai-mao, and L. Ying, "Analysis on shaft torsion response of 600mw steam turbine unit under quick load regulation", in *The 26th Chinese Control and Decision Conference (2014 CCDC)*, 2014, pp. 204–208.

[40] D. B. Reay, "Distortion of turbo-alternator rotor windings through thermal stress", *Proceedings of the IEE - Part A: Power Engineering*, vol. 102, no. 3, pp. 349–361, 1955.

[41] K. Sawatani, K. Sano, and S. Ootake, "Stator frame deformation problem in large diameter hydro-generators", *IEEE Transactions on Energy Conversion*, vol. EC-1, no. 1, pp. 33–38, 1986.

[42] K. Elkington, V. Knazkins, and M. Ghandhari, "On the rotor angle stability of power systems with Doubly Fed Induction Generators", *2007 IEEE Lausanne Power Tech*, pp. 213–218, 2007.

[43] B. Anvari, X. Li, H. A. Toliyat, A. Palazzolo, Z. Wang, and X. Han, "A coreless permanent-magnet machine for a magnetically levitated shaft-less flywheel", *2017 IEEE International Electric Machines and Drives Conference, IEMDC 2017*, 2017.

[44] L. Weili, Q. Hongbo, Z. Xiaochen, and Y. Ran, "Influence of copper plating on electromagnetic and temperature fields in a high-speed permanent-magnet generator", *IEEE Transactions on Magnetics*, vol. 48, no. 8, pp. 2247–2253, 2012.

[45] A. F. Armor, "1981 power engineering society prize paper transient, three-dimensional, finite-element analysis of heat flow in turbine-generator rotors", *IEEE Power Engineering Review*, vol. PER-1, no. 9, pp. 11–23, 1981.

[46] R. H. Qu, "Keynote talk - Design of large electrical machines", *2013 IEEE International Conference on Applied Superconductivity and Electromagnetic Devices, ASEMD 2013*, vol. 23, no. 3, p. 536, 2013.

[47] D. Manns, "Thermal endurance testing of rotor turn insulating materials", in *Conference Record of the 2006 IEEE International Symposium on Electrical Insulation*, 2006, pp. 21–24.

[48] H. Ito, S. Sekito, K. Miyaike, and S. Takahashi, "Turbo-generator life management and service technology", *IEMDC 2003 - IEEE International Electric Machines and Drives Conference*, vol. 1, pp. 403–410, 2003.

[49] F. Zheng, S. Sun, L. Zhou, W. Liu, J. Wang, and L. Han, "Study on large asynchronous motor starting check for auxiliary power system", *Asia-Pacific Power and Energy Engineering Conference, APPEEC*, no. 1, pp. 2–5, 2010.

[50] Z. Bi and C. Gao, "Power System Dynamic Voltage Stability Analysis Considering Wind Power", *2014 IEEE 12th International Conference on Dependable, Autonomic and Secure Computing*, pp. 129–132, 2014.

[51] J. Zhang, X;Zhang, H; Gerada, C; Cao, J; Li, "HZ-10 A kind of alloy designed for HSPMG rotor sleeve.", vol. 60, p. 2013, 2013.

[52] S. Tetrault, G. Stone, and H. Sedding, "Monitoring partial discharges on 4 kV motor windings", *Record of Conference Papers. IEEE Industry Applications Society 44th Annual Petroleum and Chemical Industry Conference*, pp. 159–165, 1997.

[53] S. S. Ngu, D. G. Dorrell, and C. Cossar, "Design and operation of very slow speed generators for a bristol cylinder sea wave generating device", *IEEE Transactions on Industry Applications*, vol. 50, no. 4, pp. 2749–2759, 2014.

[54] C. A. Evangelista, A. Pisano, P. Puleston, and E. Usai, "Receding Horizon Adaptive Second-Order Sliding Mode Control for Doubly-Fed Wind Turbine", *IEEE Transactions on Control Systems Technology*, vol. 25, no. 1, pp. 73–84, 2017.

[55] N. Zhao, Z. Q. Zhu, and W. Liu, "Comparison of rotor eddy current losses in permanent magnet motor and generator", *2011 International Conference on Electrical Machines and Systems, ICEMS 2011*, 2011.

[56] H. Fang, R. Qu, J. Wang, Z. Zhu, and H. Chen, "Design of a novel torque tube for a direct-drive superconducting wind generator", *IEEE Transactions on Applied Superconductivity*, vol. 25, no. 3, pp. 3–6, 2015.

[57] J. Leclerc and P. J. Masson, "Testing of a Subscale HTS Coil for Wind Turbine Generator", *IEEE Transactions on Applied Superconductivity*, vol. 26, no. 3, pp. 2–5, 2016.

[58] J. F.A. M. G. Shrestha, H. Polinder, D.J. Bang, "A New Concept for Weight Reduction of Large", *Engineering*, pp. 1–6, 2008.

[59] D. Xiang, C. Wang, and Y. Liu, "Switching frequency dynamic control for dfig wind turbine performance improvement around synchronous speed", *IEEE Transactions on Power Electronics*, vol. 32, no. 9, pp. 7271–7283, 2017.

[60] S. Ding, Z. Sun, and D. Deng Lei, "Calculation and analysis of fluid flow and heat transfer for large doubly-fed wind generator", *Proceedings of 2011 6th International Forum on Strategic Technology*, vol. 1, no. 1, pp. 619–623, 2011.

[61] N. Zhao, Z. Q. Zhu, and W. Liu, "Thermal analysis and comparison of permanent magnet motor and generator", *2011 International Conference on Electrical Machines and Systems*, vol. 47, no. 1, pp. 1–5, 2011.

[62] T. Lei, M. Barnes, and a. C. Smith, "Thermal cycling evaluation for DFIG wind turbine power converter based on joint modelling", *2013 IEEE Energy Conversion Congress and Exposition*, pp. 3845–3851, 2013.

[63] W.-l. Li, P. Cheng, S.-p. Yuan, and M.-w. Zhang, "Thermal Analyses and Calculations of 1.5MW Half-Direct Permanent Magnet Wind Power Generator When PM Embedded in Different Rotor Positions", *2011 International Conference on Computer Distributed Control and Intelligent Environmental Monitoring*, pp. 299–303, 2011.

[64] J. L. Rueda and I. Erlich, "Impacts of large scale integration of wind power on power system small-signal stability", *2011 4th International Conference on Electric Utility Deregulation and Restructuring and Power Technologies (DRPT)*, pp. 673–681, 2011.

[65] C. Guan, W. Li, and P. Zheng, "Coupled analysis on multi-physics of turbo-generator used in IGCC power station", *2010 International Conference on Power System Technology: Technological Innovations Making Power Grid Smarter, POWERCON2010*, pp. 1–6, 2010.

[66] M. Kovacic, Z. Hanic, and M. Vrazic, "Design of large synchronous turbo-generator monitoring system", *Proceedings - 2012 20th International Conference on Electrical Machines, ICEM 2012*, pp. 1631–1636, 2012.

[67] M. Testing, *Generator maintenance testing*, pp. 466–535, ISBN: 0471614475.

[68] M. Mohammadi, H. Ansari, P. Bahemmat, and A. A. Kharamani, "Thermal Analysis of the Rotor of Large Air-cooled Turbo Generators",

[69] P. L. Stephenson, "Calculation of temperature rises due to conductor losses in a radially-cooled turbogenerator rotor", in *1989 Fourth International Conference on Electrical Machines and Drives Conf. Publ. No. ??)*, 1989, pp. 150–153.

[70] Y. J. Yang, Y. P. Liang, and J. Chen, "Thermal field calculation for the rotor of large turbo-generator", *Proceedings of the 6th International Forum on Strategic Technology, IFOST 2011*, vol. 1, no. 2, pp. 584–588, 2011.

[71] L. Hitachi, *Direct measurement of strand temperature of turbo-generator with fbg sensors*, www.cigre.org/content/download/16666/677152/version/1/file/A1_109_2012.pdf, Accessed:2016-03-18.

[72] C. Mejuto, M. Mueller, M. Shanel, A. Mebarki, and D. Staton, "Thermal modelling investigation of heat paths due to iron losses in synchronous machines", in *2008 4th IET Conference on Power Electronics, Machines and Drives*, 2008, pp. 225–229.

[73] D. B.B.C. J. Neale, A; Derome, "Determination of Surface Convective Heat Transfer Coefficient by CFD", in *11th Canadian Conference on Building Science and Technology*, 2007.

[74] P. H. Connor, S. J. Pickering, C Gerada, C. N. Eastwick, C Micallef, and C Tighe, "Computational fluid dynamics modelling of an entire synchronous generator for improved thermal management", *IET Electric Power Applications*, vol. 7, no. 3, pp. 231–236, 2013.

[75] E. Jarczynski, T. Wetzel, and J. Fealey, "Evolution of air-cooled turbine generator design", *IEMDC 2003 - IEEE International Electric Machines and Drives Conference*, vol. 1, pp. 117–123, 2003.

[76] *Simulation of turbulent flows (me469b/3/gi)*, https://web.stanford.edu/class/me469b/handouts/turbulence.pdf.

[77] A. Inc., *Ansys fluent theory guide*, https://www.sharcnet.ca/Software/Ansys/16.2.3/en-us/help/flu_th/flu_th.htmll, Accessed: 2015-10-1.

[78] T. Saad, "Turbulence modeling for beginners",

[79] A. Inc., "Modeling turbulence flow: Introductory fluent training",

[80] "Turbulence modeling: Introduction to ansys fluent (15.0 release)", 2014.

[81] *Ansys inc., wall boundary conditions*, http://www.afs.enea.it/project/neptunius/docs/fluent/html/ug/node250.htm, Accessed: 2015-03-10.

[82] *Ansys inc., ansys fluent 14.0 theory guide*, https://www.scribd.com/doc/140163341/Ansys-Fluent-14-0-Theory-Guide, Accessed: 2015-02-25.

[83] *Tips and tricks: Inflation layer meshing in ansys*, https://https://www.computationalfluiddynamics.com.au/tips-tricks-inflation-layer-meshing-in-ansys/, Accessed: 2017-03-22.

[84] Y. Taniyama, Y. Kabata, Y. Hashidate, K. Shioda, and H. Katayama, "IMECE2005-80132", pp. 1–8, 2005.

[85] Z. Wang and J. Han, "Numerical simulation of air flow distribution in large air-cooled turbo generator rotor at different rotation speed and inlet pressure", *2014 17th International Conference on Electrical Machines and Systems, ICEMS 2014*, no. 50976027, pp. 2352–2355, 2015.

[86] T. L. J. Han, G. Hong and L. Yiping, "Numerical Studies on the Flow Field of Stator and Air Gap for Large Air-cooled Turbo-geneartor", in *2012 Trans Tech Publications*, 2012, pp. 970–975.

[87] O. V. Antonyuk, Z. I. Gurevich, and T. N. Kartashova, "Current Problems and Trends in Gas Cooling of Turbogenerators", *Power Technology and Engineering*, vol. 48, no. 4, pp. 316–321, 2014.

[88] Y. L. Y. Lu, W. Y. W. Yin, P. C. P. Chen, and W. L. W. Li, "Mechanism research on air mass flow rate distribution in rotor radial ducts of turbo generator with sub-slot ventilation", *2008 World Automation Congress*, 2008.

[89] T. Hayase, J. A. C. Humphrey, and R. Greif, "Numerical calculation of convective heat transfer between rotating coaxial cylinders with periodically embedded cavities", *Journal of Heat Transfer*, vol. 114, no. 3, pp. 589–597, 1992.

[90] T. L. Bergman, A. S. Lavine, F. P. Incropera, and D. P. DeWitt, *Fundamentals of heat and mass transfer*.

[91] G. Klempner and I. Kerszenbaum, *Generator Design and Construction*. Wiley, 2008.

[92] *Design of experiment study notes*, `https://www2.isye.gatech.edu/~jeffwu/isye6413/unit_06_12spring.pdf`, Accessed: 2016-09-12.

[93] *Fractional factorial design*, `http://www.six-sigma-material.com/Design-of-Experiments.html`, Accessed: 2017-07-04.

[94] *Fractional factorial design*, `http://www2.stat.duke.edu/~banks/218-lectures.dir/spec-lect3.pdf`, Accessed: 2017-07-04.

[95] *Polynomial models*, `https://www.mathworks.com/help/curvefit/polynomial.html`, Accessed: 2016-09-12.

[96] MathWorks, *Documentation: Plot*, `https://www.mathworks.com/help/stats/linearmodel.plot.html`, Accessed: 2017-10-23.